Spatial-Statistical Properties of Geochemical Variability as Constraints on Magma Transport and Evolution Processes at Ocean Ridges

Martin Lee Collier

Submitted in partial fulfillment of the
requirements for the degree
of Doctor of Philosophy
in the Graduate School of Arts and Sciences

COLUMBIA UNIVERSITY

2012

ABSTRACT

Spatial-Statistical Properties of Geochemical Variability as Constraints on Magma Transport and Evolution Processes at Ocean Ridges

Martin Lee Collier

The research presented in this thesis employs spatial and statistical properties of major element variability in basaltic lavas and mantle residues to constrain some of the processes and dynamics occurring beneath ocean ridge magmatic systems. Ocean ridges represent a critical setting for many geochemical fractionation processes involved in the chemical evolution of the silicate Earth, and are fundamental to the plate tectonic cycle. Because of the inherent inaccessibility, it remains an ongoing challenge to interpret the geochemistry of ocean ridge lavas and exposed mantle residues in order to extract information about the petrogenetic and geodynamic workings of ocean ridge magmatic systems. This endeavor continues to require a concerted effort, incorporating field work, laboratory experimentation and quantitative modeling, in which the identification of features in the spatial or statistical distribution of geochemical variability represents an important contribution. In the three main chapters of this thesis, I apply techniques of exploratory data analysis, computational statistics, and petrologic modeling to develop original ideas about the relationship between sampled major element variability and the effects of specific processes, both petrogenetic and scientific: crystallization, melt transport, and sampling.

In Chapter 2, I use spatial patterns of mid-ocean ridge basalt (MORB) glass variability to test competing hypotheses about crystallization in the thermal boundary layer beneath ocean ridges. I develop the hypothesis that *reactive crystallization* (crystallization influenced by chemical exchange with surrounding peridotite) could result in a different geochemical evolution of crystallizing magmas than expected for fractional crystallization. According to this hypothesis, "fractionation-corrected" MORB variability could be caused largely by sample-to-sample variations in the relative extents of reactive versus fractional crystallization. I demonstrate that MORB major element variability observed within 30-km-scale spatial bins contains 40-70% of globally observed variability, consistent with the predicted effects of reactive crystallization, but inconsistent with mantle temperature variations. Chapter 3 considers the effect of spatially heterogeneous sampling on apparent variability in MORB glasses. I demonstrate that MORB variability, as represented by the PetDB MORB glass

database, contains large variability in sampling density, leading to significant artifacts in the estimated relative frequency of different MORB compositions. I introduce a method for removing these artifacts, and show that the increase in MORB data availability over the past decades has not been sufficient to increase significantly the resolution with which major element variability systematics can be studied at global or regional length scales, at least in comparison to early syntheses of global MORB data (e.g., *Dick et al.*, 1984; *Klein and Langmuir*, 1987). Chapter 4 examines statistical variability within spatially defined volumes of mantle residue exposed in the Oman ophiolite. I provide a preliminary map of intermediate-scale compositional variability within the southernmost Oman ophiolite massif, in which multiple, spatially coherent, compositionally distinctive, $\sim$20-100 km^2 regions are resolved, representing the first mapping of compositional mantle domains at this length scale anywhere in the world. I interpret the observations as the consequence of regionally distinctive internal proportions of different mantle lithologies (e.g., dunite versus harzburgite), in turn reflecting the organization of focused melt transport at mid-ocean ridges into "channel-rich" and "channel-poor" zones.

This research offers a number of lessons and opportunities for future investigations. Chapter 2 strengthens the case that there is considerable melt-rock reaction involved in MORB petrogenesis, and that this may complicate inferences from major elements in lavas about conditions within ocean ridge magmatic systems. Chapter 4 provides the most detailed description to date of the intermediate-scale variability within the best available analogue of ocean-ridge-processed residual mantle. Furthermore, Chapter 4 illustrates the utility of considering the full statistical distribution of geochemical variability, as opposed to considering variability through simple summary statistics. I hope that the observational approach described in Chapter 4, as well as the examples of data analysis applications provided in Chapter 3, will also contribute to making comprehensive analysis of the spatial-statistical distribution of variability in ocean ridge samples more tractable and routine in future work by the "high-temperature geochemistry" community.

Contents

List of Tables

List of Figures

Acknowledgments

The research in this thesis could be undertaken only with the guidance, support, constructive criticism and inspiration of many friends, colleagues and mentors. I consider myself very fortunate to have had the experience of working closely with Marc Spiegelman, my primary academic advisor. I will always be thankful for the intense exposure to his style of doing science – intellectually fast-paced, uncompromisingly rigorous, yet always good-natured. I have no doubt that I will continue my scientific career with a greatly enhanced quantitative toolkit and perspective as a direct result of what I've learned from Marc, but I hope that some of his humor, wit and patience rubbed off as well... Although he was not officially my primary advisor, Peter Kelemen's influence on my scientific development and on the evolution of this thesis was just as critical as Marc's. On several occasions, Peter generously provided opportunities to learn from direct experience in the field or in the laboratory that can only be described as fantastic, and our discussions always challenged me to refine my ideas further. Peter's broad yet detailed knowledge about the geologic observations and history of thought behind present-day concepts in igneous petrology continually motivated me to study the literature more deeply and broadly myself.

I am also thankful for the opportunity to interact with masters and doctoral thesis committee members Dave Walker, Steve Goldstein, Goran Ekstrom, Al Hofman and Alberto Saal. Their time and invaluable input benefitted this thesis in numerous ways. The additional guidance and many "tricks of the trade" learned from other unofficial mentors were also essential ingredients for this thesis. Many thanks to Ben Holtzman, Raj Dasgupta, Rich Katz, Karen Hanghoj, Taber Hersum, and John Rudge, all of whom made significant impacts on my understanding of igneous petrology, quantitative scientific tools, and the scientific process in general.

Field work in Oman – one of the greatest highlights of my time in grad school – was significantly more productive and enjoyable thanks to the help and companionship of field assistants Byrdie Renik and Jill VanTongeren. Success with the subsequent lab work was made possible with the help and patience of Shahla Ali, Sidney Heming, Tony Buono, Dave Walker, Susanne Straub, and Jill VanTongeren, as well as Charlie Mandeville, Njoki Gitahi and Beth Goldoff at AMNH. Over the years I've enjoyed countless discussions and interactions with people from all over Lamont, including John Longhi, Terry Plank, Roger Buck, Bill Menke, Nick Christie-Blick, Mark Anders, Kerstin Lehnert, Karin Block, and Esteban Gazel. Special thanks to Meredith Nettles, Jim Gaherty, Spahr Webb, and everyone else in the seismology group for letting me attend the weekly meetings, and for generally taking the time to answer my simple but numerous questions. I am also very thankful for the huge amount of behind-the-scenes support provided kindly by Mia Leo, Carol Mountain, Missy

Pinckert, Jean Leote, Bree Burns, Jennifer Cho, Karen Benedetto, Bonnie Bonkowski, Dana Miller, Mary Russell, Kathryn Kennedy, and Stacey Vassallo. Many thanks to Lorenzo Polvani and the IGERT program for the large assortment of contributions to this thesis and to my graduate school experience in general (from thought-provoking seminars to lunch money to a laptop). Charlie Langmuir, Mark Ghiorso, Yaoling Niu, and Wendy Bohrson provided substantial inputs to this thesis as publication reviewers and are thanked as well.

One of the best aspects of graduate school life was the time spent with my fellow graduate students and friends. It is fun to remember (many of) the adventures we had in NYC and elsewhere, and I am very grateful to everyone for their support during some of the more difficult times as well. There are unfortunately too many to name here, but I will do my best to try anyway (in no particular order): Jill VanTongeren, Janelle Homburg, Rich Katz, Ben Holtzman, Raj Dasgupta, Ethan Coon, Karen Hanghoj, Taber Hersum, John Rudge, Tony Buono, Jessica Stuart, Jason Jweda, Dalia Bach, Ann Cook-Yockey, Katie Leonard, Irina Gorodetskaya, Kirstie Stramler, Kori Newman, Hannah Abend, Chad Holmes, Agnes Helmstetter, Anna Wall, Stacia Gordon, Kimmy Szeto, Shahla Ali, Louisa Bradtmiller, Kevin Jones, Adrienne Block, Anna Foster, Rafael Almeida, Rondi Davies, Rob Bialas, Merry Cai, Anna Cipriani, Wei Du, Heather Griffith Chadha, Vala Hjorleifsdottir. As this dissertation was being written, many a day passed where the only people I interacted with were the kind folks at Giacomo's Fine Foods (best bagels in NYC): Jose, Fatima, Omar and Sylvia. Finally, I am happiest of all to acknowledge the support and inspiration provided by Byrdie Renik. Our paths first crossed here at Lamont, but they've since continued on inseparably into the future, to Houston and beyond.

Chapter 1

Introduction

The global mid-ocean ridge system is one of Earth's dominant surface features, comprising a near-continuous, $\sim$ 60,000-km-long chain of undersea volcanoes. Mid-ocean ridges define the active boundaries of diverging tectonic plates, where hot mantle rock, drawn towards the surface through overlying plate motions, undergoes decompression-induced partial melting (*Green and Ringwood*, 1967; *Oxburgh and Turcotte*, 1968). The resulting magmatic systems are fundamental to the plate tectonic cycle (e.g., *Hess*, 1962; *Le Pichon et al.*, 1973). Ocean ridges produce the most abundant type of igneous rock, known as mid-ocean ridge basalt (MORB), which ascends to form the oceanic crust that covers nearly two-thirds of Earth's surface (*Project*, 1981; *Ahern and Turcotte*, 1979; *Cogley*, 1984). The underlying, complimentary mantle residues – themselves structurally and compositionally modified by ocean ridge magmatism – eventually cool by conduction to the surface, forming the dominant component of oceanic lithosphere (*McKenzie and Bickle*, 1988; *Dick et al.*, 1984; *Michael and Bonatti*, 1985; *Dick*, 1989; *Nicolas*, 1989). Ocean ridges also give rise to significant heat loss from Earth's interior (e.g., *Pollack et al.*, 1993), and provide the setting for a host of geochemical fractionation and mass transfer processes (e.g., *Green and Ringwood*, 1967; *Gast*, 1968; *Kushiro*, 1968; *Shaw*, 1970; *O'Hara*, 1977; *Grove et al.*, 1992; *Langmuir et al.*, 1992). For these reasons, the study of ocean ridge magmatism – through both geodynamic and petrologic perspectives – contributes to greater understanding of the thermal and compositional evolution of Earth's silicate crust and mantle throughout geologic time.

One of the primary opportunities for studying modern ocean ridges (complimentary to geophysical techniques for imaging the subsurface and to field studies of relict magmatic systems exposed in ophiolites) is through geochemical and petrologic characterization of MORB lava or abyssal peridotite samples collected from the seafloor. Although it remains impossible to observe the workings of ocean ridge magmatism more directly, this approach has led to much progress in constraining the source materials, conditions and processes involved. Conditions within the partially molten region underlying ocean ridges, for example, can be

recorded in the relative proportions of geochemical components within each sample. Laboratory studies have shown that these components display different affinities for solids and melts, and are sensitive to the ambient pressure, temperature and system composition (e.g., *Bowen*, 1928; *Yoder and Tilley*, 1962; *Grove et al.*, 1992; *Hess*, 1992). There is also increasing recognition that the dynamics of the partially molten region can give rise to additional geochemical signatures. Nearly all MORB lavas are not in chemical equilibrium with mantle peridotite at low pressures, suggesting that factors including the relative time scales of melt transport, diffusive processes, and chemical reactions, or the extent of localization in melt transport exert additional influences on geochemical variability (*Kelemen*, 1990; *Spiegelman and Kenyon*, 1992; *Kelemen et al.*, 1995; *Aharonov et al.*, 1995; *Spiegelman*, 1996; *Kelemen et al.*, 1997a; *Spiegelman and Kelemen*, 2003). Quantitative modeling approaches – informed by phase equilibria experiments – have allowed the effects of a range of petrologic processes to be predicted, including partial melting, melt transport and focusing, melt-rock reaction, mixing, and crystallization (e.g. *McKenzie and Bickle*, 1988; *Weaver and Langmuir*, 1990; *Niu and Batiza*, 1991; *Longhi*, 1991; *Kinzler and Grove*, 1992; *Ghiorso and Sack*, 1995; *Iwamori et al.*, 1995; *Danyushevsky*, 2001; *Ghiorso et al.*, 2002; *Katz et al.*, 2003; *Asimow et al.*, 2004). Other features of MORB variability have been linked to the presence of heterogeneity in the source mantle (*Tatsumoto et al.*, 1965; *Tatsumoto*, 1966; *Zindler and Hart*, 1986; *Shen and Forsyth*, 1995; *Korenaga and Kelemen*, 2000; *Hofmann*, 2003). The ability of geochemical variability in magmas and residues to impact the geodynamic properties of the magmatic system and of the resulting oceanic lithosphere has also been recognized and studied (e.g., *Kelemen et al.*, 1995).

Yet despite these advances, the sampling of ocean ridges remains relatively sparse, and the tasks of interpreting geochemical variability and evaluating its implications remain ongoing. Major outstanding research problems include:

- **The development of links between magma dynamics and petrologic or geochemical observables**, e.g.: How does melt transport impact the length scales governing along-axis igneous variability? How and where is melt transport localized within the magmatic system? How does magma transport transition from porous flow along grain boundaries to crack flow and diking? How do the competing hypotheses available to answer these questions differ in terms of the predictions they make for variability in the composition of ocean ridges?

- **The extraction of information about petrologic processes from geochemical or lithologic variability in ocean ridge samples**, e.g.: How well do current petrologic frameworks for interpreting geochemical variability account for available

observations on ocean ridge samples? How unique or distinguishable is geochemical variability arising from processes other than melting or crystallization, including (1) melt-rock reaction, (2) magma mixing, (3) thermal and compositional variability in the shallow oceanic mantle prior to melting, (4) disequilibrium melt transport, and (5) hydrothermal processes?

- **The mechanisms by which ocean ridge magmatic systems impact the geodynamics of oceanic tectonic plates**, e.g.: How is the lower oceanic crust formed, and what geochemical and structural features does ocean ridge magmatism generate in the residual mantle, e.g., through localization of magma transport and/or deformation? How do such features influence the mechanical character of oceanic lithosphere? How completely does basaltic melt generated within the mantle escape to the surface? What effect does the presence of basaltic melt have on the dynamics of rifting?

The resolution of any of these questions will most likely involve a combination of data analysis and theory derived from quantitative modeling and laboratory experimentation. The identification of pertinent features in geochemical data is among the many critical steps in this process. Although easily taken for granted, the use of traditional visualization methods (e.g., scatter plots or "spider diagrams") is becoming increasingly difficult when applied to the large and growing data compilations presently available (e.g., *Lehnert et al.*, 2000). The sheer symbol density in such plots, for example, greatly complicates the search for patterns in the relative frequency of compositions within the "data cloud." Even in cases where patterns in relative frequency can be detected, assessing robustness can introduce additional difficulties (e.g., *Parman*, 2007; *Rudge*, 2008). Although the present thesis directly addresses only a few of the "big picture" questions listed above, the topic of extracting geologically interesting features from large geochemical data compilations is a core theme. In particular, the research described here embraces three principles: (1) To extract the maximum information content from geochemical data, it is necessary to consider the full *distribution* of variability expressed within sample suites. Although it is common practice to summarize variability through simple descriptive statistics (e.g., mean, standard deviation, etc.), this approach potentially overlooks other aspects of variability such as the presence of secondary modes or the characteristics of the distribution tails that can also be of geologic interest. (2) The power of geochemical data to test specific hypotheses is increased when detailed information about the spatial context of sampling is included in the analysis. (3) Methods of exploratory data analysis and computational statistics can allow the full spatial-statistical character of variability to be explored relatively efficiently.

In essence, the present thesis comprises applications of these principles. Some of the

conclusions developed here about the workings of ocean ridge magmatism correspondingly rely on "second-order" details within the distribution of geochemical variability. Spatial systematics in the variability of ocean ridge samples plays a particularly critical role. In Chapter 2, spatial patterns of MORB glass variability are used as a critical means for testing competing hypotheses about the operation of crystallization and melt transport in the thermal boundary layer beneath ocean ridges. Chapter 3 considers the effect of spatially heterogeneous sampling on apparent variability in MORB glasses, while Chapter 4 examines variability within spatially defined volumes of mantle residue exposed in the Oman ophiolite. Applications of computational statistics techniques such as probability density estimation, classification, and resampling are also widely used throughout this thesis. These techniques offer significant advantages in coping with the special challenge of studying the full multivariate statistical distributions defined by extensive geochemical data sets. (Both of the primary data sets studied in this thesis comprise very large sample sizes, e.g., N >> 1000.) Throughout this thesis, I focus on the character and potential significance of *major element* variability within MORB lavas and mantle residues. (Major elements are defined as those chemical components that individually represent a significant fraction of the sample mass, generally ≥ 0.5 weight %.)

The research carried out for this thesis is documented in three chapters and three appendices:

- Chapter 2 evaluates the hypothesis that *reactive crystallization* (crystallization influenced by chemical exchange with surrounding peridotite) could result in a different geochemical evolution of crystallizing magmas than expected for fractional crystallization. According to this hypothesis, "fractionation-corrected" MORB variability could be largely caused by sample-to-sample variations in the relative extents of reactive versus fractional crystallization. Variations in melt transport velocity through the thermal boundary layer, in turn, are predicted to modulate the relative proportion of reactive and fractional crystallization. *We demonstrate that MORB major element variability observed within 30-km scale spatial bins comprises 40-70% of globally observed variability, consistent with the predicted effects of reactive crystallization, but inconsistent with mantle temperature variations.* This work has been accepted for publication in *Journal of Petrology.*

- In Chapter 3, the spatial and statistical character of the PetDB MORB data compilation is examined in additional detail. In particular, the potential role of biased sampling is examined. *I demonstrate that MORB variability, as represented by the PetDB MORB glass database, contains large variability in sampling density, leading*

to significant artifacts in the estimated relative frequency of different MORB compositions. I introduce a method for removing these artifacts, and show that the increase in MORB data availability over the past decades has not been sufficient to increase significantly the resolution with which major element variability systematics can be studied at global or regional length scales, at least in comparison to early syntheses of global MORB data (e.g., Dick et al., 1984; Klein and Langmuir, 1987).

- In Chapter 4, the character of variability in the mantle section of a paleo-spreading center is examined using a new detrital spinel data set collected for this study. We interpret our observations as the consequence of regionally distinctive internal proportions of different mantle lithologies (e.g., dunite versus harzburgite), in turn reflecting the organization of focused melt transport at mid-ocean ridges into "channel-rich" and "channel-poor" zones. Some variability within the mapped region could additionally reflect igneous impregnation, variable depletion during melting, or post-mid-ocean ridge magmatism associated with ophiolite emplacement. *We have provided a preliminary map of intermediate-scale compositional variability within the southernmost Oman ophiolite massif, in which multiple, spatially coherent, compositionally distinctive, ∼20-100 km^2 regions are resolved, representing the first mapping of compositional mantle domains at this length scale anywhere in the world.*

- Appendices A-C provide supplementary information about the quantitative methods used in each thesis chapter.

I believe that the implications of this thesis for future work are threefold: (1) As developed in detail throughout Chapter 2, there is a considerable potential for melt-rock reaction to complicate inferences from major elements about conditions within ocean ridge magmatic systems. The robustness of inferences should therefore be tested against this possibility in future work, e.g., based on the modeling approach developed in this study. (2) Despite the large number of MORB samples recovered globally, sampling has been very heterogeneous, with most of the global ocean ridge system represented very sparsely. Global- or regional-scale MORB major element systematics remain poorly constrained at present, and there is great need for additional sampling, particularly away from previous "sampling hot spots." (3) As developed further in Chapter 4, inferred mantle variability in the Oman ophiolite suggests that melt transport in the shallow oceanic mantle could be organized not only into "channels" and "surroundings," but also into larger-length-scale "channel-rich" and "channel-poor" regions, which could, furthermore, be related to ridge axis segmentation. The data analyzed for this thesis are preliminary, however, and further investigation is needed to test this idea. Perhaps one further implication of a broader nature may be derived

from the principles guiding this thesis: (4) The relative frequency of geochemical observations should more routinely be considered as part of the "data" against which quantitative modeling approaches are tested, and which geologic hypotheses should seek to explain in the future. It is encouraging that the generation of distinctive spatial-statistical patterns of geochemical variability appears to be predicted as a consequence of a number of existing petrologic or compositional evolution models that explicitly incorporate fluid dynamic transport together with chemical processes. Such models include simulations of magmatic systems (e.g., *Spiegelman and Kelemen*, 2003; *Perugini et al.*, 2003) and mantle convection (*Brandenburg et al.*, 2008). As further geochemical data are collected, additional spatial-statistical systematics in ocean ridge samples will likely emerge. Together with the further development and refinement of quantitative forward models, these data, exploited to their fullest, will surely provide exciting new insights into the operation of ocean ridge magmatic systems.

Chapter 2

The Case for Reactive Crystallization at Mid-Ocean Ridges

2.1 Introduction

Mid-ocean ridge basalts (MORB) provide an important record of the chemical processes giving rise to mantle differentiation and the generation of oceanic crust and lithosphere. The compositional diversity of MORB reflects variability in magmatic systems, involving chemically heterogeneous mantle material experiencing variable extents of chemical fractionation via a number of igneous processes over a range of temperatures and pressures. Although some aspects of MORB geochemical systematics remain difficult to interpret, the most prominent trend in MORB major element data corresponds well with the variation of melt compositions expected from magma crystallization. Abundant laboratory experiments constrain the low-pressure liquid line of descent (LLD) of basaltic magma crystallizing olivine, olivine + plagioclase, and olivine + plagioclase + clinopyroxene (e.g., *Grove et al.*, 1992; *Bender et al.*, 1978; *Walker et al.*, 1979; *Tormey et al.*, 1987; *Yang et al.*, 1996). Such experiments show that crystallizing magmas with differing initial compositions evolve along separate, but nearly parallel LLDs. This justifies the accepted principle that chemical variability in MORB samples corrected for the effects of crystal fractionation along the LLD (e.g., MgO = 8 wt%, (*Klein and Langmuir*, 1987)) cannot be explained by crystallization and must therefore reflect variability produced by other mechanisms. Based on 'corrected' major element data, previous studies have investigated many aspects of MORB petrogenesis, including along-axis variations in mantle potential temperature, differences in conductive lid thickness, and chemical heterogeneity in the parent mantle (e.g., *McKenzie and Bickle*, 1988; *Langmuir et al.*, 1992; *Shen and Forsyth*, 1995; *Niu and Hekinian*, 1997b; *White et al.*, 2001). These interpretations of fractionation corrected MORB compositions have implicitly relied on the assumption that, as in the experiments, no significant reaction with the surrounding rock

occurs during MORB crystallization.

Accumulating examples of pervasive melt-rock reaction in the shallow mantle beneath ridges (e.g., *Kelemen et al.*, 2007; *Niu*, 2004; *Tartarotti et al.*, 2002; *Gaetani et al.*, 1995; *Seyler and Bonatti*, 1997; *Cannat et al.*, 1992; *Dick*, 1989; *Niu and Hekinian*, 1997a) show that interaction between ascending and/or cooling magmas and surrounding mantle rock can produce significant compositional variability, at least in shallow mantle peridotites. Motivated by these observations, and building on work by (*Kelemen*, 1986) and (*Kelemen*, 1990), this study evaluates the hypothesis that most MORB liquids do not exclusively crystallize by *fractional crystallization*, but instead experience an additional increment of crystallization that is influenced by chemical exchange with the surrounding mantle rock. This distinct phase of crystallization, which we will term *reactive crystallization*, may be particularly important at the onset of crystallization, where high temperature magma transport at low melt-rock ratios could allow diffusive cation exchange of Mg^{2+} and Fe^{2+} between mantle olivine and the crystallizing melt. Such melt-rock reactions, simultaneous with crystallization, could significantly alter the proportion and composition of crystallizing phases –and therefore the compositional evolution of the residual liquid– relative to fractional crystallization. If correct, this hypothesis implies that variability in the relative importance of reactive and fractional crystallization could contribute a partial explanation for fractionation-corrected MORB major element variability that has been previously interpreted primarily in terms of mantle source composition and potential temperature.

We first apply thermodynamics and magma dynamics theory to constrain the compositional effects of reactive crystallization on basaltic liquids. Using the MELTS thermodynamic model (*Ghiorso et al.*, 2002), we predict the deviations in the LLD for reactive crystallization compared to fractional crystallization. We then estimate the possible extent of reactive crystallization beneath mid-ocean ridges from a simple calculation of advection relative to diffusion timescales in a 1-D, steady state melt transport column.

Next, we examine major element data from a global compilation of MORB glass compositions. Two key observations correspond to the predicted consequences of reactive crystallization. (1) A large fraction of the worldwide variability in fractionation-corrected major element compositions, for example in fractionation-corrected MgO content, is present within small areas (less than 30 km along the ridge axis) at most of the well sampled mid-ocean ridge localities. (2) This variability correlates negatively with spreading rate, though mean values of, e.g., corrected MgO content are not spreading rate dependent. We evaluate the ability of processes other than reactive crystallization to generate these specific observations, but find that reactive crystallization provides the best explanation. Together with fractional crystallization and magma mixing, reactive crystallization could exert an important influence

on major element variability, while variability in many other geochemical parameters, such as isotope and trace element ratios, testifies to the presence of mantle source and parental magma heterogeneity (e.g., *Langmuir et al.*, 1992; *Shen and Forsyth*, 1995; *Niu and Hekinian*, 1997b). We do not suggest that reactive crystallization can account for the full extent of MORB variability in all geochemical variables. Nevertheless, we illustrate the potential for combined reactive and fractional crystallization from a single parental liquid composition to explain major element data from several MORB suites. We close with a discussion of implications for interpreting MORB compositions in terms of reactive crystallization.

2.2 Observational Basis for the Reactive Crystallization Hypothesis

The petrography and chemistry of abyssal peridotite samples provide evidence for melt-rock reaction in the uppermost mantle beneath mid-ocean ridges (*Kelemen et al.*, 2007; *Niu*, 2004; *Niu and Hekinian*, 1997a; *Tartarotti et al.*, 2002; *Gaetani et al.*, 1995; *Seyler and Bonatti*, 1997; *Cannat et al.*, 1992; *Dick*, 1989). For example, plagioclase lherzolites recovered from ODP Leg 209, Site 1275 on the Mid-Atlantic Ridge contain mm-scale plagioclase impregnations displaying extreme chemical variability (*Kelemen et al.*, 2007). There is a large range of Ca# (defined as molar Ca/(Ca+Na), equivalent to the anorthite fraction in plagioclase) in impregnations found less than 20 m apart, while the Mg# (molar Mg/(Mg+Fe) content) of olivine crystals adjacent to impregnations remains almost constant. As shown in Figure 2-13, this compositional trend is ubiquitous in mineral and whole rock abyssal peridotite compositions, and is in marked contrast to mid-ocean ridge gabbro suites and to trends of plagioclase and olivine composition in experiments on crystallization of basalt, where Ca# is roughly proportional to Mg#. We suggest that the Site 1275 drill core samples and many other abyssal peridotite suites could represent reactive crystallization products formed within surrounding mantle rock at ∼0.6 GPa (c.f., *Kelemen et al.*, 2004). During crystallization of impregnating melts, mantle olivine may act as an "infinite reservoir" buffering the melt Mg# near ∼0.7 (in equilibrium with mantle olivine with a characteristic Mg# of ∼0.9) through Fe-Mg cation exchange, particularly during slow, high temperature crystallization at low melt-rock ratios. Although the melt Mg# would remain nearly constant, the Ca# is not constrained and could evolve freely during crystallization. Low Mg# olivine and low Ca# plagioclase are the expected products of fractional crystallization (c.f., Figure 2-13). Therefore, the observed absence of low Mg# olivine in proximity to low Ca# plagioclase within impregnated peridotites is more consistent with reactive crystallization. We have illustrated

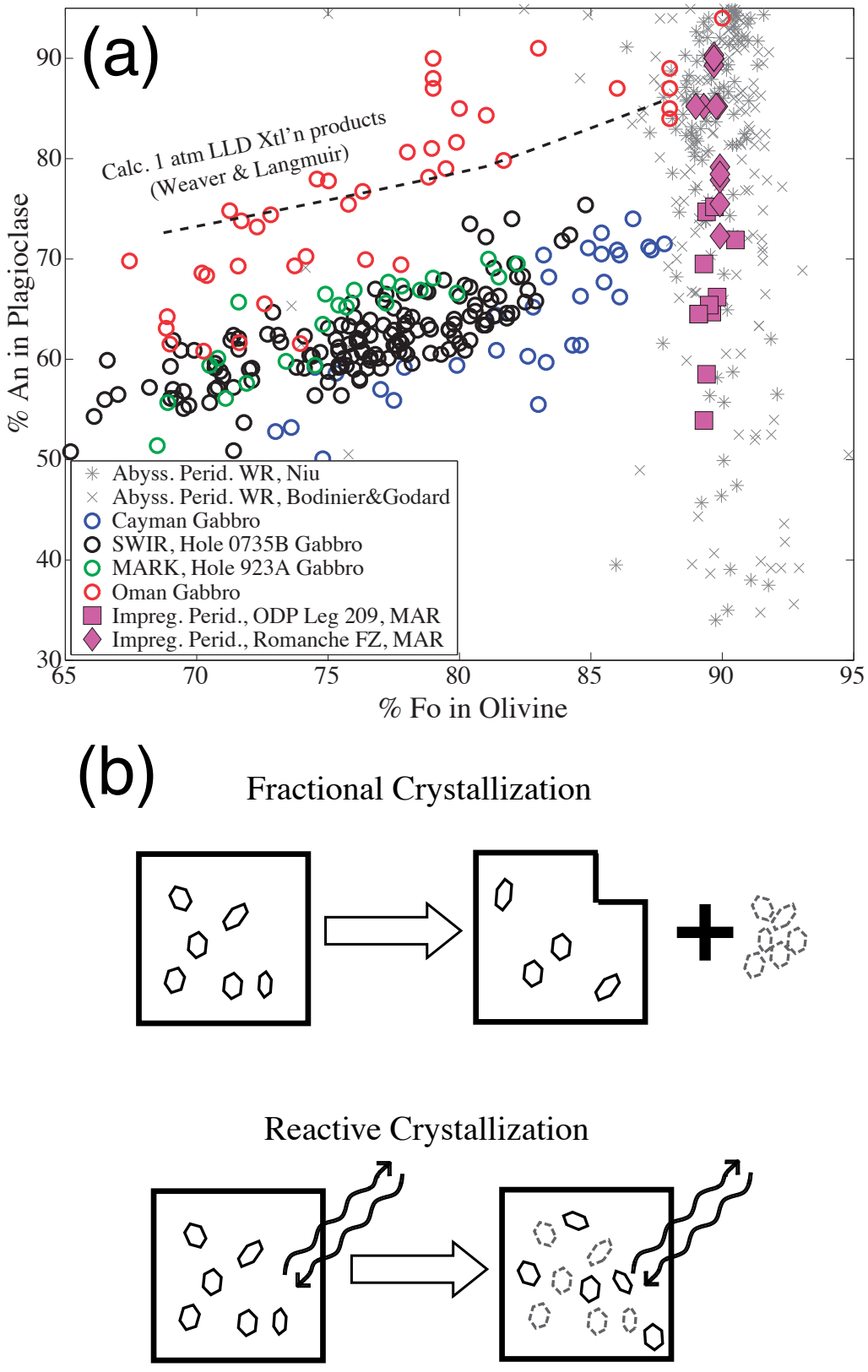

Figure 2-1: Caption given on next page.

Figure 2-1: In terms of Ca# (normative anorthite, or molar $\frac{Ca}{Ca+Na}$) in plagioclase vs Mg# (normative forsterite, or molar $\frac{Mg}{Mg+Fe^{2+}}$) in olivine, impregnated peridotite samples from ODP Leg 209, Site 1275 (14N, Mid-Atlantic Ridge) and from the Romanche Fracture Zone (Equatorial Atlantic) define similar compositional trends that are distinct from those of oceanic gabbro suites. Light grey symbols demonstrate that whole rock Ca# and Mg# for a worldwide compilation of more than 300 abyssal peridotites reproduce the trend of Site 1275 and Romanche impregnated peridotite mineral compositions. Although impregnated peridotites have a range of plagioclase Ca# that is comparable to the range in gabbros, olivine Mg# remains nearly constant at ∼89-90. Variability in Ca# at a constant, primitive Mg# is a predicted consequence of *reactive* crystallization from a single starting composition during slow melt migration at low melt-rock ratios. Oceanic gabbros from individual localities, by contrast, define trends with correlated Ca# and Mg#, consistent with experimental liquids produced by crystal fractionation from distinct initial Ca# compositions. Impregnated peridotite data sources: ODP Leg 209 (*Kelemen et al.*, 2007), Romanche (*Tartarotti et al.*, 2002), worldwide (*Bodinier and Godard*, 2003; *Niu*, 2004). Oceanic gabbro data sources: Mid-Cayman Rise (*Elthon*, 1987), Mid-Atlantic Ridge Kane FZ area (MARK), Hole 923A (*Casey*, 1997), Southwest Indian Ridge, Hole 735B (*Dick and et al.*, 2002), Oman ophiolite (Samail and Wadi Tayin massifs) (*Browning*, 1982; *Kelemen et al.*, 1997b; *Koga et al.*, 2001). We hypothesize that fractional crystallization and reactive crystallization could define separate petrologic processes with distinguishable geochemical signatures. At right, the primary distinctions between fractional and reactive crystallization are highlighted by schematic diagrams depicting the evolution of each process: In fractional crystallization, there is no chemical exchange (indicated by wavy arrows) between crystallizing magmas (indicated by boxes) and the surroundings. Crystal products from the "initial" diagram in each series are shown in gray in the "subsequent" diagram.

the differences between fractional and reactive crystallization schematically in Figure 2-13.

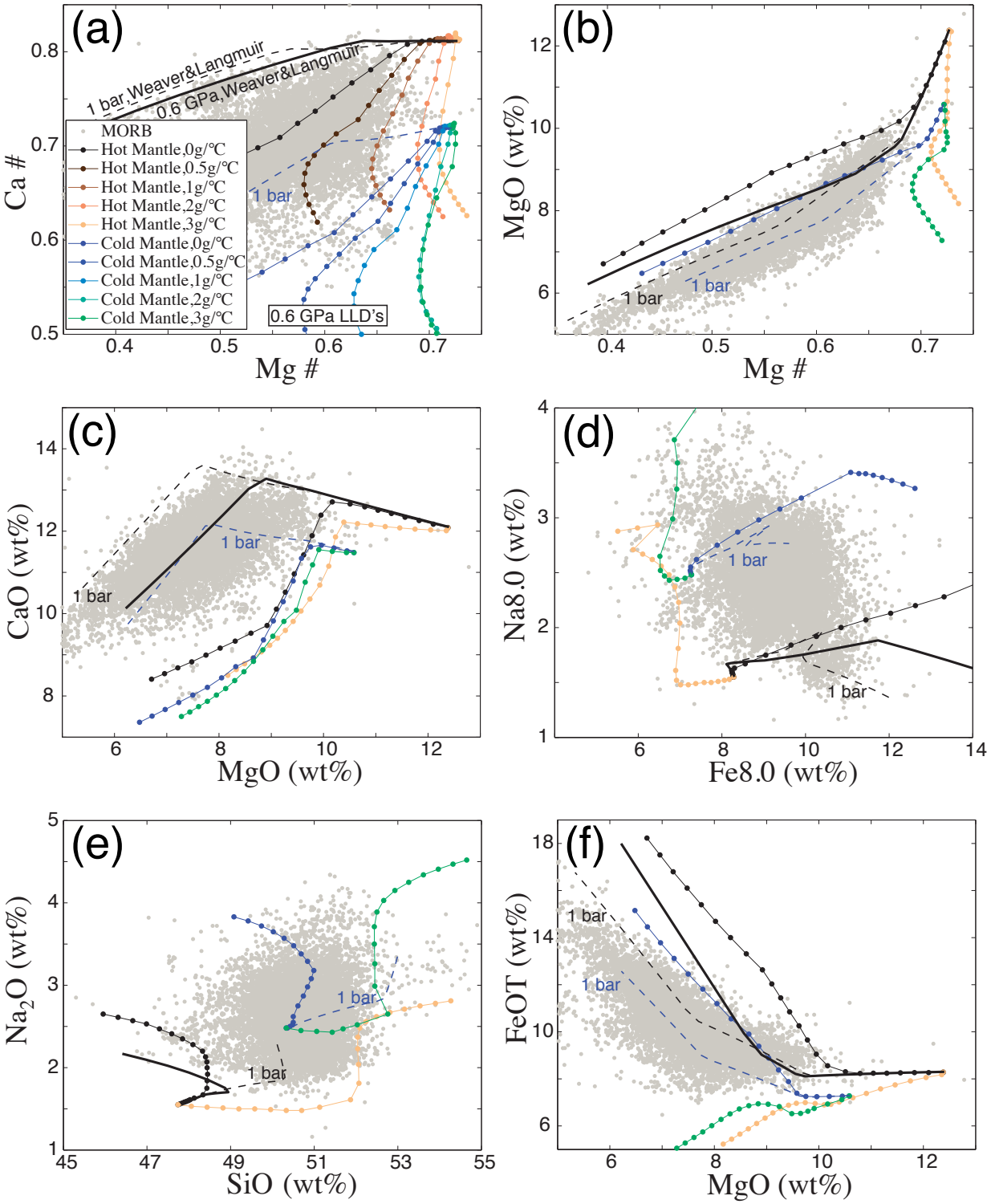

Figure 2-2: Caption given on next page.

Figure 2-2: Liquid lines of descent determined through pMELTS reactive crystallization calculations, compared to MORB glasses (gray dots). Calculated liquid lines of descent from crystallization governed by different values of the 'reactivity parameter' (the reactivity parameter is specified in terms of grams of 'average abyssal peridotite' (*Dick*, 1989) added to the thermodynamic system per °C temperature decrease). Liquid lines of descent are shown for two primitive initial liquid compositions. Warm colored LLD's correspond to a starting melt composition derived by decompression melting of a mantle source with a relatively high potential temperature, while the LLD's initiating from melt derived from a low potential temperature mantle are shown in cold colors. Initial melt compositions were taken from (*Kinzler and Grove*, 1992, Table 4) with the addition of 200 ppm H_2O following the approach of (*Asimow et al.*, 2004). Melt compositions with Mg# of about 0.7 are close to equilibrium with mantle peridotite. An additional LLD corresponding to 1 bar fractional crystallization is shown for reference (thin, dashed line), calculated using the algorithm of *Weaver and Langmuir* (1990). The solid, thick black line represents a 0.6 GPa LLD predicted by the *Weaver and Langmuir* (1990) algorithm, and should be comparable to the 0.6 GPa fractional crystallization pMELTS model, with differences resulting from different model calibration parameters and computational techniques. Unlike fractional crystallization, reactive crystallization is predicted to yield decreasing MgO at nearly constant Mg#, and can produce large variability in Na8 (Na_2O corrected to MgO = 8 wt% (*Klein and Langmuir*, 1987).

2.3 Reactive Crystallization in Theory

2.3.1 Chemical Consequences

We modeled the different LLD's generated by reactive crystallization and fractional crystallization of MORB using the thermodynamic pMELTS program (*Ghiorso et al.*, 2002). For example, an initial thermodynamic system with the bulk composition of a primitive mantle melt was cooled from its liquidus in 5 °C increments at a constant pressure of 0.6 GPa, close to the conditions inferred for formation of the impregnated peridotites at ODP Site 1275. At each cooling increment, increments of average shallow, residual peridotite composition were added to the system. These mass additions were meant to simulate expansion of the thermodynamic system relevant to the crystallization process that occurs as the result of reaction with the surrounding mantle rock (olivine). Variable rates of reactive crystallization were simulated by varying the mass of peridotite added per °C of cooling. This parameter (we will refer to it throughout as the 'reactivity parameter') could correspond physically to the relative rates of diffusive exchange versus cooling experienced by the crystallizing magma. We found model liquids produced by adding peridotite at 0 to 3% initial melt mass per °C cooling increment span most of the compositional range of MORB. Larger values of the reactivity parameter result in very similar LLD's to the case of 3% initial melt mass per °C cooling. In the next section, we will address the range of reactivity parameter values that are consistent with melt transport theory.

Figure 2-2 illustrates characteristic features of the LLD's from two primitive initial liquid compositions calculated for a range of reactivity parameter values and compared to MORB glass compositions. References for compositions used in our calculations are provided in the caption, and a sample input file used in these calculations, as well as additional Fenner-type variation diagrams contrasting model output with MORB glass compositions are included in the electronic supplement. Over a cooling interval of 100 °C, reactive crystallization LLD's maintain high Mg# while evolving to lower MgO and FeO contents and to higher SiO_2 and alkali contents than for fractional crystallization at the same Mg#, consistent with the observations at ODP Site 1275 described above. Our calculations illustrate the potential for a single primitive melt composition, evolving by a combination of reactive and fractional crystallization to generate most of the globally observed range of MORB compositions, at least in principle. Thus, the effect of reactive crystallization may be detectable in data as 'noise' in fractionation-corrected variability. For example, variations in the amount of reactive crystallization experienced by different aliquots of a given parental MORB liquid could translate to local variability in Na8 (Na_2O corrected to MgO = 8 wt%, (*Klein and Langmuir*, 1987, c.f., Figure 2f)). We have generated similar results (decreasing MgO and FeO at near-constant Mg#, higher SiO_2, etc.) by an analogous calculation using the algorithm of *Weaver and Langmuir* (1990), though the reactive crystallization calculations with this model are complicated by the lack of parameterization for orthopyroxene saturation. The diagnostic compositional effects of reactive crystallization are therefore robust, and not dependent on the modeling method. However, LLD's predicted for fractional crystallization at 0.6 GPa using pMELTS versus the *Weaver and Langmuir* (1990) algorithm display significant differences when compared quantitatively, primarily due to much earlier pyroxene saturation predicted by pMELTS (c.f., Figure 2-2). The pMELTS output therefore potentially over-predicts the decrease in liquid Ca# resulting from a given degree of crystallization, though this does not obscure the clear qualitative distinction between reactive and fractional LLD's. If this over-prediction of decreasing Ca# is significant, then reactivity parameter values greater than 3 g/°C might be therefore be required for reactive LLD's to span the range of values shown in Figure 2-2, but this would not diminish the applicability of our calculations to natural systems. As will be further discussed in a following section, reactivity parameter values that are many orders of magnitude larger than in our modeling are predicted by geologically plausible melt transport scenarios. Our modeling predicts that reactive crystallization LLD's resulting from such very large reactivity parameter values should be very similar to the "3 g/°C" LLD's shown in Figure 2-2. We will therefore focus on contrasting the end-member cases of fractional crystallization (reactivity parameter = 0) and reactive crystallization (reactivity parameter $>> 0$) throughout the rest of this contribution.

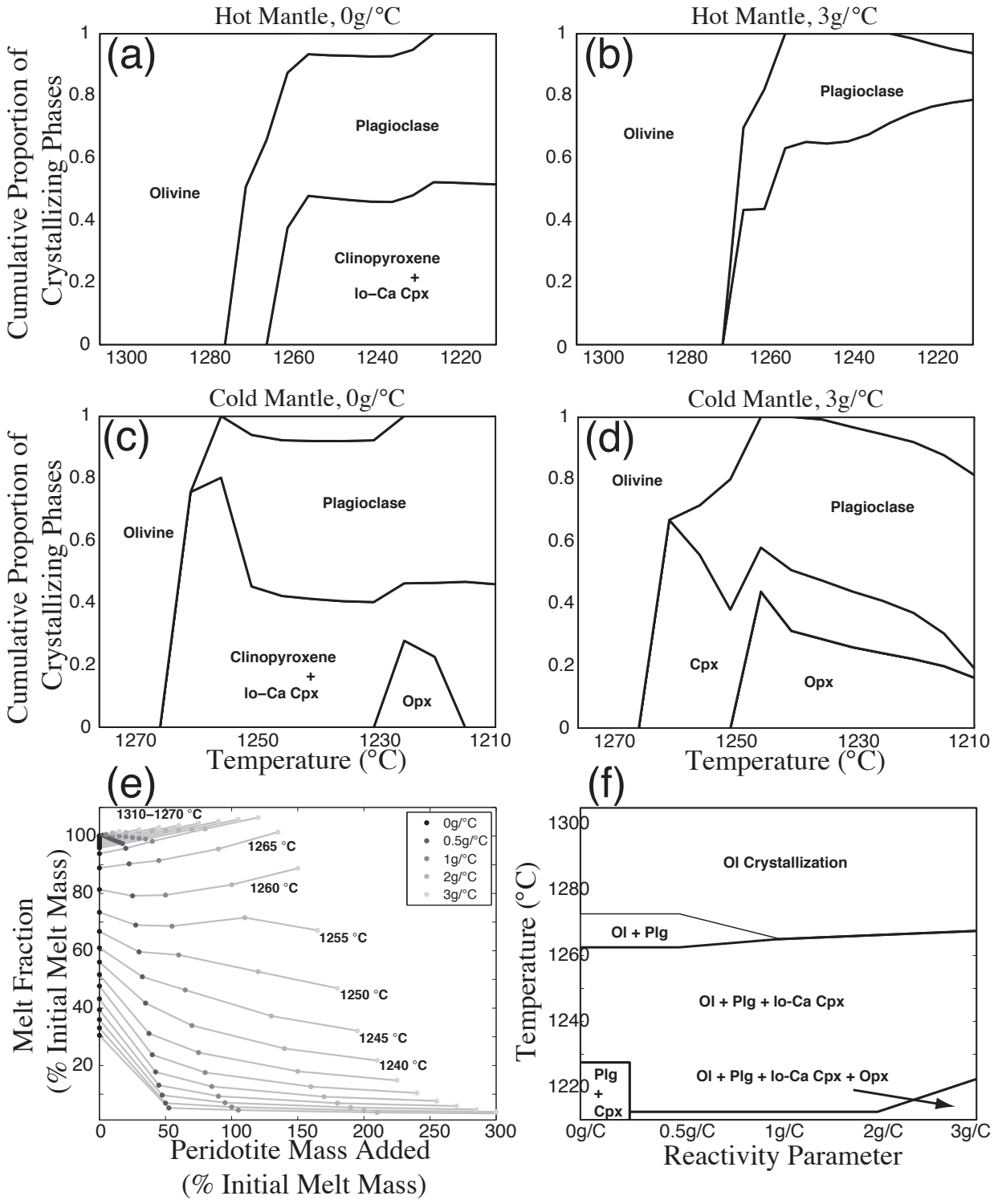

Figure 2-3: Caption given on next page.

Figure 2-3: Illustration of phase proportions crystallized leading to the end-member LLDs shown in Figure 2-2. (a-b) Respectively, crystallizing phase proportions in fractional and reactive crystallization of a parental magma corresponding to a higher degree of melting from a high potential temperature mantle source. (c) Summary of the effect of increasing degrees of reactive crystallization on residual melt fraction. Isotherms are shown as gray lines for reference. (d-e) Crystallizing phase proportions in fractional and reactive crystallization of a parental magma corresponding to a low degree of melting from a low potential temperature mantle source. Proportions shown reflect crystallizing phase proportions output by pMELTS, after subtracting the mass of crystallizing phases due to the average abyssal peridotite assimilant with 77% olivine 19% opx and 4% cpx (*Dick*, 1989). (f) Sensitivity of crystallizing phase assemblage to reactivity parameter. Decreasing temperature indicates increasing crystallization progress.

Figure 2-3 illustrates the calculated proportion of crystallizing phases in the end-member calculations corresponding to the LLD's in Figure 2-2. In the case of reactive crystallization, clinopyroxene and orthopyroxene generally precipitate more abundantly and contain less Ca than in fractional crystallization, although reactive crystallization also involves 30-50% plagioclase crystallization (c.f., subpanels 2-3a vs 2-3b and 2-3d vs 2-3e). The sensitivity of the crystallizing mineral assemblage to the reactivity parameter is shown in subpanel 2-3f. Calculated variation of melt fraction, F, with temperature and cumulative mass of peridotite added is also shown (subpanel 2-3c). As noted by *Kelemen* (1990), energetic constraints do not reduce the likelihood of very large reactivity parameter values because (a) mantle "wall rock" is not cold (instead, melt and refractory, solid peridotite co-exist at nearly the same temperature), (b) cation exchange reactions between melt and solid do not require mantle material to melt in order for "assimilation" to occur, and (c) dissolution of one phase can be balanced by crystallization of an energetically equivalent mass of another phase. Our calculations support this reasoning, showing the ratio of peridotite mass added to mass crystallized to be greater than unity at high temperatures, corresponding to a slight increase in melt fraction via reactive crystallization as compared to fractional crystallization. While reactive and fractional crystallization display little difference in F at a given temperature above ca. 1260-1255°C, our calculations predict a large decrease in F during reactive crystallization at lower temperatures (relative to fractional crystallization), consistent with previous work by *Kelemen and Aharonov* (1998). Our calculations support the possibility of up to ∼40-50% of reactive crystallization occurring over small temperature intervals, e.g., between 1270 °C and 1240 °C. By implication, large extents of reactive crystallization could occur within a narrow range of temperatures (and, therefore, pressures) after the onset of melt cooling and crystallization within ocean ridge thermal boundary layers (ridge thermal boundary layers encompass the depth interval shallower than the final depth of melting).

2.3.2 Melt Transport Dynamics

The 'Reactive' LLD's described above should be consistent with models of thermal structure and melt transport beneath mid-ocean ridges. Although many aspects of melt transport in the mantle beneath ridges are uncertain, the potential importance of reactive crystallization may be evaluated with respect to any specified forward model. Regardless of the specifics, there will be substantial reaction between migrating melt and host peridotite when magma transport occurs on time scales that are slow compared to the melt-rock reaction time scale. The ratio of advection and reaction timescales is commonly represented by the Damköhler number, Da, with higher values of Da corresponding to higher degrees of reactivity (c.f., *Hoefner and Fogler*, 1988; *Korenaga and Kelemen*, 1998). If reactions between an upwelling magma and the surrounding mantle rock are primarily cation exchange reactions with diffusion-limited kinetics, Da may be expressed as:

$$Da = \frac{LD_{FeMg}}{v_{melt}d^2} \tag{2.1}$$

where L is the characteristic distance over which melt transport occurs, D_{FeMg} is the limiting cation diffusivity in the solid, v_{melt} is the magnitude of the local melt velocity vector and d the average inter-channel distance (corresponding to the grain size in the case of grain-scale porous flow). $\frac{L}{v_{melt}}$ represents the advection timescale and $\frac{D_{FeMg}}{d^2}$ the inverse of the cation diffusion timescale. Assuming that v_{melt} is governed by Darcy's law, regardless of the specifics of the local melt conduit geometries,

$$v_{melt} = \frac{d^2\phi^n}{c\mu\phi}\Delta\rho g \tag{2.2}$$

where ϕ is the porosity, $\Delta\rho g$ is the lithostatic pressure gradient, μ is the magma viscosity and c and n are constants in the porosity-permeability relationship, then the expression for Da (c.f., (*Spiegelman and Kenyon*, 1992), where Da defined in this study is equivalent to $\frac{1}{Pe}$) becomes:

$$Da = \frac{LD_{FeMg}c\mu}{d^4\phi^{n-1}\Delta\rho g} \tag{2.3}$$

With the above assumptions, reactive crystallization should be most important in partially molten systems with small porosities, or small distances between melt conduits, and/or small melt velocities. The d^4 dependence on average inter-melt conduit distance implies that the extent of reaction, and resulting major element variability, could potentially be very sensitive to small scale variability in melt transport dynamics and conduit geometry within the thermal boundary layer beneath ridges. Reactive crystallization is unlikely to

occur in the sub-solidus region of the thermal boundary layer. Since thermal diffusivities ($\sim 10^{-6}$ m^2/s) are orders of magnitude larger than cation diffusivities ($\sim 10^{-16}$ to 10^{-17} m^2/s, e.g., *Chakraborty* (1997)), thermal interaction with wall-rock at sub-solidus temperatures will cause magmas to completely crystallize long before chemical interaction can proceed to an appreciable extent. Thus, fractional crystallization will dominate at shallower depths. On the other hand, reactive crystallization should be limited only by the timescale of advection and the small-scale details of melt conduit geometry (laterally variable permeability and/or locally variable depths of onset of diking) within the "reactive depth interval". In principle, this interval is bounded at the base by the depth at which melting ceases, and bounded at the top by the intersection depth of the geotherm and the basalt solidus (c.f., Figure 2-14).

2.3.3 Reactive Crystallization in a 'Simplest' Ocean Ridge Melt Transport Model

The thermodynamic calculations described above may be related to specific ocean ridge melt transport scenarios if the appropriate reactivity parameter values, in terms of grams of peridotite added per °C cooling, can be determined. As an example of this approach, we evaluate the potential for reactive crystallization predicted by a 1-D steady state mid-ocean ridge column model based on the equations of *McKenzie* (1984), that is essentially equivalent to the models previously used by *Sparks and Parmentier* (1991) and *Spiegelman and Elliott* (1993). This simplest mid-ocean ridge model defines 'on-axis' vertical profiles for temperature, degree of melting, porosity, and the upwelling velocities of solid and melt phases that simultaneously satisfy mass and energy conservation, as well as Darcy's law. Calculation details for this model are described in the Appendix, and an illustration of the reactivity parameter values predicted by a suite of grain-scale porous flow models with upwelling velocities of 10 and 60 mm/yr and mantle potential temperatures of 1300 and 1400 °C is provided in the electronic supplement. The predicted reactivity parameter values vary over more than two orders of magnitude between the cold mantle potential temperature, slow spreading end member (reactivity parameter $\sim 10^6$) and hot mantle potential temperature, fast spreading end member (reactivity parameter $\sim 10^4$). However, given that values of the reactivity parameter on the order of ~1-10 appear to be sufficient for a combination of reactive and fractional LLD's to generate a large fraction of the major element variability in global MORB data, we conclude that the reactivity parameter values may be sufficiently summarized as "very large" in all cases. The 'simplest model' used here therefore suggests that reactive crystallization may be a ubiquitous process at ocean ridges if melt transport at the onset of crystallization occurs by grain-scale porous flow.

Our calculations do not simulate melt transport to the surface, and only apply to melt transport below some critical depth, e.g., the depth to the solidus along the ridge geotherm. Above this depth, melt transport is dominantly in magmatic fractures in which transport allows high temperature melt to pass through cold wall rocks and erupt at the sea floor. Although our simplest model clearly cannot provide an acceptable quantitative model of likely reactivity parameter values at all depths beneath ocean ridges, it illustrates the potential for highly reactive crystallization of MORB magmas in the depth interval between the onset of crystallization and the solidus in a thick thermal boundary layer.

2.4 Reactive Crystallization and Global MORB Glass Compositions

2.4.1 Data

We draw on the catalogue of MORB glass compositions available from PetDB (*Lehnert et al.*, 2000) to evaluate the consistency of reactive crystallization with observations. The unfiltered PetDB compilation contains more than 13,000 glass compositions with complete major element data, representing nearly 3400 sampling stations from a large range of axial depths, spreading rates and seafloor morphologies. We geographically binned this global data set into 550 non-overlapping spatial windows, each representing either a morphologically homogeneous length of on-axis ridge segment or transform valley. Each spatial window was chosen to encompass 2 or more samples collected from within $\sim$30 km. We took care to select spatial windows of uniform 'geologic' context by inspecting sample locations overlain on the global seafloor bathymetry data available from GeoMapApp (http://www.geomapapp.org). We have ensured, for example, that data from a transform fault and from an adjacent ridge-axis would be placed in separate windows despite their spatial proximity. The local spreading rate at each spatial window was determined using a digital plate model (*Bird*, 2003). We have removed samples with Mg# < 0.5 from consideration to minimize errors in fractionation corrections, retaining a data set with $>$ 10,300 MORB glass samples. A list correlating glass sample names with bin assignments, as well as a spreadsheet detailing bin properties are both available as supplementary files.

2.4.2 Isolating the Chemical Signal of Reactive Crystallization in MORB Data

If reactive crystallization is an important process in MORB petrogenesis, it may be possible to recognize features in MORB major element data corresponding to trends predicted by the modeling described in a previous section. The best compositional variables for this purpose should be minimally sensitive to variations in melt generation processes. By contrast, oxides partitioning preferentially into melts, such as Na_2O, are likely to be more sensitive to variations in melting extent and are less likely to display systematics due to reactive crystallization alone.

In this study, we focus on the MgO content of olivine-saturated basalts, as this variable is dominantly controlled by temperature (*Roeder and Emslie*, 1970; *Longhi et al.*, 1978; *Ulmer*, 1989; *Gaetani and Grove*, 1998; *Asimow et al.*, 2004; *Putirka et al.*, 2007), and is relatively insensitive to variations in initial parental magma composition or pressure (at any single temperature). Since most MORB have undergone variable extents of fractional crystallization prior to eruption, we use the robust linear relationship between MgO and Mg# (c.f., Figure 2-4 a) characterizing multiply saturated (ol+plag±cpx) LLD's of MORB magmas at pressures < 1 GPa to carry out the following simple fractionation correction scheme. Using Mg# as our index of differentiation, we define 'Mg65' as the MgO content of a sample after correction for multiply saturated fractional crystallization to Mg# = 0.65 using an empirical LLD slope, analogous to the method of *Klein and Langmuir* (1987). We calculate Mg65 as follows:

$$\left.\begin{array}{ll} Mg65 = MgO_{samp} + \frac{\partial MgO}{\partial Mg\#}\left(0.65 - Mg\#_{samp}\right) & 0.65 \geq Mg\#_{samp} \\ Mg65 = NaN & otherwise \end{array}\right\} \quad (2.4)$$

where MgO_{samp} and $Mg\#_{samp}$ represent the uncorrected MgO content (in mol%) and Mg# of a MORB lava sample. Our best estimate of the LLD slope $\frac{\partial MgO}{\partial Mg\#}$=20.4 was obtained from a least-squares best fit to a compilation of > 200 multiply saturated phase equilibria experiments (c.f., Figure 2-4, data references in caption). We take the additional step of filtering out MORB samples with Mg# > 0.65 to ensure that fractionation corrections are only computed for MORB samples that are likely to satisfy the assumption of multiple saturation. Although the specific Mg# marking the onset of multiple saturation for a given liquid is dependent on crystallization pressure and melt composition, we have chosen Mg# $\sim$ 0.65 as a conservative lower bound, informed by inspection of phase equilibria experiments. Fractionation correction to higher Mg# values increasingly risks applying an incorrect LLD slope, which could result in 'artificial variability' among fractionation corrected liquid com-

positions that in fact are derived from a single parent composition. We feel that Mg65 is a particularly well-suited variable for studying reactive crystallization, as it is closely related to the MgO content and temperature of MORB samples near the onset of crystallization.

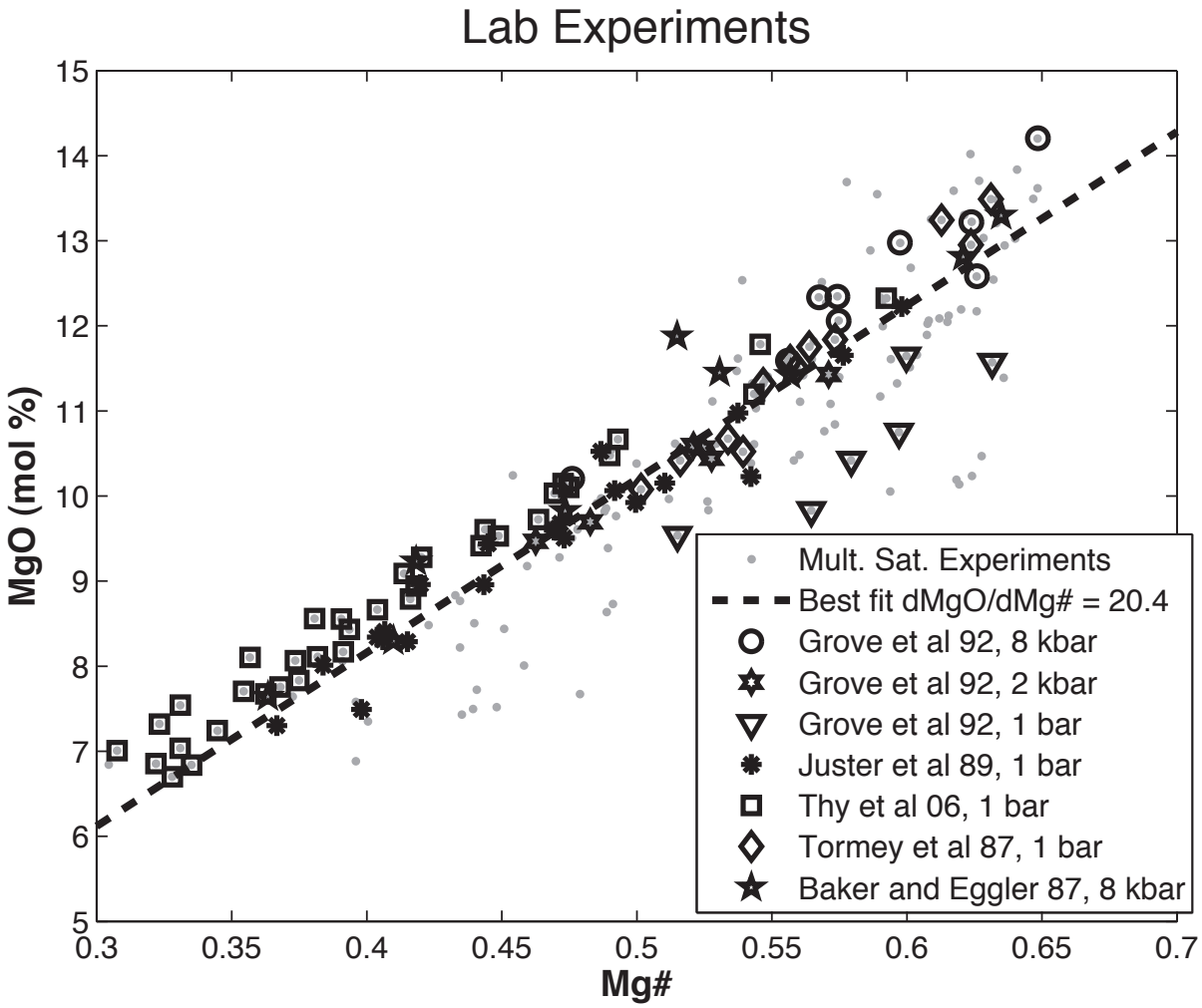

Figure 2-4: Calibration of appropriate $\frac{\partial MgO}{\partial Mg\#}$ for use in fractionation correction. All data points represent multiply saturated phase equilibria experiments at pressures in the range of 10^{-4} - 1 GPa obtained from: (*Bender et al.*, 1978; *Grove et al.*, 1982; *Grove and Bryan*, 1983; *Baker and Eggler*, 1987; *Tormey et al.*, 1987; *Juster et al.*, 1999; *Kennedy et al.*, 1990; *Kinzler and Grove*, 1992; *Grove et al.*, 1992; *Yang et al.*, 1996; *Feig et al.*, 2006; *Thy et al.*, 2006). For reference, six suites of related experiments are highlighted by specific symbols. The linear least-squares best fit to this compilation (dashed line) defines a $\frac{\partial MgO}{\partial Mg\#}$ slope of 20.4, which we take as our reference LLD slope for the fractionation correction. Note that experiment suites with different initial FeO/MgO (or, equivalently, different initial MgO at a given Mg#) define nearly parallel LLD's.

2.4.3 Linking Mg65 and Temperature

Olivine-melt geothermometers are empirical temperature-composition relationships that estimate the temperature at which basalt samples of known composition may have been in equilibrium with olivine. Via thermometry, the Mg65 value of a MORB sample implies a 'T65', physically interpretable as the equilibration temperature of the liquid near the onset of crystallization.

Given Mg65 for a sample, we calculate the composition of olivine co-existing with the liquid assuming Fe^{2+}/Total Fe = 0.88 (*Bezos and Humler*, 2005) and an Fe/Mg olivine-liquid K_d of 0.3 (*Roeder and Emslie*, 1970). The (corrected) composition of melt and (calculated) equilibrium olivine can then be related to the corrected temperature T65 (c.f., *Roeder and Emslie*, 1970). We prefer the classic geothermometer of (*Roeder and Emslie*, 1970) as it advantageously requires only the Mg# and MgO content of the melt to be known, without the need for additional fractionation correction of other major element oxides:

$$T65(^{\circ}C) = \frac{3740}{\log_{10}\left(\frac{X^{ol}_{Mg65}}{X^{liq}_{Mg65}}\right) + 1.87} - 273.15 \tag{2.5}$$

where X^{liq}_{Mg65} and X^{ol}_{Mg65} represent Mg65 in the liquid (after correction using Equation 2.4, and expressed in terms of mole fraction) and the Mg mole fraction calculated for olivine in equilibrium with a Mg# = 0.65 liquid, respectively. Figure 2-5 a) illustrates the ability of the (*Roeder and Emslie*, 1970) thermometer to recover experimental data, based on the assumptions stated above. While the T65 values presented throughout this study are calculated using this thermometer, we caution that different choices of thermometer will lead to potentially large, systematic shifts in mean calculated temperature, as well as small changes in the dispersion about the mean relative to those shown, as illustrated by the examples shown in Figure 2-5 b). However, although the specific T65 value inferred for a given sample is model dependent, we are not aware of any instances where systematic use of alternative choices of fractionation correction and geothermometry technique lead to geologic inferences different from those presented here.

2.4.4 T65 Variability at Large and Small Length Scales

We calculated T65 values for individual MORB glass samples from the PetDB compilation at each of more than 500 ($\leq$ 30 km scale) on-axis localities along the Mid-Atlantic Ridge (MAR), East Pacific Rise (EPR), Juan de Fuca Ridge (JdF) and Southeast Indian Ridge (SEIR). Figure 2-6 illustrates the resulting spatial pattern of T65 variability as a function of

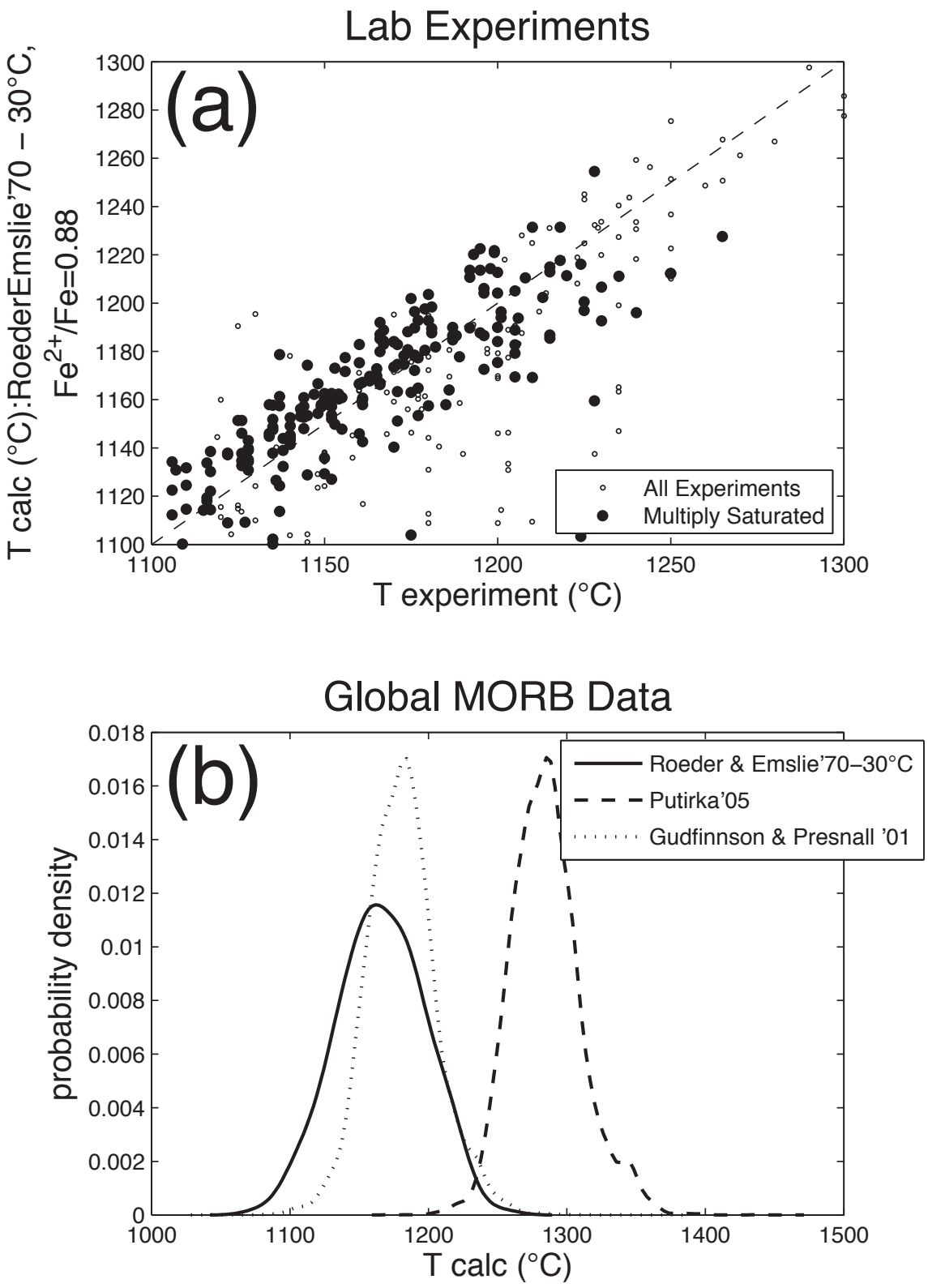

Figure 2-5: Caption given on next page.

Figure 2-5: (a) Predicted vs. observed temperatures for a compilation of 260 experiments (references in previous figure caption) validating the geothermometer method used in this study: (*Roeder and Emslie*, 1970), assuming Fe^{2+}/Total Fe = 0.88 (*Bezos and Humler*, 2005) and an Fe/Mg olivine-liquid K_d of 0.3 (*Roeder and Emslie*, 1970). We subtract 30°C from the calculated temperature, in order to eliminate an apparent systematic offset between experimentally observed and predicted temperatures. Experimental melts saturated in olivine only are shown in smaller symbols. (b) Comparison of temperatures calculated for > 10,000 MORB lavas using three different ol-melt geothermometers: (*Gudfinnsson and Presnall*, 2001; *Roeder and Emslie*, 1970; *Putirka*, 2005). Curves represent kernel density estimates summarizing the distribution of magma temperatures obtained from each method. Note the systematic differences in mean and dispersion between methods, which reflect present uncertainty in the mapping between MgO and temperature.

distance along these four MOR's. The mean and ± 1 standard deviation of the global data set are superimposed in all plots for reference. We find T65 variability at multiple length scales. The SEIR west of the Australian-Antarctic Discordance (88°E - 126°E), for example, displays a relatively low mean T65 value compared to all other ridges over a relatively long distance (∼ 1000 km). There is a comparably long wavelength trend in mean T65 along the MAR, with a maximum centered at Iceland and a minimum centered at the Azores. Smaller wavelength T65 anomalies exist as well, such as the sharp gradient in T65 in the tectonic mid-ocean ridge segment south of the Agulhas Fracture Zone (∼ 47°S, MAR). However, these ≥ 100 km length scale, systematic variations are not common. Instead, on the ∼ 100 km length scale, most spatially associated groups of mid-ocean ridge lavas have a nearly constant mean T65 that corresponds closely to the global mean.

Despite these larger scale patterns, a large proportion of T65 variability occurs at or below the 30-km binning length scale. 99% of the global MORB data yield T65 values between 1193°C and 1248°C by the methods described above. On average, ∼50% of this global range is present along any given 30 km interval of ridge axis, particularly when samples are recovered from more than 10 sampling stations. Localities containing smaller numbers of sampling stations often display smaller apparent local variabilities. Figure 2-7 shows the approximate probability of observing a given fraction of the global MORB T65 variability (e.g., between 1193°C and 1248°C) within a given 30 km interval of ridge axis, as estimated from the 49 localities in our catalogue sampled by 10 or more independent sampling stations. For reference, we also plot the probability density to be expected if the underlying T65 distribution at all 49 localities were normally distributed about the global MORB mean and with a global MORB variance.

Since fractional crystallization has been accounted for by correction to a common value of Mg#, large T65 variability at small length scales could reflect temperature variability in locally upwelling parental magmas, for which we anticipate two possible causes: (1) variation

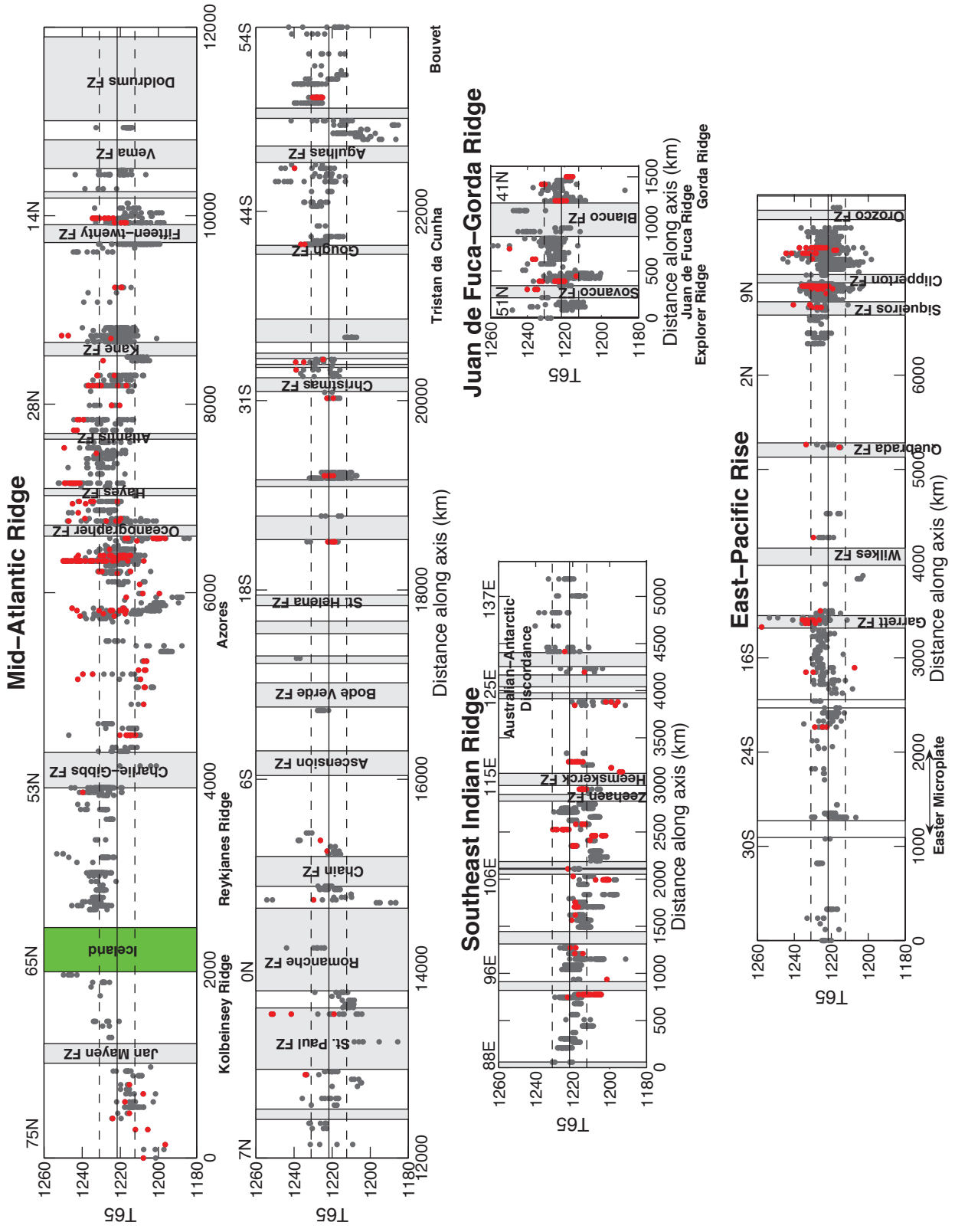

Figure 2-6: Caption given on next page.

Figure 2-6: T65 values calculated for individual on-axis or transform MORB glass samples with their relative location in terms of distance along the axial trace of four mid-ocean ridges. The most primitive samples (Mg# > 0.63) are highlighted in red. The global mean value $\pm$ 1 standard deviation is also plotted for reference. Grey patches indicate distance intervals within fracture zones, the green patch indicates the location of Iceland and white patches indicate overlapping spreading centers or microplates. Note the compositional distinction between ridges, as well as the large fraction of total variability observable at most individual localities.

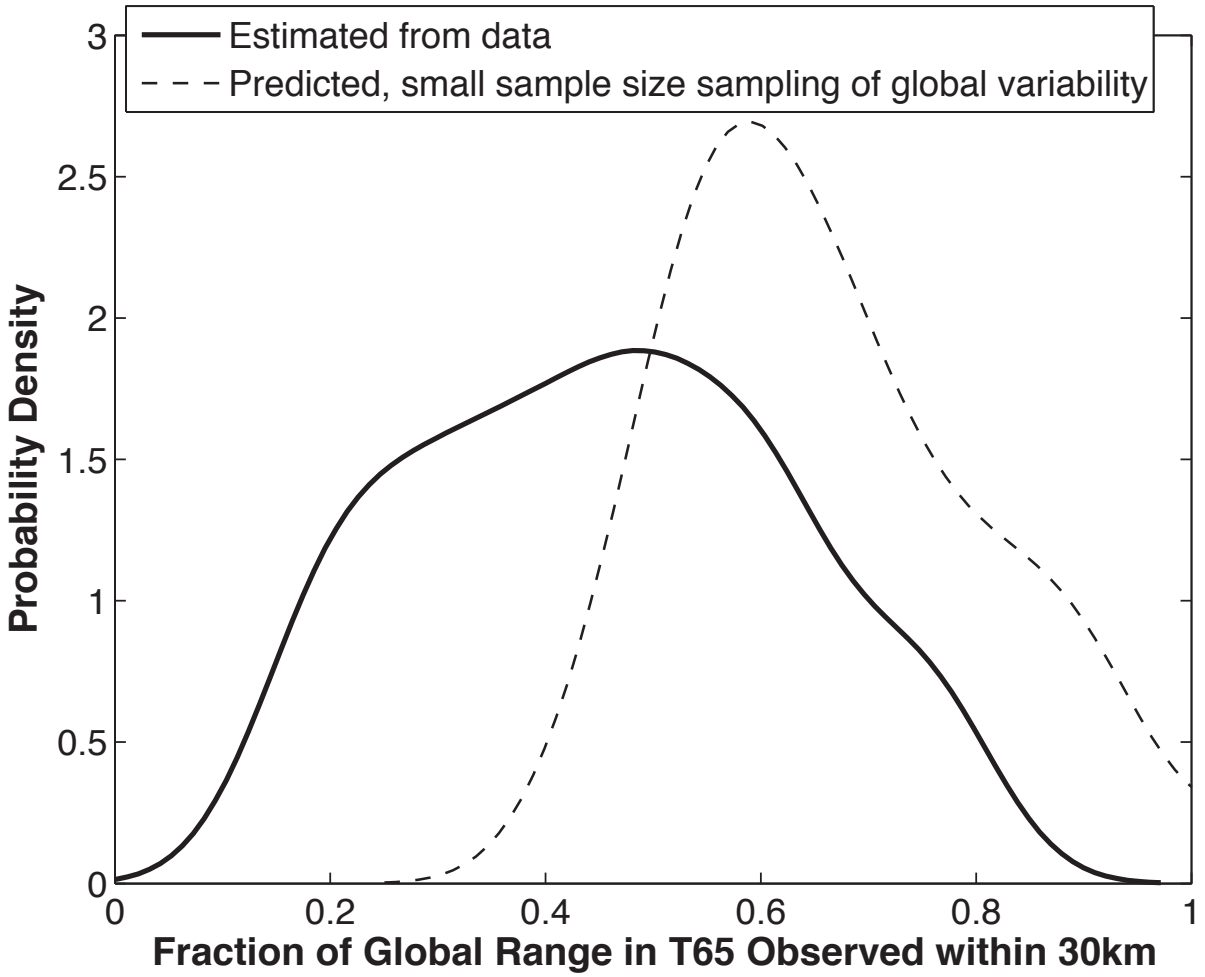

Figure 2-7: The empirical likelihood of observing within any 30 km interval of mid-ocean ridge axis a given fraction of the global T65 range containing 99% of all observations (e.g., between 1193°C and 1248°C) is shown as the solid curve. This curve is a kernel density estimate summarizing the distribution of T65 ranges observed at 49 locations that are sampled by 10 or more sampling stations, using a normal kernel function with a bandwidth of 0.1. The dashed curve, shown for reference, shows the output of a Monte Carlo simulation in which 49 sets of 10 samples are drawn from a normal distribution with the global MORB mean and standard deviation.

in the overall temperature of the upwelling mantle beneath ridges, the potential temperature; and (2) variation in the temperature at which individual aliquots of melt sample the decompression melting trajectory in the mantle (hot $\sim$ deep; colder $\sim$ shallow).

Alternatively, 30 km scale T65 variability could primarily reflect variable extents of reactive crystallization, with crystallization products from a single parental liquid recording multiple temperatures of final equilibration with mantle olivine. A comparative discussion of these effects, used to interpret the data, is offered in a later section of the paper, after another aspect of global T65 variability is developed.

2.4.5 Correlation of T65 Variability with Spreading Rate

If T65 variability is caused by reactive crystallization within the conductive, shallow mantle thermal boundary layer, the variation in ridge thermal structures at different spreading rates might give rise to T65 variability that is spreading rate dependent. As illustrated in the panels of Figure 2-8, mean T65 at any given spreading rate appears to be constant over the globally observed range of spreading rates, while the variance in T65 is inversely correlated with spreading rate. Other workers have previously identified spreading rate dependent variability (e.g., *Klein and Langmuir*, 1987; *Niu and Hekinian*, 1997b). The spreading rate dependence of MORB chemical variability has been recently studied in detail by (*Rubin and Sinton*, 2007), who demonstrate a negative correlation of uncorrected MgO with spreading rate in the PetDB compilation (their Fig. 1d). However, the lack of correlation between T65 and spreading rate implies that the uncorrected MgO-spreading rate correlation is due to variations in extent of crystal fractionation from one ridge system to another: the lavas erupted at slow-spreading ridges are generally less fractionated (and more MgO rich) compared to more fractionated, low-MgO lavas at fast-spreading ridges.

Using the binning scheme described above, we have also studied the spreading rate dependence of T65 variability *within* 30 km regions (c.f., Figure 2-8, panel c). For each of the 377 available 30-km scale spatial bins that contain data for five or more MORB samples, we plot the standard deviation of T65 versus the respective local spreading velocity. There is a clear trend, from high mean (and median) variance at slow spreading rates to low mean variance at high spreading rates. To highlight this trend, we have superimposed red crosses representing mean values of the local standard deviation for spreading rate bins containing 94 ($\sim$377/4) regional averages each. The width of the red rectangles surrounding the crosses illustrates the range of spreading rates represented by each mean value, while the height of each red rectangle illustrates $\pm$ one standard error of the mean for each bin. The visual impact of this figure, particularly the smoothly decreasing trend of the red symbols,

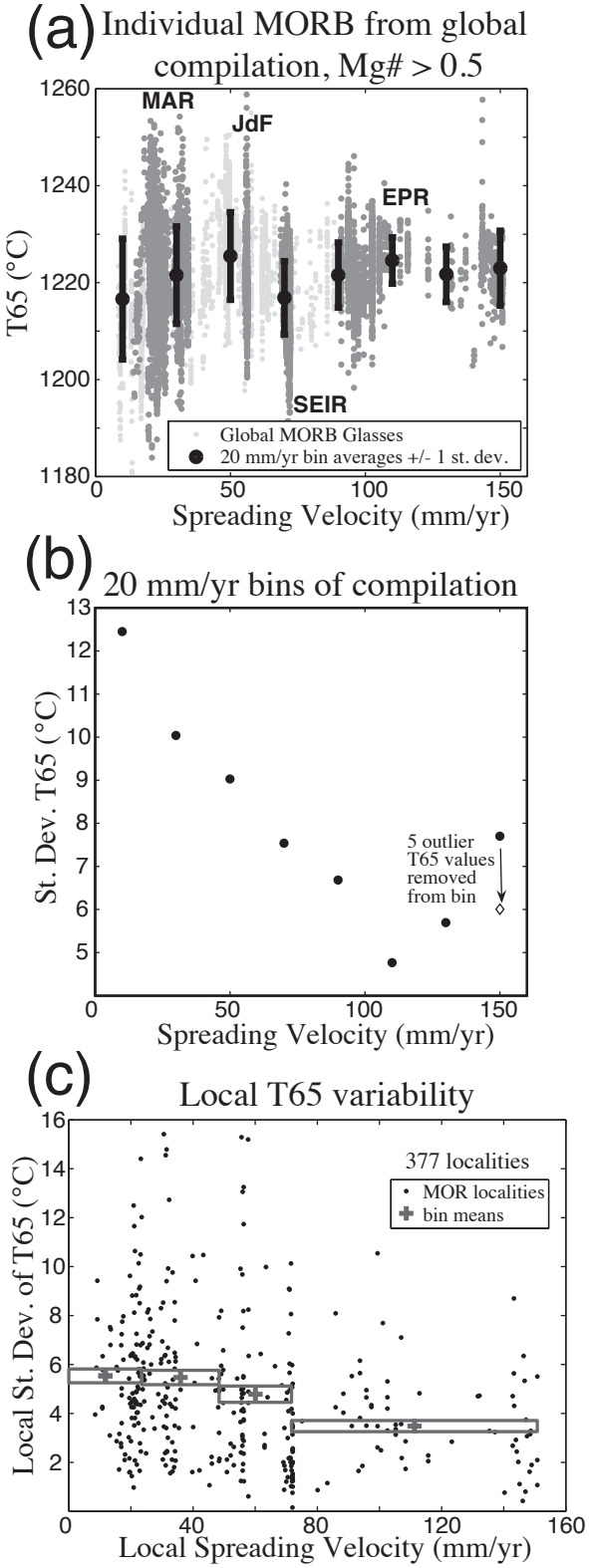

Figure 2-8: Caption given on next page.

Figure 2-8: (a) T65 as a function of spreading rate is shown for individual MORB samples (light gray dots) and 20 mm/yr bin averages (solid symbols with error bars). Error bars represent 1 standard deviation. Data from the four MORs plotted in the previous figure are highlighted in darker gray and labeled. Note that while bin means do not vary significantly over an order of magnitude in spreading rate, the variance decreases with increasing spreading rate up to ∼100 mm/yr. (b) Illustration of decreasing global variability with increasing spreading rate. (c) Summary of global systematics of locally observed T65 variability. Represented with black dots are standard deviations of individual MORB suites collected from within 30 km of each other against local spreading rate. Crosses indicate mean variability of equal sample-size bins (each bin has 94 samples), while surrounding boxes indicate the spreading rate range spanned by a given bin (horizontal extent) and the standard error of the bin mean (vertical extent). Although the visual impact of this figure is somewhat sensitive to the choice of binning scheme, there is a robust trend of higher mean local variability at slow spreading centers versus lower mean local variability at fast spreading centers.

is influenced to some extent by the specifics of the binning scheme chosen. However, in all cases the median and mean variability for the slow spreading ridges is significantly higher than for the fast spreading ridges. Thus, we infer that T65 variability at the 30 km length scale is partially controlled by spreading rate. Reactive crystallization can account for these observations, and we develop this topic further in the discussion section.

2.5 Discussion

2.5.1 Competing Interpretations of Small Spatial Scale T65 Variability

Cooling at nearly constant Mg# is the natural outcome of reactive crystallization, and variability of T65 over small distances can be explained as the result of sampled lavas undergoing variable extents of reactive crystallization starting from a single parental magma. We now assess the ability of other, more 'conventional' explanations to account for our observations of T65 variability. We investigate variations in mantle potential temperature, mantle source composition, melt extraction depth, and depth of fractional crystallization.

2.5.2 Alternative 1: Mantle Potential Temperature Variations

While along-axis variations in sub-ridge mantle potential temperature can explain the systematics of averaged major element compositions at large spatial scales (*Klein and Langmuir*, 1987), thermal variability in the parental mantle is an unsatisfactory explanation for variation in T65 at the 30 km length scale. In the passively upwelling mantle beneath an ocean ridge, neighboring parcels of mantle advecting in a laminar flow field must have been

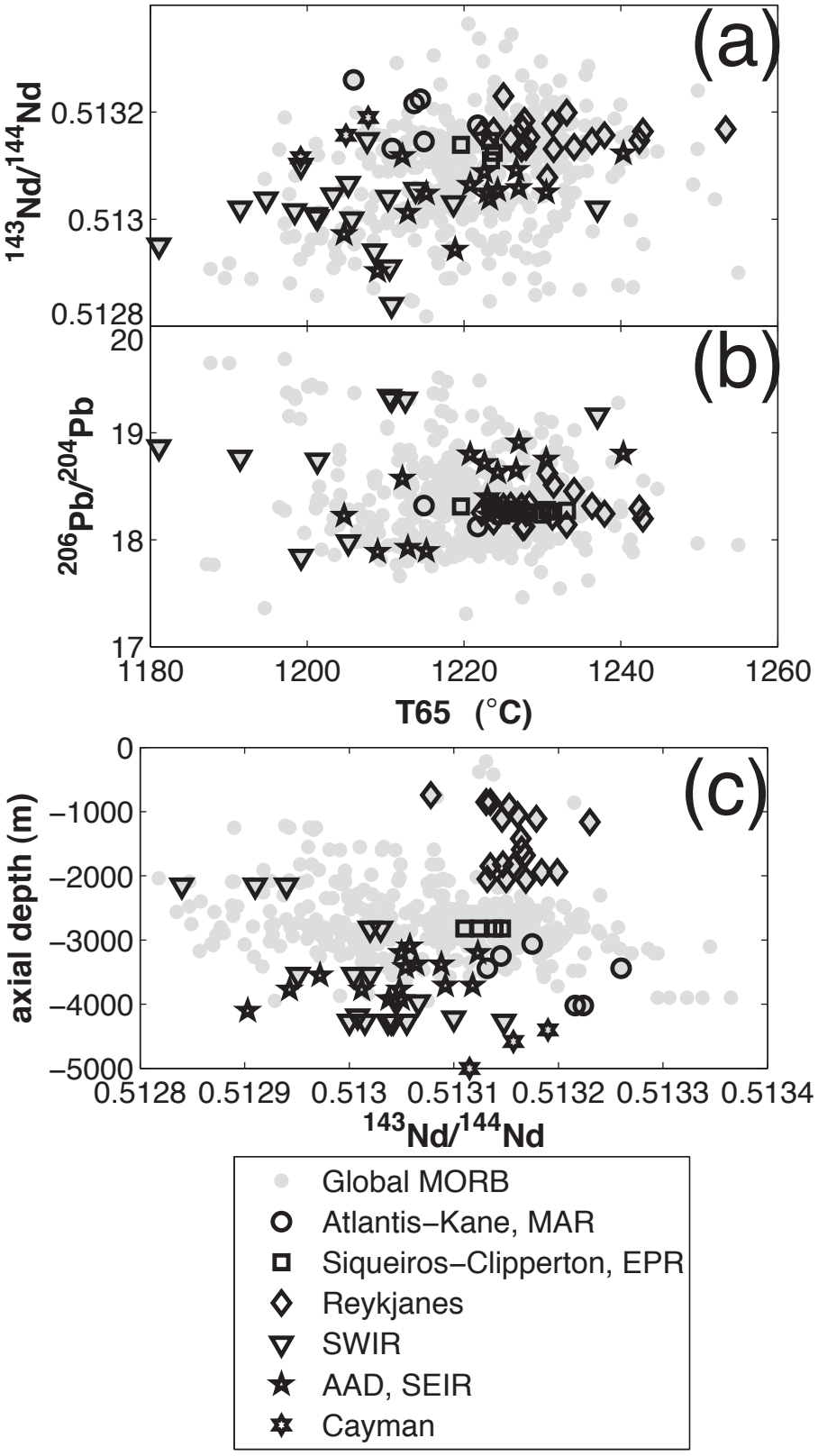

Figure 2-9: Caption given on next page.

Figure 2-9: Isotope ratios versus fractionation corrected temperature, T65, and axial depth, for MORB glass samples (all data, grey; specific localities shown as distinctive symbols). Whole rock isotope ratios are combined with T65 estimates from glass compositions for some samples in this plot in order to increase the number of available data. The poor correlation of T65 and axial depth with isotope ratios at the global and regional length scales suggests that mantle heterogeneity is not a dominant control on crustal thickness or major element variability in MORB.

adjacent for a long time prior to melting, allowing thermal equilibration over some length scale. Assuming a thermal diffusivity of 10^{-6} m^2/s and a short equilibration time of 20 Ma, thermal diffusion will have reduced initial temperature variations by a factor of $1/e$ over a 25-30 km length scale. Instead, timescales available for thermal equilibration to occur in the upper mantle source of MORB are likely to be much longer, comparable to chemical mixing and equilibration times of hundreds of millions to billions of years (e.g., *Hoffman and McKenzie*, 1985; *Donnelly et al.*, 2004), corresponding to equilibration length scales on the order of hundreds of km. Therefore, variation of mantle potential temperature in the adiabatically upwelling mantle is an unlikely explanation for variation in T65 within 30 km regions. It is well known that some long wavelength variation in mantle temperature may explain 1000 km scale variation in primitive MORB compositions, and we calculate regional, average T65 values that are elevated from the global mean at several localities, particularly at Iceland. These high mean T65 values are consistent with a high mantle potential temperature anomaly in the upwelling mantle.

2.5.3 Alternative 2: Mantle Composition Variations

Thermal diffusion over geologically reasonable times renders short wavelength temperature variations in the MORB source unlikely. It is difficult to make an analogous argument about mantle source composition, as the required time scales for solid-state diffusive homogenization of composition depend on the extent of mechanical "mingling" and may greatly exceed the age of the Earth. The spatial scales of variation in MORB source mantle compositions remain poorly constrained, but isotopic variability suggests that mantle source heterogeneity is present at length scales shorter than 30 km. If 30 km scale variability in T65 dominantly reflects variability in parental melts sourced from different long-lived mantle heterogeneities and if these are distinctive in both major and trace element composition, then fractionation-corrected major element parameters, and particularly T65, could exhibit correlations with radiogenic isotope ratios. Figure 2-9, however, shows that no significant correlation is observed between isotope ratios and T65 at the global or regional scales. As we have argued above, T65 should primarily reflect the olivine-saturated melt temperature near the onset

of crystallization and be insensitive to mantle source variability. Although melt transport within olivine-free mantle heterogeneities or anomalies in mantle source fertility could potentially contribute to T65 variability, this does not seem required to explain the MORB T65 systematics highlighted in this study. By contrast, the apparent spreading rate sensitivity of T65 variability supports the conclusion that T65 is not affected to first order by mantle compositional variations.

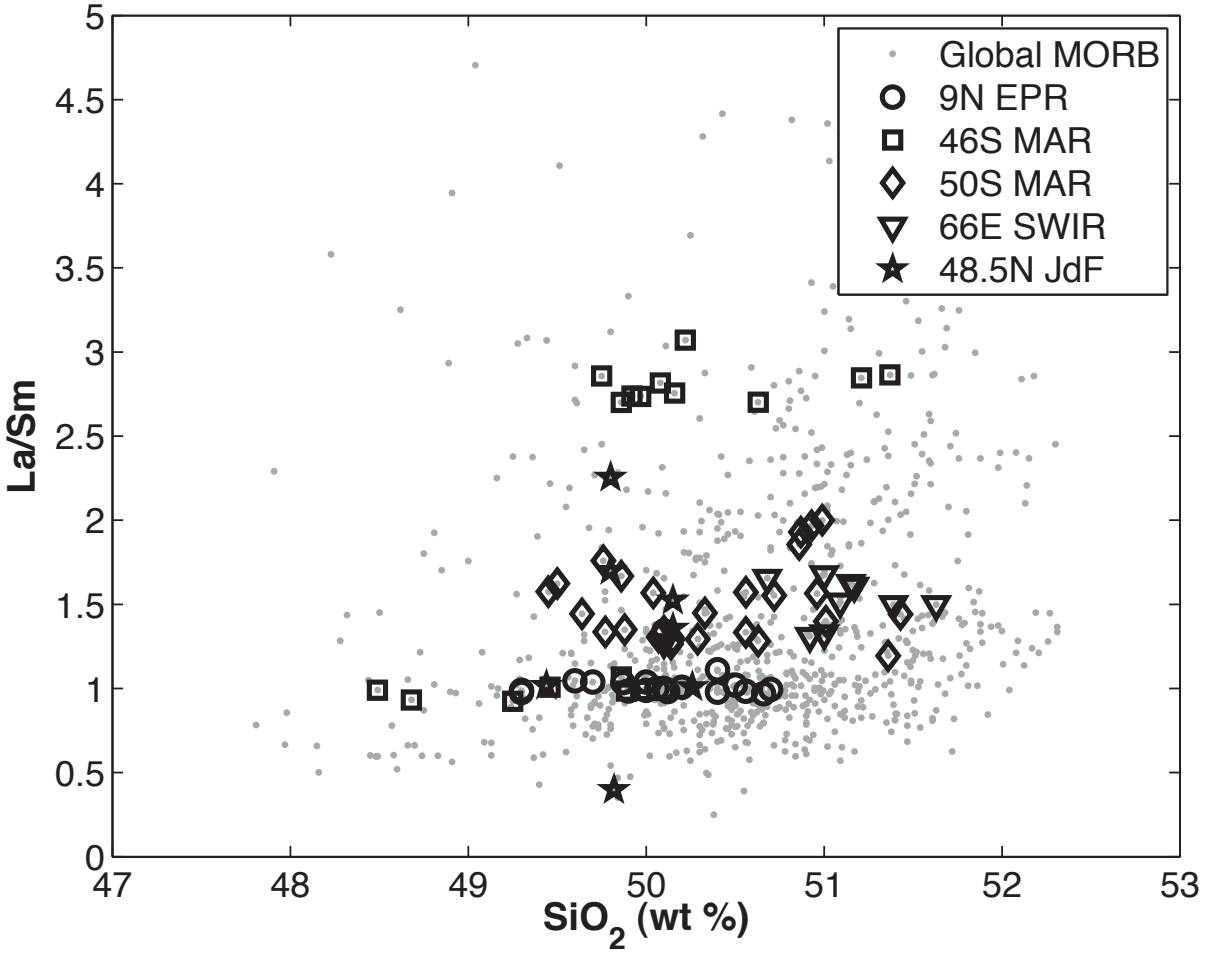

Figure 2-10: La/Sm plotted against SiO_2 from a representative suite of MORB samples collected from within 30 km. No negative correlation is observed, as would be expected if samples derived from different depths in the melting region did not reequilibrate prior to entering the thermal boundary layer. Observed SiO_2 variability at constant La/Sm is a natural consequence of reactive crystallization (e.g., *Kelemen*, 1990), while La/Sm remains unchanged for reasonable melt/rock ratios, greater than the bulk peridotite/liquid distribution coefficient for Sm (e.g., *DePaolo*, 1981).

2.5.4 Alternative 3: Variations in Melt Extraction Pressure

Variable sampling of magmas from different depths within the polybaric, decompression melting region beneath spreading ridges provides a possible explanation of the so-called Na-Fe "local trend" (*Langmuir et al.*, 1992). As a result of the positive P-T slope of the mantle solidus and adiabatic melting paths, such variable sampling is likely to yield magmas with higher T65, together with lower SiO_2, from greater depths, and lower T65, together with higher SiO_2, from shallower depths within the melting region. If this effect is a dominant source of local major and trace element variability, it should result in locally observed negative correlations of SiO_2 with incompatible trace element ratios that decrease with increasing extents of melting but are insensitive to crystal fractionation, such as La/Sm. Deeper, lower degree melts should display lower SiO_2 (due to high pressure) and higher La/Sm (due to low extents of melting). As shown in Figure 2-10, variation in SiO_2 and La/Sm are not correlated in any 30 km region along the mid-ocean ridges. We therefore conclude that T65 does not primarily reflect variations in equilibration pressure recorded in fractionation corrected MORB.

2.5.5 Alternative 4: Variations in Crystallization Pressure

The study of *Grove et al.* (1992) illustrated the potential for apparent major element variability caused by incorrect fractionation-correction when crystallization takes place over a range of pressures. That is, some fractionation corrections rely on fits to liquid lines of descent at low pressure, and do not account well for variation induced by higher pressure crystal fractionation. However, thermal constraints show that this effect should be limited at all but the slowest spreading rates at pressures higher than $\sim$ 3 kbars (c.f., Figure 2-11). Magmas will not cool below the temperature of their wall rocks, and thus the limited temperature range between the liquidus and the geotherm limits the amount of high pressure crystal fractionation that is possible beneath ridges at pressures greater than 3 kbar.

2.5.6 Reactive Crystallization and Spreading Rate Dependent T65 Variability

We conclude that none of the alternative processes considered here adequately explain the spreading rate dependent 30 km scale T65 variability that appears to be ubiquitous along the global mid-ocean ridge system. By contrast, this variability may be readily understood in terms of reactive crystallization, as demonstrated in Figure 2-12.

Other things being equal, MORB liquid temperatures at the onset of cooling and crys-

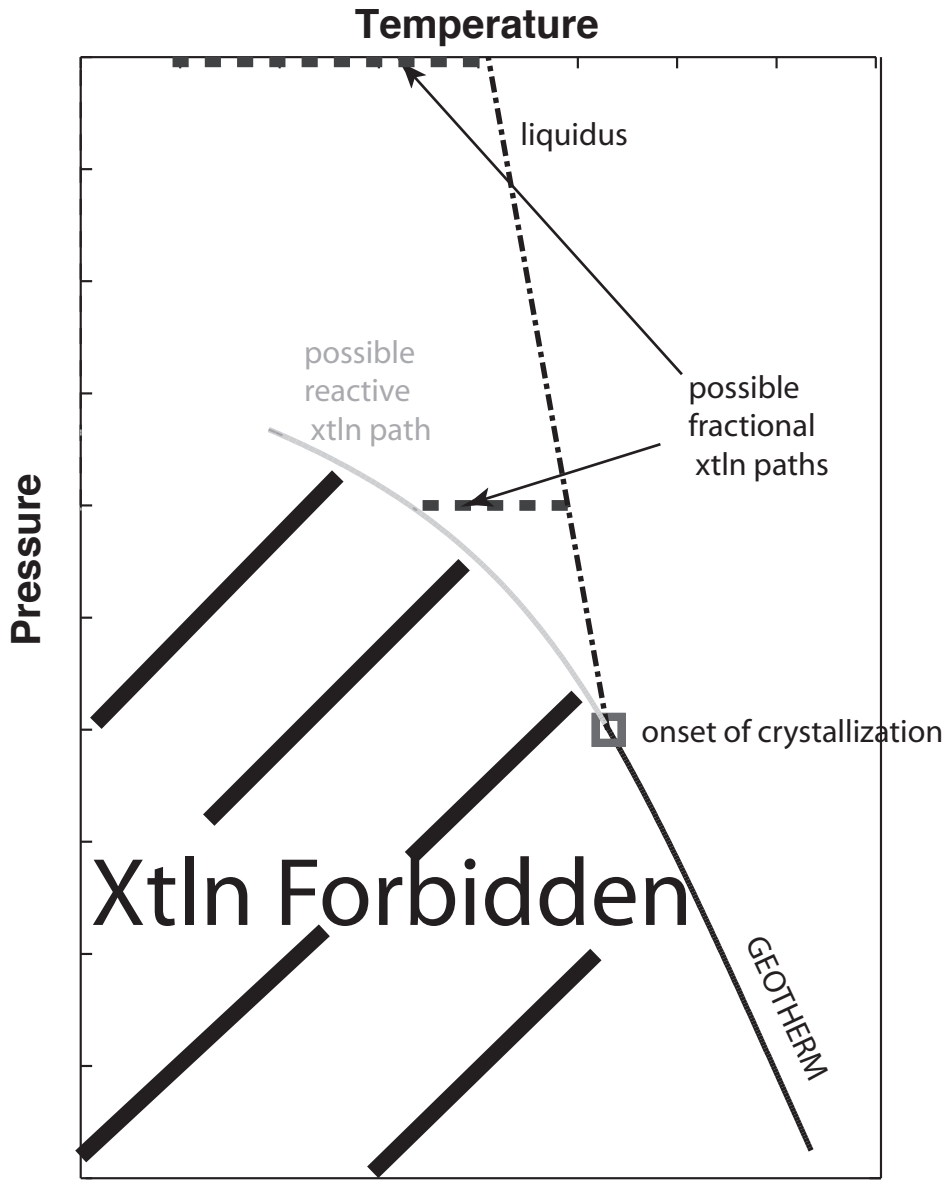

Figure 2-11: Plot of P-T trajectories for different crystallization scenarios that could potentially be experienced by an upwelling MORB liquid. Beginning at the onset of crystallization, liquids could either (a) quickly migrate towards the surface along their liquidus, out of thermal equilibrium with the surrounding mantle, or (b) migrate more slowly, in which case reactive crystallization can occur while the melt follows the geotherm. Fractional crystallization may occur at any depth shallower than the onset of crystallization, and corresponds to a decrease in liquid temperature at constant pressure. However, since liquids cannot cool below the temperature of ambient rock, the extent of fractional crystallization possible at high pressures is limited by the geotherm, making it unlikely that T65 variability is dominantly controlled by variations in the depth at which fractional crystallization occurs. Fractional crystallization paths are shown by dashed lines, while the basalt liquidus is shown by the patterned line initiating at the onset of crystallization. Reactive crystallization is shown by the gray path following the solidus.

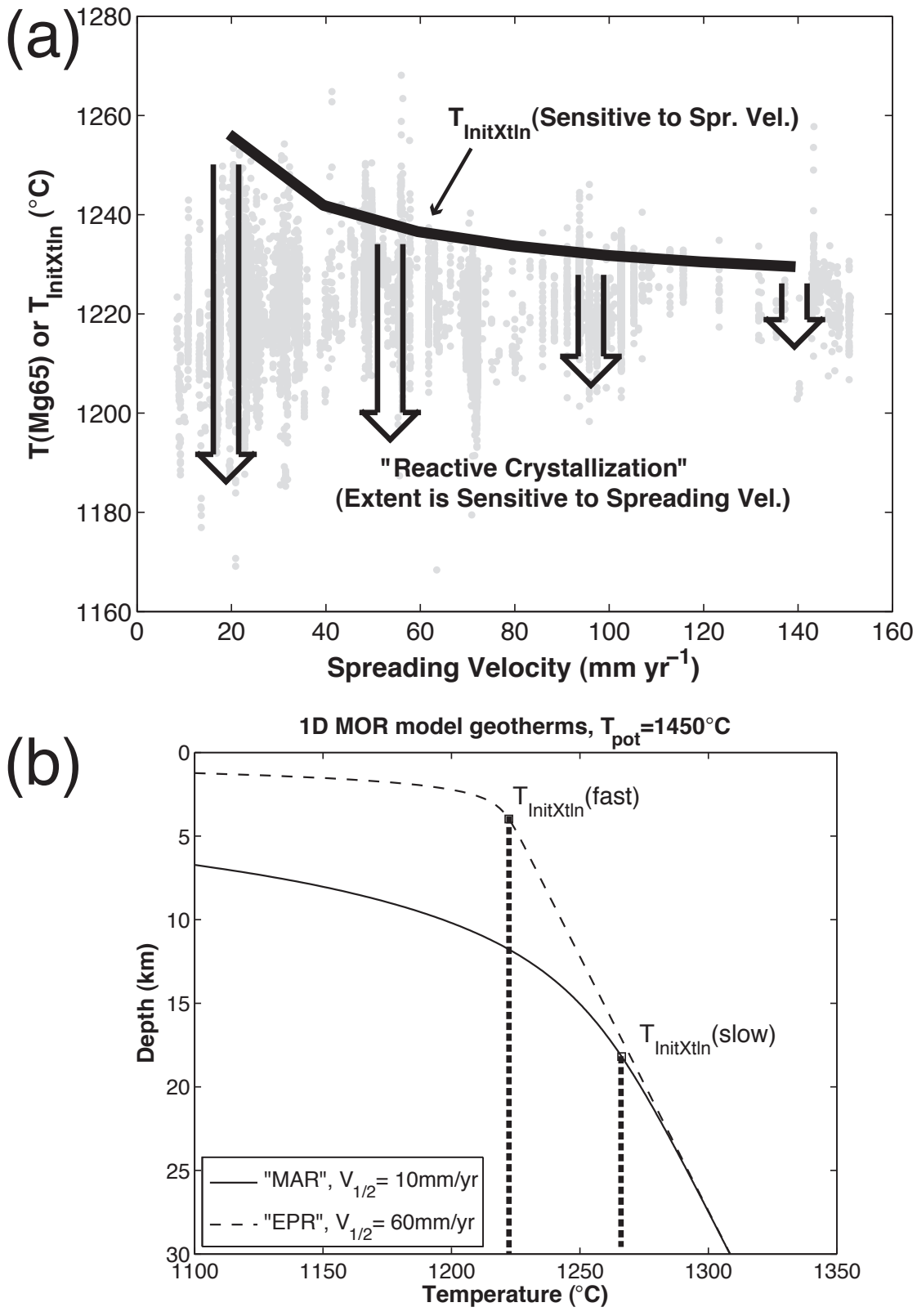

Figure 2-12: Caption given on next page.

Figure 2-12: (top panel) Illustration of our preferred interpretation of T65 variability in MORB, superimposed on a plot of T65 versus spreading rate calculated for all MORB glasses in PetDB with Mg# > 0.5. At the onset of interaction with the thermal boundary layer, MORB magma temperatures should display an inverse relationship with spreading rate since, for a given mantle potential temperature, slower spreading leads to a thicker thermal boundary layer, less melting and hotter magma temperatures at the onset of crystallization (denoted in the Figure as $T_{InitXtln}$). The solid bold line, which may be computed using the model described in the Appendix, illustrates this prediction. The initial melt temperature-spreading rate relationship is subsequently modified by variable extents of reactive crystallization (the effect of reactive crystallization shown by arrows). Decreasing temperatures at nearly constant Mg# due to reactive crystallization, lead to decreasing T65. Thicker thermal boundary layers at slower spreading ridges potentially allow for greater extents of reactive crystallization. (bottom panel) An example of the difference in temperatures of initial crystallization calculated for slow and fast spreading ridges using the thermal model described in the Appendix. The $T_{InitXtln}$ for each end-member geotherm is indicated by a vertical dashed line. Note that the crust-mantle transition is not explicitly modeled, but the depth "0 km" might be best interpreted in terms of this boundary.

tallization are predicted to be inversely related to the local spreading rate. The rationale behind this prediction is straightforward. Since the depth of the conductive thermal boundary layer should be inversely related to the spreading rate, the maximum degree of melting possible for a mantle of fixed energy content will be greatest beneath the shallow thermal boundary layers underlying fast spreading ridges. This greater extent of melting will extract additional energy via the heat of fusion, resulting in average or aggregated mantle melts at faster spreading ridges with generally cooler temperatures than at slower spreading ridges assuming melts generally maintain thermal equilibrium with the mantle throughout the melting column (The bottom panel of Figure 2-12 demonstrates this point based on calculated geotherms for slow- and fast-spreading examples using our previously described quantitative model). Predicted melt temperatures at the onset of crystallization are plotted as a bold line in the top panel of Figure 2-12. These predictions display a marked change in slope at slow spreading rates, reflecting non-linearity in the balance of advection versus diffusion of temperature in our model. Starting from this 'baseline' relationship between initial magma temperature and spreading rate, locally variable extents of reactive crystallization (schematically represented with arrows in Figure 2-12) could then introduce scatter in T65 observed at any given spreading rate. Greater amounts of reactive crystallization would lead to larger decreases in MgO at constant Mg# (and correspondingly, to lower T65). We have argued in a previous section that MORB T65 should be related to magma temperatures at the onset of crystallization, and have therefore plotted the T65 values inferred from the global MORB data in Figure 2-12. Qualitatively, the predicted relationship between initial magma temperatures and spreading rate could correspond to the upper envelope of MORB

T65 values at a given spreading rate, while the degree of scatter in T65 at a given spreading rate could be the result of differing amounts of reactive crystallization.

Several mechanisms might explain why there is more 30 km scale T65 variability at slow spreading ridges compared to fast spreading ridges. The depth interval over which reactive crystallization can take place, between the liquidus for ascending mantle melts and the solidus, for example, is much smaller at fast spreading ridges. In simple models, the depth interval over which melt –moving by porous flow– crystallizes in the thermal boundary layer, together with the melt flux determines the nature of melt transport (c.f., *Sparks and Parmentier*, 1991; *Spiegelman*, 1993; *Korenaga and Kelemen*, 1997; *Kelemen and Aharonov*, 1998; *Ghods and Arkani-Hamed*, 2000; *Rabinowicz and Ceuleneer*, 2005). At fast spreading rates, high melt fluxes and thin thermal boundary layers drive rapid crystallization rates within the thermal boundary layer, whereas at slow spreading rates, low melt fluxes and thick thermal boundary layers lead to much slower crystallization rates. When there is rapid crystallization over a short depth interval, pore space may be filled with new crystals, and the thermal boundary layer may form a permeability barrier below which most of the ascending melt beneath a ridge would pond *at nearly constant temperature*. We will refer to this as case (a). If, instead, there is slow crystallization over a large depth interval, viscous decompaction keeps pores open within the thermal boundary layer, and most of the ascending melt crystallizes at variable temperature and depth within the thermal boundary layer (case (b)).

In both cases, melt transport through the colder parts of the thermal boundary layer –particularly those beneath the solidus temperature– must occur in fractures. Also, in both cases the temperature of melt (at a given pressure) within the thermal boundary layer could range from the liquidus of primitive melt to the solidus of evolved melt. However, differences between these scenarios arise when considering the temperature distribution of porous melt within and just beneath the thermal boundary layer, before it is sampled by fractures. In case (a), most of the melt remains at nearly constant temperature beneath a permeability barrier until it is sampled by fractures. In case (b), melt temperatures are likely to be more variable, and fractures may commonly sample melt from a variety of depths within the thermal boundary layer. This simple argument may explain why local-scale T65 is more variable at slow spreading ridges compared to fast-spreading ridges. In addition, it has been advocated in previous studies that higher magma fluxes at fast spreading ridges lead to more efficient homogenization in shallow magma chambers (e.g., *Rubin and Sinton*, 2007, and references therein), potentially obscuring evidence for variable T65 in mantle-derived magmas.

2.5.7 Petrogenetic Modeling of Selected MOR Localities

It is standard practice in studies of basalt major element compositions to quantify differentiation processes in terms of "Fenner type" major element variation diagrams, with MgO and Mg# (also MgO/FeO) commonly considered as interchangeable choices for the independent variable. Yet although they are related, MgO and Mg# are not necessarily interchangeable and can be controlled by different, independent factors during magma differentiation. The MgO content of a melt dominantly reflects its temperature, as it is controlled by temperature-dependent partitioning of Mg between basaltic melts and olivine (± other Fe-Mg silicates). Mg#, on the other hand, reflects only the extent of crystal fractionation that has occurred after the melt has been transported out of equilibrium with refractory mantle olivine (± other silicates). As long as melt maintains Fe/Mg exchange equilibrium with a large reservoir of refractory olivine, Mg# cannot change, regardless of any changes in temperature or extent of crystal fractionation. Although MgO and Mg# are highly correlated during fractional crystallization, we have demonstrated that reactive crystallization can effectively diminish the correlation between these variables in basaltic liquids derived from a common parent (c.f., Figure 2-2 b). Consideration of both MgO and Mg# variation in the context of petrological forward models might allow the relative proportion of reactive and fractional crystallization recorded by specific MORB suites to be estimated in future work. At present, however, it remains difficult to define a quantitative scheme by which to "correct" MORB data for reactive crystallization. Instead, we focus on evaluating the consistency of MORB data with specific model initial liquid compositions and crystallization histories.

The panels in Figure 2-13 consist of two series of subplots that allow MORB compositional variability at five well-studied mid-ocean ridge localities to be compared with calculated end-member fractional crystallization and reactive crystallization LLD's. Each series of plots corresponds, respectively, with panels a) and b) of Figure 2-2. In the upper left panel of both sets of subplots, 0.6 GPa reactive crystallization LLD's (shown in green) were taken from the results described in a previous section, while 0.0001 GPa fractional crystallization LLD's (shown in blue dashed lines) were calculated both from the initial parent magma compositions of (*Kinzler and Grove*, 1992, , Table 4; shown as magenta boxes), and from a residual liquid composition after 50% reactive crystallization has occurred. The span of LLD's originating from a given model liquid summarizes the extent to which a combination of reactive and fractional crystallization models may account for observed distributions of basalt compositions. For example, a MORB sample with Ca# $\sim$ 0.68 and Mg# $\sim$ 0.62 could be interpreted as the product of either of the model initial liquids plotted in the upper left panel of Figure 2-13. If interpreted as a product of the Ca# $\sim$ 0.8 initial liquid, this composition would reflect $\sim$50% reactive crystallization, followed by $\sim$20-40% fractional crystallization

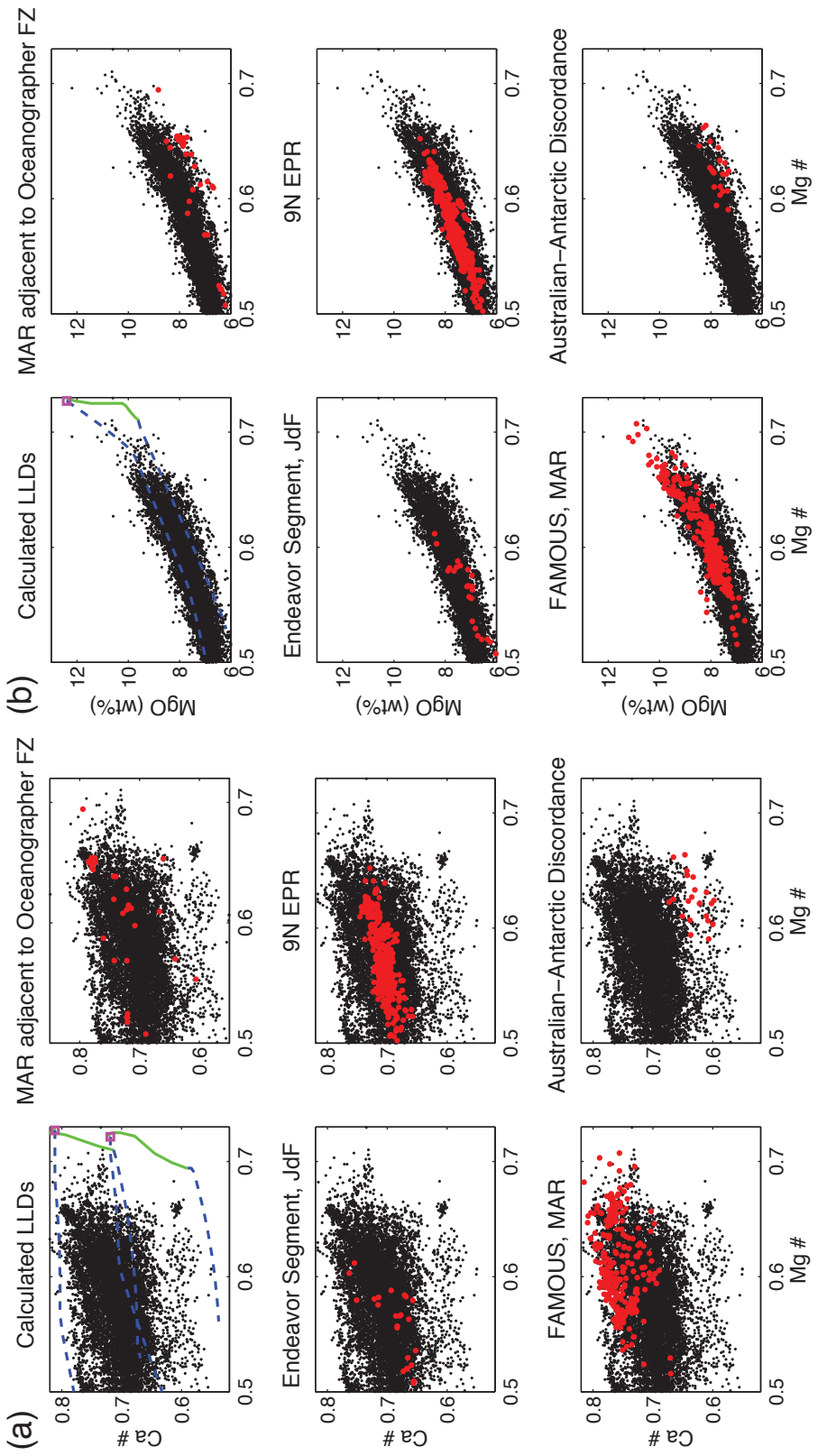

Figure 2-13: Caption given on next page.

Figure 2-13: Five case studies of well-sampled mid-ocean ridge localities, illustrating the ability of combined reactive crystallization and fractional crystallization from a single parental liquid composition to create observed lava variability. Model primary liquids are shown as magenta squares, 0.6 GPa reactive crystallization LLD's are plotted as solid green lines, 1 atm fractional crystallization LLD's are shown as dashed blue lines, and data from specific << 100km length scale localities are shown as red dots, with the full MORB data set shown in black for reference. The extent of the green reactive crystallization LLD's corresponds to 50% reactive crystallization. Data points within the span of model LLD's could be explained as crystallization products from a combination of reactive and fractional crystallization.

of the remaining liquid. Alternatively, this MORB composition could be explained as the result of $< 10\%$ reactive crystallization followed by $> 50\%$ fractional crystallization starting from the Ca# ~ 0.7 initial liquid.

The remainder of each series of subplots shows MORB glass samples from distinct localities with ∼30 km length scale (shown in red symbols) and the global MORB data in black for reference. We have ensured that the visual impact of these selected localities is representative of the global systematics: 67 of our spatial bins contain 30 or more samples, of which only 17 define relatively coherent ($R^2 > 0.7$) Ca#-Mg# and MgO-Mg# trends (such as in the 9N EPR panels) that are consistent with crystal fractionation from a single liquid composition.

Relative to variability in the global data set, the MAR localities display a very large scatter in Ca# and MgO, even after these variables are corrected to a constant reference Mg#. By implication, this variability could reflect perhaps $> 50\%$ reactive crystallization if it is assumed to be derived from initial liquids with a single, homogeneous major element composition. By contrast, the EPR data require little or no reactive crystallization to be invoked. A quantitative assessment of the extents of reactive crystallization implied by MORB lava compositions at specific areas is beyond the scope of this study, but could provide an important constraint on mid-ocean ridge melt transport as will be discussed further below.

2.6 Synthesis and Implications

We have presented theoretical arguments supporting the likelihood of reactive crystallization at mid-ocean ridges and argued that it provides the best available explanation for 30-km scale variability in Mg65 and T65. This 30-km scale variability comprises a large fraction of the total variability in fractionation-corrected, global MORB compositions. In this section, we briefly summarize our preferred conceptual model of reactive crystallization at mid-ocean

ridges, and discuss some broader implications.

Reactive crystallization requires slow cooling of melt relative to cation diffusion timescales, translating into a requirement for slow melt velocities and, particularly, melt transport through narrow channels with high surface area, such as in grain-scale porous flow. We consider the base of the thermal boundary layer beneath mid-ocean ridges as the most likely setting for reactive crystallization. Beneath the thermal boundary layer, melt transport in the upwelling mantle is mainly in chemically isolated conduits of focused flow (e.g., *Iwamori*, 1993, 1994; *Kelemen et al.*, 1995; *Aharonov et al.*, 1995; *Braun and Kelemen*, 2002; *Spiegelman and Kelemen*, 2003; *Jull et al.*, 2002)). As melt enters the thermal boundary layer, crystallization of melt in pore space leads to diverging downstream flow, culminating in uniformly distributed porous flow (*Aharonov et al.*, 1995, 1997). Low permeability caused by crystallization as rising magma begins to cool may further decrease melt velocity (e.g., *Sparks and Parmentier*, 1991; *Kelemen and Aharonov*, 1998), while super-solidus temperatures ensure melt stability over time periods sufficient for reaction to take place. Even if the initial liquid were constrained to undergo no more than 60% reactive crystallization, the commonly observed presence of lavas spanning $\sim$50% of global variability and $\sim 40-70\%$ of intra-ridge variability in MORB T65 and Mg65 within 30 km regions may be explained by crystallization from a single homogeneous parental liquid composition.

As magma ascends through increasingly cold rock and crystallizes, however, thermal (and therefore chemical) disequilibrium must occur for the melt to erupt at the surface. This precludes shallow reactive crystallization of the type that we have discussed here, though assimilation of wall rock or stoped blocks may still modify minor and trace element compositions of liquids in "magma chambers" or melt lenses. During this later phase of melt transport, fractional crystallization and magma mixing are expected to be the main controls on magmatic differentiation. This model for the role of reactive crystallization in MORB petrogenesis is summarized in Figure 2-14, representing a refinement of Figure 1c) in *Grove et al.* (1992).

In contrast to variation trends in abyssal peridotite (c.f., Figure 2-13), we have not found a continuous series of lava samples at any mid-ocean ridge locality that lies along predicted reactive crystallization LLDs. Apparently, the reactive crystallization signature of MORB is variable; the shallow melt transport system (probably, cracks) samples melts from a variety of depths, temperatures, and extents of reactive crystallization within all 30 km regions which we have examined. Additionally, melts that evolved by reactive crystallization have almost always undergone subsequent fractional crystallization and/or mixing.

In this paper, we have focused on reactive crystallization in the uppermost mantle. A similar process may well take place in the lower crust at some ridges (e.g., *Lissenberg and*

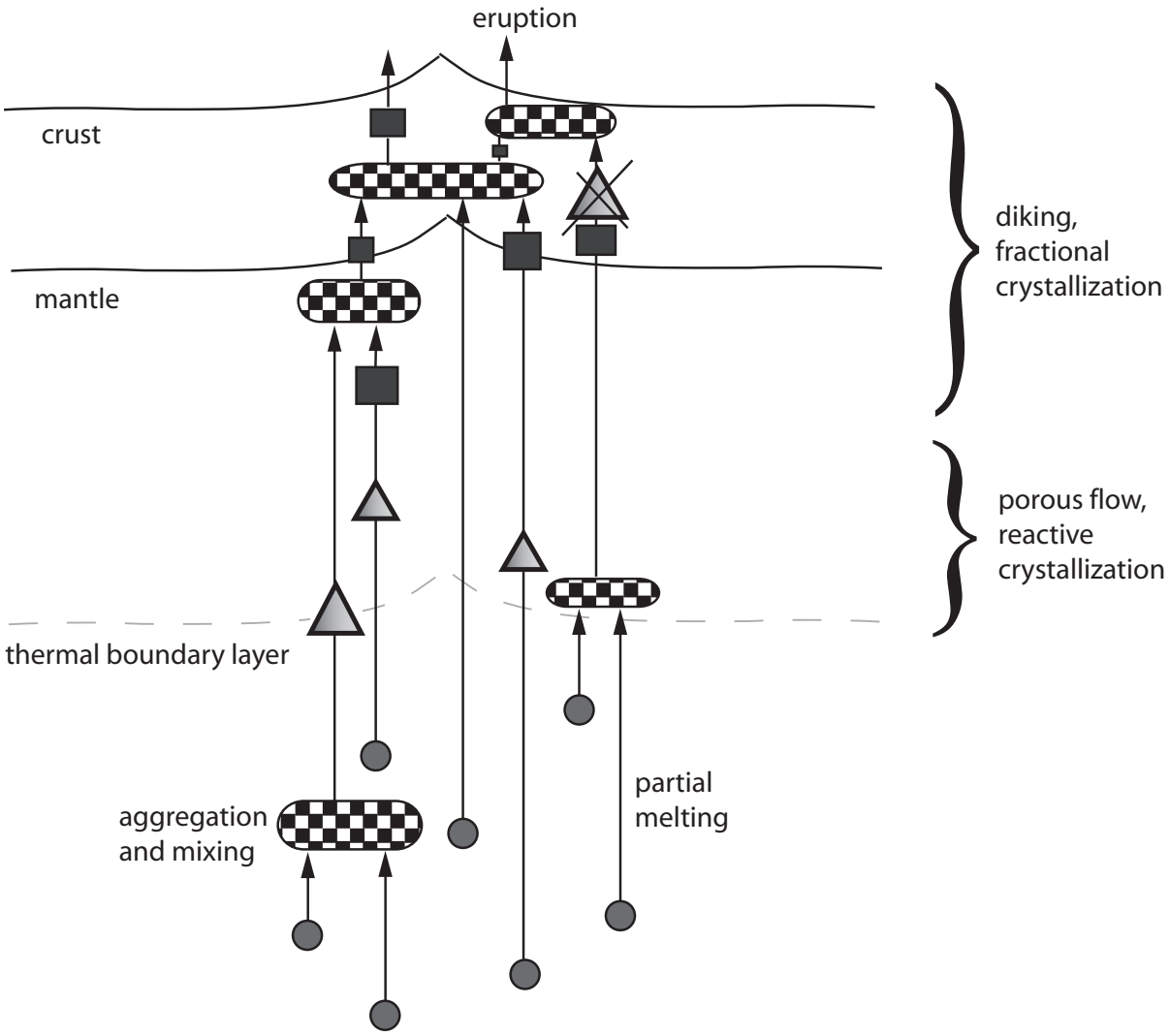

Figure 2-14: Summary diagram, modified after (*Grove et al.*, 1992), illustrating the likely role for reactive crystallization in MORB genesis. Circles represent local fractional melts, checkered fields indicate magma aggregation, triangles symbolize depths of reactive crystallization, while blue squares represent depths of fractional crystallization. Also shown are the thickness of the thermal boundary layer and the igneous crust above the Moho.

Dick, 2008). However, the main diagnostic for reactive crystallization in the shallow mantle thermal boundary layer, decreasing temperature and MgO at nearly constant Mg#, will be more subdued in interaction between lower crustal gabbro and melt due to lower proportions of olivine and pyroxene in gabbro compared to peridotite. Also, thermal constraints must generally limit the extent of lower crustal reactive crystallization compared to mantle reactive crystallization. This is reflected in the observation that trends of Ca# versus Mg# in Figure 2-13 for gabbroic suites are similar to trends produced by crystal fractionation in models and experiments, whereas the trend of Ca# versus Mg# for abyssal peridotite suites follows a reactive crystallization trend.

Reactive crystallization provides a mechanism by which variations in 'fractionation-corrected' T65 may be dominantly controlled by variable melt transport in the thermal boundary layer. Testable predictions of thermal boundary layer structure emerge from interpretations of T65 variability in MORB magmas in terms of varying extents of reactive crystallization. Where reactive crystallization occurs dominantly at mantle depths, it may be possible to link the mean degree of reactive crystallization inferred from observations of local MORB major element variability to the thickness of igneous crust, and to the proportion of gabbroic impregnations, veins and plutons emplaced into the underlying mantle. In turn, the variable vertical distribution of gabbroic rocks, above and within the shallow mantle, should produce variations in vertical seismic velocity profiles (e.g., *Lizarralde et al.* (2004)). Variability in the depth at which magma fractures arise might also potentially be predicted and observed.

2.7 Conclusions

Motivated by the chemical effect of melt-rock reaction in abyssal peridotites sampled from the mid-ocean ridges, we tested the potential for reaction with mantle wall rock during slow cooling and crystallization to create variability in primitive MORB magma compositions from a single primitive melt derived by partial melting at a single potential temperature. Thermodynamic calculations show that such reactive crystallization will cause derivative liquids to evolve along a different liquid line of descent (LLD) compared to closed-system crystal fractionation. Reactive crystallization LLD's are characterized by nearly constant Mg# and decreasing Ca# while fractional crystallization produces decreasing Mg# and Ca# in derivative liquids.

Dynamical calculations for steady-state 1D melt flow in upwelling mantle beneath a mid-ocean ridge imply that reactive crystallization is likely in flow regimes involving small melt velocities and high conduit surface area/volume (such as in grain-scale porous flow),

but not where transport is rapid (such as in cracks or dikes). We use local (30 km) scale variation in Mg65, defined as MgO corrected to a constant reference Mg# = 0.65, to infer T65, the magmatic temperature near the onset of crystallization, and use T65 to identify the effects of reactive crystallization. The global MORB dataset shows significant variability in T65 at a range of length scales. Ubiquitous variability in T65 observed within 30 km implies a range of temperatures for melts in equilibrium with the mantle beneath a small region. We find that the data are not consistent with polybaric sampling of melts along an adiabatic decompression melting path beginning with a mantle source at a single, regionally constant potential temperature. Instead, reactive crystallization can explain the 30 km scale variability in T65.

Fractionation corrected MORB compositions display variability at the 30 km scale that is inversely correlated with spreading rate, while the mean values of T65 are not correlated with spreading rate. Theoretical considerations suggest that reactive crystallization should be more extensive at slower spreading ridges, consistent with this observation. We can model suites of MORB samples in terms of variable proportions of reactive and fractional crystallization from a single initial partial melt of mantle peridotite.

Reactive crystallization provides a viable mechanism for creating chemical variability in MORB at small length scales, consistent with theoretical considerations and observations of MgO at constant Mg#, summarized by T65. Along with variability in mantle potential temperatures, sampling of polybaric, near fractional melts, or compositional heterogeneity in the mantle source, reactive crystallization may represent an additional process responsible for an important component of fractionation-corrected major element variability in MORB. Interpreted from the perspective of reactive crystallization, MORB major element compositions can be sensitive indicators of melt transport dynamics. Future work could provide new constraints on melt transport through comparison of major element variability observed at specific localities with that predicted by integrated geochemical and geodynamic models of mid-ocean ridge magmatism.

Chapter 3

Major Element Variability in Heterogeneously Sampled Ocean Ridge Basalts

3.1 Introduction

There is a rapid and ongoing increase in the quantity of geochemical data available from throughout the global network of mid-ocean ridges. One of the first syntheses of global mid-ocean ridge basalt (MORB) glass geochemistry, for example, was based on 858 samples representing 84 ocean ridge intervals of 1 - 100 km length scale, only 27 of which represented by more than 10 samples (*Klein and Langmuir*, 1987). By contrast, the largest current compilation of MORB compositions, available at www.petdb.org (*Lehnert et al.*, 2000), contains over 14,000 MORB glasses from thousands of sampling stations representing nearly two thirds of the global ocean ridge system. This accumulation of data has allowed a clearer picture of MORB variability to emerge, the result of both greater spatial coverage, as well as an enhanced ability to assess the statistical character of variability in detail. However, there is also a complication associated with the use of large sample-size global MORB data compilations that has remained largely unexamined: the sampling pattern from which the data have emerged is spatially very inhomogeneous. A few regions, such as the FAMOUS site on the Mid-Atlantic Ridge (MAR) or the East Pacific Rise (EPR) at 9N, are represented in the data set by several hundred samples, collected from nearly one hundred independent sampling stations. Most other sections of ocean ridge, by contrast, are represented with more than an order of magnitude lower sampling densities. Sampling stations themselves are also represented by a widely variable number of analyses. The potential for artifacts in apparent MORB variability due to extreme variations in spatial density of sampling stations has been previously recognized (e.g., *Rudge*, 2008). However, this topic has never been systematically

investigated.

In this study we address the potential impact of inhomogeneous sampling on the perceived character of MORB variability using techniques of exploratory data analysis and computational statistics. We will not attempt to provide geologic interpretations of MORB major element variations here. Instead, we wish to develop an up-to-date assessment of the basic spatial and statistical character of MORB variability *after the effects of heterogeneous sampling have been accounted for*, and to compare our results with conclusions from previous studies. We focus on variability in MORB major elements here, as they are of primary interest to geodynamicists and petrologists, but also because the major elements, unlike trace elements and isotopes are compiled in PetDB as a complete geochemical series with a minimum of data gaps (many multivariate analysis techniques require knowledge of all variables in all samples). Thus, only MORB major element variability can be studied in a comprehensive fashion at this time (in the sense of accounting for all variables simultaneously) without sacrificing the exceptionally large sample size available from the PetDB compilation (c.f., Figure B-2 in Appendix B for a sparsity diagram of that portion of the PetDB compilation for which major element data is available).

In this study, we analyze the PetDB compilation in conjunction with an additional piece of previous work. As described in Chapter 2 of this thesis, we have developed a scheme in which all MORB data are assigned to 30-km scale spatial bins. While the 30-km spatial binning length scale is arbitrary to this study, it is useful as a relatively high-spatial resolution binning scheme for examining global MORB systematics. This binning scheme itself represents a highly labor-intensive product, and there are no alternative binning schemes of comparable resolution available in the literature at this time.

We begin by developing a visualization scheme for MORB major element data based on an assessment of the number of independent degrees of freedom contained in global MORB variability. Our scheme allows fractionation-corrected major element variability to be visualized in scatterplots, and displays a close similarity to widely used projections in the MORB literature. We next examine the degree of compositional clustering in MORB samples collected at any single sampling station (each individual dredge, rock core, etc. is defined by a unique station ID within PetDB, which allows different hand specimens collected from a single location or outcrop to be identified). Combining all available case studies, we demonstrate significant spatial clustering of composition: we estimate that MORB samples from within a given sampling station are likely to yield fractionation-corrected variability that is only between 10 and 30 percent of the total variability present within 30 km. We also document large spatial heterogeneity in sampling density through which the global MORB data have been generated. The combination of compositional clustering of spatially associated

samples and large variations in sampling density make the presence of sampling artifacts in the PetDB compilation very likely. The effect of sampling method on perceived MORB variability is also explored, but we conclude that spatial variations in the methods used to collect MORB samples (e.g., dredges versus submersibles, etc.) are not likely to have a large impact on global MORB variability systematics. Next, we introduce a method for removing sampling bias in MORB data through multiple iterations of random subsampling. Our results are visualized through probability density estimates which describe the full, unbiased variability within a fractionation-corrected MORB data set. We first demonstrate that our MORB variability visualization scheme is robust with respect to biased sampling. We then apply our methods to three spatially separate ocean ridges. The resulting sampling-corrected probability density estimates from each ocean ridge are similar, but display systematic differences, consistent with the conclusions of previous studies (*Klein and Langmuir*, 1987; *Langmuir et al.*, 1992). We also demonstrate that the FAMOUS region of the MAR is anomalous geochemically relative to less well-sampled MAR to the south. We do not resolve any additional features of regional or ridge-scale MORB major element variability beyond those previously recognized by early studies (e.g., *Klein and Langmuir*, 1987; *Langmuir et al.*, 1992). (However, MORB variability at smaller spatial scales is, of course, also of interest, and has become much better constrained over the past decades, particularly at a relatively small number of sites such as the northern East Pacific Rise.) We explore the relationship between the estimated variability at MORB locations and the number of sampling stations available, finding a minimum of 10 independent sampling stations are required for the apparent standard deviation of MORB variability to approach the true standard deviation, although a minimum sampling density of ~ 1 independent station per km of ridge axis is much more likely to deliver a reasonable approximation to underlying variability, at least on the 30-km scale (corresponding to ≥ 30 independent sampling stations per spatial bin). We conclude with a discussion of the relationship between estimated MORB variability and spreading rate, once sampling is taken into account.

3.2 Principal Component Analysis and the Character of Variability in MORB Major Elements

Spatially separate mid-ocean ridges often display distinctive variability in terms of the seven most abundant major element oxides: SiO_2, TiO_2, Al_2O_3, FeO, MgO, CaO, and Na_2O (*Dick et al.*, 1984; *Klein and Langmuir*, 1987). Figure 3-1 illustrates this observation as reflected in the PetDB MORB compilation (*Lehnert et al.*, 2000). Although MORB samples at all

locations display some variability, it is evident from this Figure that MORB from some locations display greater compositional variability than at others (e.g., the Southwest Indian Ridge (SWIR) is more variable than the East Pacific Rise (EPR)). At least in terms of some geochemical variables (e.g., Na_2O or FeO), sample suites from specific locations can even display patterns of variability with little or no overlap with variability observed elsewhere.

As shown in Figure 3-1, the MORB major element data set we consider has seven variables. If dependencies among these variables could be revealed, this could allow significantly simpler data visualization and analysis. Principal Component Analysis (PCA) is a common technique of multivariate data analysis that seeks to (1) identify independent (orthogonal) components of variability within data and (2) determine the relative importance of these components in explaining the data. To make our results most relevant to typical MORB, we will discuss a filtered version of the global PetDB major element compilation throughout this study. We wish to remove basalt samples from consideration that have experienced especially high degrees of crystallization: we consider only MORB with Mg# ≥ 0.5 (primitive magmas, in equilibrium with the mantle have Mg# $\sim$0.7 *Roeder and Emslie* (1970)). A short introduction to PCA and details of our MATLAB implementation are provided in Section B.1 of Appendix B.

As shown in Figure 3-2, approximately half of the variability in the data is due to the first principal component, over 70 percent of the variability in the data is contained in the first two principal components, and nearly 90 percent of the variability is accounted for by the first three principal components. Our PCA therefore suggests that the original 7-dimensional set of MORB compositions may be expressed and discussed in terms of the three-dimensional principal component space defined by the first three components, with minimal loss of information. In an earlier study, *Albarède* (1992) performed PCA on a data set of basaltic liquid compositions obtained from peridotite melting experiments reflecting a range of pressures, temperatures and starting compositions. Although that study included additional parameters T, P and K_2O, the results were similar to those of this study: 80% of the data variability could be explained by three principal components, while 92% could be explained using four components. By contrast, the combined contribution of the four smallest principal components emerging from the present analysis accounts for only 10% of total variability. It is possible that these smallest principal components dominantly reflect variability introduced through factors other than igneous MORB variability, including measurement errors, rounding and data entry errors, and inter-laboratory biases (*Langmuir et al.*, 1992, *Kerstin Lehnert, personal communication).* A quantitative assessment of the likely relationship of such errors in the PetDB compilation and specific principal components, however, is beyond the scope of the present study.

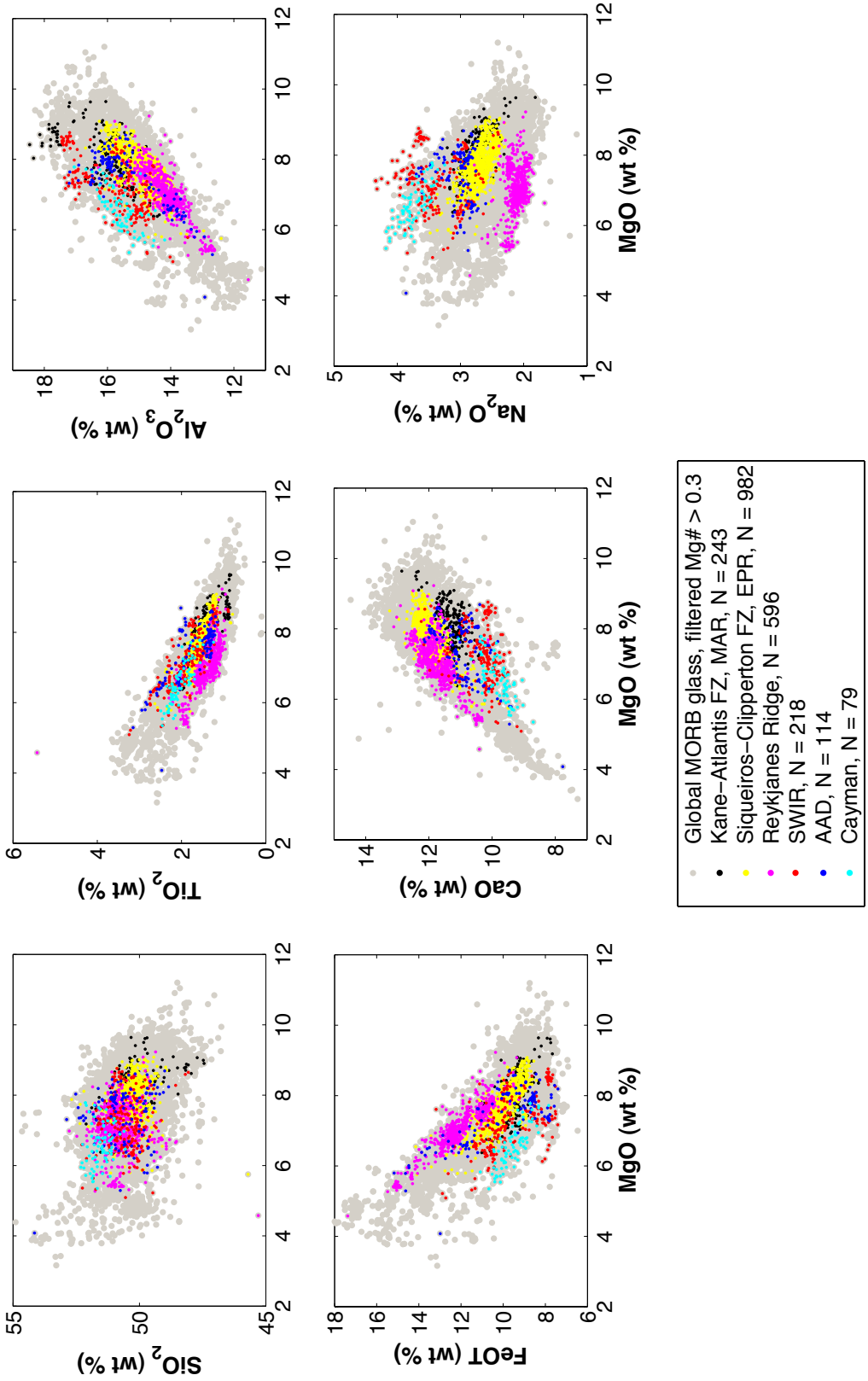

Figure 3-1: Caption given on next page.

Figure 3-1: The global MORB major element compilation available from from PetDB (*Lehnert et al.*, 2000) is visuallized here through a series of bivariate MgO-variation diagrams. The data set has been filtered to exclude highly evolved samples with Mg# values less than 0.3 (Mg# is defined as molar MgO/(MgO+FeO); basalts with Mg# values of ~ 0.7 could be in equilibrium with the mantle, while fractional crystallization leads to lower values of Mg#), retaining 12075 out of 12151 compiled on-axis MORB samples. Each symbol represents an individual MORB sample. Colors indicate samples collected from specific MOR localities that feature prominently in the MORB literature. Sample sizes available for each location are given in the legend. Note the location-dependence of compositional trends, as well as differences in the variability displayed by individual compositional trends.

There is a clear correspondence between the three main principal components determined here and the primary features of MORB data recognized and interpreted in previous work (e.g., *Langmuir et al.*, 1992; *Grove et al.*, 1992). The most obvious correlation observed in MORB major element data, for example, is long recognized to closely mirror the low-pressure compositional evolution of crystallizing basaltic magmas (e.g., *Bender et al.*, 1978; *Walker et al.*, 1979; *Tormey et al.*, 1987; *Grove et al.*, 1992). This trend is closely approximated by the first principal component (c.f., the right-hand panels of Figure 3-2), underscoring the likely relationship between the first principal component score of a given MORB sample and the extent of fractional crystallization it has experienced. As shown in Figure 3-2, positive values of the first principal component score indicate a higher than average extent of fractionation, while a negative score would indicate a relatively unfractionated sample. A key additional argument supporting our interpretation of the first principal component is the experimentally well documented fact that multiply saturated crystallizing magmas evolve along nearly linear trends when viewed in major element variation diagrams. If the compositional trend were significantly curved, for example, there could not be no direct correspondence between crystallization and any principal component. Further discussion and illustration of this point is provided in Appendix B. We feel that the second principal component of MORB major element data is also readily interpreted in terms of previous work. This principal component (abbreviated in the remainder of the text as PC2) closely matches the linear global trend defined by (*Klein and Langmuir*, 1987) using fractionation-corrected MORB data. The near-vertical appearance of this component in the Na and Fe variation diagrams shown in Figure 3-2 substantiates this point. A positive PC2 score corresponds to the "Reykjanes" compositional end-member suggested by *Klein and Langmuir* (1987), while a negative score corresponds to a "Cayman" end-member fractionation-corrected composition. The so-called local trends commonly displayed by fractionation-corrected MORB suites from spatially limited slow-spreading ridges (e.g., *Klein and Langmuir*, 1989; *Langmuir et al.*, 1992; *Niu and Batiza*, 1993) are also reflected in the principal components. These data features, roughly

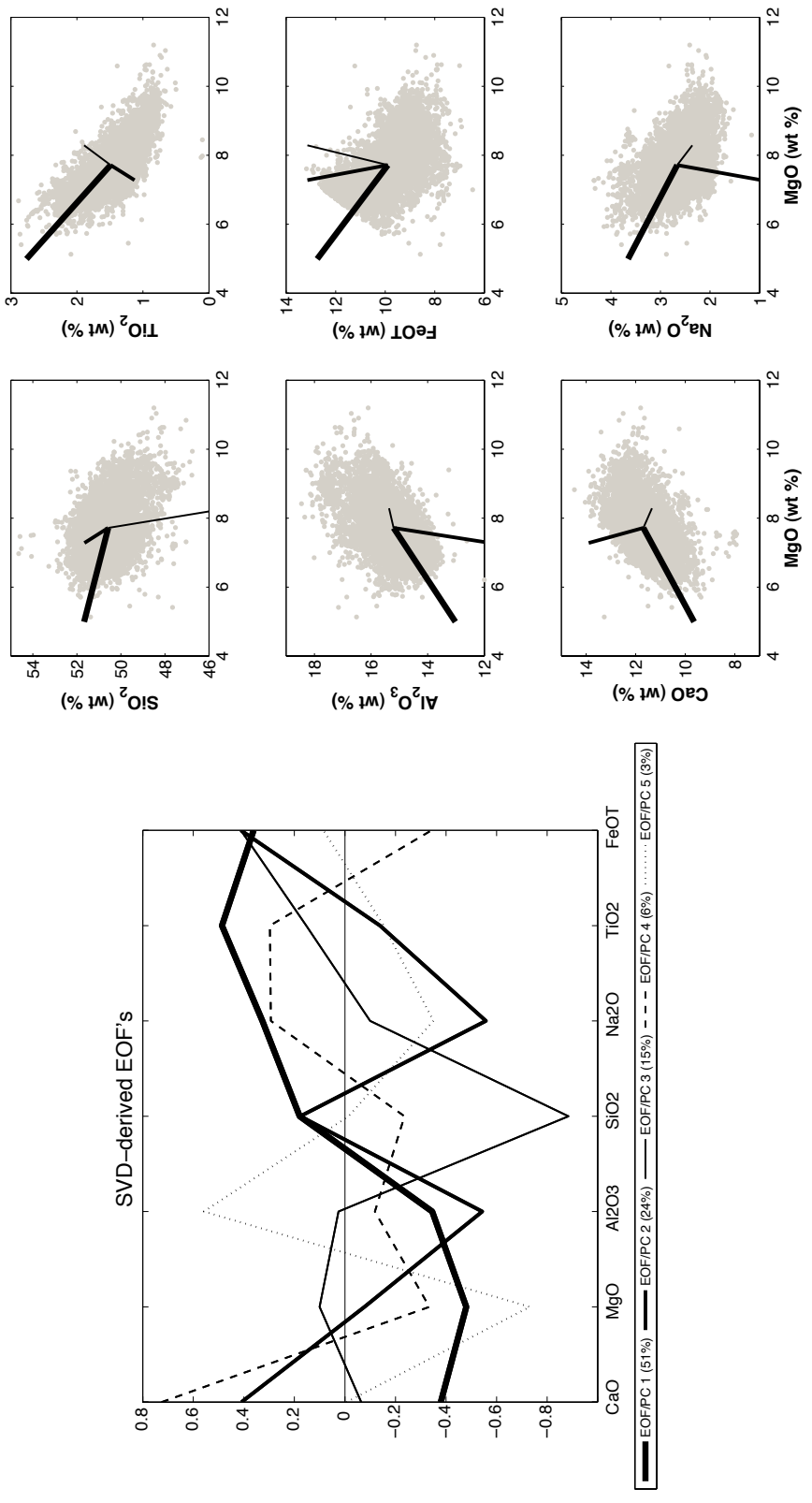

Figure 3-2: Caption given on next page.

Figure 3-2: (left) Parallel-coordinate (or "spider-diagram") visualization of the five most important Empirical Orthogonal Functions (EOF's) corresponding to the independent (orthogonal) components of variability within the global MORB data, as determined through Principal Component Analysis. The relative importance of each EOF is specified in the legend, representing the amount of MORB variability each EOF can account for individually relative to the total MORB variability. Although there are seven total EOF's, the first five account for 99% of variability. Each EOF vector is of unit length within the space defined by the demeaned, data normalized to the standard deviation of each variable. The value of each EOF with respect to a given major element variable reflects its effect on that variable. For example, the first EOF (corresponding to principal component 1) describes a simultaneous decrease in CaO, MgO, and Al_2O_3 while SiO_2 is relatively unaffected and Na_2O, TiO_2 and FeO increase. (EOF values of zero correspond to no effect, while EOF values approaching -1 or +1 reflect large changes). (right) Projection of the three largest, geologically significant EOF's into MgO variation diagrams common in the petrologic literature. The line weights correspond to the descriptions provided in the legend at left. Further discussion provided in the text.

perpendicular to the global trend, essentially correspond with the third principal component (PC3). Figure 3-3 illustrates the near-equivalence of two common visualizations of major element data from the MORB literature with the principal component projections introduced here.

Our scheme for describing MORB variability through principal components also allows fractionation correction to be performed in a straightforward manner: by omitting (or projecting out) the first principal component, we remove fractionation-parallel variability, essentially equivalent to the result of applying the fractionation-correction procedure spelled out by *Klein and Langmuir* (1987). PC2-PC3 graphs therefore allow us to visualize 90% of total fractionation-corrected major element variability in MORB. Throughout the remainder of this manuscript, we will therefore develop our arguments on the basis of variability in the second and third principal component scores of MORB samples.

3.3 The Influence of Sampling on Perceived Variability

MORB geochemical variability is often visualized using bivariate scatter plots. In general, such plots simply depict all available relevant analyses (or, alternatively, spatially binned averages of analyses), and do not take into consideration the possibility of correlations between samples. To visualize major element variability along the East Pacific Rise, for example, a scatter plot might include all MORB analyses collected from on-axis samples from between $\sim$ 40 S to $\sim$ 20 N along this ridge. In a strict sense, scatter plots of such a 'raw' compilation are representative of actual variability along the EPR only under the implicit assumption that each data point represents an independent sample from the EPR interval of interest.

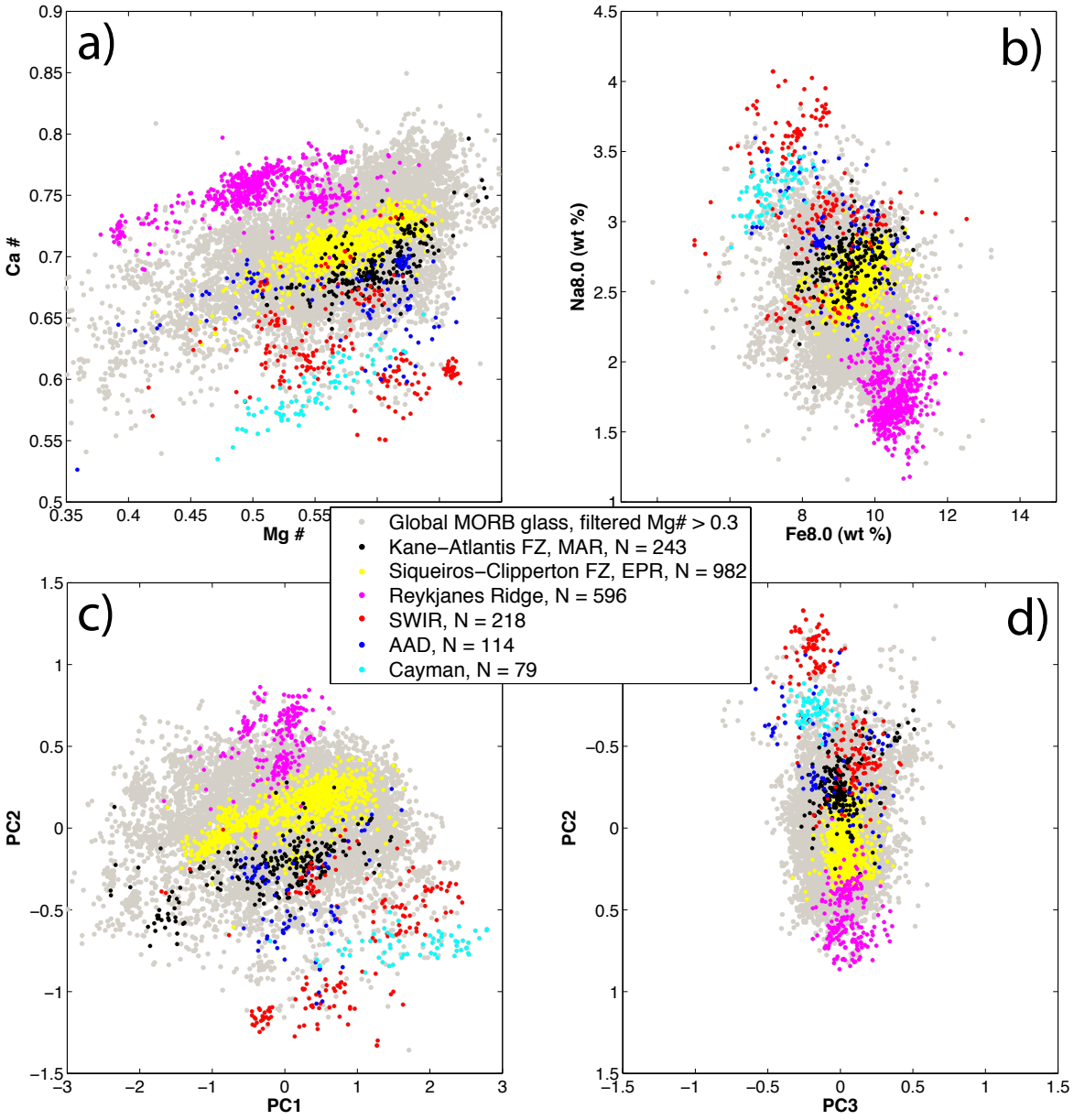

Figure 3-3: Comparison of diagrams for summarizing MORB major element variability that are common in the geologic literature (top panels) with diagrams derived from PCA (bottom panels). Panels are arranged to facilitate column-wise comparisons. Symbols are as described in the caption to Figure 3-1. Ca# indicates molar Ca/(Ca+Na) in each MORB sample. Principal component scores shown in the bottom panels describe the deviation of MORB sample compositions from the data mean along each of the principal component axes. "PC1", for example, denotes the first principal component score of each sample. Further discussion provided in the text.

The validity of this assumption depends on the relationship between length scales characterizing MORB variability erupted at the seafloor and the sampling length scale. If the length

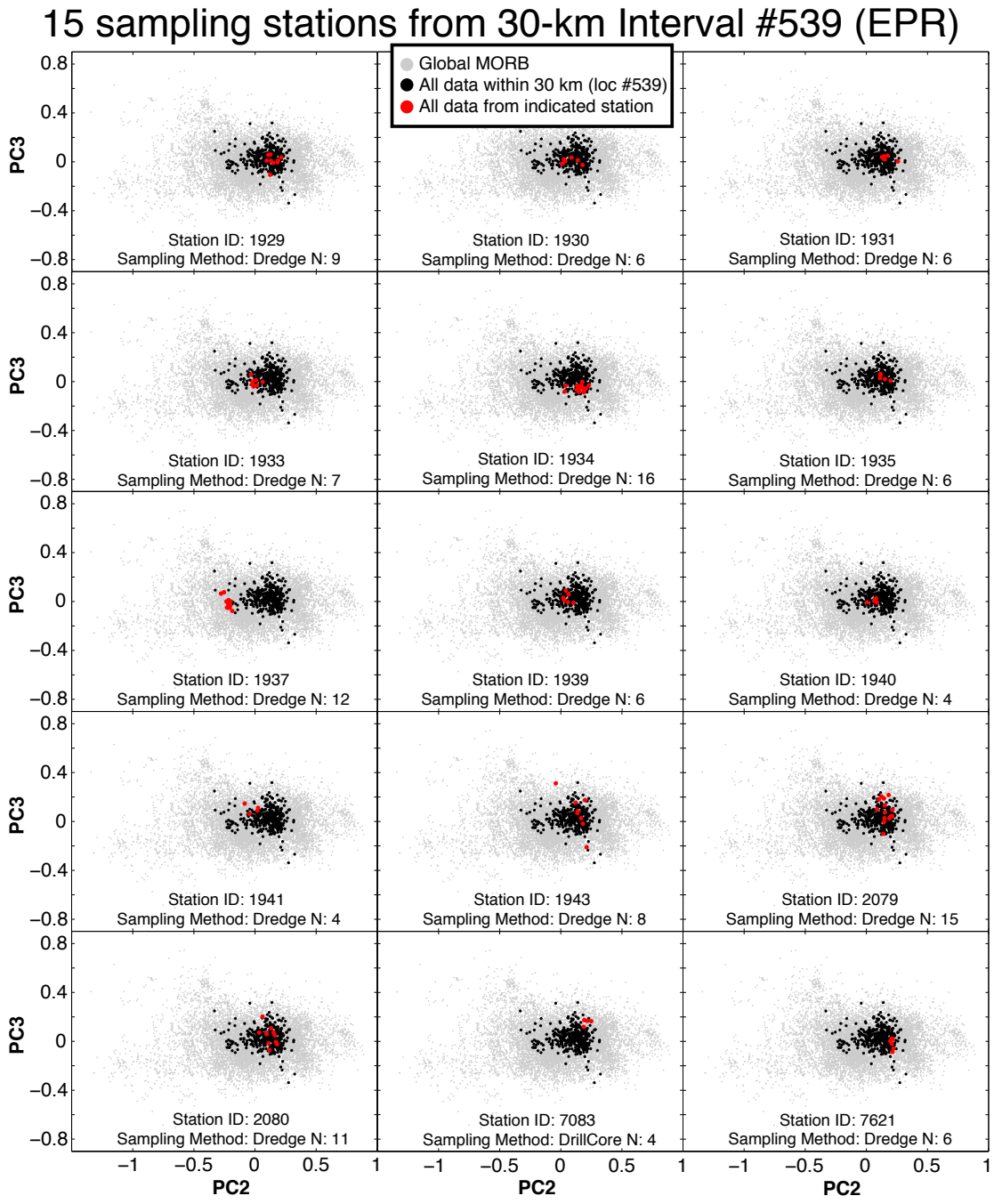

Figure 3-4: Caption given on next page.

scale of MORB variability over some ridge interval of interest is smaller than the sampling

Figure 3-4: Representative case study illustrating the character of MORB variability observed on three spatial scales. Major element variability is visualized using a plot of the second and third principal component scores, as discussed in a previous section. In each panel, data shown in black and gray is identical, representing all data from a 30-km spatial interval along the EPR at 9.57 N, approximately 60 km south of the Clipperton Fracture Zone, and the global MORB compilation, respectively. Data highlighted in red, in turn, are unique to each panel, and show MORB variability observed within each of the sampling stations from a 30-km ridge interval yielding more than two samples. Note the high degree of clustering in MORB from specific sampling stations.

length scale, then any specific composition visible within an interval of ridge axis should also be observable (at least in principle) within the data collected from a given sampling station. However, if the length scale of MORB variability is larger than the sampling length scale, samples from within a given station will not sample the full variability present. In this case, sampling is biased, and large heterogeneities in sampling density can potentially lead to artifacts in apparent MORB variability. While the length scales of MORB variability cannot be known a priori, most available sampling stations represent dredge locations, with sampling length scales between 100m and several km. Other sampling methods such as submersible grabs and core samples correspond to even smaller sampling length scales.

As a simplest test for biased sampling, we have examined the data from all sampling stations throughout the global ridge system that yield multiple MORB samples. If the internal variability at specific sampling stations is statistically similar to the variability that is visible within a 30-km ridge interval, then this observation would support the conclusion that despite large spatial heterogeneities in sampling density, sampling is not necessarily biased. However, the data do not support this argument. Figure 3-4 illustrates a representative case study from the EPR. This particular 30-km interval of ridge axis is sampled by 15 spatially separated sampling stations that are each, in turn, represented by between 4 and 16 MORB samples (additional sampling stations exist within this region, but the submersible grabs they represent only include one or two samples, and are not shown here). The key observation from this case study is that relative to the full variability observable over this 30-km interval, samples from any individual station display far smaller variability, even when more than ten samples are available. In this example, the compositions of MORB samples from within a given dredge are clearly clustered, and it would be inappropriate to represent the true MORB variability at this EPR location through a simple scatter plot of all available data. Although such a plot (not shown) will display multiple *apparent* compositional modes, these modes simply reflect the compositions prevalent at those sampling stations with a particularly large number of analyses relative to the others. Failure to take sampling heterogeneity into account could also lead to biasing of the computed average or standard deviation of MORB

compositions at this location.

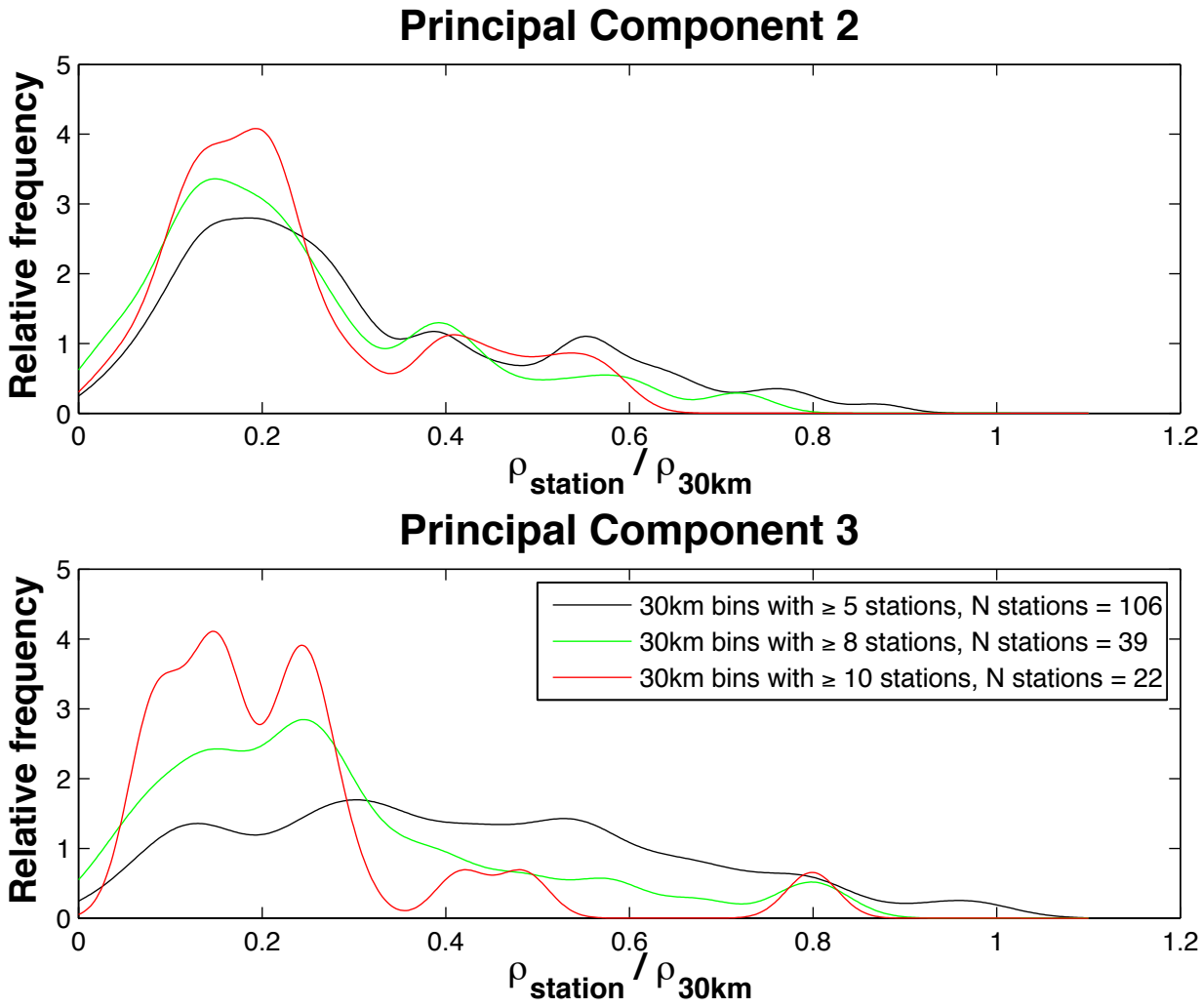

Figure 3-5: Quantitative summary of the effect illustrated in Figure 3-4. For all available locations represented in the global MORB compilation, the range in MORB compositions within a given sampling station $\rho_{station}$ is calculated relative to the total range of compositions observed within 30 km of that station ρ_{30km}. The global relative frequency of $\rho_{station}/\rho_{30km}$ is shown for all cases where a given minimum number of sampling stations are available within 30 km. Note that the variability observed within 30 km is positively correlated with the number of sampling stations available (particularly in the case of PC3). When analysis is restricted to more "well-sampled" 30 km ridge intervals with more independent sampling stations, high values of $\rho_{station}/\rho_{30km}$ become less frequent. This probably reflects underestimation of 30-km variability at locations sampled by few independent sampling stations. Further discussion is provided in the text.

To quantitatively estimate the potential impact of compositionally clustered MORB samples on variability throughout the global MORB compilation, we have calculated the range

of PC2 and PC3 scores observed at a number of individual sampling stations (represented by five or more MORB samples each), and compared this variability with the corresponding PC2 and PC3 variability observed within 30 km of each station. Our results are summarized in Figure 3-5. Although we have identified 509 sampling stations in PetDB satisfying the requirement of containing 5 or more samples, the majority of these occur in 30-km intervals of ocean ridge axis that are sampled by few or no other sampling stations, making it impossible to effectively estimate the "true" variability present within 30-km. We have nevertheless carried out our analysis for those stations that are located in 30-km spatial bins represented by more than some arbitrary minimum number of other sampling stations. Figure 3-5 demonstrates that the overwhelming majority of sampling stations within well-sampled on-axis spatial intervals display only between 10 and 30 percent of the total variability observed within 30 km. We have performed this analysis using several values for the arbitrary minimum number of other sampling stations present within 30 km to ensure our results are robust, despite the positive correlation in the absolute range of principal component scores observed within 30 km and the number of sampling stations available within a given interval. The observations summarized in Figure 3-5 demonstrate that variability observed within any single sampling station cannot provide a reliable estimate of variability at length scales much longer than the sampling length scale. Instead variability within any single sampling station systematically under-estimates variability at larger length scales. Since samples from within a given station are correlated in composition, the PetDB MORB compilation will be biased to some extent if there is variation in the number of MORB samples representing different stations. In fact, we find extreme variability in the number of samples per station, as will be detailed in a subsequent section.

3.3.1 Spatial Heterogeneity in Global MORB Sampling

Of the 3389 sampling stations examined in our study, 2094 (62% of the total) are represented by a single MORB analysis. An additional 415 stations (12%) have provided two MORB samples each, and 228 (7%) stations contain three MORB analyses. 95% of all sampling stations contain ten or fewer MORB samples. However, 178 stations worldwide contain more than 10 samples. If the number of samples per sampling station are not taken into account, these stations will therefore carry at least an order of magnitude more statistical importance than stations with only one analysis. Of these high sample size stations, six contain more than 50 samples, and two are represented by more than 100 samples (the maximum is 123 samples from one dredge), with correspondingly even greater potential for creating statistical artifacts. The global distribution of sampling heterogeneity is summarized

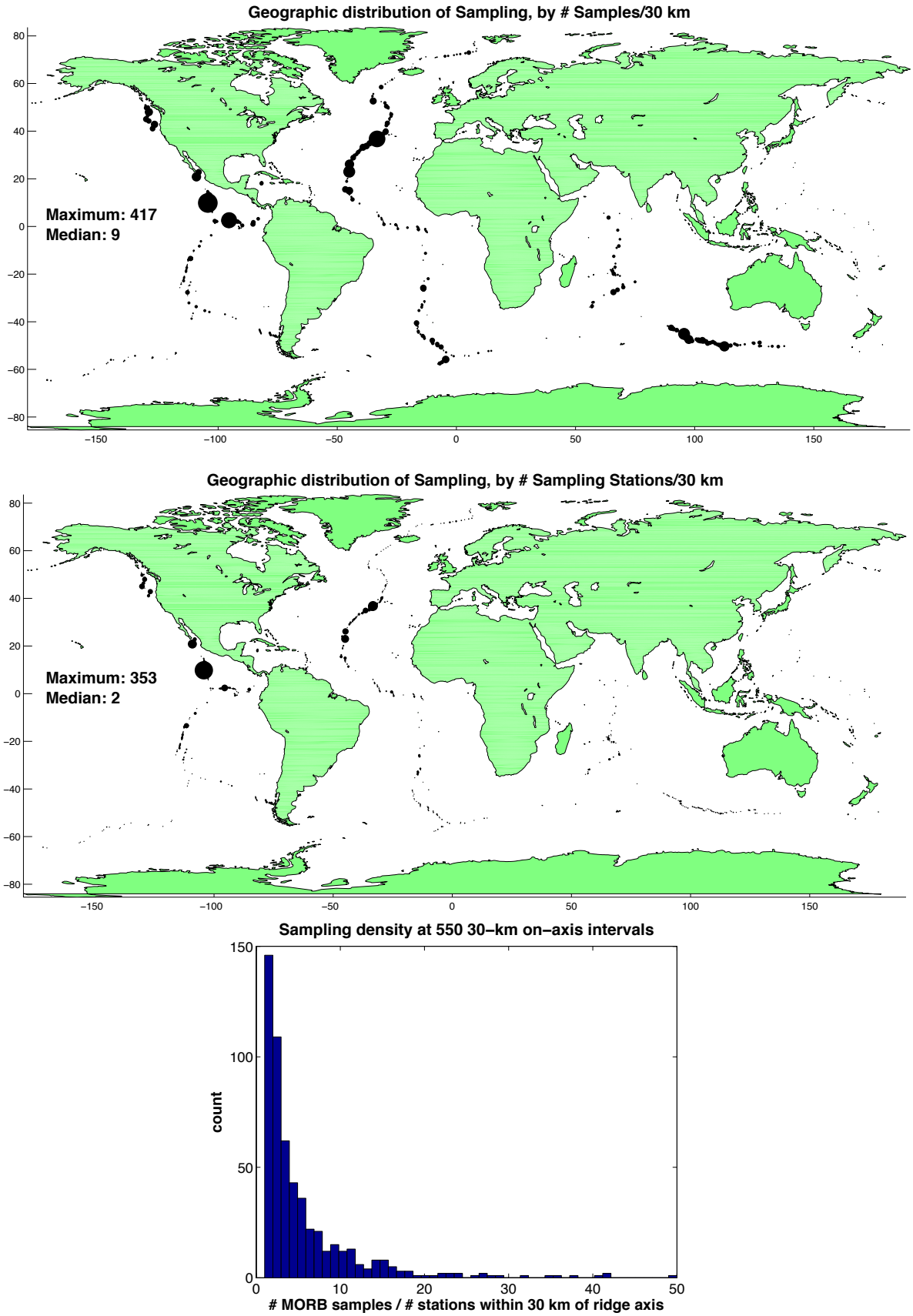

Figure 3-6: Caption given on next page.

Figure 3-6: Visualization of sampling heterogeneity throughout the global ocean ridge system. (top) Global sampling density, in terms of the number of samples available within a 30 km radius is shown with larger symbols corresponding to higher numbers of available samples. (center) Global sampling density, in terms of number of sampling stations present within 30 km. (bottom) Histogram illustrating the large variability in the number of MORB samples representing each station within 30 km globally. As discussed further in the text, the clustering of MORB sample compositions within a given sampling station (c.f., Figures 3-4 and 3-5), implies that the variability shown in this panel can lead to data artifacts related to biased sampling.

graphically in Figure 3-6.

3.3.2 Does sample collection method affect apparent variability?

A variety of methods are used to collect MORB samples from the seafloor. The PetDB compilation provides information about sampling methods used for each compiled MORB sample. The three most common methods reflected in the PetDB compilation are dredges, submersibles, and rock cores. While dredges are by far the most common sampling method, there is spatial heterogeneity along-axis in terms of the sampling methods employed (c.f., Figure 3-7). Different sampling methods sample at different length scales (e.g., a single dredge station can be represented by samples originally emplaced at the seafloor more than 1 km apart, while the relative location of samples collected by submersible is typically variable only within meters to tens of meters). Potentially, if the length scale of MORB variability on the seafloor is comparable to sampling length scales, different methods could differ in terms of the typical MORB variability recovered. In this section, we briefly compare the variability in MORB samples collected from a given location using different methods. In principle, the spatial variability in sampling methods could itself introduce artifacts into apparent global MORB variability, especially if there is a large discrepancy in the variability observed in sample suites collected from the same location by different methods. To investigate this possibility, we have identified the 36 30-km ocean ridge intervals sampled multiple times using a given sampling method, for at least two sampling methods. The bottom panels of Figure 3-7 illustrate the lack of major systematics. However it is noteworthy that the majority of outlier compositions are sampled through dredges. This could reflect the larger sampling length scale of dredges.

3.3.3 Potential Impact of Sampling Bias in MORB Data

Artifacts in the global MORB data introduced through biased sampling are likely to include spurious clusters of specific MORB compositions visible in scatter plots, and potentially such

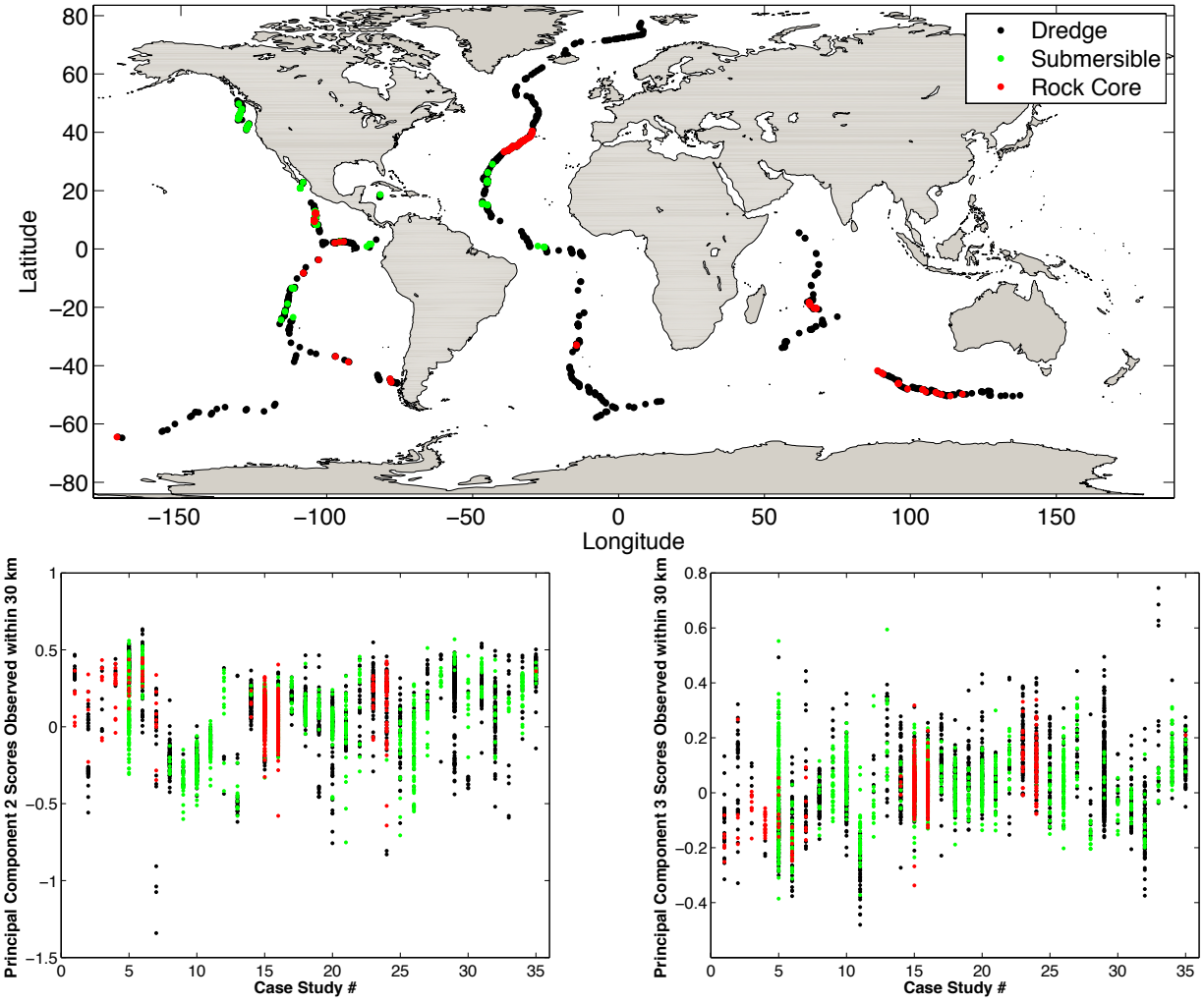

Figure 3-7: Illustration of the relative variability sampled through different methods. Panels at bottom illustrate the variability in PC2 (left) and PC3 (right) observed at each of 36 30-km spatial intervals represented by numerous MORB samples collected by multiple sampling methods. Note the tendency for extreme outliers to be sampled through dredges.

clustering could lead to skewed estimates of mean MORB composition in some cases. However, the impact of such data artifacts on inferences about ocean ridge igneous systems will depend largely on the way MORB data is analyzed. In studies aiming to demonstrate qualitative agreement between the range of observed MORB compositions and model predictions, for example, the relative abundances of specific MORB compositions are often not critical, and the impact of sampling artifacts is likely to be correspondingly low (the high symbol density in scatter plots depicting current MORB compilations can often render spurious secondary peaks in the data cloud completely invisible). However, in the application of more quantitative statistical analysis techniques (e.g., Bayesian inference) spurious clusters within MORB data can directly impact conclusions about the forward model used to interpret the data. To pave the way for future work involving the latter type of analysis, as well as to obtain a clearer qualitative picture of the character of MORB variability, we have developed a method eliminating data artifacts caused by biased sampling, the subject of a subsequent section.

3.4 Correcting for Sampling Heterogeneity through Random Subsampling

Statistical artifacts introduced by non-independent sampling may be eliminated through the general approach of identifying dependent samples, binning these into groups, and summarizing each group through a single, representative composition. The representative composition for a given group include can be determined, e.g., through averaging or subsampling. In this study, we generate a series of unbiased data sets through multiple iterations of random subsampling, and combine the analyses of each iteration to form a best estimate of unbiased MORB variability. While this is a more computationally complex approach than simply averaging over all dependent samples, our method has the advantage that it allows the uncertainty in the resulting variability estimates to be easily assessed. Our procedure is as follows: (1) for each of a number of iterations, subsets of all available data are randomly extracted such that each data point is independent of all others, e.g., each 30-km window is represented by an identical number of independent sampling stations (2) joint probability densities describing PC2-PC3 variability are estimated at each subsampling iteration using a kernel-smoothed density estimation approach (*Scott*, 1992, c.f. Appendix B for details). (3) probability density estimates from each iteration are pooled: the median probability density value determined for each (PC2,PC3) point on a discrete grid is extracted from the ensemble of density estimates. After normalization, these median values define a composite

probability density estimate incorporating the results from all subsampling iterations. As an example, we have evaluated the variability of fractionation-corrected MORB from the MAR, both with and without correcting for biased sampling. In our correction, we have performed subsampling in the following way. Each of the 209 30-km long on-axis MAR ridge intervals (comprising all such existing intervals sampled by 2 or more MORB analyses available from PetDB) is represented by one randomly selected MORB sample from one randomly selected station. Thus, more than three thousand available MORB samples from the MAR are represented by only 209 analyses at any given iteration (there are 100 iterations total). By choosing a subsampling scheme, we have corrected the problem of biased sampling, essentially providing additional, subjective information about the actual number of independent samples available. The comparison of results obtained with and without the correction is shown in Figure 3-8. While both probability density estimates are qualitatively similar, the uncorrected probability density estimate displays significantly more structure, including the presence of several compact secondary peaks that are not visible in the corrected density estimate. The reason for this difference is twofold. The subsampled data from each iteration actually contains few or no compact clusters, generally reflecting the removal of spatially correlated samples (i.e., samples from a common station). This in itself leads to smoother density estimates. More importantly, the visual impact of kernel smoothed probability density estimates is greatly affected by the kernel bandwidth used. For a review of kernel smoothed probability density estimation and the bandwidth selection problem the reader is referred to Section B.2 of Appendix B. In general, data-based bandwidth selection methods return bandwidth sizes that are inversely dependent on the available sample size, consistent with the general principle that more data allows additional detail to be statistically resolved. Since subsampling obviously leads to a decrease in sample size, the kernel bandwidth resulting from applying any empirical method to a subsampled data set will always be larger than if the raw data set were used, and the resulting probability density estimate will be smoother.

The features in the uncorrected MAR variability estimate that are absent from the corrected estimate are most likely to be spurious. Either they are purely the result of biased sampling, and have been fully removed through subsampling. Alternatively, some features could reflect actual structures (compositional clusters) in spatially independent MORB samples that are (as yet) represented by too few samples to be statistically robust. A key assumption in constructing probability density estimates is that the available data are independent and identically distributed samples from some distribution of interest. However, we have shown in a previous section that the PetDB compilation of MORB data comprises many correlated samples. Applying bandwidth selection methods to the uncorrected MORB

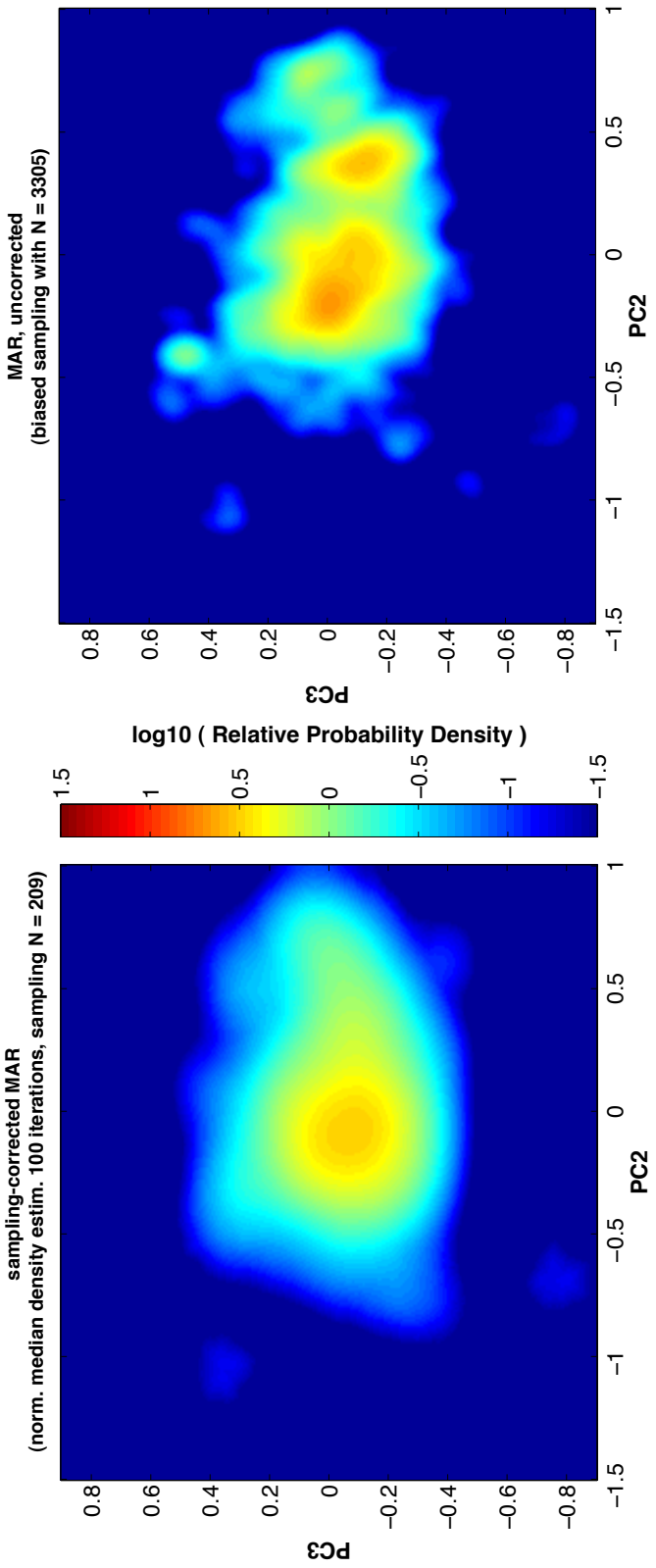

Figure 3-8: Caption given on next page.

Figure 3-8: Contrast between estimates of fractionation-corrected MORB major element variability throughout the MAR, obtained after taking into account the effect of biased sampling (left panel), versus using uncorrected data as compiled in PetDB (right panel). Each panel represents MORB variability using a kernel-smoothed probability density diagram, computed from the second and third principal component scores of individual MORB samples and a smoothing bandwidth determined by a sample size dependent formula. The sampling-corrected variability estimate is constructed by computing the median kernel-smoothed probability density estimate value of each PC2-PC3 pixel obtained from each of 100 iterations of the random sampling scheme described above, and subsequently re-normalizing (to ensure that $\sum_i p(PC2_i, PC3_i) = 1$). Additional details of the methods used are provided in Appendix B. The uncorrected estimate of MAR variability incorporates all available MORB analyses, resulting in a much larger apparent sample size, and correspondingly smaller kernel smoothing bandwiths.

data set thus results in a kernel bandwidth that is inappropriately small, in turn leading to a probability density estimate that risks rendering spurious secondary features visible.

We close the discussion of our sampling correction method with an analysis of the uncertainty in our corrected MAR estimate. Comparison of the probability density values computed at specific (PC2,PC3) points at different iterations reveals significant variability. The central panel of Figure 3-9 presents a summary of this variability, in which the standard deviation of the probability density estimate computed at all iterations is plotted is throughout PC2-PC3 space, expressed as a fraction of the maximum median probability density (shown in panel a) of the Figure). Expressed in relative percent (c.f., panel c) of the Figure), we estimate the uncertainty in the density estimate throughout the vast majority of the range of PC2-PC3 space covered by MAR data to be at between 10 and 20 percent (relative percent deviation = standard deviation of individual iteration results / median x 100). The high degrees of relative uncertainty at the boundaries of PC2-PC3 space simply reflect division by a very small number. It is important to note that the uncertainty we have estimated is dependent on the subsampling scheme and on the extent of spatial independence of available data. Alternative subsampling schemes will be associated with different uncertainties, depending on the number and variability of MORB analyses available per sampling station. For example, if 10 available MORB analyses are sourced from ten dredges, the procedure we have described will always return the same estimate of variability, while if all 10 MORB derive from a single dredge, there will be maximum variability in the estimates from different sampling iterations. Alternatively, if – other things being equal – MORB variability within individual sampling stations is large, this will be reflected by greater uncertainty in the probability density estimate from our method than would occur in a scenario with smaller intra-station variability.

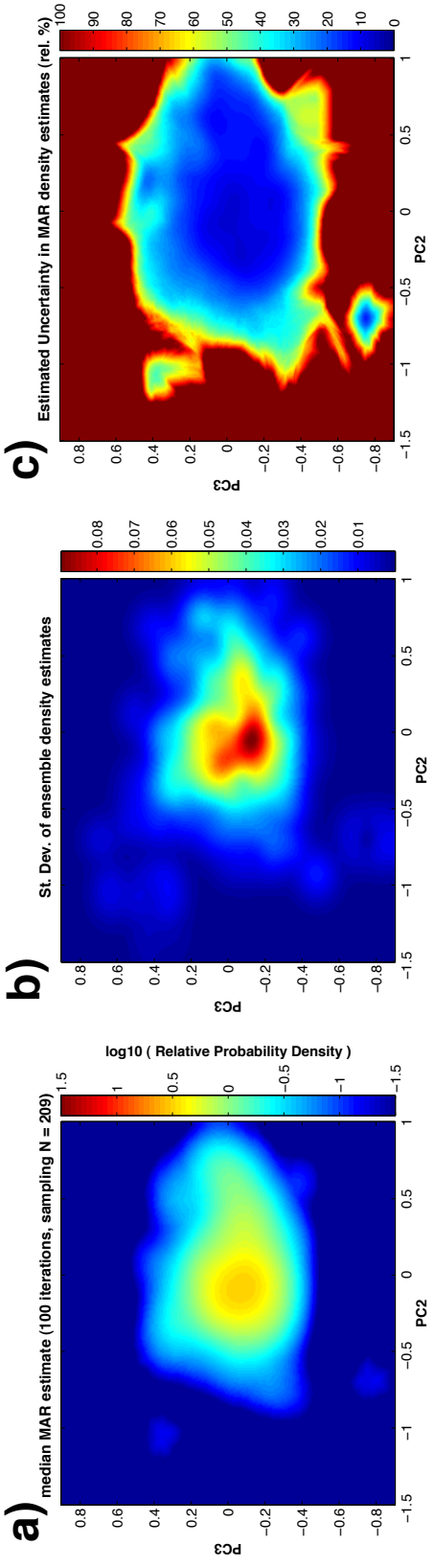

Figure 3-9: Caption given on next page.

Figure 3-9: Example illustrating the evaluation of uncertainty in sampling-corrected MORB variability estimates. a) our best estimate of the statistical distribution of fractionation-corrected MORB major element compositions erupted at the MAR, expressed in terms of principal component scores. This panel is equivalent to the left panel of the previous figure, with colors representing relative frequency relative to the maximum. b) On a pixel-by-pixel basis, the variation in probability density values computed at different subsampling iterations is shown. Colors reflect the standard deviation of probability density values computed for each pixel relative to the maximum median probability density, with red corresponding to pixels with greater variability in probability density. c) Uncertainty of the probability density in a) expressed in relative percent. For the majority of composition-space spanned by the MAR data, variability in estimates of relative frequency (shown in panel b)) is less than 10% of the median estimates shown in panel a) .

3.4.1 On the robustness of Principal Component Scores of Subsampled Data

The principal component scores providing the basis for our description of MORB variability are not intrinsic properties of each MORB sample, but are dependent on the relationship of each sample relative to the full data set. Thus the principal component analysis we have presented could be sensitive to subjective choices in data processing, e.g., variations in the choice of filtration schemes or in the implementation of subsampling schemes for eliminating biased sampling effects. We here assess the robustness of PCA in MORB data with respect to artifacts from biased sampling. For each of 100 iterations, we have randomly subsampled one MORB analysis from each globally available on-axis sampling station, and performed the principal component analysis described in a previous section on the resulting dataset (N = 3389). Figure 3-10 illustrates the results of this exercise. The first four principal component vectors display little variability in their orientation, both compared iteration-to-iteration, and in comparison to the result shown in Figure 3-2. There is one exception in that more SiO_2 variability is attributed to the second principal component (in the previous PCA, this SiO_2 variability was attributed to minor principal components). The importance of the first principal component (in terms of variability along this component relative to total variability) generally decreases by $\sim$ 10%. Spatially biased sampling is the most likely explanation for this effect, as samples from within a single station display the greatest fraction of their variability along the PC1 axis. Because of the correlation of PC1 variability with the predicted effects of crystal fractionation, biased sampling may therefore be responsible for a slight exaggeration of the importance of fractionation-related MORB variability relative to fractionation-corrected variability (the trade-off involving $\sim$ 5% of total variability). Corresponding to the modest decrease in the importance of the first principal component, the second and third principal components experience $\sim$10-20% increases in importance, while

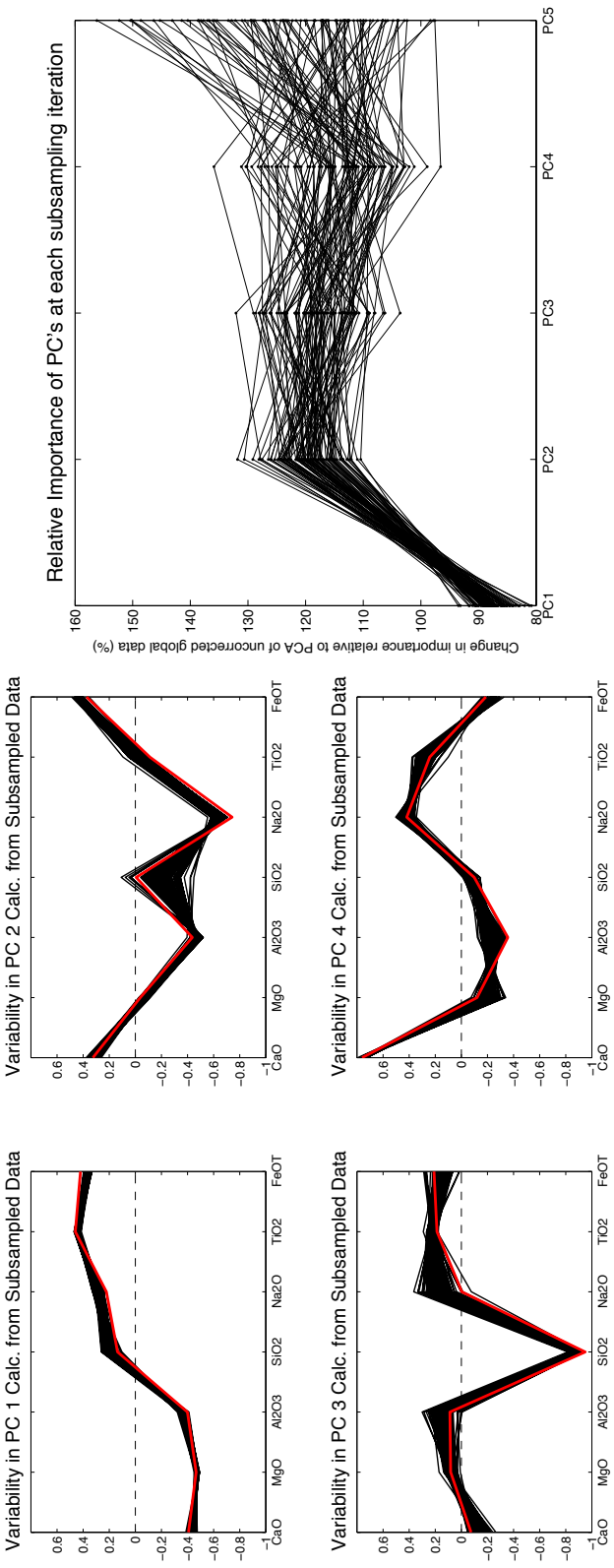

Figure 3-10: Caption given on next page.

Figure 3-10: (left) Comparison of EOF vectors defining each principal component axis, as computed from randomly subsampled MORB data (shown in black). For reference, the EOFs derived from all PetDB data – used throughout this study – are shown in red. The panels summarize 100 iterations of subsampling in which one MORB sample was extracted from all globally available sampling stations). The low variability in EOF's suggests that the results of principal component analysis are robust with respect to potential biased sampling. (right) Illustration of the change in relative importance (in terms of variability along this component relative to total variability) of each principal component once sampling bias has been taken into account through random subsampling, compared to the relative importance of each principal component computed from the full PetDB compilation, as described in a previous section (a value of 100% implies no change).

additional principal components experience up to 50% increases in importance. Despite these minor differences, we conclude that the PCA we have provided in a previous section comprises a useful, robust method for compressing seven-dimensional MORB major element data into a more easily manageable, three-dimensional data space.

3.5 Applications

Previous studies have documented differences in the variability of MORB samples collected from different locations along the global ocean ridge system (*Klein and Langmuir*, 1987; *Langmuir et al.*, 1992). In the remainder of this manuscript, we apply the methods developed above to examine the properties of MORB variability as expressed in the global PetDB compilation, and to compare these to previous work.

3.5.1 Global Systematics of MORB Variability

Figures 3-11 and 3-12 plot the global distribution of principal component scores. The global systematics first recognized by *Klein and Langmuir* (1987) and verified in many subsequent studies clearly expressed: the shallow Reykjanes Ridge defines an interval of ridge axis where high PC2, or high Fe8.0, low Na8.0 end-member compositions are concentrated, while the deep Mid-Cayman Rise and the Southwest Indian Ridge (SWIR) are rich in conspicuously low PC2, or low Fe8.0, high Na8.0 samples. Other features are visible as well, such as a general increase in PC2 score in samples from near the Azores, first noted by *Schilling et al.* (1983), and the rapid transition from lower to average PC2 score at the Australian-Antarctic Discordance (AAD). In the case of the third principal component (PC3), variability seems less location-dependent, although there are exceptions. For example, an anomalously high concentration of PC3 values appears to be localized at Iceland and Galapagos, and the AAD is also prominently visible as an abrupt transition from lower to higher PC3 values. For the

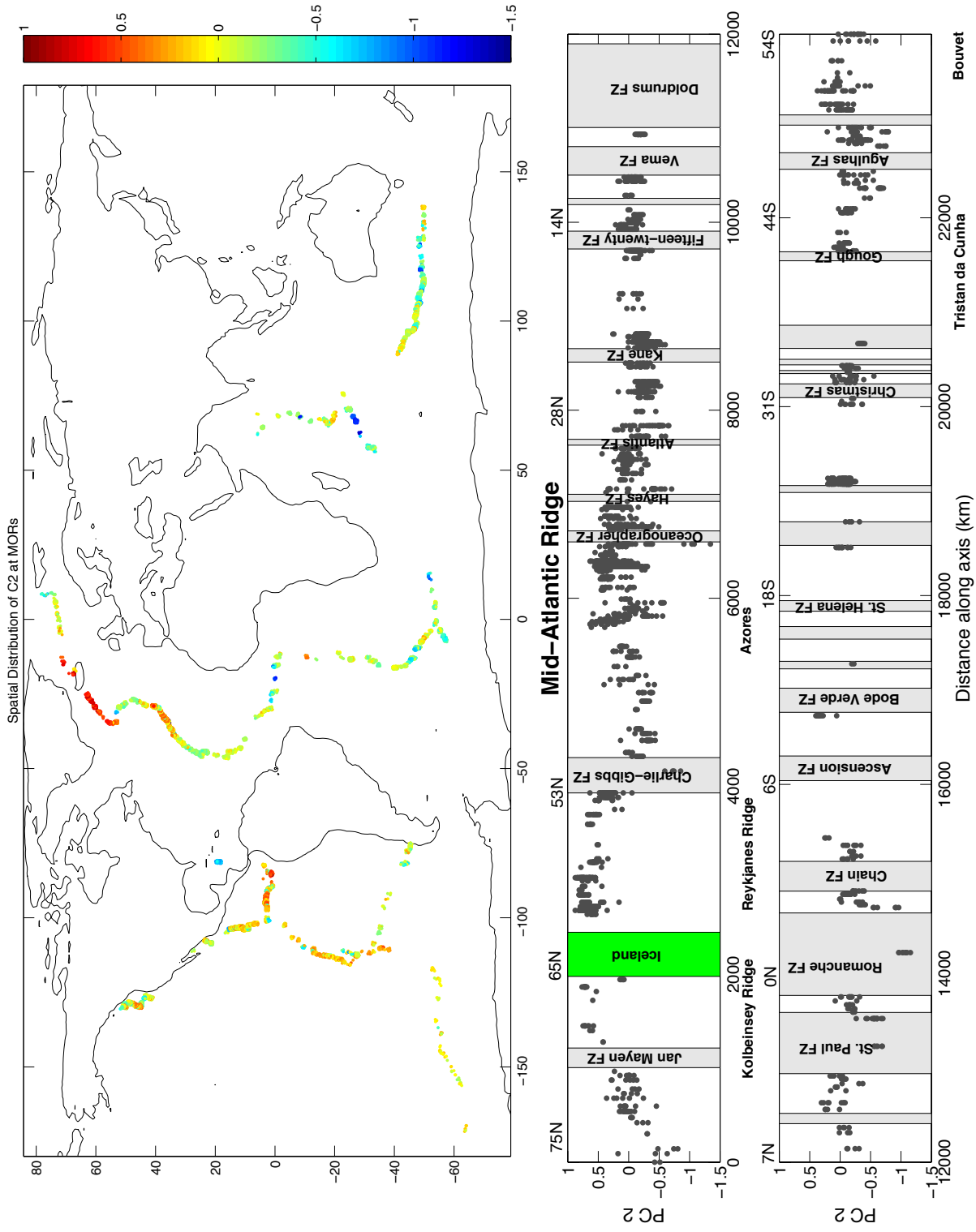

Figure 3-11: Spatial distribution of global MORB PC2 scores. Each symbol represents a MORB sample, colored by score, with the location of each sample randomly jittered by ± one degree in latitude and longitude to aid in visualizing variability in high sample density areas. At bottom, MORB PC2 scores from the Mid-Atlantic Ridge are shown in an alternate visualization scheme, plotted as a function of distance along the trace of the ridge axis. Gray intervals indicate fracture zones.

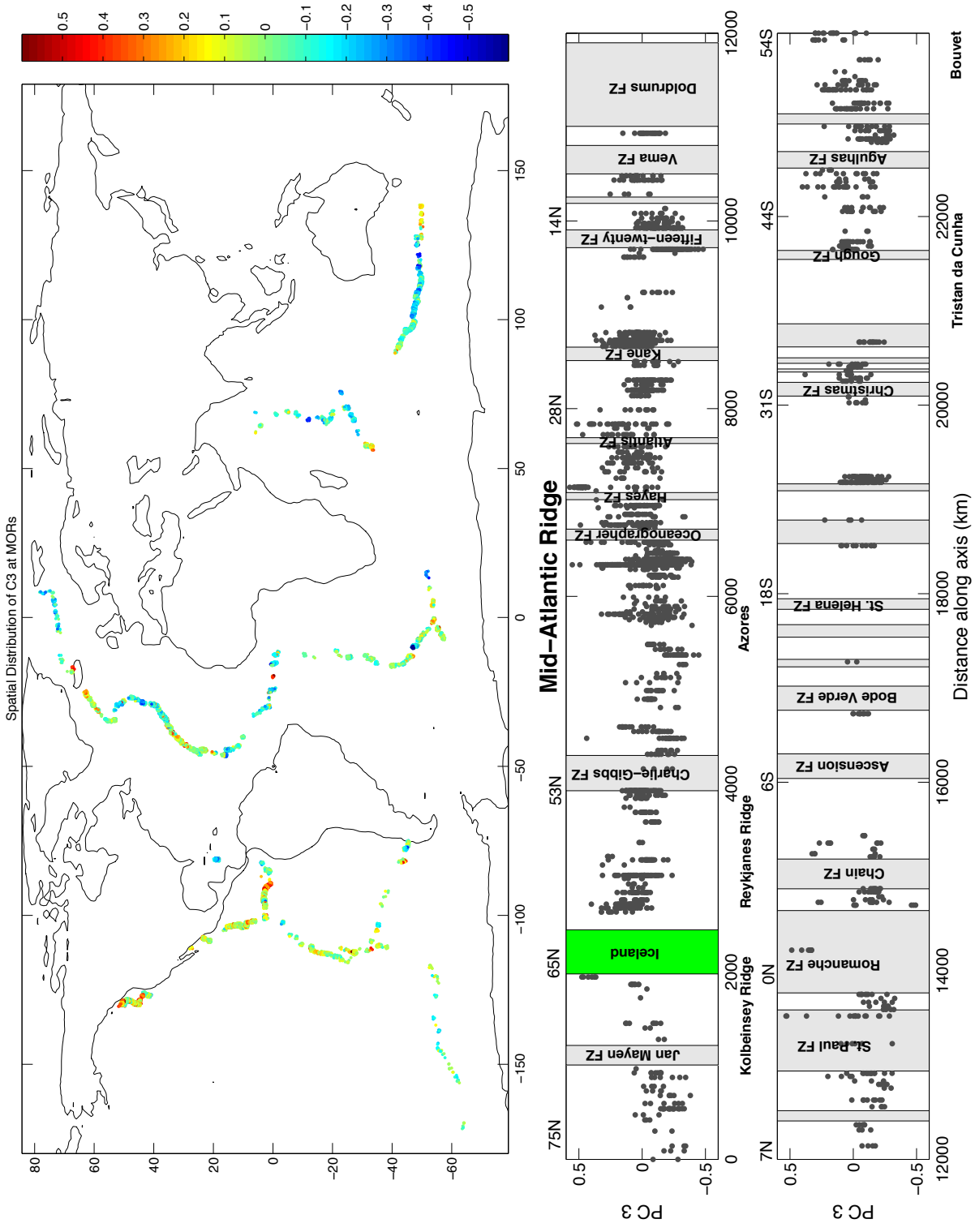

Figure 3-12: Global distribution of MORB third principal component scores. See previous figure caption for further explanation of symbols.

most part, however, PC3 scores are relatively homogeneously variable throughout all ocean ridges.

3.5.2 Differences between Ocean Ridges

In visualizations such as Figure 3-11 and Figure 3-12, it is straightforward to identify regions with highly anomalous compositional variability, and to correlate each with a known feature discussed in the MORB literature. However, the vast majority of the sampled ocean ridge system aside from such anomalies also displays MORB variability that, while less distinctive, nevertheless comprises a large fraction of total observed variability. In this section, we address the question of how different this background MORB variability is at each of three spatially separate ocean ridges after applying our correction method for removing sampling bias. We have analyzed variability at the three best-sampled ridges, the MAR, EPR and SEIR. Figure 3-13 illustrates the comparative PC2-PC3 variability of each ridge, displaying the variability at each ridge as a probability density estimate. The MAR variability estimate is the same as the one discussed in a previous section, and the same subsampling scheme described above has been used at all ridges. Apparently, each of the three best-sampled ocean ridges displays great similarity in major element variability (at the level of resolution afforded by the number of independent sampling opportunities available). Perhaps the most important negative result of this analysis is that none of these ocean ridges require the presence of multiple significant compositional modes. Interpreted through existing petrologic and geodynamic theory, the presence of such compositional modes could potentially have led to new inferences about the spatial distribution of mantle properties or melt transport processes. The MAR and EPR each display a sharp tail defined by outliers, with the outliers from the MAR primarily reflecting the Reykjanes and Kolbeinsey Ridge samples near Iceland, as well as the Azores, while the EPR outliers primarily reflect samples from the Garrett and Siqueiros Fracture Zones, as well as the Hess Deep. In general, our results agree well with the findings of previous studies. For instance, it is well established that the local trend variability is perpendicular to the global trend variability on the MAR (corresponding to larger variability in PC3) while the local trend at the EPR is parallel to the second principal component (corresponding to less PC3 variability at the EPR) (c.f., *Langmuir et al.*, 1992).

Our consideration of the largest data set available, together with our approach of considering the character of the full statistical distribution of variability (as opposed to the use of simple summary statistics), allows a more detailed assessment of regional variations in MORB compositions. By contrast, previous comparative studies of MORB variability at spatially separated ocean ridges have commonly relied on regionally averaged data, a

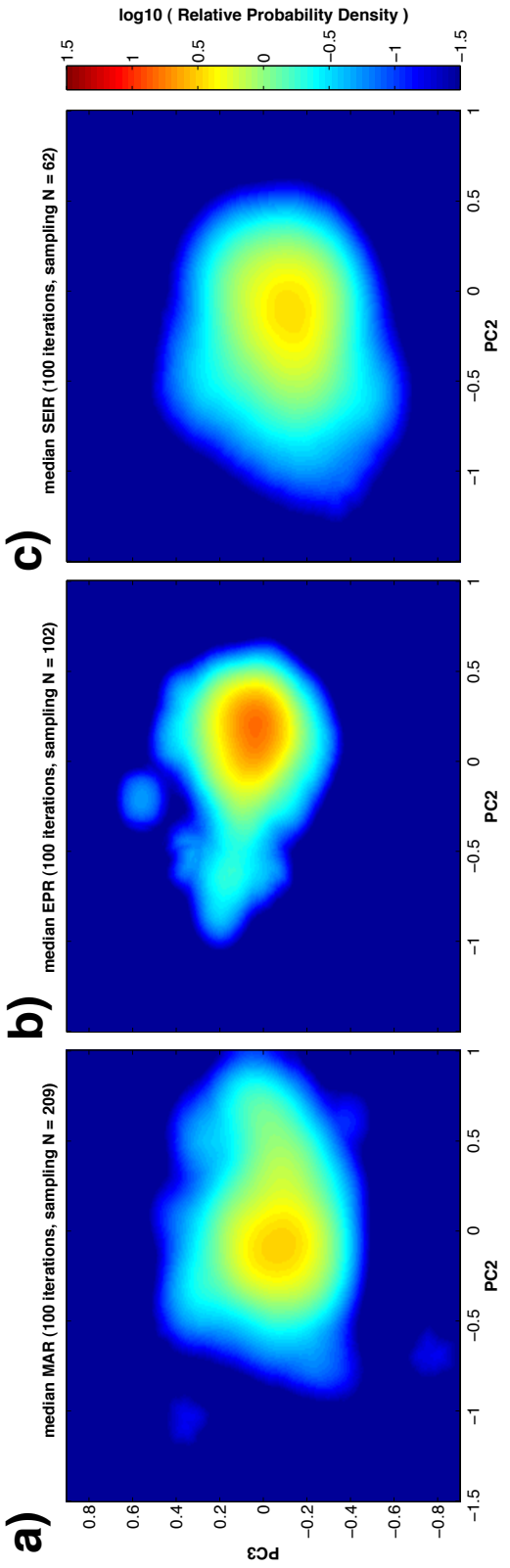

Figure 3-13: Caption given on next page.

Figure 3-13: Comparison of estimated fractionation-corrected MORB variability throughout three well-sampled ocean ridges, after sampling is taken into account through random subsampling. Panels depict variability at: a) the Mid-Atlantic Ridge b) the East Pacific Rise c) the Southeast Indian Ridge. Each panel is constructed as described in the caption of Figure 3-8.

potentially misleading practice. *Langmuir et al.* (1992), for example, states that "basalts from the Indian Ocean have systematically lower $Fe_{8.0}$ and higher $Na_{8.0}$ than basalts from the Atlantic". Comparison of panels a) and c) in Figure 3-13 corroborates this assessment: on average, the SEIR displays a slightly greater frequency of PC2 scores (corresponding to lower FeO and higher Na_2O at a given MgO, c.f. Figure 3-2) than the MAR. However, this is completely a consequence of the large low-PC2 tail in the distribution of SEIR compositions, corresponding to a heightened frequency of low PC2 outliers observed at the SEIR versus at the MAR. In fact, there is a very large overlap between the compositional ranges at which the bulk of samples plot at both the MAR and the SEIR. Although the assessment of *Langmuir et al.* (1992) is not incorrect, it also fails to accurately describe the first order relationship between MORB variability patterns expressed at these two ridges.

3.5.3 Do MORB from FAMOUS display anomalous major element compositions?

Our methods can also be applied to evaluate differences in variability occurring at different on-axis intervals within a single ocean ridge. The FAMOUS area, for example, has been identified as a site with anomalous MORB variability in previous work (e.g., *Langmuir et al.*, 1992, c.f., Figure 25). It is also the most well-sampled site along the MAR, and so perceived variability at FAMOUS could potentially be susceptible to artifacts from sampling bias. To re-evaluate the extent to which MORB variability at the FAMOUS site is truly anomalous, we contrast the sampling bias-corrected variability at FAMOUS with the variability observed at a typical MAR interval between the Kane Fracture Zone and the Atlantis Fracture Zone. It is clear from Figure 3-14 that the FAMOUS site is indeed anomalous, displaying two significant modes. The primary mode at FAMOUS has a higher PC2 score and slightly lower PC3 score than is typical at the MAR, while the secondary FAMOUS peak is closer to, but still slightly offset from the typical MAR peak. For reference, we have also plotted the variability at 9N EPR between the Siqueiros and Clipperton Fracture Zones. The variability at 9N is more compact, but consistent with the full EPR estimate shown in Figure 3-13.

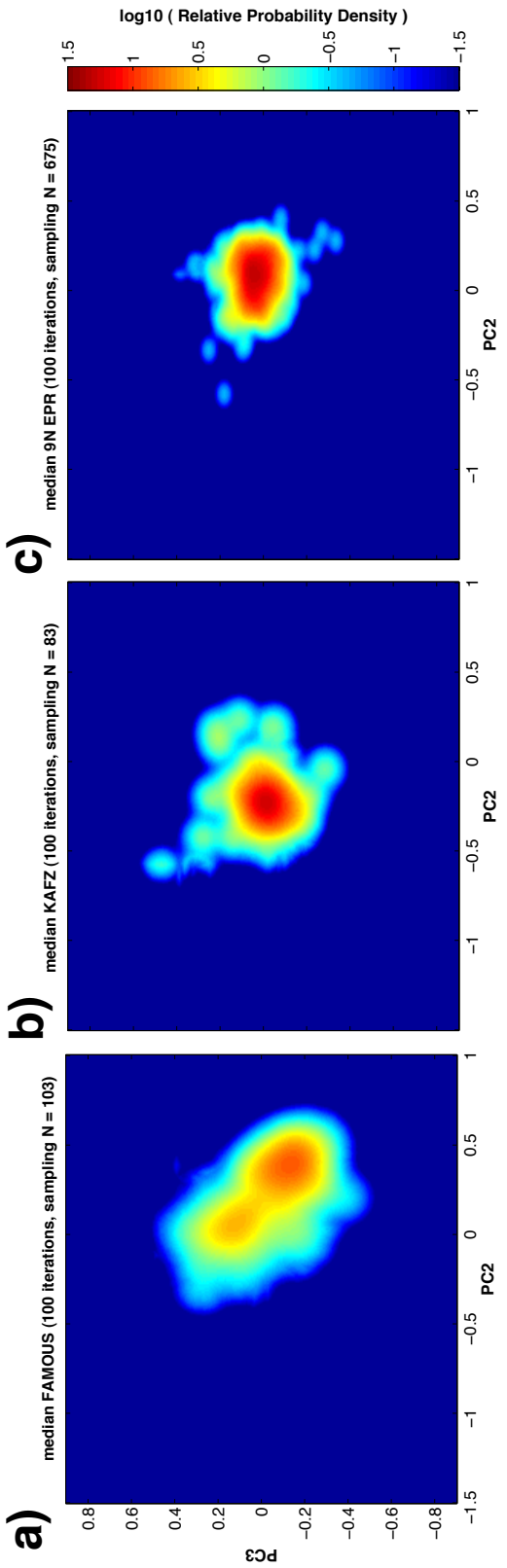

Figure 3-14: Caption given on next page.

Figure 3-14: Comparison of estimated fractionation-corrected MORB variability at three well-sampled ocean ridge segments, after sampling is taken into account through random subsampling. Panels depict variability at: a) the FAMOUS area, Mid-Atlantic Ridge b) the interval between the Atlantis and Kane fracture zones, Mid-Atlantic Ridge c) 9N East Pacific Rise, between the Clipperton and Siqueiros fracture zones. Each panel is constructed as described in the caption of Figure 3-8. Note the clear distinctions in the variability patterns between each locality.

3.5.4 Is there a rule of thumb for estimating the number of samples needed to characterize 30-km scale ocean ridge variability?

Although the vast majority of PetDB MORB samples may be classified into one of 550 30-km scale on-axis intervals (additional data is available for off-axis samples and back-arcs, but will not be considered here), 82% of these intervals are represented by five or fewer sampling stations. Given the logistical effort involved in collecting additional MORB samples, it is of interest to consider the question "How much sampling is required to get a good estimate of MORB variability present within a given 30-km ocean ridge axis interval?". In this section, we address this question quantitatively for the first time. To introduce the main concepts relevant to this question, we will begin by discussing a simple case study: sampling from a normal distribution with zero mean and unit variance. It is a basic statistical principle that estimates of variability (such as standard deviation) taken from samples of this distribution are most likely to accurately reflect the underlying variability when the sample size is as large as possible. Yet the convergence – or agreement between – estimates of such statistics changes with sample size in a manner that is neither monotone, nor bounded from above or below, as illustrated in Figure 3-15. The probability of obtaining a more accurate estimate, however, increases monotonically (as illustrated graphically by the narrowing bands comprising the range of variability estimates produced by a large number of random sampling simulations in Figure 3-15). These results are also applicable generally, although compared to Figure 3-15, the specific sample size needed to achieve a desired degree of confidence in an estimate (corresponding to a given narrowness of the) will be variable, depending on the estimator of variability being used (e.g., standard deviation versus inter-quartile range, etc.) as well as on the character of the statistical distribution being sampled (e.g., a gaussian distribution can have different convergence compared to one with multiple peaks or large distribution tails). Thus, to address the question of sample size in the context of MORB major elements, our approach is to identify the best-sampled 30-km intervals worldwide and to empirically examine the robustness of standard deviation estimates at these locations over a range of sample sizes. We have conducted the following experiment at each of the eight best-sampled

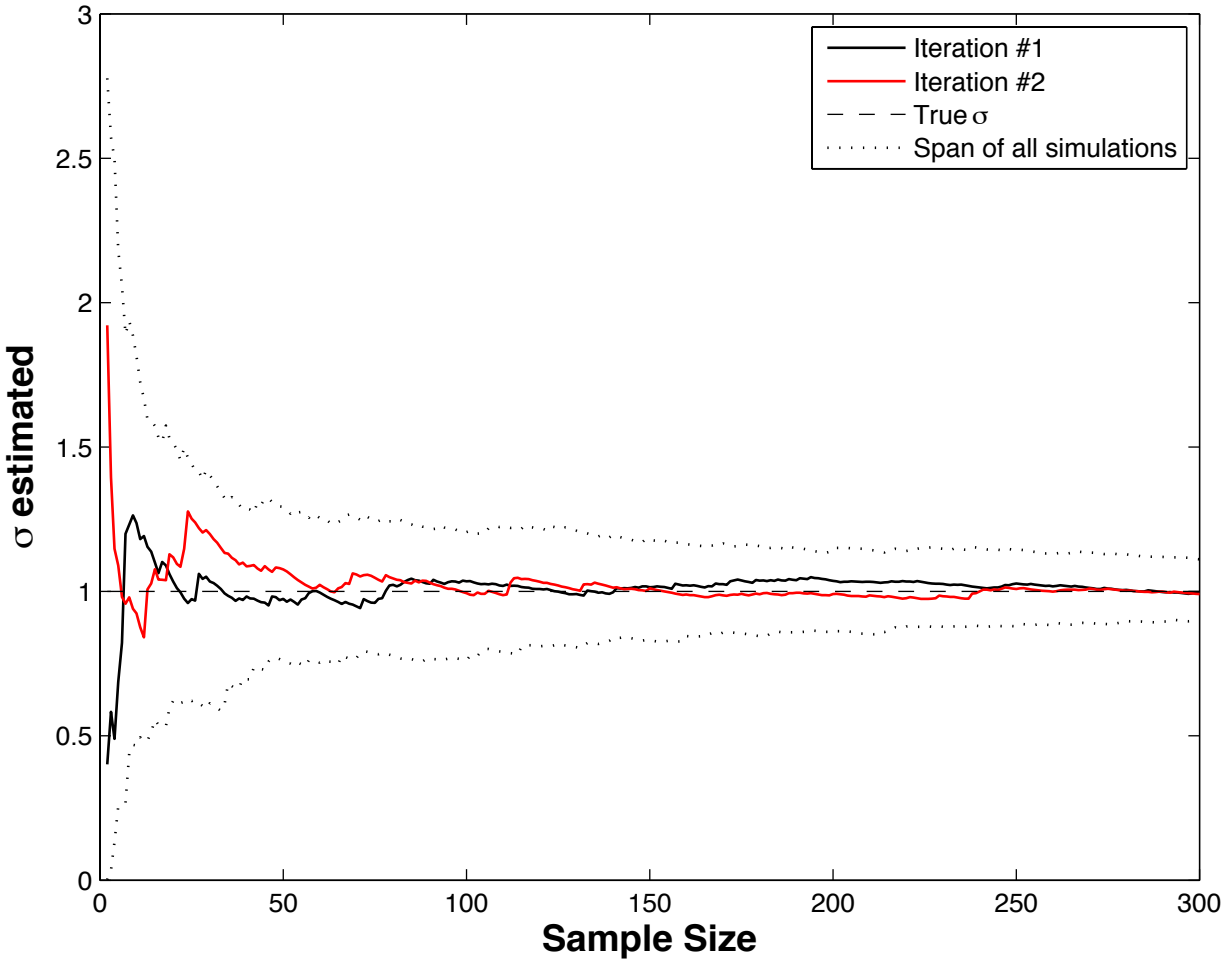

Figure 3-15: Illustration of the convergence of standard deviation (σ)estimates as a function of sample size. The solid black and red curves illustrate two independent iterations of a simulation in which N samples are drawn sequentially from a normal distribution with zero mean and unit standard deviation. The estimated standard deviation is calculated after each successive sample is drawn, incorporating all previously available data, plus the new sample. Although revisions to the estimated standard deviation due to each additional data point can both increase and decrease the error of the estimate relative to the true standard deviation, there is overall convergence of the estimate. This is illustrated by the decrease in the 'Span of all simulations', summarizing the minimum and maximum value of the standard deviation estimated over 200 iterations of this experiment at a given sample size. The top row comprises locations on the MAR, while the other locations are all along the northern EPR.

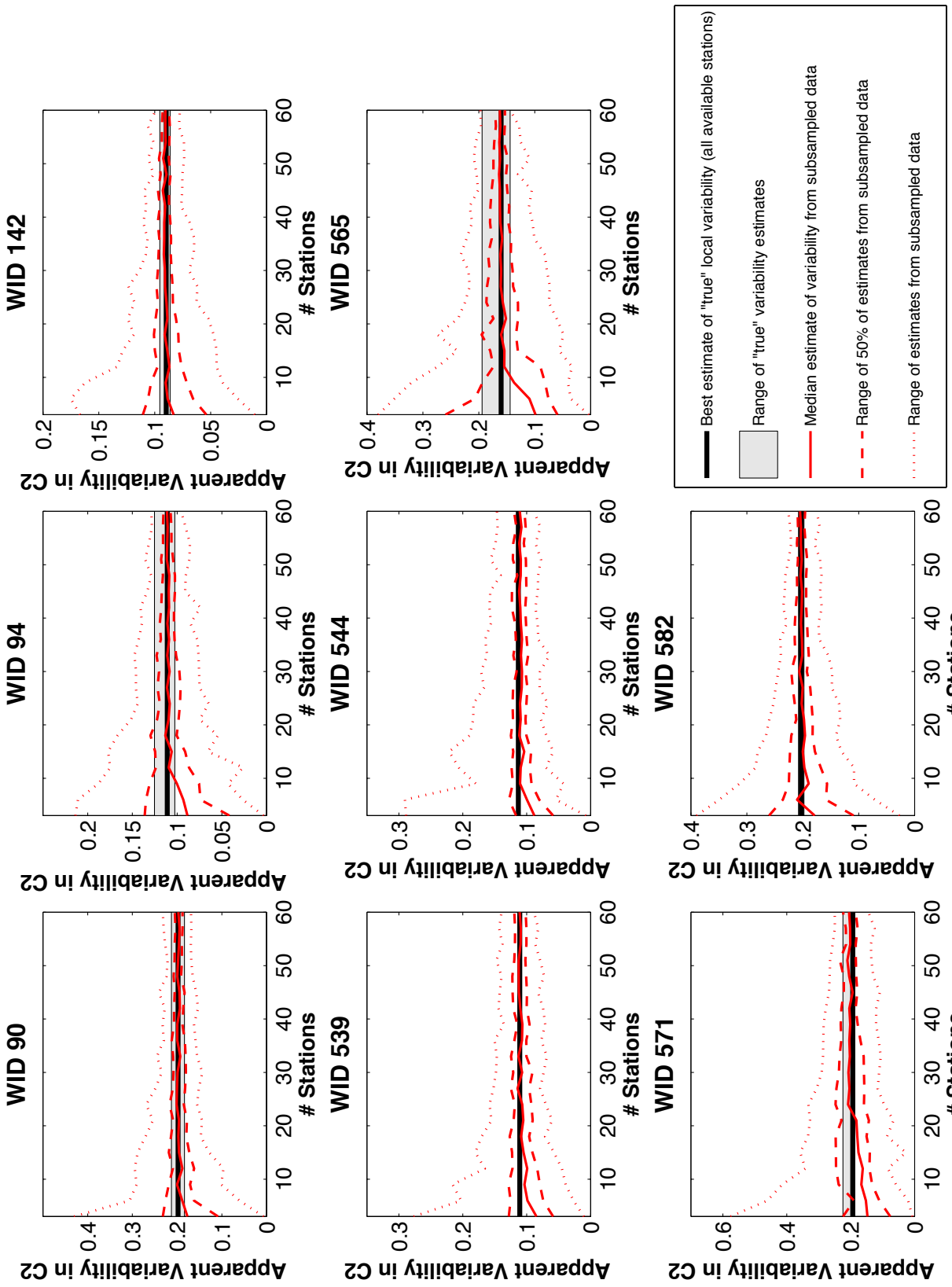

Figure 3-16: Caption given on next page.

Figure 3-16: The well-sampledness of a given ridge axis segment depends on the number of independent sample stations available. Convergence of PC2 standard deviation estimated from randomly subsampled data sets of a given sample size (number of independent sampling stations) is shown relative to the best estimate from all available data for each of the best sampled 30-km MOR axis segments. Solid black horizontal line represents the median standard deviation estimate computed from 100 random sampling iterations in which one MORB glass was extracted from all available sampling stations. The gray patch indicates the range of all estimates computed when all available sampling stations are represented. Red lines indicate standard deviation estimates from subsampled data sets in which fewer stations are used to calculate the estimate. 50% of all random subsampling simulations yield estimates plotting within the bold, dashed red lines, while all simulations plot within the light red lines (100 simulations total).

20-km ridge intervals (each represented between 60 and 353 sampling stations): randomly subsample the data from a subset of all available stations, and evaluate the variability within subsampled data in comparison to the total variability observed in all available data. The results of this experiment are plotted in Figures 3-16 and 3-17. Although the spatial coverage of these case studies is limited (five represent the northern EPR, while three represent the northern MAR), a qualitative argument can be made from them that at least 10 sample stations are required to achieve a reasonable probability that sampled variability provides a good approximation to the true underlying variability, while at least 20 to 30 stations seem necessary for variability on the 30 km length scale to be be characterized with a high degree of confidence. This corresponds to a minimum density of $\sim$ one sampling station per km along axis. According to this rule of thumb, only between $\sim$ 20-30 distinct 30 km ridge intervals exist worldwide that have been well-sampled, in turn reflecting approximately 1% of the global ridge system. By contrast, if it is assumed that at least 50 independent sampling stations are required, only eight well-sampled stations exist worldwide (corresponding to $\sim$ 0.4% of the global ridge system). Clearly, additional data collection is desirable. Yet it also deserves emphasis that increases in sample size added to any particular existing along-axis MORB data set will not guarantee a higher fidelity estimate of local variability, and can actually lead to a less accurate estimate, particularly if the increase in sample size is small.

3.5.5 On the spreading rate dependence of MORB major element variability

The velocity of plate divergence is among the primary geodynamic variables governing ocean ridge magmatism (e.g., *Sleep*, 1975; *Langmuir et al.*, 1992; *Shen and Forsyth*, 1995; *Niu and Hekinian*, 1997b; *Rubin and Sinton*, 2007). The global ocean ridge system comprises ridge segments spanning more than an order of magnitude of spreading rates. In this section, we

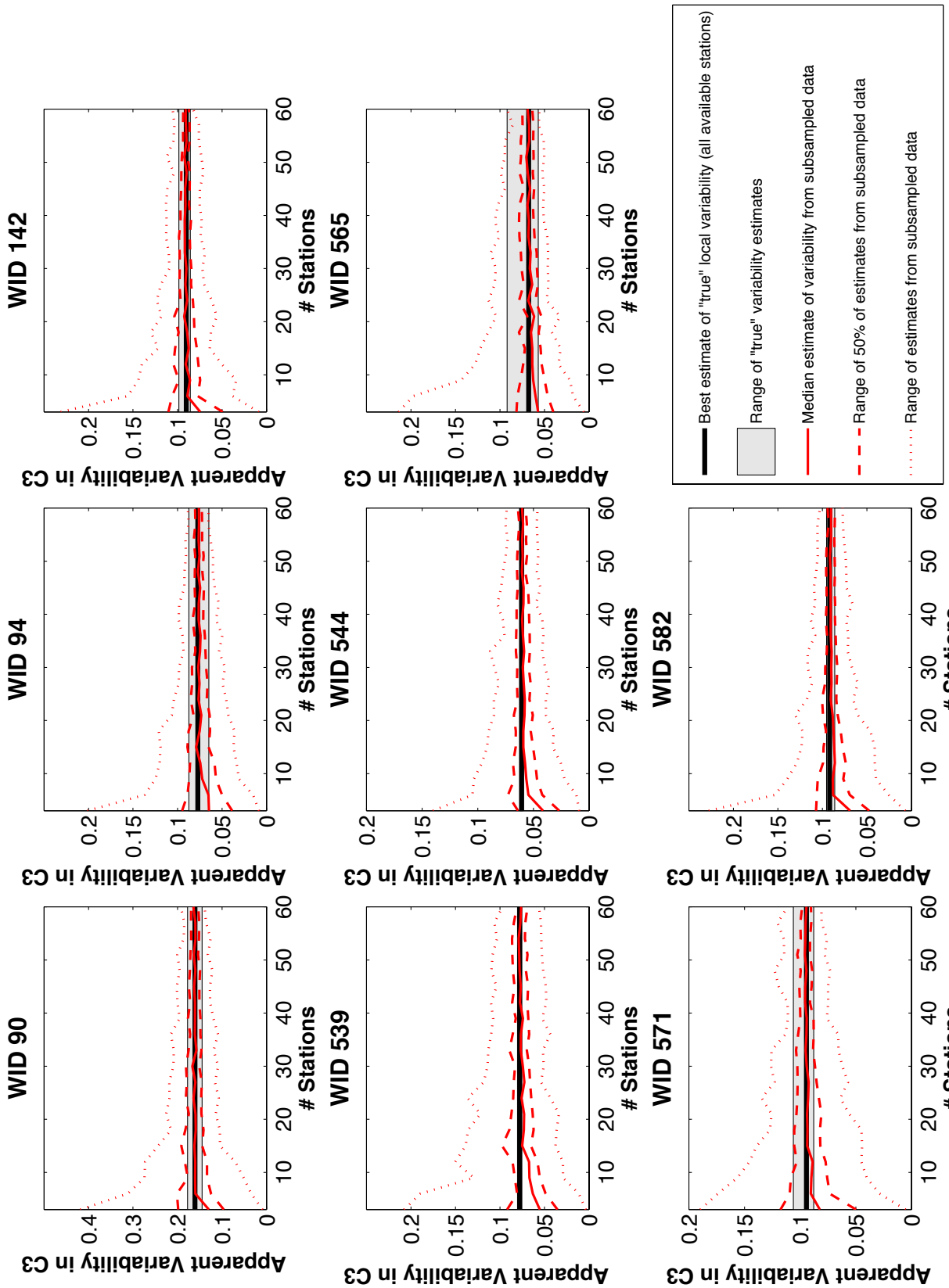

Figure 3-17: Caption given on next page.

Figure 3-17: Convergence of PC3 standard deviation estimated in randomly subsampled data relative to the best estimate from all available data is shown for each of the best sampled MOR locations. See the caption of the previous figure for additional details.

re-evaluate the systematics of major element variability with spreading rate while simultaneously accounting for heterogeneous sampling. The most obvious issue in using global data

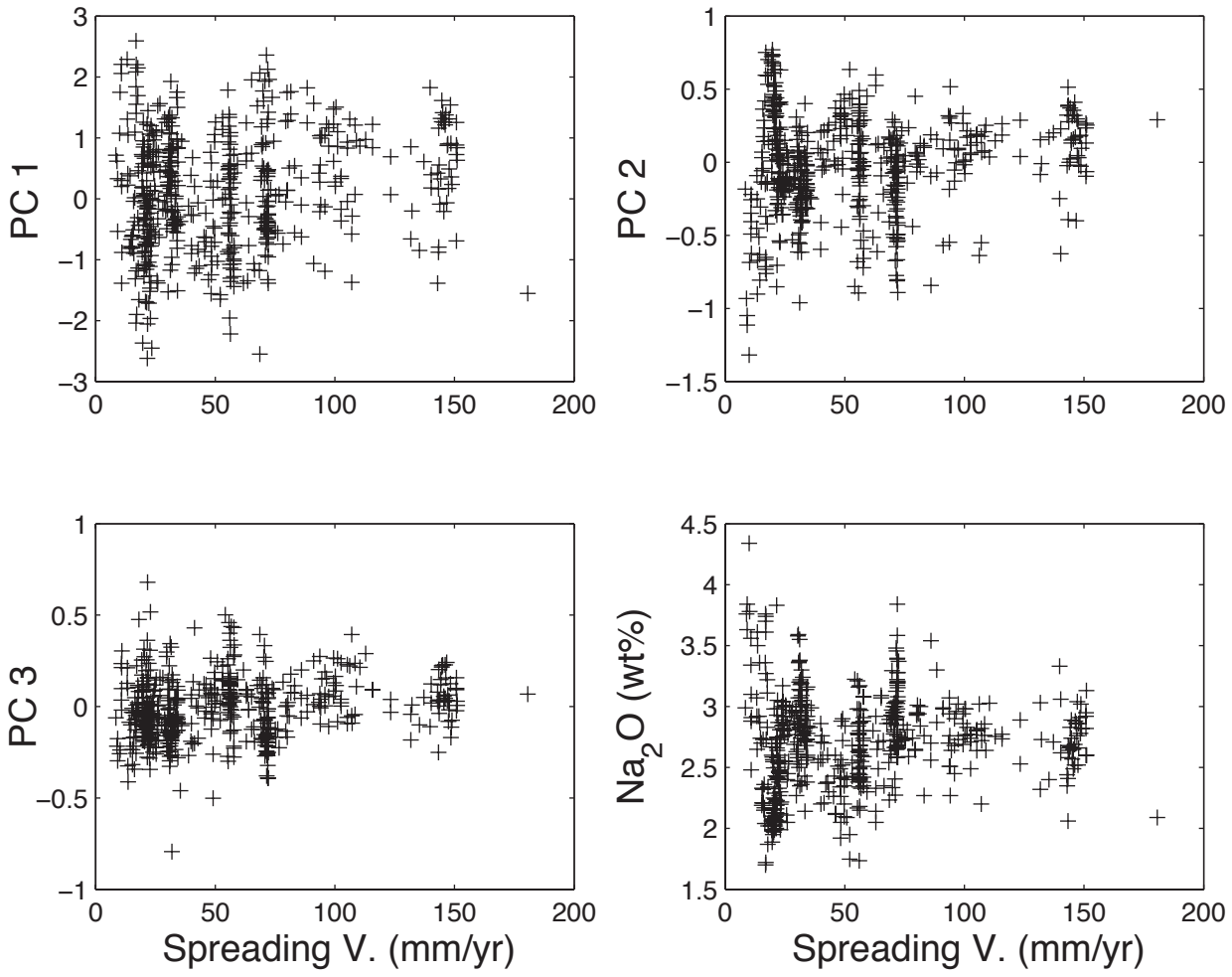

Figure 3-18: Global MORB variability plotted as a function of spreading velocity. This series of plots depicts the $\geq$ 30 km scale variability present in the PetDB compilation. Small spatial scale variability has been removed: each symbol represents a single MORB glass analysis randomly selected from all available data within a 30-km spatial bin. More than 3000 separate 30-km spatial bins are represented in this way, comprising all available 30-km on-axis bins in PetDB containing $\geq$ 2 MORB samples with major element data available. Note that there is a large proportion of sampled ridge axis representing slow spreading rates, while data from faster spreading rates comes from relatively few intervals of ridge axis.

compilations to examine spreading rate dependent variability, illustrated in Figure 3-18, lies in the fact that spreading rates throughout the global ocean ridge system are not distributed in a regular fashion, and are correspondingly not sampled evenly. Most of the global ocean ridge system is characterized by slow spreading rates, and this disproportionate representation can lead to ambiguity in the interpretation of plots such as Figure 3-18 (similar plots depicting spatially binned variability as a function of spreading rate are increasingly common in the literature (e.g., *Niu and Hekinian*, 1997b; *Rubin and Sinton*, 2007)). For example, the apparent decrease in variability in most major element variables with increasing spreading rate could be attributed to spreading rate dependence in the operation of igneous systems. Alternatively, this relationship between variability and spreading rate could be interpreted as an artifact of sampling: the high variability observed at slow spreading rates might be expected because of abundant sampling over a considerable spatial interval, while the opposite might apply at fast spreading rates (fewer outlier observations and correspondingly lower variability might be expected when there are fewer and more spatially confined sampling opportunities). While it remains difficult to conclusively resolve this question of $\gg$ *30 km scale* systematics, it is possible to at least constrain the $\leq$ *30 km scale* systematics in more detail. In Figures 3-19 and 3-20 we have re-plotted the PetDB compilation, essentially weighting each symbol in Figure 3-18 by the number of independent samples available in each spatial bin. In this visualization scheme, the locations with the largest number of independent samples – those most likely to provide a good approximation to true local variability – dominate the visual impression of the Figure. We have discussed in a previous section how variability estimates drawing on small sample size data sets are less likely to represent the true variability, and can generate spurious apparent variability that can both overrepresent and underrepresent that of MORB, c.f., Figure 3-15. Indeed, smaller sample size based variability estimates plot both above and below the well sampled estimates at all spreading rates. We will therefore consider only the larger points plotted in Figures 3-19 and 3-20 in the following discussion. Several previously known results are recovered from our plots. (1) On average, faster spreading ridges have more fractionated compositions (higher PC1 scores) than slower spreading ridges. (2) With respect to the global trend of *Klein and Langmuir* (1987), reflected in PC2, the end-member compositions (Reykjanes versus Cayman Rise) are observed only at slow spreading ridges, while fast spreading ridges plot at a moderate position along this trend (corresponding to intermediate PC2 scores). (3) The Indian ocean basalts are compositionally distinctive compared to Atlantic and Pacific MORB (plotting at $\sim$ 60-70 mm/yr, they display lower PC2 and PC3 scores than other basalts). The relationship between spreading rate and sampling-corrected variability, however, is less straightforward. While the data are consistent with a trend towards lower 30 km

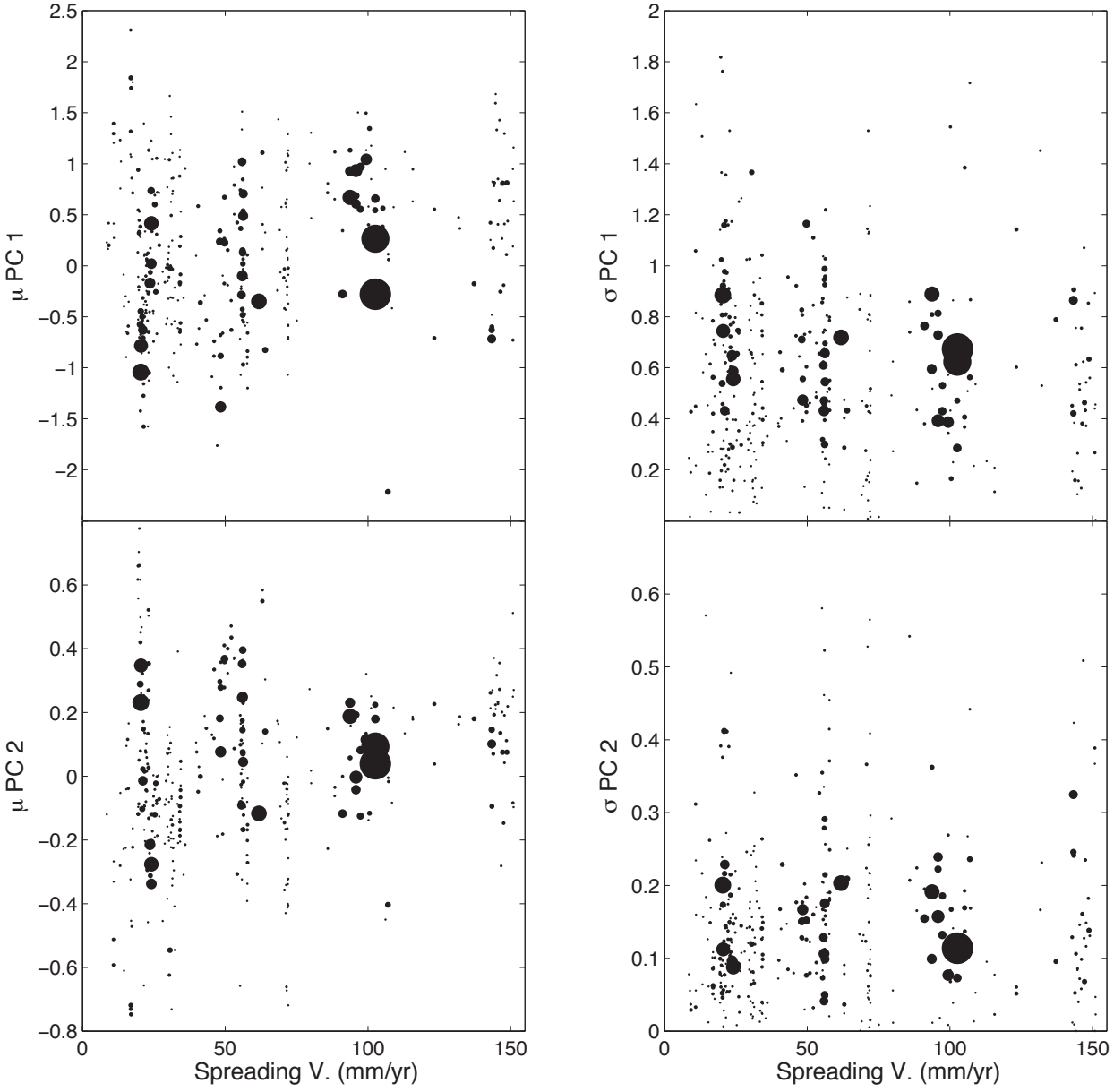

Figure 3-19: For each of the 30 km spatial bins represented in the PetDB catalogue, we have plotted – with respect to the first and second principal component scores PC1 and PC2 – the mean (μ, shown in left column) and standard deviation (σ, shown in right column) of all available sampling stations from within 30 km (one sample was randomly extracted from each station, the character of this plot is robust with respect to random subsampling). Symbol size depicting each spatial bin represents N, the number of independent samples used to compute μ and σ. The smallest symbols correspond to $N = 2$, while the largest symbols at spreading rate < 30 mm/yr correspond to $N =$ 40-80. The largest symbols (9N EPR) correspond to $N \sim 350$. See text for further discussion.

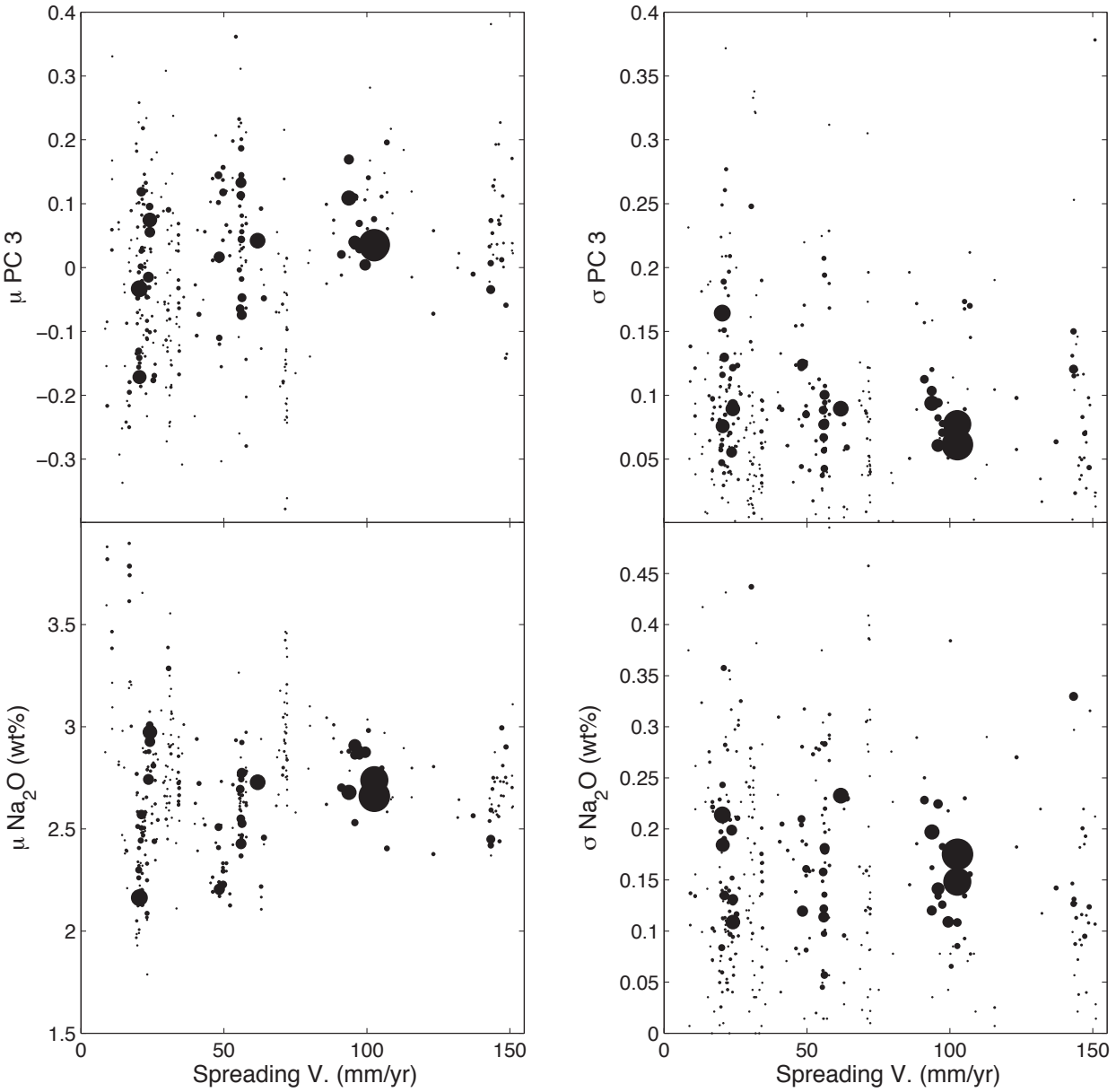

Figure 3-20: Systematics of global MORB with spreading rate (with respect to PC3 and Na_2O) plotted as in the previous Figure. See caption of previous Figure for details.

scale PC1 and PC3 variability within 30-km intervals with faster spreading rates, there is no discernible relationship between spreading rate and PC2 variability. MORB Na_2O also does not appear to display a systematic change in variability with spreading rate. Although a rigorous evaluation of the consistency of these results with geologic interpretations from the literature is beyond the scope of this study, the lack of a systematic decrease in 30 km scale variability of MORB with increasing spreading rate – at least at well sampled sites where we have maximum confidence that observed variability is a good approximation to that of underlying MORB – is inconsistent with increased extents of homogenization through magma mixing at fast spreading rates (increased spreading rates could lead to higher probability of MORB magma homogenization in shallow magma chambers, (e.g., *Rubin and Sinton*, 2007)). Instead, the apparent spreading-rate dependent variability in MORB appears to arise primarily from large, $\gg$ 30 km scale variations in mean local MORB composition, perhaps arising from factors including variable mantle source properties that could be variable over long length scales.

3.6 Conclusions

We have examined the global variability of MORB glass major element data available from PetDB. Principal component analysis indicates that this variability comprises three major independent components of variability, each corresponding to previously recognized patterns in the data. We have identified sampling bias as a non-negligible complication in data analysis, demonstrating that large heterogeneity in sample sizes available for studying MORB variability at the sampling station, 30-km, and regional, and global scales can lead to large data artifacts (c.f., Figure 3-8). This reflects compositional clustering of spatially correlated samples: e.g., MORB samples from within a given sampling station systematically display significantly less variability than is observed in all available data from within 30 km. From the perspective of understanding global or regional-scale MORB variability, increasing the number of measured samples from a single sampling station cannot substitute for an increase in the number of independent sampling stations. We have removed sampling bias through the approach of random subsampling, and find that the resulting corrected data allow the results of previous workers to be recovered, but do not suggest the presence of additional, previously unrecognized data features. Apparently, the increase in MORB data over the past decades is not sufficient to significantly increase the resolution with which major element variability can be studied on a global or regional length scale, at least in comparison to early syntheses of global MORB data. Throughout this manuscript, we have quantified geochemical variability through visualization of the full statistical distribution of variability

instead of relying on analysis of summary statistics. Kernel-smoothed probability density estimation provides a flexible, compact, practical representation of the information contained within a geochemical data. Probability density estimates are superior to simple scatter-plots of large geochemical data sets in that they more readily allow variations in relative frequency of specific compositions to be evaluated. Such variations could potentially define new, geologically interesting observations.

Chapter 4

A Preliminary Map of Discrete, Compositionally Distinctive Mantle Regions within the Southern Oman Ophiolite

4.1 Introduction

The composition of Earth's mantle is variable at length scales ranging from the hemispheric scale to the microscopic scale (*Hart et al.*, 1973; *Dupré and Allègre*, 1983; *Hart*, 1984; *Klein et al.*, 1988; *Saal et al.*, 1998; *Sobolev et al.*, 2000; *Korenaga and Kelemen*, 2000; *Donnelly et al.*, 2004). The characteristics of this variability represent primary constraints on the operation of igneous processes and convective dynamics in the mantle throughout geologic time (*Armstrong*, 1968; *Zindler and Hart*, 1986; *Hofmann*, 1997; *Helffrich and Wood*, 2001). Ocean ridge magmatism is thought to play a major role in modulating mantle variability through processes including melting, magma segregation and reactive melt transport. In principle, spatial patterns of variability in ocean ridge processed mantle could record information about factors influencing magmatic systems, e.g., the ambient rheology or the mechanisms of melt localization and focusing (*Spiegelman*, 1993; *Hirth and Kohlstedt*, 1996; *Braun et al.*, 2000; *Braun and Kelemen*, 2002; *Spiegelman and Kelemen*, 2003; *Katz et al.*, 2006; *Gregg et al.*, 2009). Yet while its impact on the geochemical and lithologic character of residual mantle is relatively well understood, the role of ocean ridge magmatism in generating or modifying spatial patterns of variability has remained difficult to constrain, particularly at intermediate length scales ($\sim$0.1-100 km). Uncertainties about melt generation, transport, and shallow mixing processes complicate inferences from lava samples collected at modern ocean ridges, while extensive alteration and logistical accessibility limit

the sampling density available from abyssal peridotite exposures. Field studies of ophiolites – sections of oceanic crust and mantle emplaced at the surface by plate tectonic processes – provide an alternative approach to observing the residues of ocean ridge magmatism that can allow spatial patterns of variability to be characterized in detail. Recent work has made significant progress in developing links between outcrop scale mantle variability patterns and specific igneous processes (e.g., *Bodinier et al.*, 1990; *Kelemen et al.*, 1995; *Braun and Kelemen*, 2002; *Bodinier and Godard*, 2003). The present study builds on this work, contributing the first intermediate-scale map depicting changes in the statistical distribution of geochemical variability within a large, continuous exposure of ophiolitic mantle peridotite. We have constructed an integrated spatial-statistical data set in which major element variability in large ($N \sim 100$) detrital spinel samples collected from a series of peridotite-sourced drainages is combined with quantitative spatial information about each sampled watershed. We resolve multiple spatially coherent mantle regions with distinctive internal patterns of spinel variability, and our data display additional systematic relationships between sampling length scale, sampling location and spinel variability. Previously established correlations between spinel compositions and other lithologic and compositional parameters in the respective host rocks allow our data to constrain the relative proportions of mantle lithologies and to estimate the distribution of dunite widths present within the mantle exposure. Our results suggest that the spatial distribution of focused melt transport beneath ocean ridges could be heterogeneous at intermediate length scales, clustered into comparatively channel rich and channel poor regions. Furthermore, igneous impregnation, variable depletion during melting, or episodes of magmatism associated with ophiolite emplacement could represent major controls on mantle variability near the ophiolite's basal detachment.

4.2 Geologic Context and Observational Approach

Most of the Oman ophiolite's igneous rocks – including a continuous layer of sheeted dikes overlain by pillow basalts – formed at a submarine spreading center. On the basis of radiometric age data, subdued crustal thickness variations, a general lack of paleo-fracture zones, a nearly continuous layer of gabbro between volcanics and mantle, and other geological observations, it is probable that the ophiolite formed at a medium- to fast-spreading ocean ridge (e.g., *Nicolas*, 1989). In contrast to the well-exposed and studied northern Oman massifs that show a polygenetic history with the importance of a "subduction component" increasing over time (e.g., *Alabaster et al.*, 1982; *Augé*, 1987; *Lippard et al.*, 1986), the few data on dikes and lavas from the southern Oman massifs (Samail, Wadi Tayin) are indistinguishable from MORB, and there is no evidence for a second, depleted lava series (*Pallister*

and Knight, 1981). Orthopyroxene is essentially absent from the lower crustal section (e.g., *Pallister and Hopson*, 1981), although orthopyroxene-bearing cumulates form small, isolated intrusions and dikes in the mantle section (e.g., *Benoit et al.*, 1996; *Kelemen et al.*, 1997b; *Amri et al.*, 1996). Spinel compositions from the southern massifs' mantle section are also consistent with those from abyssal peridotites (*Boudier and Coleman*, 1981; *Kelemen et al.*, 1995, 1997b; *Monnier et al.*, 2006; *Hanghøj et al.*, 2010). More than 95% of the igneous rocks from the southern massifs can be described by a single liquid line of descent which is similar to typical MORB differentiation, and which lies within the compositional field defined by mid-ocean ridge samples (*Pallister and Hopson*, 1981; *Pallister and Knight*, 1981; *Browning*, 1984; *Benoit et al.*, 1996; *Korenaga and Kelemen*, 1997; *Koga et al.*, 2001; *Garrido et al.*, 2001). Petrographically distinct wehrlite intrusions into the gabbro section also have similar REE patterns to gabbros at modern ocean ridges (*Koga et al.*, 2001). The southern massifs primarily record a single stage process that was free, or nearly free, of a subduction component. There is a gradient in the igneous processes forming the Oman ophiolite involving more complexity than a single stage ocean ridge process. However, provided this is kept in mind, our understanding of the southern massifs of the Oman ophiolite justifies the use of geochemical data to constrain the partially molten region beneath submarine spreading ridges.

With an area of nearly 20×50 km^2, the mantle section of the Wadi Tayin massif provides perhaps the best available, spatially extensive structural and compositional analogue to shallow mantle lithosphere that has been processed by ocean ridge magmatism. Although the mantle outcrop consists predominantly of harzburgite, other lithologies (including dunite, pyroxenite, and igneous cumulates) are present at length scales ranging from < 1 m to > 100 m at Wadi Tayin (*Boudier and Coleman*, 1981; *Nicolas*, 1989; *Godard et al.*, 2000; *Braun and Kelemen*, 2002; *Python and Ceuleneer*, 2003; *Braun*, 2004; *Gerbert-Gaillard*, 2002) and in other massifs of the Oman ophiolite (*Lippard et al.*, 1986; *Takazawa et al.*, 2003; *Tamura and Arai*, 2006). Previous inferences on the geochemical character of Wadi Tayin mantle over spatial scales greater than ~ 100 m have relied on extrapolation from observations collected from a relatively small number of well-characterized outcrops, or alternatively, on low spatial density sampling (e.g., *Braun and Kelemen*, 2002; *Braun*, 2004; *Le Mée et al.*, 2004; *Monnier et al.*, 2006). It has remained logistically difficult to characterize the geochemical variations present at larger scales because of the very large number of in-situ samples required. For the present study, we have instead relied on sediment samples from modern fluvial deposits to efficiently sample the underlying variability within mantle rocks. We focus on the major element composition of chromian spinel minerals recovered from the sediment. Spinel is a widely used petrogenetic indicator mineral with the ability to

preserve its original, igneous composition in terms of variables such as Cr/Al ratio and TiO_2 content during later metamorphism (e.g., *Irvine*, 1967; *Dick and Bullen*, 1984; *Arai*, 1992). Potential impacts on spinel Cr# (molar Cr/(Cr+Al)) and TiO_2 caused by diffusive exchange with the surroundings are additionally limited by the fact that spinel is the major host of Cr, Ti, and to a lesser extent, Al in Oman peridotites. Spinel compositions in abyssal and ophiolitic peridotites are also correlated with whole rock major and trace element variables (e.g., *Hellebrand et al.*, 2001; *Godard et al.*, 2000; *Monnier et al.*, 2006; *Hanghøj et al.*, 2010). For the present study, we have analyzed $\sim$ 2000 detrital spinel grains representing 17 spatially distinct watersheds (contributing areas $\sim$1-20 km^2) situated throughout the Wadi Tayin massif. We have supplemented these data with spatial information about the sampled watersheds, extracted from a Digital Elevation Model (DEM). Details about sampling and geochemical analysis methods, as well as about the topographic characterization of sampled drainages are provided in Appendix C (c.f., Sections C.1,C.2). Following the approach of previous studies (*Reisberg and Zindler*, 1986; *Arai et al.*, 2006), our method assumes that detrital spinel minerals provide a representative sample of the underlying variability within mantle rocks. For a discussion of the statistical reproducibility of variability estimates obtained by our method, and the dependence of estimates on sample size, the reader is referred to Sections C.3 and C.4 of Appendix C.

4.3 The Character of Detrital Spinel Variability

Consistent with previous studies, we find spinel variability at Wadi Tayin spanning the range of Cr# and TiO_2 content observed globally in abyssal peridotite (*Kelemen et al.*, 1995; *Braun*, 2004; *Hanghøj et al.*, 2010). Mg# (molar Mg/(Mg+Fe^{2+}), where Fe^{2+} is calculated from total Fe using mineral stoichiometry) is generally negatively correlated with Cr# – expected for olivine-spinel isotherms (*Irvine*, 1965; *Dick and Bullen*, 1984) – although this trend displays an offset of $\sim$ 0.05-0.1 lower Mg# at a given Cr# relative to abyssal peridotites. This offset probably reflects metamorphic exchange reactions at slower cooling rates associated with ophiolite emplacement. Variation in spinel Mg# does not affect the results of this study and is not considered further here. Instead, we focus on spatial variations in the character of the statistical variability defined by spinel Cr# and TiO_2, visualized using the standard non-parametric technique of kernel density estimation (*Scott*, 1992). Figure 4-1 depicts our sampling locations and their source catchments in the context of a recent geologic map (*Nicolas et al.*, 2000). Although variability within any individual drainage generally displays a single dominant compositional mode with low TiO_2, we have detected large differences between drainages in terms of, e.g., the composition and dispersion of the

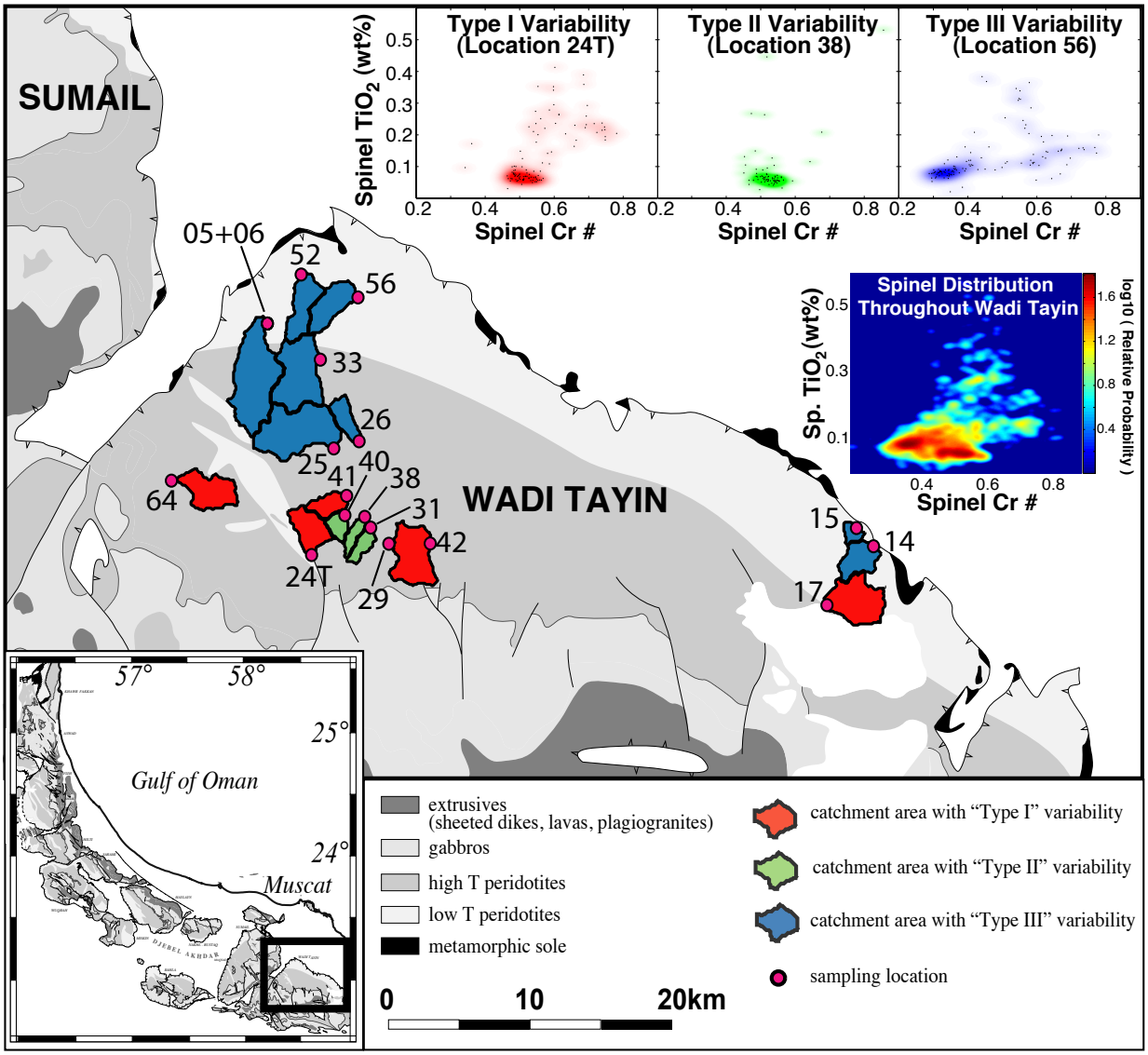

Figure 4-1: Map of sampling site locations (magenta symbols), and corresponding catchment areas overlaid onto a geologic map of the Wadi Tayin massif, modified from *Nicolas et al.* (2000). Catchment areas are derived from a DEM, and the category of each sample is denoted by the color of the catchment area. Overlaid are representative probability density estimates from individual samples of each kind of variability. An estimate of the probability density governing spinel variability throughout the Wadi Tayin mantle is also shown.

locally dominant mode, and the character of distribution tails. Cluster analysis (unsupervised learning) algorithms suggest that variability patterns observed at each of our sampling locations comprise a minimum of three basic categories, consistent with visual inspection of the data. We will refer to these categories (illustrated by insets to Figure 4-1) using the following terminology: 'Type I variability' defines a spinel distribution with a dominant compositional mode with Cr# $\approx$ 0.5 and $TiO_2 \approx 0.05$ wt%, and with a substantial distribution tail concentrated at higher Cr# and TiO_2. 'Type II variability' is similar to Type I and displays a statistically indistinguishable mode, although there are few or no outliers beyond this peak. 'Type III variability' is characterized by a Cr#-TiO_2 mode that is centered on lower Cr# and higher TiO_2 values (Cr# $\approx$ 0.35 and $TiO_2 \approx 0.1$ wt%) than in Type I or Type II variability. Type III probability densities are also generally more dispersed, with a relatively large proportion of outliers displaying a very wide range in Cr# (0.3 - >0.7). Further discussion of our implementations of probability density estimation and cluster analysis are provided in Appendix C (c.f., Sections C.5 and C.6).

By combining the data from individual drainages, we have also constructed an estimate of the relative frequency of spinel compositions throughout the Wadi Tayin mantle. We employed random resampling (details given in Section C.6.1 of Appendix C) to simulate spatially independent sampling throughout Wadi Tayin, incorporating spinel data from each location in proportion to the drainage area represented. Shown as an inset to Figure 4-1, the resulting statistical model of spinel variability within Wadi Tayin may be summarized in terms of its key features: (1) The vast majority of spinel compositions plot between Cr# $\sim$ 0.3 and 0.6, and $TiO_2 < 0.15$ wt.%, (2) Two significant compositional modes occur within this compositional region, centered on Cr# $\sim$ 0.35 and 0.5, (3) Two distinctive probability density tails extend beyond the region defined in (1), the first with TiO_2 generally less than 0.19, and the other with TiO_2 generally greater at a given Cr#. We suspect that spinel variability at Wadi Tayin contains further spatially coherent features, although we cannot demonstrate the robustness of these features at present. For example, there could be a systematic distinction between locations with Type III variability in the eastern versus the western portions of Wadi Tayin (separated by $\sim$ 30 km from the western sample locations, the available data from eastern locations do not display a dominant spinel compositional mode, but show a nearly uniform random distribution of spinel compositions within the same compositional range as seen in the western samples). Although data from eastern Wadi Tayin is distinguished through open symbols in Figure 4-2, we depict only the most robust statistical data classification in Figure 4-1 for clarity.

Since the three main spinel variability types are defined by cluster analysis without incorporating any spatial information, it is remarkable that the variability types are organized

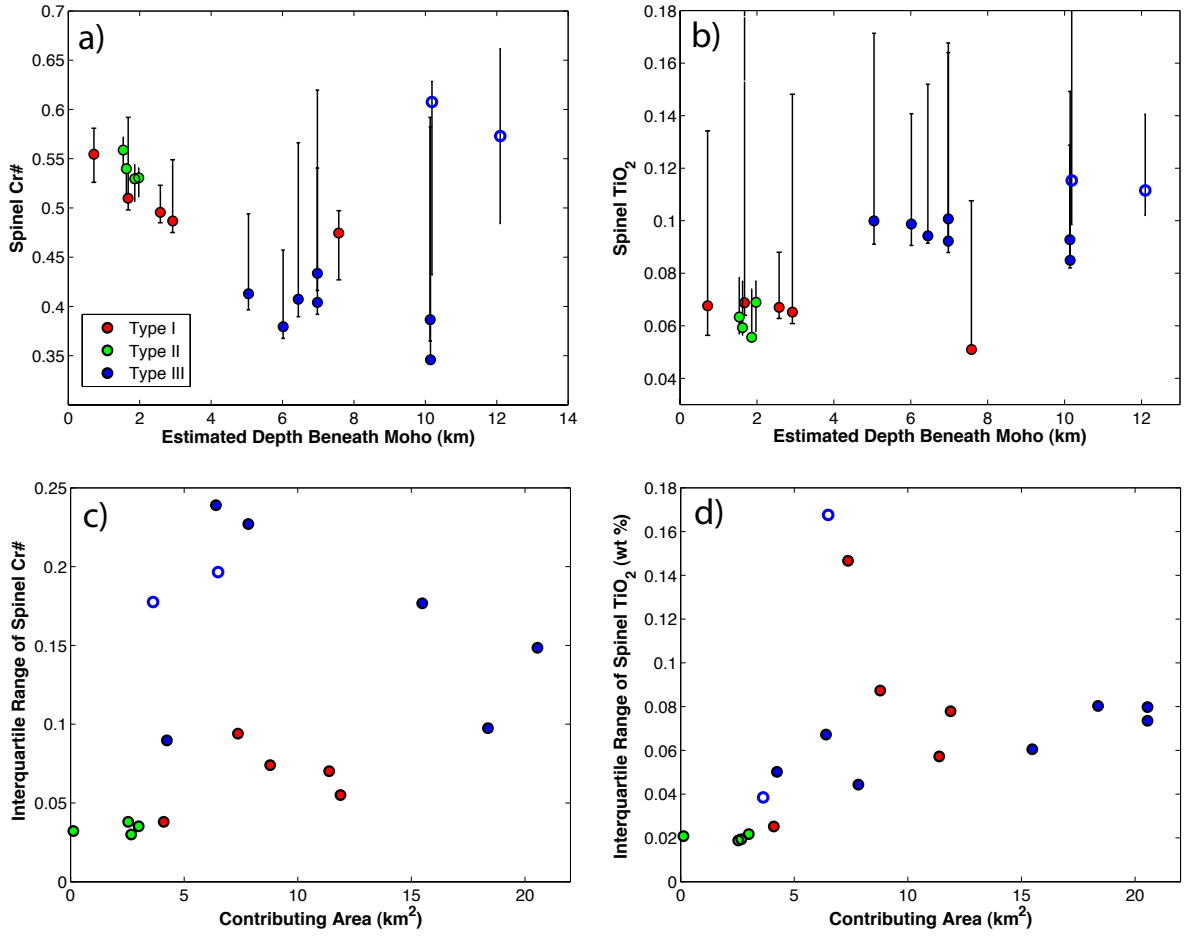

Figure 4-2: (a-b) Variation of locally most likely Cr# and TiO_2 detrital spinel composition with distance to the crust-mantle transition. Each symbol represents the maximum likelihood composition inferred at a single sampled drainage. Symbol colors correspond to the classification scheme shown in the previous Figure. (Open symbols distinguish Type III drainages from the eastern portion of Wadi Tayin.) Vertical error bars represent the first and third quartiles of the data, and thus span the central 50% of observations (the first quantile defines the data value relative to which 25% of data has smaller values and 75% has larger values). Symbols that are not centered with respect to their error bars are an expression of the asymmetry in the underlying probability densities. (c-d) Illustration of the effect of sampling length scale (equivalent to the contributing area of sampled drainages) on detrital spinel variability. Similar to the standard deviation, the interquartile range is a measure of dispersion that is robust with respect to outliers (for normally distributed data, the interquartile range $\approx 1.349\ \sigma$). Note that although large variability can exist over small sampling length scales, smaller drainages are generally characterized by less variability, while spinel samples from larger drainages always display a high degree of variability.

in a coherent spatial pattern. This result would be extremely unlikely if the distribution of mantle variability at Wadi Tayin were purely "homogeneously heterogeneous" (in the sense that mantle variability is present, but statistically identical at all possible sampling locations) at length scales comparable to the watersheds we have sampled. Instead, our data strongly suggests that mantle variability previously observed at the outcrop-scale (e.g., $\sim$ 1-100 m extent (e.g., tabular dunites *Nicolas*, 1989; *Kelemen et al.*, 1997a)) is further organized into coherent spatial patterns that are comparable in size or larger than sampled watersheds. Additional discussion is contained in Section C.8 of Appendix C. We interpret Figure 4-1 to depict the map pattern of intermediate-scale mantle variability as resolved in our data. In principle, the extent of mantle outcrop corresponding to each spinel variability type could be mapped in additional detail throughout Wadi Tayin using the methods of this study. At least three additional spatial trends exist in our spinel data, illustrated in Figure 4-2. First, the dominant spinel composition within individual watersheds is correlated with mantle depth: spinel populations from greater depths display lower Cr# and higher wt% TiO_2 modes than populations at shallower depths, particularly where the inferred mantle depth is less than 10 km (c.f., panels a) and b) of Figure 4-2). (Our method for estimating depth beneath the crust-mantle transition at Wadi Tayin is described in Section C.7 of Appendix C.) Second, greater Cr# variability is observed at greater inferred mantle depths, corresponding to the exclusive occurrence of variability Type III at inferred mantle depths greater than $\sim$ 5 km. Third, drainages with Type I and Type II spinel variability display a positive correlation between their catchment area and the degree of compositional dispersion present, depicted in panels (c-d) of Figure 4-2. By contrast, variability in sampling length scale should not lead to any change in the apparent variability of samples from a homogeneously heterogeneous mantle outcrop (for further discussion, c.f. Section C.8 of Appendix C).

4.4 Spatial Variability in the Distribution of Mantle Lithologies

Spinel compositions within the Oman mantle are generally dependent on their host rock lithology (e.g., *Kelemen et al.*, 1995, 1997a; *Hellebrand et al.*, 2001; *Godard et al.*, 2000; *Le Mée et al.*, 2004; *Braun*, 2004; *Arai et al.*, 2006; *Monnier et al.*, 2006; *Hanghøj et al.*, 2010). Statistical variability in detrital spinel should therefore reflect the relative proportions of mantle lithologies in the outcrop (e.g., dunite, harzburgite, etc.). We have quantitatively estimated these proportions by first using the approach of Bayesian classification to assign each spinel composition to a maximum likelihood source lithology, and then applying this

classification to the observed spinel variability introduced in a previous section. Our method is calibrated from training data consisting of southern Oman ophiolite mantle samples of known lithology (references are provided in the caption of Figure 4-3), and our approach is developed further in in Section C.9 of Appendix C). Although our approach allows the treatment of additional lithological complexity, we will consider three simple classification schemes here, illustrated in the left panel of Figure 4-3: (1) all detrital spinel are assumed to be sourced from either a harzburgite or dunite lithology; (2) spinel compositions can additionally be attributed to pyroxenite, as well as to dunite or harzburgite; (3) in addition to the components present in (2), transitional mantle rocks comprising harzburgites in close proximity ($\leq$ 1 m) to large intervals of dunite (or vice versa) define an additional, distinctive compositional component (c.f., *Braun*, 2004). These three classification schemes are meant to reflect – in progressively greater detail – the dominant mantle lithologies at Wadi Tayin, and we consider (3) to provide the best compromise between realism (i.e., accounting for the spectrum of mantle lithologies documented by previous studies), and simplicity (involving a minimum number of components). We will therefore primarily make use of classifier (3), although results from the more simplified two and three component classifiers are provided to enable the robustness of our inferences to be assessed. Since harzburgite, dunite and pyroxenite each contain roughly comparable modal proportions of spinel (reported variability in spinel content in samples of any single lithology is large compared to differences between lithologies, where each lithology generally contains $\sim$ 1-5% spinel, although dunites can contain up to 10 volume % spinel, e.g., *Boudier and Coleman*, 1981; *Python et al.*, 2008; *Hanghøj et al.*, 2010), we do not expect any of these lithologies to be represented in detrital spinel samples in proportions largely different from their relative abundance in the outcrop. Additional discussion of our of preferred quaternary classifier is provided in Section C.10 of Appendix C, but it deserves mention that detrital spinel compositions plotting within the lower-TiO_2 distribution tail could correspond to both pyroxenites or to compositionally distinctive dunites from northern Oman (*Augé*, 1987; *Tamura and Arai*, 2006). Our training data compilation contains only one dunite analysis plotting in this low-TiO_2 dunite field from southern Oman. Because of this uncertainty we will refer to the pyroxenite component of our classifier as "pyroxenite and low-TiO_2 dunite" (PLTD). From our estimate of spinel variability throughout Wadi Tayin – shown as an inset to Figure 4-1 – we infer the following lithologic proportions: 79-94% harzburgite 4-6% dunite, 8-9% PLTD and up to 9% transitional harzburgite-dunite (Tables contrasting the inferred abundances obtained by each classifier are provided in Section C.9 of Appendix C, both for individual watersheds and for Wadi Tayin as a whole). These results are generally in agreement with previous estimates of lithologic proportions derived from field mapping (the study of *Boudier and*

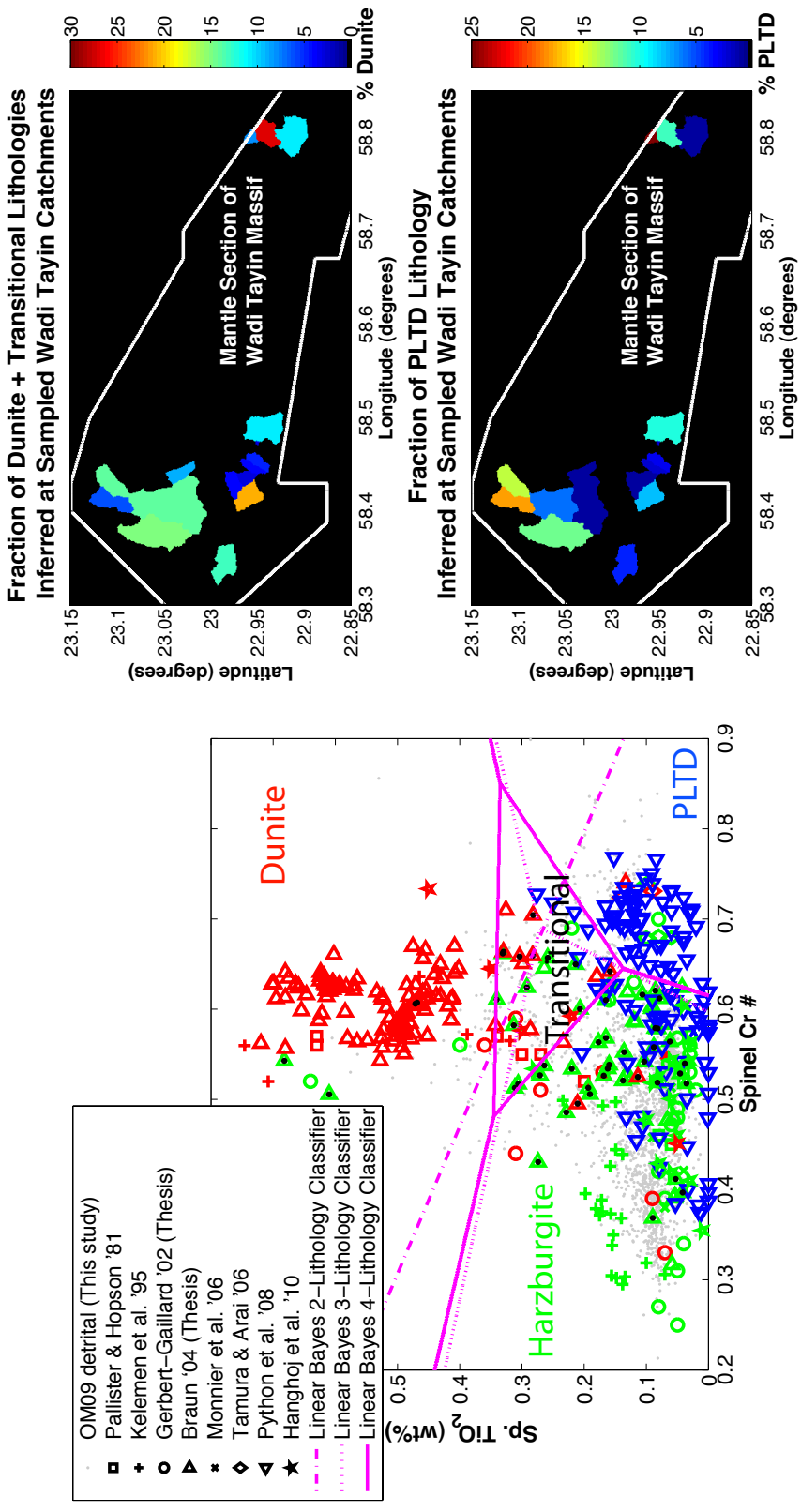

Figure 4-3: Caption given on next page.

Figure 4-3: Estimation of the relative proportion of mantle lithologies within Wadi Tayin using two, three and four component linear Bayes classifiers. (left) A compilation of spinel analyses from hand specimens of known lithology is used as a training data set (green symbols indicate harzburgites, red symbols indicate dunites, blue symbols indicate pyroxenites (representing the PLTD lithology, c.f., discussion in the text), and black dots specify transitional lithologies comprising harzburgites sampled $\leq$ 1 m from wide dunites and vice versa, and symbol types indicate data source). Data were compiled from: (*Pallister and Hopson*, 1981; *Kelemen et al.*, 1995; *Braun*, 2004; *Monnier et al.*, 2006; *Tamura and Arai*, 2006; *Python et al.*, 2008; *Hanghøj et al.*, 2010; *Gerbert-Gaillard*, 2002). The quantitative method used to train the classifier is discussed in Section C.9 of Appendix C. The magenta lines define the Bayes decision boundaries between regions in which a given spinel analysis is more likely to be obtained from a given lithology. We prefer the 4-Lithology Classifier, as it provides the best available balance between geologic realism and relative simplicity, as discussed further in the text and in Section C.10 of Appendix C. (right) Visualization of spatial variation in inferred lithologic proportions. Colors indicate respective proportions of dunite (top) and PLTD (bottom) at each sampled location using our preferred, quaternary classifier.

Coleman (1981) reports locally 5-50% dunite within harzburgite at the Wadi Tayin massif, with typical proportions in the range of 5-15%). In all cases, the dominant compositional peaks in our data correspond to a harzburgite source, while the distribution tails are most consistent with dunite or pyroxenite sources. Interpreted through our preferred, quaternary classifier, the distribution tail with higher TiO_2 at a given Cr# corresponds to the presence of dunite, while the lower TiO_2 trend reflects PLTD. In addition to variations in PLTD proportions (occuring primarily in regions of Type III variability), there is apparently considerable variability in the local abundances of dunite throughout Wadi Tayin, illustrated in the right panel of Figure 4-3. The significance of this result is discussed further in a following section.

The distribution of tabular dunite widths represents an additional characteristic of mantle variability that may be constrained using our data, given that the TiO_2 content of spinel in the interior of dunites is positively correlated with dunite width, and to distance from harzburgite/dunite contacts within wide dunites (*Braun*, 2004). The relative frequency of dunite widths in the Oman mantle section has been studied previously by *Braun and Kelemen* (2002) using a series of 1-D transects across selected mantle outcrops of different length scales, suggesting that dunite widths define a power law distribution over more than four orders of magnitude. To test this result, we have isolated those spinel compositions in our data set classified as dunite-sourced or transitional (based on the four component classifier discussed above), and resampled these data to correct for variations in spatial sampling density (c.f., our discussion of constructing an estimate of Cr#-TiO_2 variability throughout Wadi Tayin in a previous section). The relative frequency of dunite compositions thus obtained was then transformed via a parameterization of the data from (*Braun*, 2004)

– as specified further in Section C.6.1 of Appendix C – to infer the relative abundances of dunite widths throughout Wadi Tayin. Our results are shown in Figure 4-4, and are broadly consistent with the conclusion of (*Braun and Kelemen*, 2002) that the cumulative frequency of dunites as a function of size is governed by a power law distribution $Freq. = const./width^D$ with exponent $D = 1.11$.

4.5 Implications for Ocean Ridge Magmatism

If the Wadi Tayin mantle underwent partial melting beneath an ocean ridge (via polybaric, near-fractional, decompression melting during upwelling and corner flow associated with plate spreading (*Bottinga and Allègre*, 1973, 1976; *McKenzie and Bickle*, 1988; *Klein and Langmuir*, 1987; *Johnson et al.*, 1990)), then regions with the greatest inferred depths in the mantle column could have experienced lower extents of melting than those near the crust-mantle transition. The observed trend in spinel compositions relative to their inferred vertical depth beneath the crust-mantle transition (c.f., Figure 4-2) is consistent with this expectation, since spinel compositions with higher Cr# reflect higher degrees of melting or depletion (partial melting removes incompatible components including Al_2O_3, TiO_2 while compatible elements such as Cr_2O_3 are enriched, c.f., *Dick and Bullen*, 1984; *Hellebrand et al.*, 2001; *Le Mée et al.*, 2004; *Monnier et al.*, 2006). However, factors such as hydrous melting could also increase the proportion of melting occurring at greater depths, resulting in less variation in the extent of melting at shallow depths than expected in simpler melting scenarios (e.g., *Braun et al.*, 2000). In addition, fractionation due to melt extraction can be obscured or completely overprinted by open system processes such as (1) "impregnation" via addition of trapped melt or crystals formed from migrating, cooling melt (e.g., *Dick*, 1989; *Saal et al.*, 2001; *Niu*, 2004; *Le Roux et al.*, 2007), (2) chromatographic exchange between migrating melt and host minerals (e.g., *Kelemen*, 1986; *Navon and Stolper*, 1987; *Iwamori*, 1993; *Lundstrom et al.*, 1995; *Spiegelman and Kelemen*, 2003), or (3) mineral dissolution reactions (e.g., *Boudier and Nicolas*, 1972; *Quick*, 1981; *Kelemen*, 1986; *Bodinier*, 1988; *Kelemen*, 1990). Assuming that melting occured up to the crust-mantle transition with a productivity of 1%/kbar (*Langmuir et al.*, 1992; *Ahern and Turcotte*, 1979), even after the exhaustion of clinopyroxene (*Asimow et al.*, 2004), the deepest mantle outcrops at Wadi Tayin (vertical depth estimated at $\sim$ 10-12 km) should record extents of melting F that are $\sim$4% lower than the maximum observed at the crust-mantle transition. The equation $F = 10\ln(Cr\#) + 24$ developed by (*Hellebrand et al.*, 2001) yields a maximum degree of melting of about 18.5% at the top of the melting column, and a minimum degree of melting of about 13.2% near the base of the Wadi Tayin mantle section, consistent with a decrease

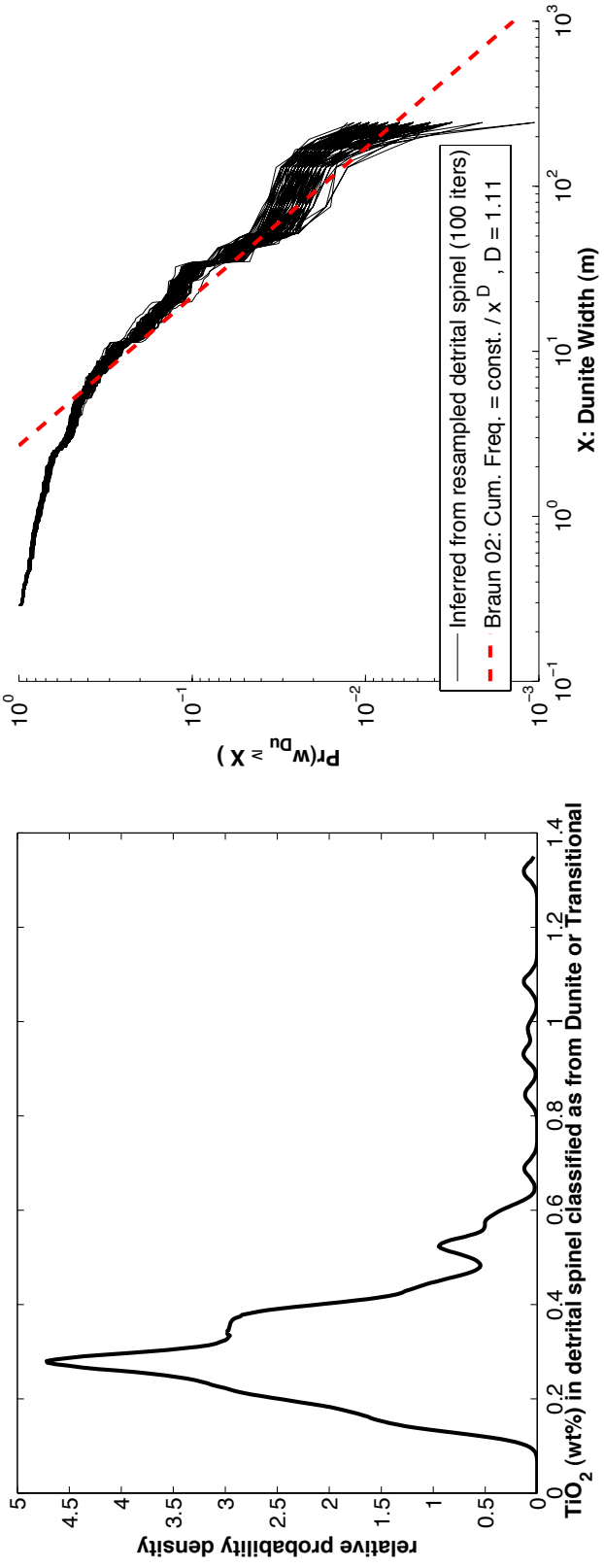

Figure 4-4: Caption given on next page.

Figure 4-4: (left) after detrital spinel data is randomly resampled to account for spatially non-uniform sampling (c.f., the text for discussion), we estimate the relative frequency of detrital spinel TiO_2 compositions with inferred source lithologies corresponding to dunite or transitional peridotite. Using the results of (*Braun*, 2004), this distribution of spinel TiO_2 allows the cumulative frequency of dunites widths in the Wadi Tayin outcrop to be constrained. Results from 100 iterations of random resampling are depicted in the right panel to illustrate the robustness of our findings with respect to the resampling method. Our data, interpreted through the parameterization described in Section C.6.1 of Appendix C, is consistent with the power law exponent describing the relative proportion of large and small dunites of $D = 1.11$, as determined by (*Braun and Kelemen*, 2002)

in F of about 5%. However, we caution that the observed absence of residual clinopyroxene and overall light rare earth element depletion in harzburgites throughout Wadi Tayin (e.g., *Kelemen et al.*, 1995; *Hanghøj et al.*, 2010) suggests that the minimum value of F – at the base of the Wadi Tayin section – was greater than these calculations would imply, most likely exceeding the value commonly derived for exhaustion of clinopyroxene, $\geq 15\%$ (e.g., *McKenzie and Bickle*, 1988; *Johnson et al.*, 1990; *Katz et al.*, 2003).

Although variations in melting extent might be the cause of some aspects of our data, several additional features of our data are not readily accounted for by this simple explanation, and suggest additional complexity. Interpreted through the Bayesian classifiers shown in Figure 4-3, mantle outcrops with Type I variability may contain $\gg 5\%$ small-scale dunite bodies within harzburgite, while those with Type II variability suggest a relatively low proportion of dunite. Based on Figure 4-1, the distribution of dunite within the Wadi Tayin mantle exposure is therefore not homogenous, even when considered at a constant depth relative to the crust-mantle transition and over intermediate length scales much larger than those of individual dunite bodies. The positive correlation between the area of sampled catchments and observed spinel variability provides an additional line of evidence that dunite is not distributed homogenously over the observational length scales of this study. Since dunites are likely the consequences of reactive melt transport (e.g., *Kelemen et al.*, 1995), we believe that the $\sim$ 5 x 5 km region of Type II variability surrounded by Type I variability that we have mapped in the shallowest mantle section of Wadi Tayin could represent a primary, igneous feature, corresponding to a large region of reduced reactive melt transport. In turn, the relatively low spinel Cr# of the dominant mode in Type II variability could be due to inefficient melt extraction, or to near-equilibrium porous flow rather than near fractional melting and melt transport in the dunite poor regions. Spatial heterogeneity in permeability or variations in other thermal boundary layer properties, e.g., related to axial discontinuities could potentially have given rise to such intermediate-scale organization of melt transport. It is noteworthy that the present study provides the first available geochemical mapping

of a mantle outcrop at length scales directly comparable to those of seismic tomographic imaging. Thus, there could be a correspondence between spatial features imaged in modern magmatic systems with geochemical observations developed here. For example, along-axis variations in compressional wave velocities at shallow mantle depths ($\sim$ 8-9 km) appear to be spatially correlated with axial discontinuities at the modern East Pacific Rise (e.g., *Dunn et al.*, 2000), and could represent the complementary seismic expression of the organization of melt transport into channel rich and channel poor regions.

Perhaps the most obvious inconsistency with the simple ocean-ridge melting model is the apparent sharp discontinuity between mantle regions of Types I and II variability versus regions with Type III variability (most models of ocean ridge melting generate a continuous increase in the extent of depletion with increasing proximity to the top of the melting column). The contrast in statistical character between variability Types I and II compared to variability of Type III could correspond to the sharp lithological transition from depleted harzburgite to "cpx-harzburgite" identified by *Godard et al.* (2000). However, if so, our data imply that this transition occurs several kilometers farther south than previously mapped (c.f., Figure 4-1). The relatively diffuse character of Type III variability might not be a consequence of ocean ridge magmatism at all, but instead might represent the product of small-scale variability in the extent of, e.g., aluminum enrichment through mantle metasomatism or late-stage magmatism related to ophiolite emplacement (*Godard et al.*, 2000; *Takazawa et al.*, 2003). The basal detachment of the ophiolite could represent a preferred transport pathway for late-stage melts, with variable melt fluxes or Al_2O_3 contents giving rise to large variability in Cr#. The boundary between Types I and II versus Type III variability could therefore represent the boundary between metasomatically modified mantle and the portions of Wadi Tayin representing a relatively unperturbed geochemical analogue of ocean ridge proccessed residual mantle. It is also noteworthy that observed spinel compositions with Cr# $>$0.65 and TiO_2 less than $\sim$ 0.18 wt.% correspond well with compositions observed at supra-subduction zone settings, and are less consistent with spinel data from abyssal settings (where Cr# is generally $<$ 0.65) (e.g., *Dick and Bullen*, 1984; *Arai et al.*, 2006). The large, ubiquitous variations in Cr# present within areas of $<$ 5 km^2, particularly in areas characterized by Type III variability, are also more easily explained by open-system processes than by near-fractional melting. If interpreted through model relationships between spinel Cr# and the degree of melting (e.g., *Hellebrand et al.*, 2001), large Cr# variations would imply a variation of more than 30 % in the local melting extent over very small spatial scales, unless there has been substantial thinning and repetition of section within the Wadi Tayin mantle section. Furthermore, thermal anomalies over small length scales could not persist over the times involved in mantle convection and ridge magmatism because of thermal

diffusion. Finally, detrital spinel variability could also reflect the presence of relict geochemical or lithologic heterogeneity inherited from parental mantle material prior to ocean ridge magmatism, although we do not observe any specific data features that require this.

In summary, we derive lithologic proportions of 79-94% harzburgite, 4-6% dunite, 8-9% low Ti pyroxenite or dunite, and up to 9% transitional harzburgite-dunite in the Wadi Tayin mantle section. Based on the relationship between dunite width and Ti in spinel, we derive an independent confirmation of the results of *Braun and Kelemen* (2002) that there is a power law distribution between dunite width and dunite frequency. Our data demonstrate that there is spatial variability in lithological proportions and in the composition of proportionately dominant harzburgites, at length scales of 0 to 20 km within the mantle section of the Wadi Tayin massif, and by analogy in the residual, shallow mantle beneath oceanic spreading ridges. In general, compositional variability is positively correlated with the spatial scale of sampling. Decreasing spinel Cr# and increasing spinel TiO_2 contents with increasing distance below the crust-mantle transition zone are broadly consistent with the predicted outcome of near-fractional, polybaric fractional melting. Smaller scale variability in spinel compositions, on the other hand, is probably due to open-system processes such as impregnation, chromatographic exchange, or mineral dissolution reactions, whose chemical effects are superimposed on those of melting and melt extraction. Finally, we demonstrate that there is spatial clustering of dunites, interpreted as conduits for focused melt transport, and infer that the harzburgites far from dunite clusters have undergone less efficient melt extraction, and/or more open system exchange with migrating melt, compared to harzburgites close to dunite clusters. These results have important implications for the physical and chemical nature of mantle melting and melt transport in the shallow mantle beneath oceanic spreading centers. Furthermore, our data, together with observations on variation of rock composition that are correlated with spinel composition (e.g., *Monnier et al.*, 2006) can be used to predict the length scale and nature of isotopic variability resulting from isotopically evolving residues of melting and melt extraction.

Bibliography

Aharonov, E., J. A. Whitehead, P. B. Kelemen, and M. Spiegelman (1995), Channeling instability of upwelling melt in the mantle, *J. Geophys. Res.*, *100*, 20,433–20,450.

Aharonov, E., M. Spiegelman, and P. B. Kelemen (1997), Three-dimensional flow and reaction in porous media: Implications for the Earth's mantle and sedimentary basins, *J. Geophys. Res.*, *102*, 14,821–14,833.

Ahern, J. L., and D. L. Turcotte (1979), Magma migration beneath an oceanic ridge, *Earth Plan. Sci. Lett.*, *45*, 115–122.

Alabaster, T., J. A. Pearce, and J. Malpas (1982), The volcanic stratigraphy and petrogenesis of the Oman ophiolite complex, *Contr. Min. Pet.*, *81*, 168–183.

Albarède, F. (1992), How deep do common basaltic magmas form and differentiate?, *J. Geophys. Res.*, *97*, 10,997–11,009.

Amri, I., M. Benoit, and G. Ceuleneer (1996), Tectonic setting for the genesis of oceanic plagiogranites: Evidence from a paleo-spreading structure in the Oman ophiolite, *Earth Plan. Sci. Lett.*, *139*, 177–194.

Arai, S. (1992), Chemistry of chromian spinel in volcanic rocks as a potential guide to magma chemistry, *Min. Mag.*, *56*, 173–184.

Arai, S., K. Kadoshima, and T. Morishita (2006), Widespread arc-related melting in the mantle section of the northern Oman ophiolite as inferred from detrital chromian spinels, *J. Geol. Soc. London*, *163*, 869–879.

Armstrong, R. L. (1968), A model for the evolution of Strontium and Lead isotopes in a dynamic Earth, *Rev. Geophys.*, *6*, 175–199.

Asimow, P. D., J. E. Dixon, and C. H. Langmuir (2004), A hydrous melting and fractionation model for mid-ocean ridge basalts: Application to the Mid-Atlantic Ridge near the Azores, *Geochem. Geophys. Geosys.*, *5*, doi:10.1029/2003GC000568.

Augé, T. (1987), Chromite deposits in the northern Oman ophiolite: Mineralogical constraints, *Min. Deposita*, *22*, 1–10.

Baker, D. R., and D. H. Eggler (1987), Compositions of anhydrous and hydrous melts coexisting with plagioclase, augite, and olivine or low-Ca pyroxene from 1 atm to 8 kbar – application to the Aleutian volcanic center of Atka, *Am. Mineral.*, *72*, 12–28.

Bender, J. F., F. N. Hodges, and A. E. Bence (1978), Petrogenesis of basalts from the project FAMOUS area: Experimental study from 0 to 15 kbars, *Earth Plan. Sci. Lett.*, *41*, 277–302.

Benoit, M., M. Polvé, and G. Ceuleneer (1996), Trace element and isotopic characterization of mafic cumulates in a fossil mantle diapir (Oman ophiolite), *Chem. Geol.*, *134*, 199–214.

Bezos, A., and E. Humler (2005), The $Fe^{3+}/\sigma Fe$ ratios of MORB glasses and their implications for mantle melting, *Geochim. Cosmochim. Acta*, *69*, 711–725.

Bird, P. (2003), An updated digital model of plate boundaries, *Geochem. Geophys. Geosys.*, *4*, doi:10.1029/2001GC000252.

Bodinier, J.-L. (1988), Geochemistry and petrogenesis of the Lanzo peridotite body, Western Alps, *Tectonophysics*, *149*, 67–88.

Bodinier, J.-L., and M. Godard (2003), Orogenic, ophiolitic, and abyssal peridotites, in *Treatise on Geochemistry, vol. 2: Mantle and Core*, edited by R. Carlson, pp. 103–170, Elsevier, Amsterdam, The Netherlands.

Bodinier, J.-L., G. Vasseur, J. Vernières, C. Dupuy, and J. Fabriès (1990), Mechanism of mantle metasomatism: Geochemical evidence from the Lherz orogenic peridotite, *J. Petrol.*, *31*, 597–628.

Bottinga, Y., and C. J. Allègre (1973), Thermal aspects of seafloor spreading and the nature of the oceanic crust, *Tectonophysics*, *18*, 1–17.

Bottinga, Y., and C. J. Allègre (1976), Geophysical, petrological and geochemical models of the oceanic lithosphere, *Tectonophysics*, *32*, 9–59.

Boudier, F., and R. G. Coleman (1981), Cross-section through the peridotite in the Samail ophiolite, southeastern Oman mountains, *J. Geophys. Res.*, *86*, 2573–2592.

Boudier, F., and A. Nicolas (1972), Fusion partielle gabbroique dans la lherzolite de Lanzo, *Bull. Suisse Min. Pet.*, *52*, 39–56.

Bowen, N. L. (1928), *The Evolution of the Igneous Rocks*, Dover, New York, NY, 332 pp.

Brandenburg, J., E. Hauri, P. van Keken, and C. Ballentine (2008), A multiple-system study of the geochemical evolution of the mantle with force-balanced plates and thermochemical effects, *Earth Plan. Sci. Lett.*, *276*, 1–13.

Braun, M. G. (2004), Petrologic and microstructural constraints on focused melt transport in dunites and the rheology of the shallow mantle, Ph.D. thesis, Massachusetts Institute of Technology.

Braun, M. G., and P. B. Kelemen (2002), Dunite distribution in the Oman ophiolite: Implications for melt flux through porous dunite conduits, *Geochem. Geophys. Geosys.*, *3*, doi:10.1029/2001GC000289.

Braun, M. G., G. Hirth, and E. M. Parmentier (2000), The effects of deep damp melting on mantle flow and melt generation beneath mid-ocean ridges, *Earth Plan. Sci. Lett.*, *176*, 339–356.

Browning, P. (1982), The petrology, geochemistry, and structure of the plutonic rocks of the Oman ophiolite, Ph.D. thesis, The Open University, Milton Keynes, England, 404 pp.

Browning, P. (1984), Cryptic variations within the cumulate sequence of the Oman ophiolite: Magma chamber depth and petrological implications, *Geol. Soc. London Spec. Pub.*, *13*, 71–82.

Cannat, M., D. Bideau, and H. Bougault (1992), Serpentinized peridotites and gabbros in the Mid-Atlantic Ridge axial valley at 15°37'N and 16°52'N, *Earth Plan. Sci. Lett.*, *109*, 87–106.

Casey, J. F. (1997), Comparison of major- and trace-element geochemistry of abyssal peridotites and mafic plutonic rocks with basalts from the MARK region of the Mid-Atlantic Ridge, in *Proc. ODP, Sci. Results*, vol. 153, edited by J. A. Karson, M. Cannat, D. J. Miller, and D. Elthon, pp. 181–241, Ocean Drilling Program, College Station, TX.

Chakraborty, S. (1997), Rates and mechanisms of Fe-Mg interdiffusion in olivine at 980°-1300°C, *J. Geophys. Res.*, *102*, 12,317–12,331.

Chaudhuri, P., and J. Marron (1999), SiZer for exploration of structures in curves, *J. Am. Stat. Assoc.*, *94*, 807–823.

Cogley, J. G. (1984), Continental margins and the extent and number of the continents, *Rev. Geophys. Space Phys.*, *22*, 101–122.

Danyushevsky, L. V. (2001), The effect of small amounts of H_2O on crystallization of mid-ocean ridge and backarc basin magmas, *J. Volc. Geotherm. Res.*, *110*, 265–280.

DePaolo, D. J. (1981), Trace element and isotopic effects of combined wall rock assimilation and fractional crystallization, *Earth Plan. Sci. Lett.*, *53*, 189–202.

Dick, H. J. B. (1989), Abyssal peridotites, very slow spreading ridges and ocean ridge magmatism, in *Magmatism in the ocean basins*, *Geological Society Special Publications*, vol. 42, edited by A. D. Saunders and M. J. Norry, pp. 71–105, Geological Society of London, London.

Dick, H. J. B., and T. Bullen (1984), Chromian spinel as a petrogenetic indicator in abyssal and alpine-type peridotites and spatially associated lavas, *Contr. Min. Pet.*, *86*, 54–76.

Dick, H. J. B., and et al. (2002), Primary silicate mineral chemistry of a 1.5-km section of very slow spreading lower ocean crust: ODP Hole 735B, Southwest Indian Ridge, in *Proc. ODP, Sci. Results*, vol. 176, edited by J. H. Natland, H. J. B. Dick, D. J. Miller, and R. P. Von Herzen, pp. 1–60, Ocean Drilling Program, College Station, TX.

Dick, H. J. B., R. L. FIsher, and W. B. Bryan (1984), Mineralogical variability of the uppermost mantle along mid-ocean ridges, *Earth Plan. Sci. Lett.*, *69*, 88–106.

Donnelly, K. E., S. L. Goldstein, C. H. Langmuir, and M. Spiegelman (2004), Origin of enriched ocean ridge basalts and implications for mantle dynamics, *Earth Plan. Sci. Lett.*, *226*, 347–366.

Dunn, R. A., D. R. Toomey, and S. C. Solomon (2000), Three-dimensional seismic structure and physical properties of the crust and shallow mantle beneath the East Pacific Rise at 9°30'N, *J. Geophys. Res.*, *105*, 23,537–23,555.

Dupré, B., and C. Allègre (1983), Pb-Sr isotope variation in Indian Ocean basalts and mixing phenomena, *Nature*, *303*, 142–146.

Efron, B., and R. J. Tibshirani (1994), *An introduction to the Bootstrap*, Chapman and Hall, London, 456 pp.

Elthon, D. (1987), Petrology of gabbroic rocks from the Mid-Cayman Rise spreading center, *J. Geophys. Res.*, *92*, 658–682.

Feig, S. T., J. Koepke, and J. E. Snow (2006), Effect of water on tholeiitic basalt phase equilibria: An experimental study under oxidizing conditions, *Contr. Min. Pet.*, *152*, 611–638.

Gaetani, G. A., and T. L. Grove (1998), The influence of water on melting of mantle peridotite, *Contr. Min. Pet.*, *131*, 323–346.

Gaetani, G. A., S. E. DeLong, and D. A. Wark (1995), Petrogenesis of basalts from the Blanco Trough, northeast Pacific: Inferences for off-axis melt generation, *J. Geophys. Res.*, *100*, 4197–4214.

Garrido, C.-J., P. B. Kelemen, and G. Hirth (2001), Variation of cooling rate with depth in lower crust formed at an oceanic spreading ridge: Plagioclase crystal size distributions in gabbros from the Oman ophiolite, *Geochem. Geophys. Geosys.*, *2*, 2000GC000136.

Gast, P. W. (1968), Trace element fractionation and the origin of tholeiitic and alkaline magma types, *Geochim. Cosmochim. Acta*, *32*, 1057–1068.

Gerbert-Gaillard, L. (2002), Caracterisation geochimique des peridotites de l'ophiolite d'Oman, Ph.D. thesis, Univ. Montpellier.

Ghiorso, M. S., and R. O. Sack (1995), Chemical mass-transfer in magmatic processes. IV. a revised and internally consistent thermodynamic model for the interpolation and extrapolation of liquid-solid equilibria in magmatic systems at elevated temperatures and pressures, *Contr. Min. Pet.*, *119*, 197–212.

Ghiorso, M. S., M. M. Hirschmann, P. W. Reiners, and V. C. I. Kress (2002), The pMELTS: A revision of MELTS aimed at improving calculation of phase relations and major element partitioning involved in partial melting of the mantle at pressures up to 3 GPa, *Geochem. Geophys. Geosys.*, *3*, doi:10.1029/2001GC000217.

Ghods, A., and J. Arkani-Hamed (2000), Melt migration beneath mid-ocean ridges, *Geophys. J. Int.*, *140*, 687–697.

Godard, M., D. Jousselin, and J.-L. Bodinier (2000), Relationships between geochemistry and structure beneath a palaeo-spreading centre: A study of the mantle section in the Oman ophiolite, *Earth Plan. Sci. Lett.*, *180*, 133–148.

Green, D. H., and A. E. Ringwood (1967), The genesis of basaltic magmas, *Contr. Min. Pet.*, *15*, 103–190.

Gregg, P. M., M. D. Behn, J. Lin, and T. L. Grove (2009), Melt generation, crystallization, and extraction beneath segmented oceanic transform faults, *J. Geophys. Res.*, *114*, doi: 10.1029/2008JB006100.

Grove, T. L., and W. B. Bryan (1983), Fractionation of pyroxene-phyric MORB at low-pressure – an experimental study, *Contr. Min. Pet.*, *84*, 293–309.

Grove, T. L., D. C. Gerlach, and T. W. Sando (1982), Origin of calc-alkaline series lavas at Medicine Lake volcano by fractionation, assimilation and mixing, *Contr. Min. Pet.*, *80*, 160–182.

Grove, T. L., R. J. Kinzler, and W. B. Bryan (1992), Fractionation of mid-ocean ridge basalt (MORB), in *Mantle flow and melt generation at mid-ocean ridges*, *Geophysical Monograph*, vol. 71, edited by J. Phipps Morgan, D. K. Blackman, and J. M. Sinton, pp. 281–310, American Geophysical Union, Washington, DC.

Gudfinnsson, G. H., and D. C. Presnall (2001), A pressure-independent geothermometer for primitive mantle melts, *J. Geophys. Res.*, *106*, 16,205–16,211.

Hair, J. F., W. Black, B. Babin, R. E. Anderson, and R. L. Tatham (2005), *Multivariate Data Analysis, Sixth Edition*, Prentice Hall, New York, 928 pp.

Hanghøj, K., P. B. Kelemen, D. Hassler, and M. Godard (2010), Composition and genesis of depleted mantle peridotites from the Wadi Tayin massif, Oman ophiolite; major and trace element geochemistry, and Os isotope and PGE systematics, *J. Petrol.*, *51*, 201–227.

Hart, S. R. (1984), A large-scale isotope anomaly in the southern hemisphere mantle, *Nature*, *309*, 753–757.

Hart, S. R., J.-G. Schilling, and J. L. Powell (1973), Basalts from Iceland and along the Reykjanes Ridge: Sr isotope geochemistry, *Nature*, *246*, 104–107.

Helffrich, G. R., and B. J. Wood (2001), The Earth's mantle, *Nature*, *412*, 501–507.

Hellebrand, E., J. E. Snow, H. J. B. Dick, and A. W. Hofmann (2001), Coupled major and trace elements as indicators of the extent of melting in mid-ocean-ridge peridotites, *Nature*, *410*, 677–681.

Hess, H. (1962), History of ocean basins, in *Petrologic Studies: A Volume in Honour of A. F. Buddington*, edited by A. E. J. Engel, pp. 599–620, Geological Society of America, Boulder.

Hess, P. C. (1992), Phase equilibria constraints on the origin of ocean floor basalts, in *Mantle flow and melt generation at mid-ocean ridges*, *Geophysical Monograph*, vol. 71, edited by J. Phipps Morgan, D. K. Blackman, and J. M. Sinton, pp. 67–102, American Geophysical Union, Washington, DC.

Hirschmann, M. M. (2000), Mantle solidus: Experimental constraints and the effects of peridotite composition, *Geochem. Geophys. Geosys.*, *1*, doi:10.1029/2000GC000070.

Hirth, G., and D. L. Kohlstedt (1996), Water in the oceanic upper mantle: Implications for rheology, melt extraction and the evolution of the lithosphere, *Earth Plan. Sci. Lett.*, *144*, 93–108.

Hoefner, M. L., and H. S. Fogler (1988), Pore evolution and channel formation during flow and reaction in porous media, *AIChE Journal*, *34*, 45–54.

Hoffman, N. R. A., and D. P. McKenzie (1985), The destruction of geochemical heterogeneities by differential fluid motions during mantle convection, *Geophys. J. R. Astron. Soc.*, *82*, 163–206.

Hofmann, A. (1997), Mantle geochemistry – the message from oceanic volcanism, *Nature*, *385*, 219–229.

Hofmann, A. (2003), Sampling mantle heterogeneity through oceanic basalts: Isotopes and trace elements, in *Treatise on Geochemistry, vol. 2: Mantle and Core*, edited by R. Carlson, pp. 61–101, Elsevier, Oxford, UK.

Homburg, J. M., G. Hirth, and P. B. Kelemen (2010), Investigation of the strength contrast at the Moho: A case study from the Oman ophiolite, *Geology*, *38*, 679–682.

Irvine, T. N. (1965), Chromian spinel as a petrogenetic indicator, part 1 theory, *Can. J. Earth Sci.*, *2*, 648–671.

Irvine, T. N. (1967), Chromian spinel as a petrogenetic indicator, part 2 petrologic applications, *Can. J. Earth Sci.*, *4*, 71–103.

Iwamori, H. (1993), Dynamic disequilibrium melting model with porous flow and diffusion-controlled chemical equilibrium, *Earth Plan. Sci. Lett.*, *114*, 301–313.

Iwamori, H. (1994), U-238–Th-230–Ra-226 and U-235–Pa-231 disequilibria produced by mantle melting with porous and channel flows, *Earth Plan. Sci. Lett.*, *125*, 1–16.

Iwamori, H., D. McKenzie, and E. Takahashi (1995), Melt generation by isentropic mantle upwelling, *Earth Plan. Sci. Lett.*, *134*, 253–266.

Johnson, K. T. M., H. J. B. Dick, and N. Shimizu (1990), Melting in the upper mantle: An ion microprobe study of diopsides in abyssal peridotites, *J. Geophys. Res.*, *95*, 2661–2678.

Jones, M. C., J. S. Marron, and S. J. Sheather (1996), A brief survey of bandwidth selection for density estimation, *J. Am. Stat. Assoc.*, *91*, 401–407.

Jull, M., P. B. Kelemen, and K. Sims (2002), Consequences of diffuse and channelled porous melt migration on Uranium series disequilibria, *Geochim. Cosmochim. Acta*, *66*, 4133–4148.

Juster, T. C., T. L. Grove, and M. R. Perfit (1999), Experimental constraints on the generation of FeTi basalts, andesites, and rhyodacites at the Galapagos spreading center, 85°W and 95°W, *J. Geophys. Res.*, *94*, 9251–9274.

Katz, R. F., M. Spiegelman, and C. H. Langmuir (2003), A new parameterization of hydrous mantle melting, *Geochem. Geophys. Geosys.*, *4*, doi:10.1029/2002GC000433.

Katz, R. F., M. Spiegelman, and B. Holtzman (2006), The dynamics of melt and shear localization in partially molten aggregates, *Nature*, *442*, 676–679.

Kelemen, P. B. (1986), Assimilation of ultramafic rock in subduction-related magmatic arcs, *J. Geology*, *94*, 829–843.

Kelemen, P. B. (1990), Reaction between ultramafic rock and fractionating basaltic magma I. phase relations, the origin of calc-alkaline magma series, and the formation of discordant dunite, *J. Petrol.*, *31*, 51–98.

Kelemen, P. B., and E. Aharonov (1998), Periodic formation of magma fractures and generation of layered gabbros in the lower crust beneath oceanic spreading centers, in *Faulting and Magmatism at Mid-Ocean Ridges*, *Geophysical Monograph*, vol. 106, edited by W. R. Buck, P. T. Delaney, J. A. Karson, and Y. Lagabrielle, pp. 267–289, American Geophysical Union, Washington, DC.

Kelemen, P. B., N. Shimizu, and V. J. M. Salters (1995), Extraction of mid-ocean ridge basalt from the upwelling mantle by focused flow of melt in dunite channels, *Nature*, *375*, 747–753.

Kelemen, P. B., G. Hirth, N. Shimizu, M. Spiegelman, and H. J. B. Dick (1997a), A review of melt migration processes in the adiabatically upwelling mantle beneath spreading ridges, *Philos. Trans. R. Soc. London*, *355*, 283–318.

Kelemen, P. B., K. Koga, and N. Shimizu (1997b), Geochemistry of gabbro sills in the crust-mantle transition zone of the Oman ophiolite: Implications for the origin of the oceanic lower crust, *Earth Plan. Sci. Lett.*, *146*, 475–488.

Kelemen, P. B., E. Kikawa, D. J. Miller, and et al. (2004), *Proceedings of the ocean drilling program, part A: Initial Reports*, vol. 209, Ocean Drilling Program, College Station, TX, doi:10.2973/odp.proc.ir.209.2004, 167 pp.

Kelemen, P. B., E. Kikawa, D. J. Miller, and et al. (2007), Leg 209 summary: Processes in a 20-km-thick conductive boundary layer beneath the Mid-Atlantic Ridge, 14^{c}*irc*-16^{c}*irc*N, in *Proc. ODP, Sci. Results*, vol. 209, edited by P. B. Kelemen, E. Kikawa, and D. J. Miller, pp. 1–33, Ocean Drilling Program, College Station, TX, doi:10.2973/odp.proc.sr.209.001.2007.

Kennedy, A. K., T. L. Grove, and R. W. Johnson (1990), Experimental and major element constraints on the evolution of lavas from Lihir Island, Papua-New-Guinea, *Contr. Min. Pet.*, *104*, 722–734.

Kinzler, R. J., and T. L. Grove (1992), Primary magmas of mid-ocean ridge basalts 1. experiments and methods, *J. Geophys. Res.*, *97*, 6885–6906.

Klein, E. M., and C. H. Langmuir (1987), Global correlations of ocean ridge basalt chemistry with axial depth and crustal thickness, *J. Geophys. Res.*, *92*, 8089–8115.

Klein, E. M., and C. H. Langmuir (1989), Local versus global variation in ocean ridge basaltic composition: A reply, *J. Geophys. Res.*, *94*, 4241–4252.

Klein, E. M., C. H. Langmuir, A. Zindler, and H. Staudigel (1988), Isotope evidence of a mantle convection boundary at the Australian-Antarctic discordance, *Nature*, *333*, 623–629.

Koga, K., P. B. Kelemen, and N. Shimizu (2001), Petrogenesis of the crust-mantle transition zone and the origin of lower crustal wehrlite in the Oman ophiolite, *Geochem. Geophys. Geosys.*, *2*, doi:10.1029/2000GC000132.

Korenaga, J., and P. B. Kelemen (1997), Origin of gabbro sills in the Moho transition zone of the Oman ophiolite: Implications for magma transport in the oceanic lower crust, *J. Geophys. Res.*, *102*, 27,729–27,749.

Korenaga, J., and P. B. Kelemen (1998), Melt migration through the oceanic lower crust: A constraint from melt percolation modeling with finite solid diffusion, *Earth Plan. Sci. Lett.*, *156*, 1–11.

Korenaga, J., and P. B. Kelemen (2000), Major element heterogeneity in the mantle source of the North Atlantic igneous province, *Earth Plan. Sci. Lett.*, *184*, 251–268.

Kushiro, I. (1968), Compositions of magmas formed by partial zone melting of the Earth's upper mantle, *J. Geophys. Res.*, *73*, 619–634.

Langmuir, C. H., E. M. Klein, and T. Plank (1992), Petrological systematics of mid-ocean ridge basalts: Constraints on melt generation beneath ocean ridges, in *Mantle flow and melt generation at mid-ocean ridges*, *Geophysical Monograph*, vol. 71, edited by J. Phipps Morgan, D. K. Blackman, and J. M. Sinton, pp. 183–280, American Geophysical Union, Washington, DC.

Le Mée, L., J. Girardeau, and C. Monnier (2004), Mantle segmentation along the Oman ophiolite fossil mid-ocean ridge, *Nature*, *432*, 167–172.

Le Pichon, X., J. Francheteau, and J. Bonnin (1973), *Plate Tectonics*, Elsevier, Amsterdam, The Netherlands, 300 pp.

Le Roux, V., J.-L. Bodinier, A. Tommasi, O. Alard, J.-M. Dautria, A. Vauchez, and A. J. V. Riches (2007), The Lherz spinel lherzolite: Refertilized rather than pristine mantle, *Earth Plan. Sci. Lett.*, *259*, 599–612.

Lehnert, K., Y. Su, C. H. Langmuir, B. Sarbas, and U. Nohl (2000), A global geochemical database structure for rocks, *Geochem. Geophys. Geosys.*, *1*, doi:10.1029/1999GC00026.

Lippard, S. J., A. W. Shelton, and I. G. Gass (1986), *The ophiolite of northern Oman*, *Geological Society of London Memoir*, vol. 11, Blackwell, Oxford, UK, 178 pp.

Lissenberg, C. J., and H. J. B. Dick (2008), Melt-rock reaction in the lower oceanic crust and its implications for the genesis of mid-ocean ridge basalt, *Earth Plan. Sci. Lett.*, *271*, 311–325.

Lizarralde, D., J. B. Gaherty, J. A. Collins, G. Hirth, and S. D. Kim (2004), Spreading-rate dependence of melt extraction at mid-ocean ridges from mantle seismic refraction data, *Nature*, *432*, 744–747.

Longhi, J. (1991), Comparative liquidus equilibria of hypersthene-normative basalts at low-pressure, *Am. Mineral.*, *76*, 785–800.

Longhi, J., D. Walker, and J. F. Hays (1978), Distribution of Fe and Mg between olivine and lunar basaltic liquids, *Geochim. Cosmochim. Acta*, *42*, 1545–1558.

Lundstrom, C. C., J. Gill, Q. Williams, and M. R. Perfit (1995), Mantle melting and basalt extraction by equilibrium porous flow, *Science*, *270*, 1958–1961.

McKenzie, D. (1984), The generation and compaction of partially molten rock, *J. Petrol.*, *25*, 713–765.

McKenzie, D., and M. J. Bickle (1988), The volume and composition of melt generated by extension of the lithosphere, *J. Petrol.*, *29*, 625–679.

Michael, P. J., and E. Bonatti (1985), Peridotite composition from the North Atlantic: Regional and tectonic variations and implications for partial melting, *Earth Plan. Sci. Lett.*, *73*, 91–104.

Monnier, C., J. Girardeau, L. Le Mée, and M. Polvé (2006), Along-ridge petrological segmentation of the mantle in the Oman ophiolite, *Geochem. Geophys. Geosys.*, *7*, doi: 10.1029/2006GC001320.

Navon, O., and E. Stolper (1987), Geochemical consequences of melt percolation: The upper mantle as a chromatographic column, *J. Geology*, *95*, 285–307.

Nicolas, A. (1989), *Structures of ophiolites and dynamics of oceanic lithosphere*, Kluwer Academic, Dordrecht, 367 pp.

Nicolas, A., and F. Boudier (2008), Large shear zones with no relative displacement, *Terra Nova*, *20*, 200–205.

Nicolas, A., F. Boudier, B. Ildefonse, and E. Ball (2000), Accretion of Oman and United Arab Emirates ophiolite- discussion of a new structural map, *Marine Geophys. Res.*, *21*, 147–179.

Niu, Y., and R. Batiza (1991), An empirical method for calculating melt compositions produced beneath mid-ocean ridges: Application to axis and off-axis (seamounts) melting, *J. Geophys. Res.*, *96*, 21,753–21,777.

Niu, Y., and R. Batiza (1993), Chemical variation trends at fast and slow spreading mid-ocean ridges, *J. Geophys. Res.*, *98*, 7887–7902.

Niu, Y., and R. Hekinian (1997a), Basaltic liquids and harzburgitic residues in the Garrett Transform: A case study at fast-spreading ridges, *Earth Plan. Sci. Lett.*, *146*, 243–258.

Niu, Y. L. (2004), Bulk-rock major and trace element compositions of abyssal peridotites: Implications for mantle melting, melt extraction and post-melting processes beneath mid-ocean ridges, *J. Petrol.*, *45*, 2423–2458.

Niu, Y. L., and R. Hekinian (1997b), Spreading-rate dependence of the extent of mantle melting beneath ocean ridges, *Nature*, *385*, 326–329.

O'Hara, M. J. (1977), Geochemical evolution during fractional crystallization of a periodically refilled magma chamber, *Nature*, *266*, 503–507.

Oxburgh, E. R., and D. L. Turcotte (1968), Mid-ocean ridges and geotherm distribution during mantle convection, *J. Geophys. Res.*, *73*, 2643–2661.

Pallister, J. S., and C. A. Hopson (1981), Samail ophiolite plutonic suite: Field relations, phase variation, cryptic variation and layering, and a model of a spreading ridge magma chamber, *J. Geophys. Res.*, *86*, 2593–2644.

Pallister, J. S., and R. J. Knight (1981), Rare-earth element geochemistry of the Samail ophiolite near Ibra, Oman, *J. Geophys. Res.*, *86*, 2673–2697.

Parman, S. W. (2007), Helium isotopic evidence for episodic mantle melting and crustal growth, *Nature*, *446*, 900–903.

Perugini, D., G. Poli, and R. Mazzuoli (2003), Chaotic advection, fractals and diffusion during mixing of magmas: Evidence from lava flows, *J. Volc. Geotherm. Res.*, *124*, 255–279.

Pollack, H. N., S. J. Hurter, and J. R. Johnson (1993), Heat flow from the Earth's interior: Analysis of the global data set, *Rev. Geophys.*, *31*, 267–280.

Project, B. V. S. (1981), *Basaltic Volcanism on the Terrestrial Planets*, Pergamon Press, Inc., New York, 1286 pp.

Putirka, K. D. (2005), Mantle potential temperatures at Hawaii, Iceland, and the mid-ocean ridge system, as inferred from olivine phenocrysts: Evidence for thermally driven mantle plumes, *Geochem. Geophys. Geosys.*, *6*, doi:10.1029/2005GC000915.

Putirka, K. D., M. Perfit, F. J. Ryerson, and M. G. Jackson (2007), Ambient and excess mantle temperatures, olivine thermometry, and active vs. passive upwelling, *Chem. Geol.*, *241*, 177–206.

Python, M., and G. Ceuleneer (2003), Nature and distribution of dykes and related melt migration structures in the mantle section of the Oman ophiolite, *Geochem. Geophys. Geosys.*, *4*, doi:10.1029/2002GC000354.

Python, M., G. Ceuleneer, and S. Arai (2008), Chromian spinels in mafic-ultramafic mantle dykes: Evidence for a two-stage melt production during the evolution of the Oman ophiolite, *Lithos*, *106*, 137–154.

Quick, J. E. (1981), The origin and significance of large, tabular dunite bodies in the Trinity peridotite, Northern California, *Contr. Min. Pet.*, *78*, 413–422.

Rabinowicz, M., and G. Ceuleneer (2005), The effect of sloped isotherms on melt migration in the shallow mantle: A physical and numerical model based on observations in the Oman ophiolite, *Earth Plan. Sci. Lett.*, *229*, 231–246.

Reisberg, L., and A. Zindler (1986), Extreme isotopic variability in the upper mantle: Evidence from Ronda, *Earth Plan. Sci. Lett.*, *81*, 29–45.

Roeder, P. L., and R. F. Emslie (1970), Olivine-liquid equilibrium, *Contr. Min. Pet.*, *19*, 275–289.

Rubin, K. H., and J. M. Sinton (2007), Inferences on mid-ocean ridge thermal and magmatic structure from MORB compositions, *Earth Plan. Sci. Lett.*, *260*, 257–276.

Rudge, J. (2008), Finding peaks in geochemical distributions: A re-examination of the Helium-continental crust correlation, *Earth Plan. Sci. Lett.*, *274*, 179–188.

Saal, A., S. Hart, N. Shimizu, E. Hauri, and G. Layne (1998), Pb isotopic variability in melt inclusions from oceanic island basalts, Polynesia, *Science*, *282*, 1481–1484.

Saal, A., E. Takazawa, F. Frey, N. Shimizu, and S. R. Hart (2001), Re-Os isotopes in the Horoman peridotite: Evidence for refertilization?, *J. Petrol.*, *42*, 25–37.

Schilling, J.-G., M. Zajac, R. Evans, T. Johnston, W. White, J. D. Devine, and R. Kingsley (1983), Petrological and geochemical variations along the Mid-Atlantic Ridge from 29°N to 73°N, *Am. J. Sci.*, *283*, 510–586.

Scott, D. W. (1992), *Multivariate Density Estimation: Theory, Practice, and Visualization*, John Wiley & Sons, New York, 376 pp.

Seyler, M., and E. Bonatti (1997), Regional-scale melt-rock interaction in lherzolitic mantle in the Romanche Fracture Zone (Atlantic Ocean), *Earth Plan. Sci. Lett.*, *146*, 273–287.

Shaw, D. M. (1970), Trace element fractionation during anatexis, *Geochim. Cosmochim. Acta*, *34*, 237–243.

Sheather, S. J., and M. C. Jones (1991), A reliable data-based bandwidth selection method for kernel density estimation, *J. R. Stat. Soc., Ser. B Stat. Methodol.*, *53*, 683–690.

Shen, Y., and D. W. Forsyth (1995), Geochemical constraints on initial and final depths of melting beneath mid-ocean ridges, *J. Geophys. Res.*, *100*, 2211–2237.

Silverman, B. (1986), *Density Estimation for Statistics and Data Analysis*, Chapman and Hall, London, 175 pp.

Sleep, N. H. (1975), Formation of oceanic crust: Some thermal constraints, *J. Geophys. Res.*, *80*, 4037–4042.

Sobolev, A., A. Hofmann, and I. Nikogosian (2000), Recycled oceanic crust observed in "ghost plagioclase" within the source of Mauna Loa lavas, *Nature*, *404*, 986–990.

Sparks, D. W., and E. M. Parmentier (1991), Melt extraction from the mantle beneath spreading centers, *Earth Plan. Sci. Lett.*, *105*, 368–377.

Spiegelman, M. (1993), Physics of melt extraction – theory, implications and applications, *Philos. Trans. R. Soc. London*, *342*, 23–41.

Spiegelman, M. (1996), Geochemical consequences of melt transport in 2-D: The sensitivity of trace elements to mantle dynamics, *Earth Plan. Sci. Lett.*, *139*, 115–132.

Spiegelman, M., and T. Elliott (1993), Consequences of melt transport for Uranium series disequilibrium in young lavas, *Earth Plan. Sci. Lett.*, *118*, 1–20.

Spiegelman, M., and P. B. Kelemen (2003), Extreme chemical variability as a consequence of channelized melt transport, *Geochem. Geophys. Geosys.*, *4*, doi:10.1029/2002GC000336.

Spiegelman, M., and P. Kenyon (1992), The requirements for chemical disequilibrium during magma migration, *Earth Plan. Sci. Lett.*, *109*, 611–620.

Suhr, G., E. Hellebrand, J. E. Snow, H. A. Seck, and A. W. Hofmann (2003), Significance of large, refractory dunite bodies in the upper mantle of the Bay of Islands ophiolite, *Geochem. Geophys. Geosys.*, *4*, doi:10.1029/2001GC000277.

Takazawa, E., T. Okayasu, and K. Satoh (2003), Geochemistry and origin of the basal lherzolites from the northern Oman ophiolite (northern Fizh block), *Geochem. Geophys. Geosys.*, *4*, doi:10.1029/2001GC000232.

Tamura, A., and S. Arai (2006), Harzburgite-dunite-orthopyroxenite suite as a record of supra-subduction zone setting for the Oman ophiolite mantle, *Lithos*, *90*, 43–56.

Tarboton, D. G. (1997), A new method for the determination of flow directions and upslope areas in grid digital elevation models, *Water Resources Res.*, *33*, 309–319.

Tarboton, D. G., R. L. Bras, and I. Rodriguez-Iturbe (1991), On the extraction of channel networks from digital elevation data, *Hydrol. Processes*, *5*, 81–100.

Tartarotti, P., S. Susini, P. Nimis, and L. Ottolini (2002), Melt migration in the upper mantle along the Romanche Fracture Zone (equatorial Atlantic), *Lithos*, *63*, 125–149.

Tatsumoto, M. (1966), Genetic relations of oceanic basalts as indicated by Lead isotopes, *Science*, *153*, 1094–1101.

Tatsumoto, M., C. Hedge, and A. E. J. Engel (1965), Potassium, Rubidium, Strontium, Thorium, Uranium, and the ratio of Strontium-87 to Strontium-86 in oceanic tholeiitic basalt, *Science*, *150*, 886–888.

Thy, P., C. E. Lesher, T. F. D. Nielsen, and C. K. Brooks (2006), Experimental constraints on the Skaergaard liquid line of descent, *Lithos*, *92*, 154–180.

Tormey, D. R., T. L. Grove, and W. B. Bryan (1987), Experimental petrology of normal MORB near the Kane Fracture Zone: 22°-25°N, Mid-Atlantic Ridge, *Contr. Min. Pet.*, *96*, 121–139.

Ulmer, P. (1989), The dependence of the Fe^{2+}-Mg cation-partitioning between olivine and basaltic liquid on pressure, temperature and composition – an experimental study to 30 kbars, *Contr. Min. Pet.*, *101*, 261–273.

Walker, D., T. Shibata, and S. E. DeLong (1979), Abyssal tholeiites from the Oceanographer Fracture Zone II. phase equilibria and mixing, *Contr. Min. Pet.*, *70*, 111–125.

Wark, D. A., C. A. Williams, E. B. Watson, and J. D. Price (2003), Reassessment of pore shapes in microstructurally equilibrated rocks, with implications for permeability of the upper mantle, *J. Geophys. Res.*, *108*, doi:10.1029/2001JB001575.

Weaver, J. S., and C. H. Langmuir (1990), Calculation of phase equilibrium in mineral-melt systems, *Comput. Geosci.*, *16*, 1–19.

White, R. S., T. A. Minshull, M. J. Bickle, and C. J. Robinson (2001), Melt generation at very slow-spreading oceanic ridges: Constraints from geochemical and geophysical data, *J. Petrol.*, *42*, 1171–1196.

Yang, H.-J., R. J. Kinzler, and T. L. Grove (1996), Experiments and models of anhydrous, basaltic olivine-plagioclase-augite saturated melts from 0.001 to 10 kbar, *Contr. Min. Pet.*, *124*, 1–18.

Yoder, H. S., Jr., and C. E. Tilley (1962), Origin of basalt magmas: An experimental study of natural and synthetic rock systems, *J. Petrol.*, *3*, 342–532.

Zindler, A., and S. Hart (1986), Chemical geodynamics, *Annu. Rev. Earth Planet. Sci.*, *14*, 493–571.

Appendix A

Supplementary Material for Chapter 2

A.1 A Simple, 1-D Porous Flow Model for Evaluating Reaction versus Advection Time Scales Beneath Ocean Ridges

We begin by calculating a 1-D 'mid-ocean ridge' temperature field for the on-axis depth interval between the initial depth of melting ($z = z_{max}$) and the sea floor ($z = 0$) using a very similar approach to *Sparks and Parmentier* (1991). We apply separate energy conservation equations to a "shallow and cold" subdomain and to a "deep and partially molten" subdomain, which are defined to be, respectively, above and below z_{melt}, the intersection depth of the geotherm and peridotite solidus (these subdomains correspond with Regions A and B as defined by *Sparks and Parmentier* (1991), with corresponding energy conservation equations given in their Equation 12). Unlike *Sparks and Parmentier* (1991), we do not extend our model to depths exceeding that of the onset of melting.

To facilitate our calculation, we have constructed a very simple approximate peridotite melting phase diagram using a best-fit line to the preferred solidus of *Hirschmann* (2000) to represent the onset of melting and by specifying the liquidus to be parallel to the solidus with a ΔT = 600 °C. The melt fraction F as a function of temperature and pressure is then given by:

$$F(T, P) = 0.0017°C^{-1}T - 0.1958GPa^{-1}P - 1.8805 \tag{A.1}$$

If we approximate the melting rate, Γ, characterizing decompression melting of peridotite with density ρ that is upwelling at velocity W as:

$$\Gamma = -\rho W \left(\frac{\partial F}{\partial P}\frac{\partial P}{\partial z} + \frac{\partial F}{\partial T}\frac{\partial T}{\partial z} \right), \tag{A.2}$$

where derivatives of the melt fraction F with respect to temperature and pressure are taken from Equation A.1, and if we adopt the further approximation for the latent heat of fusion, H_{fus} during melting:

$$T\Delta S = H_{fus} = const, \tag{A.3}$$

the dimensional energy conservation equations for the "shallow" and "deep" subdomains of our calculation may be expressed as (*McKenzie* (1984), App. A):

$$\left.\begin{array}{ll} \kappa\frac{\partial^2 T}{\partial z^2} + W\frac{\partial T}{\partial z} = 0 & \\ \kappa\frac{\partial^2 T}{\partial z^2} + W\left(1 + \frac{H_{fus}}{c_p}\frac{\partial F}{\partial T}\right)\frac{\partial T}{\partial z} + W\frac{H_{fus}}{c_p}\frac{\partial F}{\partial P}\frac{\partial P}{\partial z} = 0 & \end{array}\right\} \begin{array}{l} z < z_{melt} \\ z > z_{melt} \end{array} \tag{A.4}$$

where κ is the thermal diffusivity, and c_p is the specific heat capacity of peridotite. Calculations presented in Figure A-2 use the following parameter values: $H_{fus} = 5 \times 10^5$ J/kg, $\kappa = 10^{-6} m^2/s$, and $c_p = 10^3$ J/(kg K). The approximations given by Equations A.1-A.3 lead to a constant coefficient ordinary differential equation (ODE) (Equation A.4) and are adopted to minimize computational complexity (although these approximations are not fundamental to our model).

The "shallow" subdomain is governed by advection-diffusion, while the conservation equation for the "deep" subdomain additionally accounts for the latent heat of melting. In the "deep", partially molten region, the melt is assumed to be in local thermal equilibrium with the solid (reasonable for porous flow of a volumetrically small melt fraction), with the implication that the melt phase does not advect sufficient energy to modify the solid-state geotherm directly and only affects the temperature field of the solid mantle by undergoing phase transition (melting or crystallization).

With reference to the seafloor temperature T_{surf} and solidus temperature $T_{sol}(z)$, we introduce non-dimensional depth z' and temperature T':

$$z = z' z_{max} \tag{A.5}$$

$$T = T_{surf} + T'(T_{sol}(z_{max}) - T_{surf}) \tag{A.6}$$

substituting these non-dimensional variables into Equations A.4 and dropping primes, we have:

$$\left.\begin{array}{ll} \frac{1}{Pe}\frac{\partial^2 T}{\partial z^2} + \frac{\partial T}{\partial z} = 0 & \\ \frac{1}{Pe}\frac{\partial^2 T}{\partial z^2} + \left(1 + M\frac{\partial F}{\partial T}\right)\frac{\partial T}{\partial z} + M\frac{\partial F}{\partial P}\frac{\partial P}{\partial z} = 0 & \end{array}\right\} \begin{array}{l} z < z_{melt} \\ z > z_{melt} \end{array} \tag{A.7}$$

where the non-dimensional numbers Pe and M are are given by:

$$Pe = \frac{W z_{max}}{\kappa} \tag{A.8}$$

$$M = \frac{H_{fus}}{c_p \Delta T} \tag{A.9}$$

The Peclet number Pe characterizes the relative importance of advection and diffusion, and therefore controls the location of z_{melt}, while the "Melting number" M controls the extent to which temperatures in the partially molten region can deviate from the solidus.

Equation A.7 is subject to the following boundary conditions:

$$T_{shallow}(z=0) = 0 \tag{A.10}$$

$$T_{deep}(z=1) = 1 \tag{A.11}$$

$$T_{shallow}(z=z_{melt}) = T_{deep}(z=z_{melt}) \tag{A.12}$$

$$\frac{\partial}{\partial z} T_{shallow}(z=z_{melt}) = \frac{\partial}{\partial z} T_{deep}(z=z_{melt}) \tag{A.13}$$

Thus, the problem consists of solving two linear, 2nd order ODEs with constant coefficients:

$$\left.\begin{array}{ll} c_1 \frac{\partial^2 T}{\partial z^2} + \frac{\partial T}{\partial z} = 0 & \\ c_1 \frac{\partial^2 T}{\partial z^2} + c_2 \frac{\partial T}{\partial z} + c_3 = 0 & \end{array}\right\} \begin{array}{l} z < z_{melt} \\ z > z_{melt} \end{array} \tag{A.14}$$

The coefficients are given by:

$$c_1 = \frac{1}{Pe} \tag{A.15}$$

$$c_2 = 1 + M \frac{\partial F}{\partial T} \tag{A.16}$$

$$c_3 = M \frac{\partial F}{\partial P} \frac{\partial P}{\partial z} \tag{A.17}$$

These equations have solutions of the form:

$$\left.\begin{array}{l} T_{shallow}(z) = A + B e^{-\frac{1}{c_1} z} \\ T_{deep}(z) = -C \frac{c_1}{c_2} e^{-\frac{c_2}{c_1} z} - \frac{c_3}{c_2} z + D \end{array}\right\} \begin{array}{l} z < z_{melt} \\ z > z_{melt} \end{array} \tag{A.18}$$

where A-D are undetermined coefficients of integration. Application of the boundary condi-

tions yields an expression for each of these coefficients as a function of z_{melt}:

$$C(z_{melt}) = \frac{-\frac{\frac{c_1 c_3}{c_2}}{e^{-\frac{1}{c_1}z_{melt}}} - \frac{\frac{c_3}{c_2}(1-z_{melt})+1}{1-e^{-\frac{1}{c_1}z_{melt}}}}{\frac{\frac{c_1}{c_2}\left(e^{-\frac{c_2}{c_1}}-e^{-\frac{c_2}{c_1}z_{melt}}\right)}{1-e^{-\frac{1}{c_1}z_{melt}}} - \frac{c_1 e^{-\frac{c_2}{c_1}z_{melt}}}{e^{-\frac{1}{c_1}z_{melt}}}} \tag{A.19}$$

$$A(z_{melt}) = \frac{C(z_{melt})\frac{c_1}{c_2}\left(e^{-\frac{c_2}{c_1}} - e^{-\frac{c_2}{c_1}z_{melt}}\right) + \frac{c_3}{c_2}(1-z_{melt}) + 1}{1-e^{-\frac{1}{c_1}z_{melt}}} \tag{A.20}$$

$$D(z_{melt}) = 1 + \frac{c_3}{c_2} + C(z_{melt})\frac{c_1}{c_2}e^{-\frac{c_2}{c_1}} \tag{A.21}$$

$$B(z_{melt}) = -A(z_{melt}) \tag{A.22}$$

The location of z_{melt} corresponds physically with the shallowest depth at which melt can exist stably. It should therefore be true that:

$$T_{shallow}(z_{melt}) = T_{deep}(z_{melt}) = T_{sol}(z_{melt}) \tag{A.23}$$

We use a linear expression to approximate the peridotite solidus as a function of depth:

$$T_{sol}(z) = b\frac{\partial P}{\partial z}z + c \tag{A.24}$$

where b = 118 °C/GPa and c = 1128°C, obtained from a linear best-fit to the peridotite solidus of *Hirschmann* (2000). The value of z_{melt} is given by the solution to:

$$T_{shallow}(z) - T_{sol}(z) = 0 \tag{A.25}$$

Once z_{melt} is determined, $T(z)$ may be calculated from Equation A.18.

With $T(z)$ known, $F(z)$ is determined using Equation A.1. We then calculate the porosity field, melt and solid velocities, denoted here as ϕ, w and W, respectively, assuming melt transport via Darcy flow. In the case of a 'simplest' 1-D steady state column model, conservation of mass of melt and solid phases, together with Darcy's law, yields the following

system (c.f., *Spiegelman and Elliott* (1993)):

$$w(z) = \frac{\rho_s F(z)}{\rho_f \phi(z)} W_o \tag{A.26}$$

$$W(z) = \frac{1 - F(z)}{1 - \phi(z)} W_o \tag{A.27}$$

$$\phi(z) \left(\frac{w(z) - W(z)}{W_o} \right) = \frac{d^2 \Delta\rho g}{c\mu W_o} \phi(z)^n \left(1 - \phi(z)\right) \tag{A.28}$$

where d is the typical inter-conduit distance, ρ_s and ρ_f represent the solid and melt densities, g is the gravitational acceleration, μ the melt viscosity, and c a constant in the porosity-permeability relationship. A_o may be defined as:

$$A_o = \frac{d^2 \Delta\rho g}{c\mu W_o} \tag{A.29}$$

Given the uncertainty in the porosity-permeability relationships relevant to natural partially molten systems, A_o may be independently calibrated as follows (*Spiegelman and Elliott* (1993)):

$$A_o = \frac{\left(\frac{\rho_s F_{max}}{\rho_f} - \frac{\phi_o (1 - F_{max})}{(1 - \phi_o)} \right)}{\phi_o^n \left(1 - \phi_o\right)} \tag{A.30}$$

Where F_{max} is the maximum F found in the column, and ϕ_o is the porosity occurring at this value of F. In this approach, ϕ_o must be determined from external information. In this study we use a value of 0.01, consistent with recent experimental and field data on permeability (e.g., *Wark et al.* (2003)), and melt generation of 1% per 3 km upwelling, for slow spreading ridges and passive mantle upwelling. For fast spreading ridges, a value of 0.02 might represent a better choice for ϕ_o. Using equations (A.26-A.30), ϕ(z) can be found from the roots of the following polynomial:

$$A_o \phi(z)^n \left(1 - \phi(z)\right)^2 + \phi(z) \left(1 + \left(\frac{\rho_s}{\rho_f} - 1 \right) F(z) \right) - \frac{\rho_s}{\rho_f} F(z) = 0 \tag{A.31}$$

Given ϕ(z), $w(z)$ and $W(z)$ are then determined by equations (A.26) and (A.27).

Based on the simple 1-D mid-ocean ridge model we have just developed, we consider the evolution of a melt volume that is initially located at depth z_{init}, and that is migrating towards the surface with velocity $w(z)$ within a cylindrical conduit of radius $r(z)$. Given the porosity ϕ(z), and typical distance between conduits d (to represent grain-scale porous flow,

our calculations use $d = 1$ mm), the radius of the conduit is:

$$r(z) = \sqrt{\frac{\phi(z)d^2}{\pi}} \tag{A.32}$$

We consider our initial volume of upwelling melt as a thermodynamic system of mass M_{sys}. As cation diffusion occurs between the melt and surrounding rock, the surrounding mantle rock is progressively 'incorporated' over time, resulting in an increased in mass and volume of the thermodynamic system. The time available for reaction is given by:

$$\partial t(z) = \frac{\partial z}{w(z)} \tag{A.33}$$

$$t(z) = \int_z^{z_{init}} \partial t(z) dz \tag{A.34}$$

The distance from the center of the melt volume to the edge of the thermodynamic system, $R(z)$, is (with the assumption of isotropic diffusivity D_{FeMg} within the solid mantle material) given by:

$$R(z) = r(z) + \sqrt{D_{FeMg} t(z)} \tag{A.35}$$

$M_{sys}(z)$, as a fraction of initial system mass, can therefore be calculated given $w(z)$ (and thus $t(z)$) by:

$$\begin{aligned} M_{sys}(z) &= \frac{\rho_s \pi \left(R(z)^2 - r(z)^2\right) + \rho_f \pi r(z)^2}{\rho_f \pi r(z)^2} \\ &= \frac{\rho_s}{\rho_f} \left(\frac{2\sqrt{D_{FeMg} t(z)}}{r(z)} + \frac{D_{FeMg} t(z)}{r(z)^2} \right) + 1 \end{aligned} \tag{A.36}$$

The spatial and temporal derivatives of M_{sys} may be calculated numerically using a discretization such as:

$$\frac{\partial M_{sys}}{\partial z}(z_i) = \frac{M_{sys}(z_i) - M_{sys}(z_{i+1})}{z_{i+1} - z_i} \tag{A.37}$$

$$\frac{\partial M_{sys}}{\partial t}(z_i) = \frac{\partial M_{sys}}{\partial z}(z_i) \frac{\partial z}{\partial t(z_i)} \tag{A.38}$$

The rate of reaction versus cooling, as a function of depth, $\Re$(z) in grams added/$^\circ C$ may then be calculated by:

$$\Re(z) = \frac{\frac{\partial M_{sys}}{\partial t}(z)}{\frac{\partial T}{\partial t}(z)} \tag{A.39}$$

It is clear from the results of such calculations, discussed in the text and illustrated in

Figure A-2 of this Appendix, that magma upwelling by grain-scale porous flow through the thermal boundary layer of a mid-ocean ridge should experience extensive reactive crystallization due to Fe-Mg cation exchange.

A.2 pMELTS Input

The following input file, saved with a '.melts' extension generates the 3g/°C reactive crystallization end-member from the 'hot mantle' primitive melt composition discussed in the text:

```
Title: Ex_KG_tbl4_1_3gC_ReactXtln
Initial Composition: SiO2 47.7366
Initial Composition: TiO2 0.8089
Initial Composition: Al2O3 16.9775
Initial Composition: Fe2O3 1.2487
Initial Composition: FeO 7.1555
Initial Composition: MgO 12.3836
Initial Composition: CaO 12.0840
Initial Composition: Na2O 1.5479
Initial Composition: K2O 0.0399
Initial Composition: H2O 0.0200
Initial Temperature: 1310.00
Final Temperature: 1190.00
Initial Pressure: 6000.00
Final Pressure: 6000.00
Increment Temperature: 5.00
Increment Pressure: 0.00
dp/dt: 0.00
log fo2 Path: FMQ
Assimilant: Temperature 1240.00
Assimilant: Mass 375.00
Assimilant: Increments 25.00
Assimilant: Liquid Mass 100.00
Assimilant: Units Wt %
Assimilant: SiO2 43.89
Assimilant: TiO2 0.00
Assimilant: Al2O3 1.19
```

```
Assimilant: Fe2O3 0.00
Assimilant: Cr2O3 0.00
Assimilant: FeO 8.27
Assimilant: MnO 0.00
Assimilant: MgO 45.50
Assimilant: NiO 0.00
Assimilant: CoO 0.00
Assimilant: CaO 1.14
Assimilant: Na2O 0.02
```

Supplementary Figures

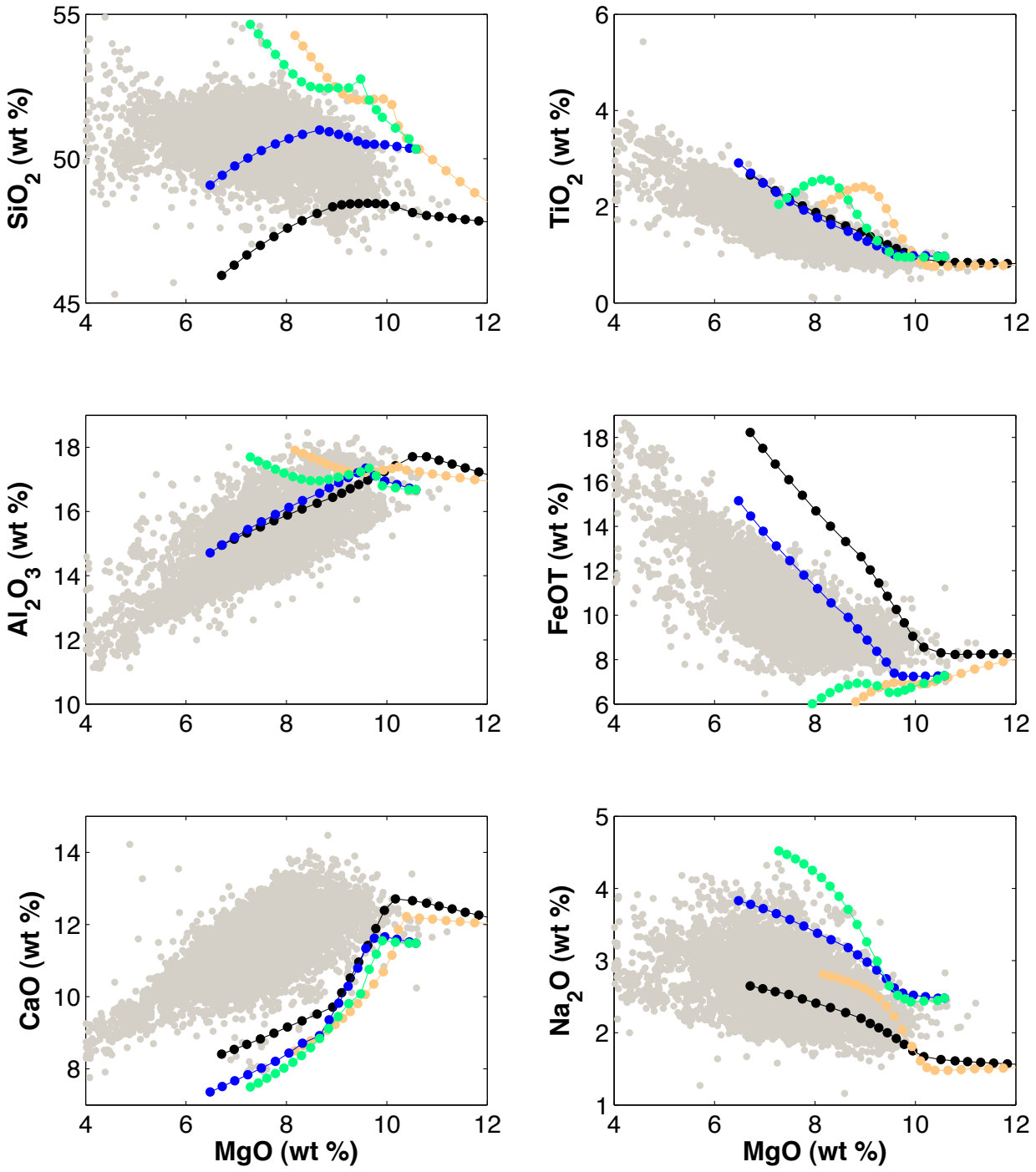

Figure A-1: Illustration of the 0.6 GPa end-member reactive and fractional liquid lines of descent predicted using pMELTS. Color scheme as in Figure 2-2 of the main text.

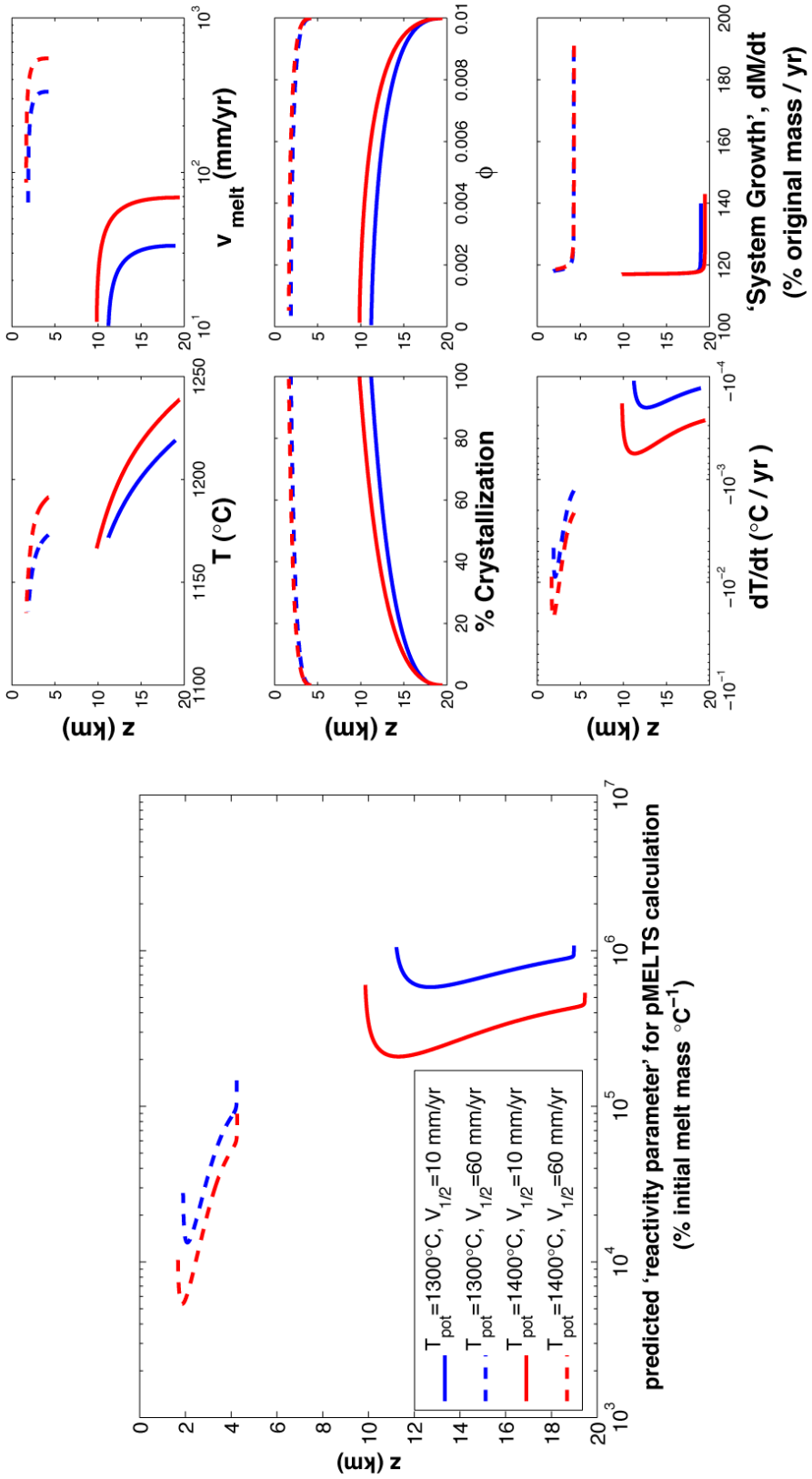

Figure A-2: Caption given on next page.

Figure A-2: (left) Illustration of the range of reactivity parameter values (corresponding to the mass of peridotite added per C cooling in corresponding pMELTS calculations) predicted by a 1-D steady state model of grain-scale porous flow beneath a mid-ocean ridge for mantle potential temperatures T_{pot} = 1300°C and 1400°C and upwelling velocities of 10 and 60 mm/yr. These models are meant to roughly correspond to possible Mid-Atlantic Ridge (solid lines) or East-Pacific Rise (dashed lines) mantle geotherms spanning a range of possible mantle potential temperatures (colors). Although this simple model does not explicitly describe the crust-mantle boundary, it is possible to meaningfully calculate reactivity parameter values for the potentially reactive depth interval between the depth of final melting (onset of crystallization) and the intersection of geotherm and basalt solidus. This is the depth interval at which crystallization from a thermodynamically stable melt phase may occur. The reactivity parameter is predicted to be very large for all depths in this interval. (right) A summary of physical properties calculated for the depth interval between onset of crystallization and the intersection of geotherm and solidus is shown in this series of panels.

Appendix B

Supplementary Material for Chapter 3

B.1 PCA and the SVD

Principal Component Analysis (PCA, also known as Empirical Orthogonal Function analysis) is a widely used technique for analyzing multivariate data sets, often leading to simplified visualization and analysis. The goals of PCA are 1) to find the set of orthogonal components best aligned with the various directions of maximum uncorrelated variability in a given data set, and 2) to evaluate the relative importance of these components. Using the results of PCA, data may be projected into lower dimensional subspaces spanned by only the most important independent components. This creates a more convenient, (often considerably) reduced dimensionality representation of a multivariate dataset with minimal loss of any information contained in the variability. The Singular Value Decomposition (SVD) provides a versatile method for exploring the mathematical structure of any arbitrary matrix. For purposes of PCA, the SVD yields component vectors that are optimally aligned with axes of maximum, independent variability in the rows and columns of the input matrix, as well as information about the components' relative significance. The SVD is a robust technique applicable to any data matrix that is free of data gaps or NaNs. While the SVD is very similar to PCA in its output, it is a distinct operation equivalent to PCA only when applied to a centered (demeaned) data matrix. PCA and the SVD also differ in computational method: PCA can be carried out through explicit evaluation of the sample covariance matrix, while the SVD avoids this. In practice, PCA using the SVD is perhaps the most convenient and computationally efficient method, particularly in the case of large data sets.

B.1.1 The PCA/SVD Method (+ Implementation in MATLAB)

This section describes the method of PCA, via the SVD, given some data matrix of interest. In the following discussion, the $m \times n$ data matrix, A, is assumed to consist of m rows each

representing a sample with n variables (columns). Prior to performing the SVD, each column is normalized by its mean value, as the dominant component of an unnormalized data set would simply reflect the data mean. Further normalization, e.g. by the standard deviation of each variable is usually also desirable. The SVD of the normalized data matrix, A^* is given by:

$$A^* = U\Sigma V^T \tag{B.1}$$

The n rows of V^T (columns of V) formally define an orthonormal basis spanning the rowspace of A^*, with each column corresponding to one of the principal components aligned with some axis of variability in the data. These principal components correspond to the eigenvectors of the covariance matrix of A^* (i.e., $A^{*T}A^*$). Σ is a diagonal matrix containing the singular values, $\sigma_{i,i}$, each indicating the relative importance of the corresponding principal component. $\Sigma^T\Sigma$ corresponds to the diagonal matrix of eigenvalues of the covariance matrix. The fraction of variability explained by principle component i is given by:

$$X_i = \frac{\sigma_{i,i}^2}{\sum_i \sigma_{i,i}^2} \tag{B.2}$$

The n columns of U each contain the expansion coefficients, also known as scores, defining values for the m samples along each principle component axis. The columns of U also define the eigenvectors of the matrix A^*A^{*T}.

The following MATLAB code implements a rapid calculation of principal components and their relative importance for any data matrix, including matrices with large sample sizes:

```
% PCA of data matrix M by SVD (rows:samples, cols:variables)
% --------------------------

% normalize M
means=nanmean(M);
stdevs=nanstd(M);
M_norm=M-repmat(means,size(M,1),1); % remove mean from each column
M_norm=M_norm./repmat(stdevs,size(M,1),1); % normalize by st.dev. of each column

% calculate economy-sized svd
[U,S,V]=svd(M_norm,0); % columns of V are the principal components

% calculate scores for each data point and relative importance of each component
```

```
C=U*S; % scores are weighted by singular values
D=S'*S; D=D(1:5,1:5); % identify 5 most important eigenvalues
pervar=diag(D)./trace(D); % calculate their importance
```

B.1.2 Geologic Interpretation of Results

The transformation of data into the orthogonal principal component space maintains the geometric structure in the data, such as distances and angles. However, geologic interpretation is often not straightforward, even after the transformation. The principal component axes do not necessarily correspond with any single process, e.g. a liquid line of descent or a mixing line between isotopic end-members. Figure B-1 illustrates three 'pathological' examples in which variability sources cannot be cleanly decomposed along PC axes.

B.2 Probability Density Estimation and the Bandwidth Selection Problem

For this study, we seek a flexible, quantitative method for evaluating the full statistical distribution of MORB variability. In general, starting from a data set of n observations $[\vec{X_1}, ...\vec{X_n}]$, each comprising d attributes, we seek to estimate the probability density $f(\vec{x})$ from which our data was generated. In the case of geochemical data, this probability density corresponds to an ideal, complete statistical description of geochemical variability within a region of interest. The objective of recovering $f(\vec{x})$ is well served using the empirical approach of kernel-smoothed probability density estimation. We here employ the most basic multivariate kernel density estimator, the product kernel, $\hat{f}_{pke}(\vec{x})$, given by:

$$\hat{f}_{pke}(\vec{x}) = \frac{1}{nh_1...h_d} \sum_{i=1}^{n} \left[\prod_{j=1}^{d} K\left(\frac{x_j - X_{ij}}{h_j} \right) \right] \tag{B.3}$$

where K is a kernel function, h_k denotes the smoothing bandwidth, and i tracks components while j tracks data attributes. The multivariate kernel function at each data point is simply the product of univariate kernels corresponding to each data dimension. We here employ a Gaussian kernel function:

$$K(t) = \frac{1}{\sqrt{2\pi}} \exp\left(\frac{-t^2}{2} \right) \tag{B.4}$$

The most critical factor in achieving a good estimate of the probability density $f(\vec{x})$ is the

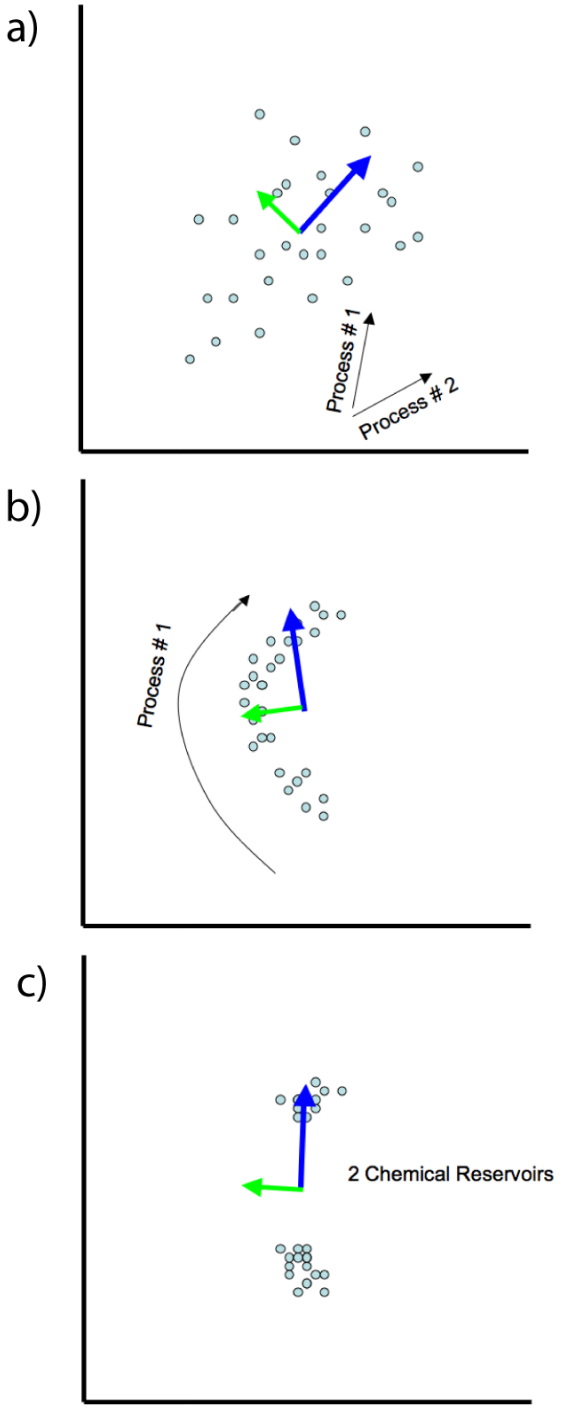

Figure B-1: Illustration of three cases in which principal components do not correspond to variability generated by geological processes a) 2 processes creating non-perpendicular variability b) one process creating non-linear variability c) sampling of bimodal distribution. Colored arrows correspond to the first (blue) and second (green) principal components from PCA of these data.

selection of an appropriate smoothing bandwidth. This parameter is similar to the binning interval of a histogram, in that a large kernel bandwidth effectively provides a high degree of smoothing in the apparent distribution of variability, while a small bandwidth allows more data features such as secondary peaks to become visible. Choosing an inappropriately large bandwidth could 'blur' out secondary peaks or other data features of interest (essentially a 'Type II error'), while a bandwidth that is too small can lead to the appearance of spurious additional structure in the probability density estimate (a 'Type I error'). Thus, an optimal bandwith is desired such that $\hat{f}_{pke}(\vec{x})$ approximates $f(\vec{x})$ as closely as possible. A number of approaches to bandwidth selection have emerged from the statistical literature (e.g. *Silverman*, 1986; *Sheather and Jones*, 1991; *Jones et al.*, 1996). Although these approaches vary in complexity, they share a key property in that the optimal smoothing bandwidth is dependent on the available sample size. This point is of central importance to the present study. If the assumption that the n available observations are independent realizations from the underlying distribution is violated (as we have demonstrated is the case in the PetDB MORB compilation), the *effective* sample size (the number of independent samples) will be smaller than the apparent sample size. Failure to account for this will lead to a systematic underestimation of the smoothing bandwidth appropriate to a given data set, regardless of the specific bandwidth selection algorithm used. Correspondingly, probability density estimation on data uncorrected for sampling bias can be susceptible to revealing geologically spurious –if not statistically spurious– additional structure. The magnitude of this problem, of course, depends on the reduction in effective sample size due to sampling bias. In the analysis of MORB global systematics, compositional clustering in spatially associated samples can potentially decrease the effective sample size by more than an order of magnitude, depending on the subjective judgements of sample independence supplied by the investigator. Application of feature significance tests (e.g., *Chaudhuri and Marron*, 1999) can also lead to spurious detection of 'significant' variability features, as these too are rooted in the assumption of data independence. The role of bandwidth selection and the topic of feature 'significance' has been previously discussed in the context of an analysis of Helium isotope ratios in ocean island basalts (*Rudge*, 2008). Appendix A of that study develops the arguments applied here in additional mathematical detail. In the present study, the bandwidths h_k required for each univariate kernel were determined using the data-driven bandwidth selector of Z. I. Botev ("A Novel Nonparametric Density Estimator", Technical Report, The University of Queensland, manuscript available at `http://espace.library.uq.edu.au/eserv/UQ:12535/Nonparametric_estimation.pdf`). Bandwidths selected by this method correspond closely to those using the method of *Sheather and Jones* (1991). For additional information about multivariate probability density estimation, c.f. *Scott* (1992).

B.3 A Sparsity Diagram of PetDB

See Figure B-2.

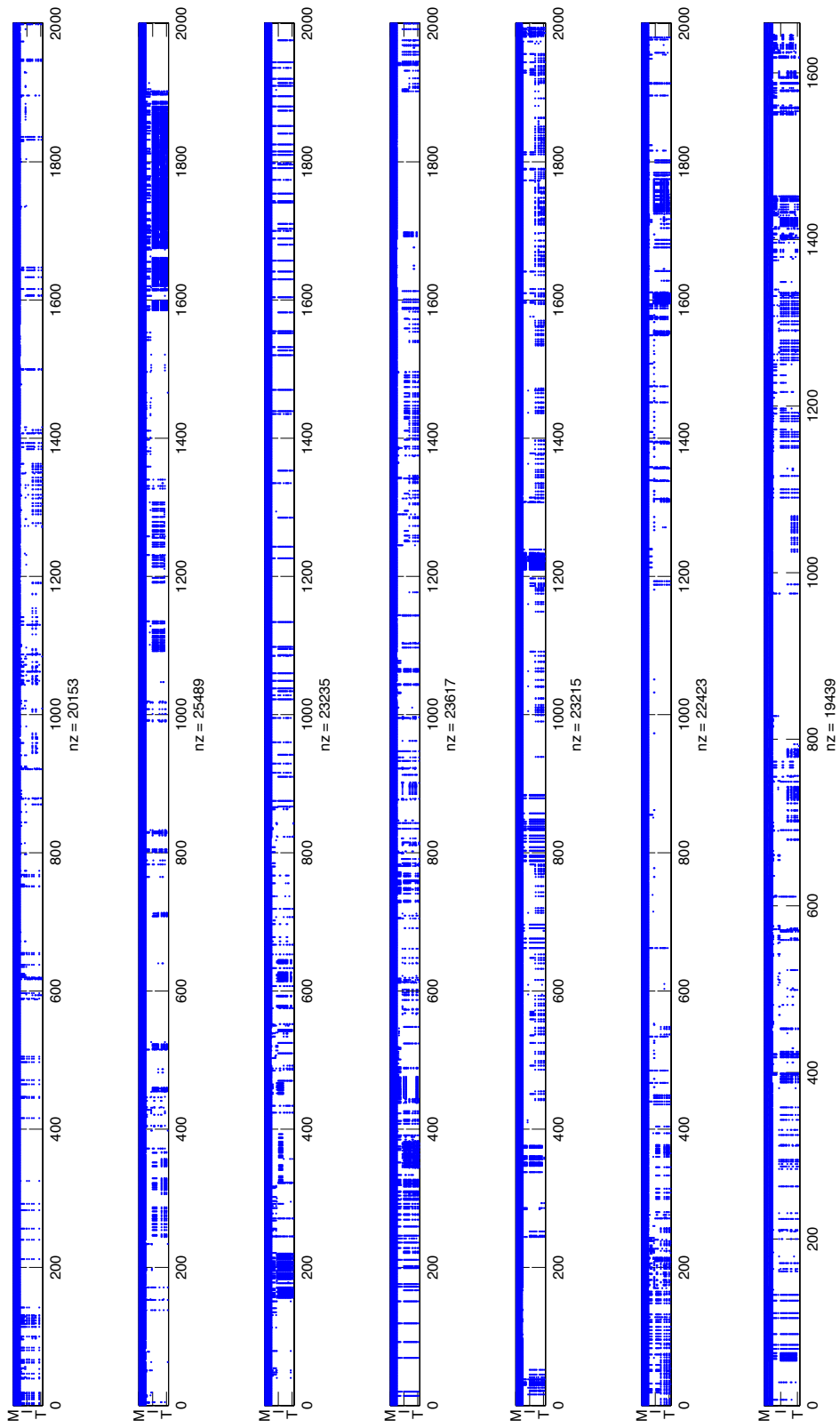

Figure B-2: Caption given on next page.

Figure B-2: Sparsity diagram depicting the simultaneous availability of data on major element (M), trace element (T) and isotope (I) data for each compiled basalt glass in PetDB for which complete major element data is available (N = 13659, each represented by a column in the data matrix). This is a visual representation of a single data matrix that is $\sim$ 20 rows (each corresponding to a specific geochemical variable) per column and that has been arbitrarily segmented for visualization purposes. For a given sample and compositional variable, blue indicates data availability while white indicates an absence of data. Labels on the x-axis are arbitrary indices tracking sample numbers, and 'nz' for each segment indicates the number of available data values (the sum of all compositional variables available over all samples). Not all geochemical parameters compiled in PetDB are depicted: The most commonly reported isotope ratios (Sr, Nd and Pb), as well as ca. 15 selected trace element parameters were chosen to represent their respective categories of data. Note that a small fraction of MORB samples have even two out of three of these basic data categories measured on them. For this reason, we here focus on a multivariate analysis of MORB major element data.

Appendix C

Supplementary Material for Chapter 4

C.1 Methods of Sampling, Sample Preparation, and Geochemical Analysis

At each of 17 sampling sites, approximately 1 kg of sediment was collected from the wadi floor after sieving in the field had removed particles > 1 mm in size. A typical sampling site and recovered spinel sample are shown in Figure C-1. In practice, nearly any 10 m^2 area of wadi floor contained some concentration of fine sediment suitable for sampling, with the exception of narrow, distal tributaries that commonly consist of polished bedrock. To maximize the chance of obtaining a representative sample, material from each location was collected by shovel from at least 10 distinct, randomly selected spots within a ∼30m wide sampling zone spanning the full width of the wadi floor. This procedure was intended to strongly reduce the potential for biased sampling, e.g., from a single fragmented upstream boulder, which would result in artifacts such as frequency spikes of a single composition that are not representative of the true source rock variability throughout the drainage basin. We further separated the 500-710 μm size fraction in the laboratory for analysis. This size fraction was selected because larger size fractions consist almost completely of poly-crystalline fragments, while smaller size fractions are less easily processed, particularly with respect to preventing cross-contamination between different samples. After removal of alteration minerals using LST heavy liquid (density =2.85), spinels were hand-picked from the remaining concentrate, generally yielding between 100-200 spinel grains per 100 mL of the 500-710 μm grain size fraction extracted from each sediment sample. Spinel grains were mounted on microprobe stages using epoxy resin, and grain mounts were then ground down $\sim$ 50-100 μm to expose the fresh mineral interior of all grains. Spinel major element analyses were then obtained after polishing the grain mounts using the Cameca Sx 100 electron microprobe at The American Museum of Natural History. Between two and eight analyses were performed on each spinel

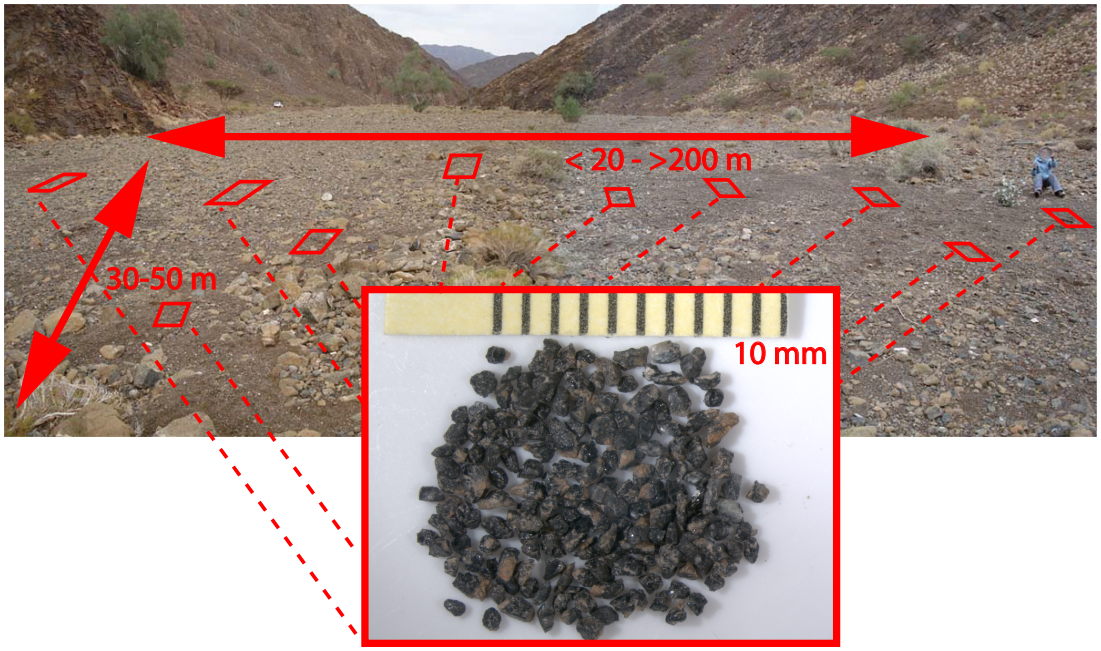

Figure C-1: Illustration of sampling site and method.

grain with a 5 μm electron beam size at 20 nA beam current and 15 kV accelerating voltage. Our calibration was evaluated through repeated measurements on independent standards KLB8315 and synthetic $MgCr_2O_4$. The mean of analyses from a given microprobe session recovered standard compositions with an accuracy of better than 0.001 in Cr# and 0.005 in TiO_2. Precision (reproducible over 4 microprobe sessions) in Cr# and TiO_2 was $\pm$ 0.002 and $\pm$ 0.015, respectively. In total, 1951 spinel grains from 17 locations were analyzed. Table C.1 provides the location and other attributes associated with each sampling site.

C.2 Spatial Characterization of Drainages

To evaluate the spatial extent of drainages corresponding to the source areas for our sampling sites, we draw on a digital elevation model (DEM) derived from the USGS/NASA Shuttle Radar Topography Mission C-band data (Jarvis A., H.I. Reuter, A. Nelson, E. Guevara, 2008, Hole-filled seamless SRTM data V4, International Centre for Tropical Agriculture (CIAT). This DEM is available on the internet from http://srtm.csi.cgiar.org). We extract the detailed network geometry of each drainage within the Wadi Tayin massif using a three-step procedure, originally developed for quantitative hydrologic modeling (*Tarboton et al.*, 1991). The first step is to "flood" all local topographic minima, known as pits, in the DEM. These features are generally data artifacts and, if uncorrected, can lead to inappropriate trunca-

Sample ID	*Lat. (deg. N)*	*Lon. (deg. E)*	*Contr. Area* (km^2)	*# Spin. Anal.*	*Variab. Type*
OM09SP24T	22.94284	58.41738	7.37	106	I
OM09SP42	22.95044	58.50113	11.88	113	I
OM09SP56	23.11166	58.45015	6.4	116	III
OM09SP17	22.91007	58.78116	11.38	89	I
OM09SP64	22.99162	58.31841	8.78	99	I
OM09SP06	23.09457	58.38617	20.55	143	III
OM09SP38	22.96794	58.4549	2.54	75	II
OM09SP40	22.96896	58.44087	2.67	69	II
OM09SP05	23.09457	58.38617	20.55	152	III
OM09SP14	22.94864	58.81414	6.49	53	III
OM09SP33	23.07095	58.42362	15.48	111	III
OM09SP52	23.12674	58.40994	7.82	126	III
OM09SP29	22.95028	58.47197	0.124	147	II
OM09SP15	22.96058	58.80206	3.63	123	III
OM09SP25	23.01269	58.43304	18.37	128	III
OM09SP26	23.01733	58.45087	4.24	131	III
OM09SP41	22.98163	58.44204	4.1	129	I
OM09SP31	22.96085	58.45914	3	41	II

Table C.1: Summary of key spatial and statistical attributes for each sampled location.

tions within inferred drainage networks, resulting in the extraction of numerous smaller, incompletely drained basins. By raising the elevation of internal pits to that of the nearest outflowing pixel, the topographic surface is made "drainable", allowing meaningful further analysis. Next, a drainage direction corresponding to the locally steepest gradient is assigned to each pixel using the algorithm of (*Tarboton*, 1997). Finally, an influence map is calculated which identifies the upstream pixels that drain through a given pixel. The contributing area for each pixel is computed by multiplying the total number of upstream pixels by the area corresponding to one pixel. Figure C-2 illustrates this process. Since each of our sediment sampling locations can be interpreted as "drainage outlets" for specific watersheds, we have calculated influence maps and contributing areas for the DEM pixels corresponding to each of our samples. This allows sampled catchments to be compared quantitatively. We used the MATLAB Upslope Area Toolbox implemented by Steven Eddins (available at MATLAB central file exchange) to perform these calculations.

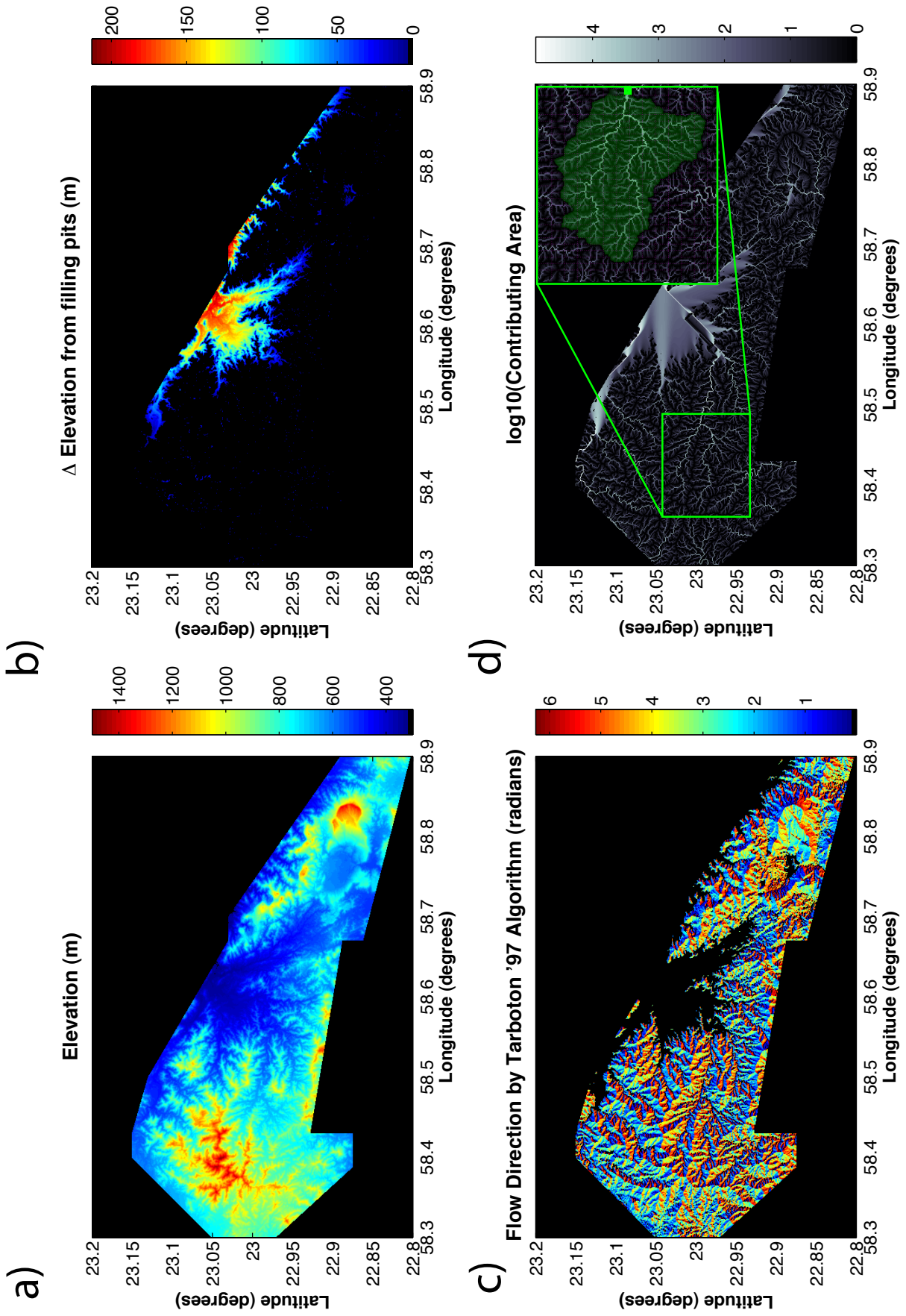

Figure C-2: Caption given on next page.

Figure C-2: Illustration of the procedure for calculation of drainage properties from a digital elevation data. Although calculations are performed over a larger area (WESN: [58,58.95,22.8,23.3]), surroundings outside the mantle section of the Wadi Tayin massif have been masked out for illustrative purposes. (a) Topography of the Wadi Tayin mantle section provides the input for the calculation. (b) Elevation changes to internal basins (generally due to data artifacts) within the DEM resulting from the "flooding" step. This allows all internal pixels to drain to the of the DEM edges, essential for further analysis. (c) Flow directions indicating the direction of the steepest local topographic gradient computed by the algorithm of *Tarboton* (1997). (d) Map of contributing areas derived from (c). Pixels with highest contributing areas correspond to the locations of wadi floors, while dark areas represent drainage divides. Shown as an inset is the dependence map (light green area) representing the drainage basin corresponding to a hypothetical sampling location shown as a green symbol at right.

C.3 Are Detrital Spinel Samples Representative of Variability Within the Source Catchment?

In order for our sediment samples to accurately represent the actual distribution of spinel variability within sampled catchment areas, the following criteria should be satisfied:

1. All locations within the catchment area have an equal probability of being represented in our sample. Equivalently, differential erosion and hydrological transport effects should be minimal.

2. The timescale of sediment transport is much smaller than the timescale over which erosion modifies the spatial geometry of drainage boundaries

3. Cross-contamination between adjacent wadis, e.g. by flooding or aeolian transport is negligible.

Although it is not possible to directly verify the validity of these criteria in the present study, we feel that several indirect arguments suggest that these criteria are met with an acceptable degree of confidence. Perhaps the most compelling argument in favor of accepting these assumptions is the strong spatial coherence of variability patterns observed throughout Wadi Tayin. In particular, spinel compositions should not display systematic variations with catchment area or inferred paleo-vertical depth if variability contained a large component of random errors resulting from violations of the above criteria. Furthermore, the relatively small length scales of drainages studied should minimize the potential for hydrologic sorting effects, and we observed no evidence for differential erosion rates in the major mantle lithologies discussed in this study. For these reasons, any violations of the above assumptions are likely to be minor. Additional support for the validity of our observational

approach may be found in the recent study by *Arai et al.* (2006). These authors report recovering compositional variability from detrital spinels in the Horoman ophiolite and Lizard peridotite complex that closely matched variability within in situ peridotite samples. As a further test of our assumption that detrital spinel compositions robustly reflect the proportions of each composition throughout a given drainage, we collected samples OM09SP05 and OM09SP06 from the same location, although purposely within slightly different hydrologic regimes to maximize the chance of sample-to-sample mismatch if our assumptions are violated (OM09SP05 was collected from a "hydraulic trap" or concentration of fine, dense minerals on the outside bend of the wadi channel, while OM09SP06 was collected from a "shelf" several meters higher up on the inside bend). According to our assumptions, both samples should yield identical variability patterns, regardless of the detailed sampling scheme used. The agreement between sampled spinel compositions and associated probability density estimates is shown in Figure C-3.

C.4 The Effect of Sample Size

See Figure C-4.

C.5 Probability Density Estimation

Statistical features within large sample size data sets often emerge more clearly when visualized in terms of an empirical probability distribution, since the high symbol density of scatterplots can make it difficult to evaluate the relative probabilities of compositions that are abundantly represented in the data. Visualization of probability densities also simplifies comparison between data sets and can allow the relative significance of outliers to be more easily appreciated. In this study, we estimate the probability densities of bivariate spinel compositions using the most basic multivariate kernel density estimator, the product kernel. Starting from a data set of n observations $[\vec{X}_1, ...\vec{X}_n]$, each comprising d attributes, we seek to estimate the probability density $f(\vec{x})$ from which our data was generated. The product kernel estimate, $\hat{f}_{pke}(\vec{x})$ is then given by:

$$\hat{f}_{pke}(\vec{x}) = \frac{1}{nh_1...h_d} \sum_{i=1}^{n} \left[\prod_{j=1}^{d} K\left(\frac{x_j - X_{ij}}{h_j} \right) \right] \tag{C.1}$$

where K is a kernel function, h_k denotes the bandwidth, and i tracks components while j tracks data attributes. The multivariate kernel function at each data point is thus the

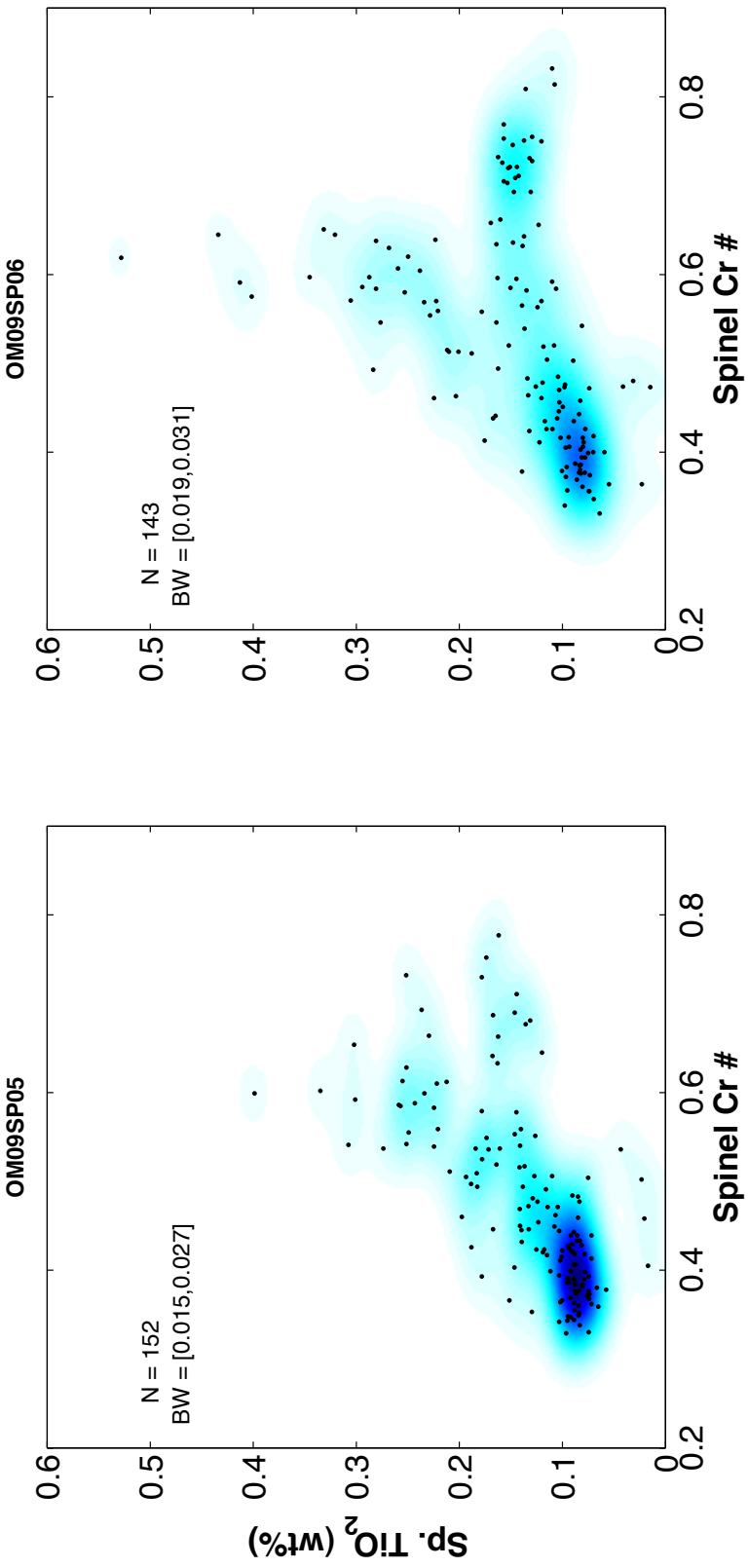

Figure C-3: Caption given on next page.

Figure C-3: Comparison of detrital spinel variability in two sediment samples collected from the same location. The agreement between these estimates supports the validity of the assumptions underlying this study.

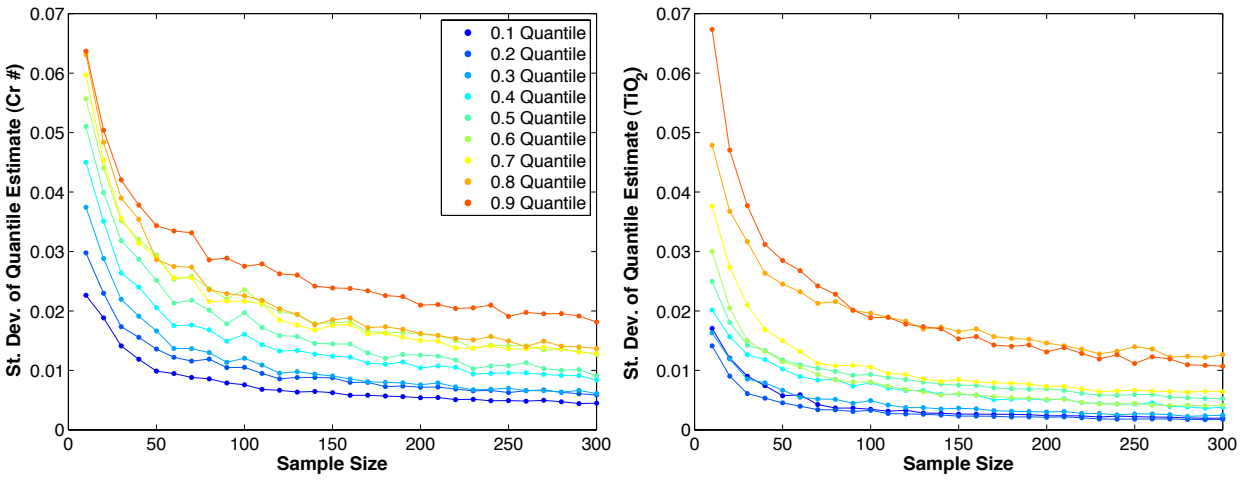

Figure C-4: Illustration of the relationship between robustness in descriptive statistics and sample size. For each of 500 bootstrap Monte Carlo samples from the pooled datasets OM09SP05 and OM09SP06 (both represent the same location), we estimated various quantiles characterizing the empirical probability densities of spinel Cr# and TiO_2. The standard deviation of replicate estimates for each quantile (at a given sample size) is shown here. The increased variability of higher quantiles reflects greater uncertainty in their value due to assymetry in the probability density and corresponding lower data density in the distribution tail. Although the quantile estimates remain sensitive to sample size above N = 300, the greatest reduction in quantile uncertainty occurs over the range N $\sim$ 50-150.

product of univariate kernels corresponding to each data dimension. We here employ a Gaussian kernel function:

$$K(t) = \frac{1}{\sqrt{2\pi}} \exp\left(\frac{-t^2}{2}\right) \tag{C.2}$$

The bandwidths h_k required for each univariate kernel were determined using the data-driven bandwidth selector of Z. I. Botev ("A Novel Nonparametric Density Estimator", Technical Report, The University of Queensland, manuscript available at `http://espace.library.uq.edu.au/eserv/UQ:12535/Nonparametric_estimation.pdf`). Bandwidths selected by this method correspond closely to those using the method of *Sheather and Jones* (1991). For additional information about multivariate probability density estimation, c.f. *Scott* (1992).

C.6 Cluster Analysis of Detrital Spinel Samples

Cluster analysis encompases a range of unsupervised data analysis algorithms for identifying structure in data sets. Based on some metric of "distance" or dissimilarity, the goal is to identify a natural partitioning of the data objects within a data set into a number of "clusters", each comprising those data objects that are most similar to each other. For our analysis, we have taken the Euclidean distance, D_{ij}, as our similarity metric, which between the ith and jth samples is given by:

$$D_{ij} = \sqrt{\left(\vec{X}_i - \vec{X}_j\right)^T \left(\vec{X}_i - \vec{X}_j\right)} \tag{C.3}$$

To compute D_{ij} between each of our 17 sampling locations, we evaluated the difference between kernel-smoothed probability density estimates of the local joint Cr#-TiO_2 distributions on a pixel-by-pixel basis. Given D_{ij}, we then applied each of the five main hierarchical clustering algorithms for assigning clusters (single, complete, average, centroid, and Ward's linkage, for more information, c.f. *Hair et al.*, 2005), finding that each gives similar results. An example of the output from this analysis is shown in the dendrogram at the bottom of Figure C-5. The higher up links between samples or clusters are depicted in this figure (horizontal bars), the greater their dissimilarity. K-means clustering provides another commonly used algorithm for clustering in which the grouping of data objects that minimizes the intra-group sum of squares is determined (*Hair et al.*, 2005), although the number of clusters involved must be specified in advance by the user. We find very good agreement between K-means output and results from hierarchical clustering. Furthermore we find that quantitative clustering methods support a subjective partitioning of detrital spinel data from Wadi Tayin into three categories which we determined in advance through visual inspection of the data. The three category classification presented in the main text is therefore robust, and is

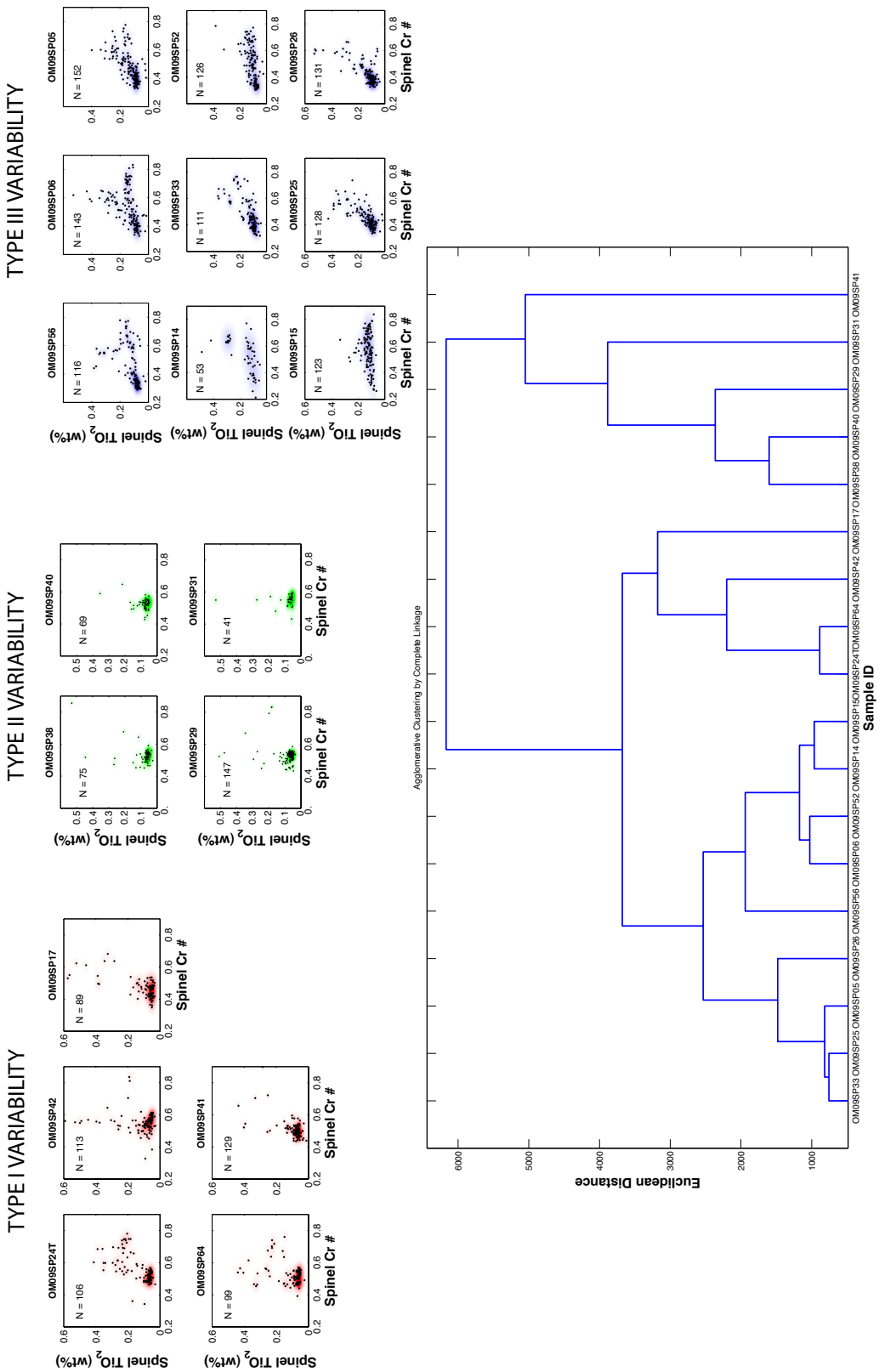

Figure C-5: Caption given on next page.

Figure C-5: (top) Detrital spinel variability patterns observed at each of 17 drainages are shown, grouped according to the robust classification emerging from a range of quantitative clustering algorithms. (bottom) A dendrogram illustrating the relative similarity of variability patterns facilitates hierarchical clustering. See accompanying text for discussion.

discussed further in the text. The MATLAB statistics toolbox contains implementations of all methods employed in this analysis.

C.6.1 Constructing inferences on spinel variability throughout Wadi Tayin from data with heterogeneous spatial coverage

In principle, the data presented in this study allows the distribution of spinel variability throughout Wadi Tayin to be estimated, which is equivalent to estimating the conditional probability of observing a given spinel composition, once it is specified that the spinel originated somewhere in the mantle section of the Wadi Tayin massif. (Such a probability density estimate could be used by future studies, e.g., for statistical comparison with variability from other localities). We have sampled 17 drainages, with combined contributing area ~ 130 km^2, which comprise $\sim$ 10-15% of the total mantle exposure at Wadi Tayin. However, the data from each of our sampling locations represents a different catchment area, and thus, a different fraction of the total region of interest. A data set of "Wadi Tayin spinel compositions" derived from simply pooling all available spinel analyses from all sample locations will therefore contain spatial biases in sampling, with some portions of Wadi Tayin represented by a larger number of spinel analyses per km^2 while other areas are relatively under-represented. We account for such catchment-to-catchment differences in sampling density by an additional random resampling step. For each sampling location, we draw (with replacement) from all available data a number of spinel analyses proportional to the contributing area of the drainage. Thus, for small drainages, analyses are effectively subsampled, while for larger drainages, the number of draws can exceed the number of analyses available. This procedure is also known as bootstrap sampling (e.g., *Efron and Tibshirani*, 1994), and is premised on the approach of using the data itself to approximate the true underlying distribution of variability (which is unknown and potentially complicated). The next step is to pool the randomly resampled data from all locations. The resulting compilation then contains the best available approximation to spatially independent sampling from throughout Wadi Tayin at a constant sampling density. Here, we use a normalized sampling density of ~ 14 km^{-2}, chosen so that the resampled number of data points is close to the total number of available analyses, with a minimum number of drainage basins represented by more random

samples than original data points. Repeatedly carrying out this procedure leads to a number of kernel-smoothed probability density estimates for the spinel variability throughout Wadi Tayin. Our final estimate of this probability density (in terms of Cr# and TiO_2) is shown as an inset to Figure 4-1 and depicts the median value of each Cr#-TiO_2 pixel after normalization ($\sum_i p(Cr\#_i, TiO_{2,i}) = 1$), summarizing 100 independent realizations of the random sampling and density estimation procedure described above.

C.7 Structural Model of Wadi Tayin Mantle

To facilitate our analysis, we have created a simple structural model allowing the vertical depth relative to the crust-mantle boundary to be estimated for any location within the Wadi Tayin mantle, illustrated in Figure C-6. We have extracted all strike and dip measurements taken on cumulate layered gabbros proximal to the crust-mantle transition at Wadi Tayin (1:100,000 geologic maps of the Samad and Ibra Quadrangles, Oman Bureau of Minerals and Petroleum), and we interpret these as proxy paleo-horizontal surfaces. We furthermore assume that these orientations may be extrapolated throughout the Wadi Tayin mantle section. The inferred vertical distance beneath the crust-mantle transition, Z_{cmt}, is then calculated as follows, with the numerical values of parameters reflecting regionally averaged strike and dip measurements:

$$\left.\begin{array}{ll} Z_{cmt}(lat,lon) = \frac{(1.0934lon+lat-86.7141)}{\sqrt{2.1955}} \times sin(40^\circ) \times 111(km/deg.) & WMSZ \\ Z_{cmt}(lat,lon) = \frac{(0.1666lon+lat-32.6595)}{\sqrt{1.0278}} \times sin(30^\circ) \times 111(km/deg.) & EMSZ, lon \leq 58.67^\circ \\ Z_{cmt}(lat,lon) = \frac{(0.2576lon+lat-37.9776)}{\sqrt{1.0664}} \times sin(60^\circ) \times 111(km/deg.) & lon > 58.67^\circ \end{array}\right\} \quad \text{(C.4)}$$

where latitude and longitude are specified in decimal degrees, position relative to the Makhibiyah SZ (MSZ) is specified by "EMSZ" or "WMSZ", and Z_{cmt} is in km. The MSZ is defined by coordinates:

$$\begin{bmatrix} lat \\ lon \end{bmatrix} = \begin{bmatrix} 23.05 & 22.95 \\ 58.33 & 58.4 \end{bmatrix}$$

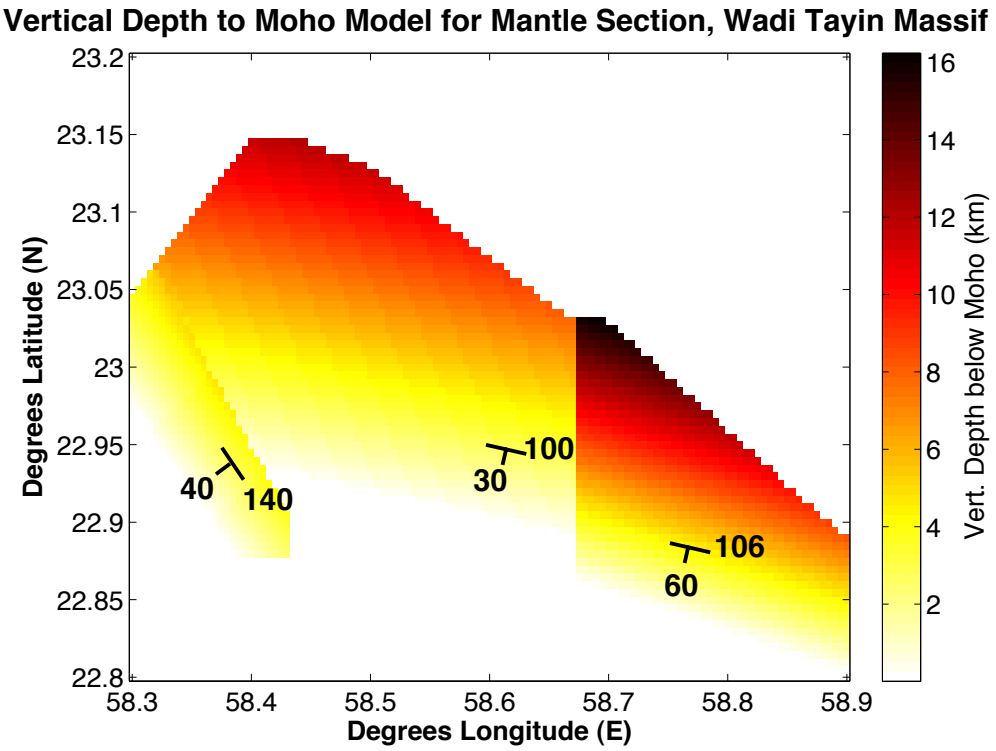

Figure C-6: Simplified model depicting the inferred vertical depth beneath the crust-mantle transition for the entire Wadi Tayin mantle section. Note that the primary constraint of this model is the orientation of layered gabbro units near the crust-mantle transition. The large discontinuity in estimated mantle depth at $\sim$ 58.68 degrees E therefore reflects a significant change in the fabric of overlying units and should not be interpreted as a mantle structure. No sampled catchments are located near this discontinuity, and it does not impact the results of our study. By contrast, the discontinuity at $\sim$ 58.4 degrees E reflects the Makhibiyah shear zone, a well known mantle structure (*Nicolas and Boudier*, 2008). Strikes and dips shown summarize regionally averaged orientations of layered gabbros near the crust-mantle transition, and are assumed to be constant throughout each mantle region.

C.8 Interpreting Geochemical "Images" of Mantle Variability

The present study seeks to "image" spatial variability in mantle compositions through random sampling over spatially bounded regions. Although we have generally sampled mantle variability on the $\sim$ 1-5 km length scale, we discuss here in additional detail how the statistical character of our observations can constrain the presence or distribution of mantle variability over a much wider range of length scales. A key variable governing the relationship between geochemical variability in the mantle and its observational expression is the relative magnitude of the length scales characterizing "mantle heterogeneities" (which we define as any spatially coherent mantle domains throughout which geochemical variability can be modeled by sampling from a single probability distribution) compared to the spatial length scales over which sampling occurs. To illustrate this point, we discuss three basic cases, illustrated in Figure C-7. Only when the length scale of sampling is significantly smaller than the length scale of heterogeneity (Case 1) can the spatial distribution of individual spatially coherent features or heterogeneities in the form of 'blobs' or 'veins' be explicitly mapped. In this case, when different sampling regions are commonly completely within mantle outcrop corresponding to a single such feature, variations in their sampling length scale or location will generally not – by definition – change the observed relative proportions of different compositions, except for cases when sampling regions exceed the boundary delimiting the extent of the heterogeneity. Thus, the boundaries of individual mantle heterogeneities would be detectable by plotting the spatial extent of different sampling regions in a manner reflecting the locally inferred variability found within. In the second case, when the length scale of sampling is comparable to that of mantle heterogeneity, the observational approach of this study can severely blur the boudaries delimiting individual geochemically distinct mantle heterogeneities, and it can be impossible to cleanly map such mantle domains. However, this case generally yields a distinctive and diagnostic observable effect: Relatively small changes in the sampling length scale can correspond to systematic, significant changes in the observed statistical distribution of variability within samples. In mantle characterized by heterogeneities that are of comparable spatial extent to sampling areas, any changes in the spatial extent between two specific sampling areas will likely result in each sampling a different proportion compositionally distinctive mantle regions. With respect to any specific mantle heterogeneity, larger sampling areas that are centered on this heterogeneity will, in general, sample a higher proportion of mantle that is outside the limits of that heterogeneity, while smaller sampling regions centered on the same feature will reflect less influence from the surroundings. As a result, systematic changes in the locally inferred

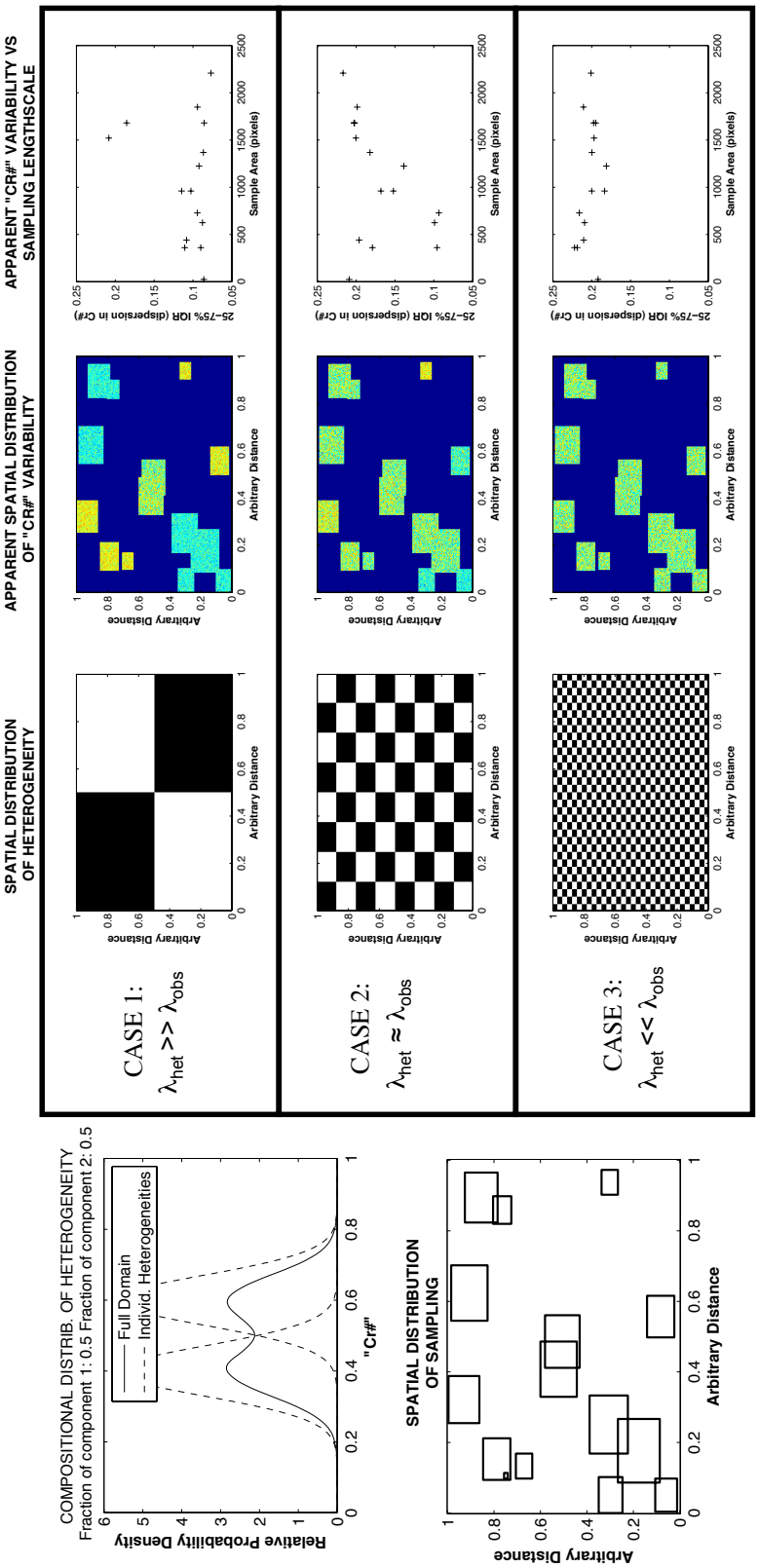

Figure C-7: Caption given on next page.

Figure C-7: Simulated random sampling from three synthetic "mantle heterogeneity" patterns illustrating the way the character of observed variability is dependent on the length scale of mantle heterogeneity, λ_{het}, relative to the sampling length scale, λ_{obs}. For each case, two compositional domains (shown as "black" vs "white" areas in the left panel corresponding to each case) are distributed in spatial arrangements corresponding to end-member relationships in relative length scales. The distribution of synthetic "Cr#" variability within each compositional domain, as well the total geochemical variability throughout the synthetic "mantle outcrop" is shown in the top panel at far left, and is identical in all cases. The randomly generated sampling areas, indicated by rectangles in the bottom panel at far left, are intended to mimic the observational method of this study. We have plotted the spatial pattern of synthetic variability in each case in the corresponding central panel, while variability in each synthetic sample is plotted in the right panel for each case. These plots are based on $\sim$ 200 synthetic "Cr#" analyses per sample area generated by sampling from the statistical mixture model defined by the probability densities governing each individual component, weighted by the local proportion of each component in the sampling area. Further discussion is provided in the text.

distribution of mantle compositions can emerge, especially when the comparative internal variability between the reference heterogeneity discussed here and the surrounding mantle is very different. The specific change in statistical variability to be expected cannot be easily predicted without knowledge of the underlying pattern of mantle variability. However, since systematic relationships between the variability of mantle samples and their length scale are not predicted by either of the other cases discussed here, such relationships are nevertheless diagnostic of the presence of mantle heterogeneity at the approximate length scale of sampling. In the final case, (Case 3) the length scale of sampling is significantly larger than the length scale of heterogeneity. Here, geochemical variability within a given sample represents the aggregated geochemical contribution of numerous small-scale features or heterogeneities, while information about the corresponding spatial distribution of heterogeneity is completely lost. In this case, the mantle appears "homogeneously heterogeneous" in that multiple sampling regions with different length scales or locations will all yield the same statistical distribution of internal mantle variability. We feel that all three cases are required to explain the spinel variability documented in this study, illustrated in Figure C-8. While our mapping of spatially coherent regions corresponding to variability types I, II and III corresponds to the first case described above, the positive correlation between observed variability and sampling length scale appears to require the existence of mantle heterogeneity at the length scale of sampling. The internal variability within each sampled watershed reflects the third case, where any features that are much smaller than sampled drainages are represented in proportion to their abundance in the outcrop, integrated over spatial scales comparable to sampled drainages.

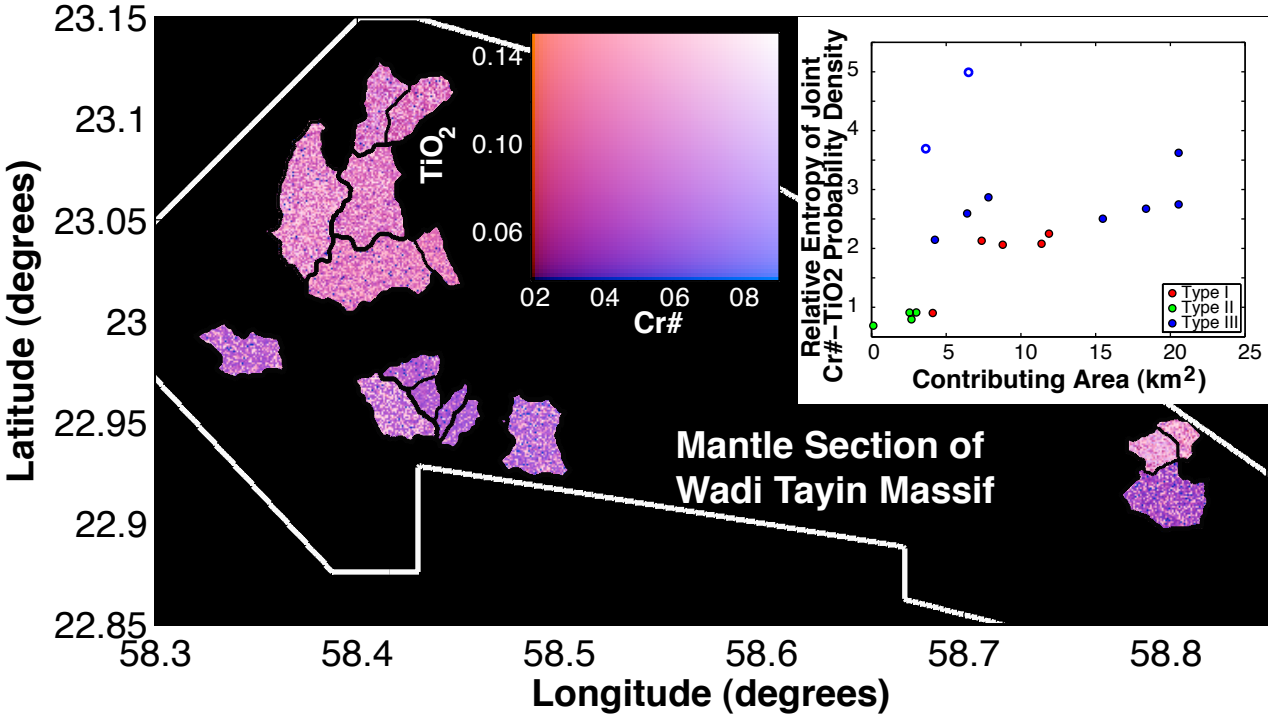

Figure C-8: Geochemical image of detrital spinel variability within Wadi Tayin, comparable to the output of simulation depicted in the previous Figure. Each pixel within a given drainage is assigned a color corresponding to a randomly selected spinel analysis from that catchment. Bivariate composition-color mapping is shown as inset. The corresponding catchment area-variability systematics are illustrated in a further inset using the relative entropy, $H(\vec{P})$, of each probability density estimate, a bivariate measure of the relative randomness of the detrital spinel data from each catchment. This quantity is computed using $H(\vec{P}) = -\sum_{i=1}^{S} p_i \log_2 p_i$, where $\vec{P}$ denotes the relative frequencies, p_i, of all S possible states that the probability density may take. Because gray-scale images are commonly assigned integer values between 0 and 255, we have binned our continuous spinel probability density estimates correspondingly (a probability density of zero corresponds to zero, while the maximum corresponds to 255) to make use of MATLAB's image processing toolbox function "entropy.m". This binning scheme is arbitrary and the use of other binning schemes or logarithm bases will yield quantitatively different values of $H(\vec{P})$ than shown here, although the 'relative entropies' shown will not differ. Note that compositional variability in samples with greater Moho-depth (type III variability) do not display sensitivity to the sampling length scale, while those closer to the Moho do. Sample sizes at each drainage vary between ~ 50 and 150 samples, c.f., Figure C-5 in this Appendix for more details. Individually considered, Cr# and TiO_2 also display the same systematics (c.f., Figure 4-2 of the main text, where symbols are explained in caption).

C.9 Recovery of Information About Source Rock Lithology Using a Linear Bayes Classifier

Detrital spinel grains do not retain a direct record of the source rock lithology from which they derive. However, different mantle lithologies (e.g., dunites versus harzburgites) generally contain spinels with statistically distinctive compositions. We here use a Bayesian statistical framework to classify detrital spinel compositions by their most likely source lithology, and use this classification to recover information about relative lithologic abundances within sampled mantle regions. For each lithology considered, a statistical model is generated to describe the likelihood of observing a given spinel composition, provided that it is sourced from this lithology. The relative likelihood of all considered lithologies is then evaluated as a function of spinel composition, allowing classification boundaries to be computed. The posterior probability $p\left(l|C_s\right)$ that a specific lithology, e.g., $l = [\text{“}Hz\text{”}; \text{“}Du\text{”}]$ has given rise to an observed detrital spinel composition $C_s = [Cr\#, TiO_2]$ is given by Bayes' theorem:

$$p\left(l|C_s\right) = \frac{p\left(C_s|l\right)p\left(l\right)}{p\left(C_s\right)} \tag{C.5}$$

We assume conditional independence of Cr# and TiO_2, given some l, to obtain the linear naive Bayes classifier f_{nb}:

$$f_{nb}\left(C_s\right) = \underset{l}{\operatorname{argmax}}\, p(l)p\left(Cr\#|l\right)p\left(TiO_2|l\right) \tag{C.6}$$

where $p\left(Cr\#|l\right)$ and $p\left(TiO_2|l\right)$ are provided by gaussian fits to training data, with maximum likelihood means estimated individually for each lithology, while the variance is estimated from the pooled data. It is not necessary to determine $p(C_s)$ as it is common to the posterior probabilities of all lithologies, and thus cancels out. For this study, we have compiled training data – shown in Figure 4-3 of the main text – consisting of previously published spinel analyses comprising 88 spinels from dunites and 129 spinel measurements from harzburgites, as well as 113 pyroxenites. 50 of the spinel data from dunite or harzburgites, additionally, have been identified as transitional, in that they represent harzburgites collected within 1 m of the boundary to large dunites and/or small dunites surrounded by abundant harzburgite. Although we recognize that our data compilation is influenced to some extent by spatially dependent sampling, we have used it “as is” since correcting for spatial inter-dependences (e.g., multiple measurements from the same dunite) would lead to a large decrease in sample size. It is understood that these probabilities are strictly applicable only to the southern massifs of the Oman ophiolite. Although it is desirable to incorporate the most accurate

estimates of the relative abundances of different components as prior information into this type of analysis, these proportions remain relatively poorly constrained. For each of the lithologic components introduced in the main text, we have employed priors that reflect the dominance of harzburgite as the primary lithology, and that comprise geologically reasonable upper bounds on the proportions of the other, non-harzburgite components within each classification scheme. In our 2-component classifier we have used $p(Du) = 0.3$, $p(Hz)$=0.5, while in our 3-component classifier we have used $p(Du) = 0.35$, $p(Hz)$=0.5 $p(Px)$=0.15, and our 4-component classifier uses $p(Du)$=0.2 $p(Hz)$=0.5 $p(PLTD)$=0.1 $p(Hz - Du)$=0.2. Use of other priors can result in significant changes in, e.g., estimated dunite proportions relative to the ones reported here. The sensitivity of estimates of relative lithologic proportions is most important where the data from different lithologies display the most overlap. Tables C.2 and C.3 summarize the results of our two, three and four component classifiers. Once classification boundaries have been computed, the proportion of any specific mantle lithology can be estimated by integrating the distribution of spinel compositions representing a region of interest over the compositional interval demarcated by the appropriate classification boundaries. For example, integrating the detrital spinel probability density over all compositions with greater TiO_2 at a given Cr# compared to the linear, "2-Lithology" classification boundary shown at left in Figure 4-3 would provide an estimate of the local dunite proportion.

C.10 Additional remarks on the classification of mantle lithologies at Wadi Tayin

The distribution of spinel variability throughout Wadi Tayin displays complexity, including multiple primary modes and at least two Cr#-TiO_2 trends defining distinct distribution tails (c.f., the inset of Figure 4-1). To maximize confidence in our interpretations of this complexity, we seek to incorporate the best available knowledge of the likely lithologic components reflected in the data in the design of our classification scheme. We prefer a quaternary classification scheme (discussed in the previous section) because it is relatively simple, but also avoids inconsistencies between the variability expressed in detrital spinel samples versus in the available training data for each lithology. To illustrate such a potential inconsistency, we note that of the two distribution tails characterizing Wadi Tayin spinel variability, only the tail with higher TiO_2 at a given Cr# appears to correspond with spinel from dunite samples contained in our training data compilation (which in turn only comprises data from the southern Oman ophiolite). Neither distribution tail corresponds well with harzburgite

Sampling Location	*Lithology Fractions from 2, 3 and 4 Component Classifiers (%)*								
	Hz	Du	Hz	Du	PLTD	Hz	Du	PLTD	Hz-Du Transit.
OM09SP24T	92	8	80	7	13	71	4	8	17
OM09SP42	92	8	80	8	12	79	6	10	5
OM09SP56	98	2	80	5	15	72	3	14	11
OM09SP17	91	9	90	10	$<< 1$	89	8	$<< 1$	3
OM09SP64	95	5	88	5	7	83	4	4	9
OM09SP05+06	96	4	83	4	13	73	2	12	13
OM09SP38	97	3	94	3	3	94	3	2	1
OM09SP40	99	1	98	1	< 1	97	1	$<< 1$	2
OM09SP14	87	13	73	12	15	62	4	11	23
OM09SP33	93	7	86	5	10	80	2	6	12
OM09SP52	99	1	80	01	19	76	1	18	5
OM09SP29	97	3	96	2	2	95	2	2	1
OM09SP15	99	1	65	1	34	59	$<< 1$	32	8
OM09SP25	94	6	91	8	1	86	5	$<< 1$	9
OM09SP26	94	6	93	6	1	90	4	1	5
OM09SP41	96	4	95	3	2	95	2	1	2
OM09SP31	97	3	93	3	4	92	2	3	3

Table C.2: Proportion of lithologies inferred at each sampling location using the linear Bayes classifiers. PLTD refers to pyroxenite and low-TiO_2 dunite.

Classifier	*Harzburgite Fraction (%)*	*Dunite Fraction (%)*	*PLTD Fraction (%)*	*Hz-Du Transitional Fraction (%)*
2-Comp.	94	6	–	–
3-Comp.	85	6	9	–
4-Comp.	79	4	8	9

Table C.3: Proportion of lithologies throughout Wadi Tayin inferred from the linear Bayes classifiers applied to randomly subsampled data, as discussed in the main text.

compositions. Application of a simple two-component (dunite, harzburgite) classifier to this data set would then lead to a conundrum: "How can the lower TiO_2 distribution tail be reliably classified, since neither dunite nor harzburgite training data provide a good explaination of these spinel compositions?" The studies of, e.g., (*Augé*, 1987; *Tamura and Arai*, 2006) demonstrate that spinel compositions plotting within the lower-TiO_2 distribution tail correspond well with those found in dunites from northern Oman, consistent with a more arc-like igneous environment (*Dick and Bullen*, 1984; *Suhr et al.*, 2003). Yet previous studies (e.g., *Hanghøj et al.*, 2010, and references therein) also demonstrate that such high Cr# spinels are very rare in dunites and harzburgites in the Wadi Tayin mantle section, and the training data compilation used to calibrate our classification scheme only contains one dunite analysis from southern Oman that plots within this low-TiO_2 dunite field. Instead, the "depleted suite" pyroxenites identified by *Benoit et al.* (1996); *Kelemen et al.* (1997b); *Python and Ceuleneer* (2003); *Python et al.* (2008) appear to be most consistent with lower-TiO_2, high Cr# detrital spinel compositions. There is potentially further complexity arising from the presence of additional, minor lithologic heterogeneities within Wadi Tayin (e.g., *Nicolas*, 1989; *Kelemen et al.*, 1997a; *Python and Ceuleneer*, 2003). Correspondingly, there is no single, unambiguous choice of lithologic components that should be used to model mantle variability at Wadi Tayin, although additional constraints on this question may be expected as further data accumulates. As it is beyond the scope of this study to assess competing interpretations of lower-TiO_2, high Cr# detrital spinel compositions in detail, we will refer to the lithology generating these compositions through the neutral terminalogy "pyroxenite and low-TiO_2 dunite" (PLTD). We have chosen to incorporate one further compositional component into our preferred classifier, the so-called transitional peridotite lithology consisting of either harzburgite in close proximity ($\leq$ 1 m) to large intervals of dunite (or vice versa). This reflects recent evidence that spinel compositions within harzburgite and dunite can be influenced by the presence of nearby, large quantities of other lithologies (*Braun*, 2004).

It is noteworthy that drainages with elevated PLTD contents – as well as the drainage with the single highest inferred dunite content – are generally proximal to metamorphic sole defining the ophiolite's basal detachment. Additional dunite-rich locations are in close spatial proximity to the Makhibiyah shear zone (*Nicolas and Boudier*, 2008). Elevated dunite contents at each of these locations could reflect localized, reactive melt transport (*Kelemen et al.*, 1995), as discussed further in the main text. Recent field work has also revealed that the Makhibiyah catchment labeled 05+06 in Figure 4-1 contains elevated abundances of secondary igneous dikes in addition to the presence of dunite (e.g., *Nicolas and Boudier*, 2008; *Homburg et al.*, 2010), similar to those documented by *Python and Ceuleneer* (2003).

Both higher and lower TiO_2 distribution tails are expressed in the spinel variability at this location (shown in Figure C-3), respectively corresponding to expectations for dunite and PLTD lithologies. If PLTD is assumed to fully account for the lower TiO_2 distribution tail throughout the Type III variability region of Wadi Tayin, then outcrop abundances of this lithology would be inferred to be greater than 15%. This is not consistent with most field observations, but Kelemen, Gnos and Kogg (pers. comm.) observed a gabbronorite to websterite pluton comprising several square kilometers in outcrop in 1994 during reconnaissance field work within the region comprising the head of the Wadi Miss drainage, so it is possible that the spinel classification process is confirming this qualitative observation.

C.11 Parameterization of dunite width as a function of spinel TiO_2 content

Recent work by (*Braun*, 2004) has demonstrated that the TiO_2 content of spinels within dunites is sensitive to the width of dunites, with spinels in the interior of larger dunites displaying higher TiO_2. We have parameterized the results of that study through the simple polynomial relationship between spinel TiO_2 and dunite width w_{Du}:

$$w_{Du} = 306.24 \times (TiO_2)^2 - 118.55 \times (TiO_2) + 11.76 \tag{C.7}$$

Combining this relationship with the detrital spinel compositions of this study that have been classified as corresponding to dunite or transitional lithologies (c.f., the previous section of this Appendix) allows the relative frequency of dunite widths to be estimated, as discussed further in the main text.